TU Delft

Delft University of Technology

Quantum Sensing and Fabrication of Color Centers in Diamond
Toward a Quantum Biosensor based on CMOS-integrated NV Centers

Varveris, I.

DOI
10.4233/uuid:5f51d2c5-6e96-4409-a14d-e18d0d04ff45

Publication date
2026

Document Version
Final published version

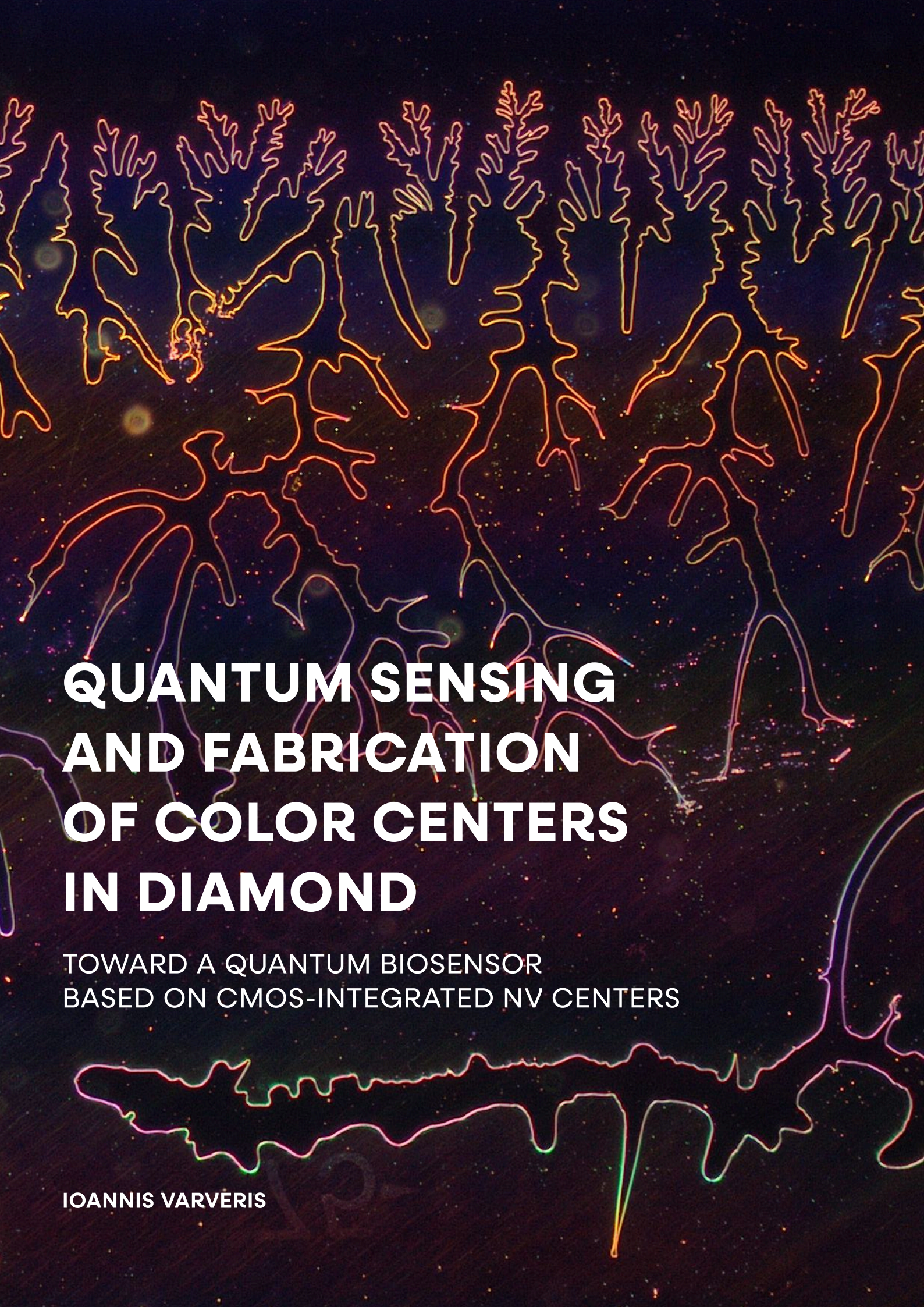
Citation (APA)
Varveris, I. (2026). *Quantum Sensing and Fabrication of Color Centers in Diamond: Toward a Quantum Biosensor based on CMOS-integrated NV Centers*. [Dissertation (TU Delft), Delft University of Technology]. https://doi.org/10.4233/uuid:5f51d2c5-6e96-4409-a14d-e18d0d04ff45

Important note
To cite this publication, please use the final published version (if applicable).
Please check the document version above.

Copyright
Other than for strictly personal use, it is not permitted to download, forward or distribute the text or part of it, without the consent of the author(s) and/or copyright holder(s), unless the work is under an open content license such as Creative Commons.

Takedown policy
Please contact us and provide details if you believe this document breaches copyrights.
We will remove access to the work immediately and investigate your claim.

This work is downloaded from Delft University of Technology.
For technical reasons the number of authors shown on this cover page is limited to a maximum of 10.



QUANTUM SENSING AND FABRICATION OF COLOR CENTERS IN DIAMOND

TOWARD A QUANTUM BIOSENSOR BASED ON CMOS-INTEGRATED NV CENTERS

IOANNIS VARVERIS

QUANTUM SENSING AND FABRICATION OF COLOR CENTERS IN DIAMOND

TOWARD A QUANTUM BIOSENSOR BASED ON CMOS-INTEGRATED NV CENTERS

QUANTUM SENSING AND FABRICATION OF COLOR CENTERS IN DIAMOND

TOWARD A QUANTUM BIOSENSOR BASED ON CMOS-INTEGRATED NV CENTERS

Dissertation

for the purpose of obtaining the degree of doctor
at Delft University of Technology,
by the authority of the Rector Magnificus, Prof.dr.ir. H. Bijl,
chair of the Board for Doctorates,
to be defended publicly on **Wednesday 28 January 2026 at 10:00 o'clock**

by

Ioannis VARVERIS

This dissertation has been approved by the promotors.

Composition of the doctoral committee:

Rector Magnificus,	Chairperson
Dr. R. Ishihara,	Delft University of Technology, *promotor*
Dr. S. Nur,	Delft University of Technology, *copromotor*
Independent members:	
Prof. dr. P.J. French	Delft University of Technology
Prof. dr. B. Juliá-Díaz	University of Barcelona, Spain
Dr. ir. B.J. Hensen	Leiden University
Dr. R.H.M. van Veldhoven	Delft University of Technology / NXP Semiconductors
Prof. dr. ir. R.E. Kooij	Delft University of Technology, reserve member



Keywords: quantum sensing, NV centers, SnV centers, optically detected magnetic resonance, ODMR, biosensing, SPAD array, CMOS integration, diamond fabrication, quantum integration technology

Copyright © 2026 by I. Varveris
All rights reserved. No part of this book may be reproduced, stored in a retrieval system, or transmitted, in any form or by any means, without prior permission from the copyright owner.

ISBN 978-94-6518-223-0

An electronic version of this dissertation is available at
http://repository.tudelft.nl/.

Dedicated to my grandparents <3

Ioannis Varveris

CONTENTS

Summary xi

Samenvatting xiii

Nomenclature xv

1 Introduction 1
- 1.1 Quantum biosensing: A brief introduction . . . 2
  - 1.1.1 NV center-based quantum biosensing overview . . . 3
- 1.2 What is an NV center? . . . 4
- 1.3 CMOS technology integration: State-of-the-art . . . 6
- 1.4 NV-based strain sensing for 3D quantum hardware integration . . . 7
- 1.5 Evaluating SnV centers for quantum sensing and 3D-integrated quantum computing . . . 8
- 1.6 Research Goals . . . 10
- 1.7 Dissertation overview . . . 13

2 Color centers in diamond: Theory, ODMR & biosensing 21
- 2.1 Diamonds: An introduction . . . 22
  - 2.1.1 Diamond classification . . . 22
  - 2.1.2 Diamond coloration . . . 23
  - 2.1.3 The diamond crystal structure . . . 24
  - 2.1.4 Color centers in diamond . . . 25
- 2.2 NV centers in diamond . . . 26
  - 2.2.1 Atomic Structure . . . 26
  - 2.2.2 A quick overview of the neutral state NV^0 . . . 28
  - 2.2.3 The negatively charged state NV^- . . . 29
  - 2.2.4 Electronic and optical properties . . . 29
  - 2.2.5 Microwave driving and magnetic properties . . . 32
  - 2.2.6 Spin relaxation and decoherence times . . . 33
  - 2.2.7 NV Hamiltonian . . . 37
- 2.3 SnV centers in diamond . . . 42
  - 2.3.1 Atomic Structure . . . 42
  - 2.3.2 Electronic and Optical Properties . . . 43
  - 2.3.3 Effect of magnetic field and microwave driving in spin state manipulation . . . 44
  - 2.3.4 Emission, coherence, sensitivity . . . 45
  - 2.3.5 SnV Hamiltonian . . . 46

2.4 Introduction to ODMR . . . 47
2.4.1 Fundamentals of ODMR . . . 47
2.4.2 Continuous-wave (CW) vs. pulsed ODMR . . . 48
2.5 ODMR Experimental Setup . . . 50
2.5.1 Excitation laser . . . 50
2.5.2 Neutral-density filter . . . 52
2.5.3 Steering mirrors and alignment irises . . . 52
2.5.4 Variable attenuation optics system . . . 52
2.5.5 Dichroic mirror . . . 53
2.5.6 Objective lens . . . 53
2.5.7 Microwave Delivery System . . . 53
2.5.8 Piezoelectric scanning stage . . . 55
2.5.9 Magnet-housing plate & detachable sample mounting plate . . . 55
2.5.10 External magnetic field control and application . . . 57
2.5.11 Magnetic shielding metal plates . . . 58
2.5.12 Longpass filter . . . 59
2.5.13 Fiber-coupling system . . . 59
2.5.14 Photodetection and time-tagging . . . 59
2.5.15 Arbitrary Waveform Generator (AWG) & MW power amplifier . . . 59
2.5.16 Keplerian beam expander . . . 61
2.5.17 Digital camera & white LED . . . 63
2.5.18 Spectrometer . . . 63
2.6 Software implementations overview . . . 64
2.6.1 Serpentine scan . . . 64
2.6.2 Tilt correction . . . 64
2.6.3 Periodic auto-zeroing . . . 65
2.6.4 Z-scan . . . 65
2.7 Methods . . . 66
2.7.1 Diamond sample mounting . . . 66
2.7.2 Measurement preparation . . . 66
2.7.3 Running the measurement . . . 67
2.8 Biosensing with ODMR . . . 68
2.8.1 The biosample: HEK cells . . . 68
2.8.2 Superparamagnetic iron oxide nanoparticles (SPIONs) . . . 68
2.8.3 Diamond preparation, cell culture & SPION incorporation . . . 70
2.8.4 ODMR biosample measurement method . . . 71
2.9 Experimental Results and Analysis . . . 73
2.10 Conclusion . . . 77

3 Fabrication & ion implantation of NV and SnV centers 89
3.1 Introduction to color center fabrication . . . 90
3.1.1 A brief recapitulation of diamond types . . . 90
3.2 Diamond growth methods . . . 91
3.2.1 Chemical Vapor Deposition (CVD) . . . 91
3.2.2 High-Pressure High-Temperature (HPHT) . . . 92
3.2.3 Diamond cutting & crystallographic planes . . . 93

3.3 Ion Implantation Methods . . . 95
3.3.1 Broad beam implantation . . . 95
3.3.2 Single ion implantation: Focused Ion Beam (FIB) . . . 97
3.4 Diamond overgrowth . . . 99
3.5 Annealing techniques . . . 100
3.5.1 Furnace annealing . . . 100
3.5.2 Laser annealing . . . 101
3.6 Simulation & Fabrication of color centers . . . 103
3.6.1 Introduction to mask implantation preparation, simulation & fabrication processes . . . 103
3.6.2 Simulations of masks for NV centers . . . 103
3.6.3 Simulations of masks for SnV centers . . . 108
3.6.4 Cleanroom fabrication of SnV centers . . . 115
3.6.5 Substrate preparation for single ion implantation using FIB . . . 125
3.7 Optical characterization of Sn-implanted diamond substrates . . . 129
3.7.1 Characterization following overgrowth . . . 129
3.7.2 Characterization following annealing . . . 132

4 Strain effects in a directly bonded diamond-on-insulator substrate 141
4.1 Introduction to integration technology . . . 142
4.2 Direct bonding process overview . . . 143
4.3 Strain effects in the DOI system . . . 146
4.3.1 Origin and mechanisms of strain in directly bonded DOI structures . 146
4.3.2 Strain physics in NV centers . . . 147
4.4 Method . . . 150
4.5 Results and Discussion . . . 153
4.6 Conclusion . . . 156

5 Characterization and integration of SPAD arrays with NV centers in diamond 163
5.1 Introduction . . . 164
5.1.1 Background . . . 164
5.1.2 State-of-the-art SPAD arrays in 40 nm technology . . . 164
5.2 SPAD Basics . . . 165
5.2.1 Operating principles . . . 165
5.2.2 Overview of SPAD parameters . . . 166
5.3 Designing the SPADs . . . 167
5.3.1 Design considerations . . . 167
5.3.2 Chip specifications . . . 167
5.3.3 Individual chip design overview . . . 169
5.3.4 SPAD chip modeling . . . 172
5.3.5 On-chip circuitry . . . 173
5.4 Electrical characterization . . . 176
5.4.1 PCB Design . . . 176
5.4.2 Electrical characterization results . . . 179

5.5 Integration of diamond with CMOS chip . . . 181
5.5.1 SPAD array readout . . . 181
5.5.2 SPAD array operation tests . . . 183
5.5.3 Implementation of the widefield ODMR setup . . . 184
5.5.4 Experimental results . . . 187

6 Conclusion **195**
6.1 Summary . . . 196
6.2 Challenges & Discussion . . . 198
6.3 Future work & outlook . . . 200

Acknowledgements **203**

A Theory **205**

B ODMR and SPAD control software **211**

C Cleanroom process manuals **215**

D Direct bonding processing parameters **235**

E CV-IV Plots **237**

List of Publications **241**

Curriculum Vitæ **243**

SUMMARY

This dissertation presents advancements toward the development of a compact quantum biosensor by integrating nitrogen-vacancy (NV) centers in diamond with CMOS-fabricated Single-Photon Avalanche Diode (SPAD) arrays. It combines efforts across various research domains and includes simulations, design, and experimental work, in order to tackle challenges in quantum sensing, imaging, fabrication, and device integration.

A custom confocal Optically Detected Magnetic Resonance (ODMR) setup was designed and employed to study magnetic properties in biosamples. HEK293T cells cultured on diamond substrates were tagged with superparamagnetic nanoparticles to act as magnetic probes. Measurements included photoluminescence (PL) mapping and 2D ODMR scans. Although the weak magnetization of the nanoparticles limited magnetic field detection, it still proved the feasibility of such a bio-imaging method and highlighted areas for improvement.

To enable enhanced quantum sensing with NV centers and scalable quantum computing interfaces with tin-vacancy (SnV) centers, the ion implantation process was investigated. Simulations were performed that allowed optimization of the cleanroom processing and implantation parameters, for the near-deterministic generation of color centers. Inspection under SEM confirmed a desirable sub-50 nm aperture fabrication for ion implantation. Consequently, samples were fabricated, ion-implanted through a lithographic mask, overgrown with a diamond layer, and characterized using Raman, PL spectroscopy and ODMR measurements, before and after annealing. The characterization process resulted in evident SnV center generation for blanket-implanted samples, validating the implantation process steps, but also indicating the need for more extensive characterization of the masked-implanted substrates.

Additionally, the previously developed ODMR setup was used to characterize strain effects in directly bonded diamond-on-insulator (DOI) substrates. Such strain effects near the DOI interface arise from thermal expansion mismatch during heating and cool-down processes. PL interference fringes identified bonding irregularities, while ODMR maps revealed volumetric and shear strain increases of approximately 0.45 MHz and 0.71 MHz, respectively. However, ODMR contrast and peak linewidth were essentially unchanged, indicating that the emitters' optical properties remained intact. Overall, this work establishes a methodology for evaluating bonding quality and its impact on NV center performance.

In parallel, CMOS SPAD arrays were fabricated using TSMC's 40 nm technology. Electrical characterizations showed breakdown voltages between -15.5 V and -17.7 V, typical for such devices. Although the fabricated chips did not exhibit expected SPAD pulse behavior, a functional SPAD chip was instead integrated into an adapted, more compact widefield ODMR setup to validate its design. This proof-of-concept demonstrated the feasibility of CMOS-NV integration for high-sensitivity quantum imaging and sensing.

The aforementioned contributions lay a strong foundation for expanding the acquired knowledge into integrated cutting edge quantum biosensing, imaging and computing technologies.

SAMENVATTING

Deze dissertatie beschrijft vorderingen in de ontwikkeling van een compacte kwantumbiosensor door de integratie van stikstof-vacature (NV) centra in diamant met CMOS-gefabriceerde Single-Photon Avalanche Diode (SPAD) arrays. Hiertoe zijn inspanningen uit diverse onderzoeksdomeinen gecombineerd, variërend van simulaties en ontwerp tot experimentele studies, om de uitdagingen op het gebied van kwantumdetectie, beeldvorming, fabricage en apparaat-integratie te overwinnen.

Een op maat gemaakte, confocale Optically Detected Magnetic Resonance (ODMR) opstelling is ontwikkeld en ingezet voor de studie van magnetische eigenschappen in biologische monsters. HEK293T-cellen op diamantsubstraten zijn gelabeld met superparamagnetische nanodeeltjes als magnetische sondes. Metingen omvatten fotoluminescentie (PL) mapping en 2D ODMR scans. Hoewel de zwakke magnetisatie van de nanodeeltjes de velddetectie beperkte, bevestigde dit de haalbaarheid van bio-imaging met NV-centra en identificeerde optimalisatiepunten.

Om hoogwaardige kwantumsensing met NV-centra en schaalbare interfaces voor kwantumcomputing met tin-vacature (SnV) centra mogelijk te maken, is het ionimplantatieproces onderzocht. Met behulp van simulaties zijn cleanroomprocessen en implantatieparameters geoptimaliseerd voor een bijna-deterministische generatie van kleurcentra. SEM-inspectie bevestigde de realisatie van sub-50 nm aperturen die geschikt zijn voor ionimplantatie. Vervolgens zijn monsters gefabriceerd, via een lithografisch masker geïonimplanteerd, overgroeid met een diamantlaag en vóór en na de annealing gekarakteriseerd met Raman-, PL-spectroscopie en ODMR-metingen. De karakterisatie resulteerde in duidelijke SnV-centra in blanket-geïmplanteerde monsters, waarmee de implantatiestappen werden gevalideerd, maar tevens werd de noodzaak aangetoond voor uitgebreidere karakterisatie van de gemaskerd-geïmplanteerde substraten.

De eerder ontwikkelde ODMR-opstelling is daarnaast gebruikt om spanningseffecten in direct gebonden diamond-on-insulator (DOI) substraten te karakteriseren. Door mismatch in thermische uitzettings-coëfficiënten ontstaan spanningen nabij de DOI interface. PL-interferentiepatronen wezen op binding-onregelmatigheden, terwijl diepte-opgeloste ODMR een volumetrische en een schuifspanningscomponent van respectievelijk circa 0.45 MHz en 0.71 MHz onthulden. ODMR-contrast en piekbreedte bleven echter ongewijzigd, wat aantoont dat de optische eigenschappen van de NV-emitters intact bleven. Deze gecombineerde PL/ODMR-methodiek biedt een robuuste aanpak voor de beoordeling van bindingskwaliteit en het effect op NV-centra.

Parallel zijn CMOS-SPAD-arrays vervaardigd in TSMC's 40 nm-technologie. Elektrische karakteriseringen lieten doorslagspanningen van -15,5 V tot -17,7 V zien, typisch voor dit type apparaat. Hoewel de chips het verwachte SPAD-pulsgedrag misten, werd een werkende SPAD chip geïntegreerd in een compacte widefield-ODMR-opstelling voor ontwerpvalidatie. Deze proof-of-concept demonstreert de haalbaarheid van CMOS-NV-integratie voor ultrasensitieve kwantumbeeldvorming en -detectie.

De genoemde bijdragen vormen een degelijk fundament voor verdere ontwikkeling van geavanceerde kwantumbiosensors, beeldvormingstechnieken en kwantumcomputingtoepassingen.

NOMENCLATURE

ABBREVIATIONS

Abbreviation	Definition
AC	Alternating Current
Al	Aluminum
APD	Avalanche Photodiode
Ar	Argon
AQC	Active Quenching Circuit
AWG	Arbitrary Waveform Generator
B	Boron
BC	Bond-Centered
BNC	Bayonet Neill–Concelman (Connector)
BSP	Beam Splitter
C	Carbon
CCD	Charge-Coupled Device
CMOS	Complementary Metal-Oxide-Semiconductor
Co	Cobalt
Cr	Chromium
CVD	Chemical Vapor Deposition
CW	Continuous-Wave
DC	Direct Current
DCR	Dark Count Rate
DI	De-ionized
DM	Dichroic Mirror
DNA	Deoxyribonucleic Acid
DOI	Diamond-On-Insulator
DPSS	Diode-Pumped Solid-State
DW	Debye–Waller factor
EBL	Electron Beam Lithography
ES	Excited State
ESD	Electrostatic Discharge

Abbreviation	Definition
FCC	Face-Centered Cubic
Fe	Iron
FIB	Focused Ion Beam
FID	Free Induction Decay
FLIM	Fluorescence Lifetime Imaging Microscopy
FPGA	Field-Programmable Gate Array
Ga	Gallium
Ge	Germanium
GeV	Germanium Vacancy
GPIO	General-Purpose Input/Output
GS	Ground State
GUI	Graphical User Interface
H	Hydrogen
HAZ	Heat-Affected Zone
He	Helium
HEK	Human Embryonic Kidney
HPHT	High-Pressure High-Temperature
HSQ	Hydrogen Silsesquioxane
IC	Integrated Circuit
I/O	Input/Output
IPA	Isopropyl Alcohol
IR	Infrared Radiation
ISC	Intersystem Crossing
LASER	Light Amplification by Stimulated Emission of Radiation
LED	Light-Emitting Diode
LiDAR	Light Detection And Range
LMIS	Liquid Metal Ion Source
LPF	Longpass Filter
LVS	Layout Versus Schematic
MIBK	Methyl Isobutyl Ketone
MNP	Magnetic Nano Particle
MRI	Magnetic Resonance Imaging
MW	Microwave
N	Nitrogen
NA	Numerical Aperture
ND	Neutral-Density

Abbreviation	Definition
NDs	Nanodiamonds
Ni	Nickel
NIR	Near-Infrared Radiation
NV	Nitrogen Vacancy
O	Oxygen
OD	Optical Density
ODMR	Optically Detected Magnetic Resonance
PbV	Lead Vacancy
PCB	Printed Circuit Board
PDE	Photon Detection Efficiency
PECVD	Plasma-Enhanced Chemical Vapor Deposition
PEX	Parasitic Extraction
PhC	Photonic Crystal (Cavities)
PISO	Parallel-In-Serial-Out
PL	Photo-Luminescence
PMMA	Polymethyl Methacrylate
ppm	parts-per-million
ppb	parts-per-billion
QCE	Quantum & Computer Engineering
QIT	Quantum Integration Technology
RPM	Revolutions Per Minute
RT	Room Temperature
SCD	Single Crystal Diamond
SEM	Scanning Electron Microscope
Si	Silicon
SiC	Silicon Carbide
SIMS	Secondary Ion Mass Spectrometry
SIPO	Serial-In-Parallel-Out
SiV	Silicon Vacancy
SLM	Single Longitudinal Mode
SMA	SubMiniature version A
SMP	SubMiniature Push-on
Sn	Tin
SnV	Tin Vacancy
SNR	Signal-to-Noise Ratio
SOI	Silicon-On-Insulator

Abbreviation	Definition
SPAD	Single-Photon Avalanche Detector
SPCM	Single-Photon Counting Module
SPI	Serial Peripheral Interface
SPION	Superparamagnetic Iron Oxide Nanoparticle
SRIM	Stopping and Range of Ions in Matter
TCSPC	Time-Correlated Single-Photon Counting
Ti	Titanium
TIR	Total Internal Reflection
ToF	Time-of-Flight (Imaging)
TRIM	Transport of Ions in Matter
TSMC	Taiwan Semiconductor Manufacturing Company
TTL	Time-To-Live
USB	Universal Serial Bus
UV	Ultraviolet
V	Vacancy
WD	Working Distance
ZFS	Zero Field Splitting
ZPL	Zero Phonon Line

SYMBOLS

Symbol	Physical Quantity (Unit)
T_a	Activation temperature (K)
$\vec{E}$	Applied electric-field vector ($\mathrm{V\,m^{-1}}$)
I_{SPAD}	Avalanche current (A)
E_g	Bandgap energy (eV)
μ_B	Bohr magneton ($\mathrm{J\,T^{-1}}$)
k_B	Boltzmann constant ($\mathrm{J\,K^{-1}}$)
d	Bond length (Å)
f_{clock}	Clock frequency (Hz)
$[N]$, n	Concentration (ppb/ppm, %)
P_{xtalk}	Crosstalk probability (%)
t_{cycle}	Cycle time (s)
t_{dead}	Dead time (s)
e^{-2W}	Debye–Waller factor (unitless)
ε_b	Electron binding energy (eV)
$d^{(\mathrm{electric})}$	Electric dipole coupling tensor ($\mathrm{Hz\,m\,V^{-1}}$)
$\vec{\mu}_e$	Electric dipole moment (C m)
$\vec{E}$	Electric field ($\mathrm{V\,m^{-1}}$)
g_e	Electron g-factor (unitless)
$\tau_{\mathrm{e-p}}$	Electron-phonon coupling time (s)
$\hat{S}$	Electron spin operator (unitless)
$\vec{B}$	External magnetic field (T)
η	Field sensitivity ($\mathrm{T}/\sqrt{\mathrm{Hz}}$)
τ	Fluorescence lifetime (s)
F	Gas flow rate (N_2, SiH_4, TN_2O) (sccm)
γ	Gyromagnetic ratio ($\mathrm{GHz\,T^{-1}}$)
$\mathbf{A}$	Hyperfine coupling tensor (MHz)
Γ_{ISC}	Intersystem crossing rate ($\mathrm{s^{-1}}$)
I	Intensity ($\mathrm{W\,cm^{-2}}$)
E_i	Ion energy (keV)
D_i, Φ	Ion implantation fluence ($\mathrm{ions/cm^2}$)
R_i	Ion range (nm)
P_{focus}, P_0	Laser power (W)
τ	Laser (fs) pulse duration (s)

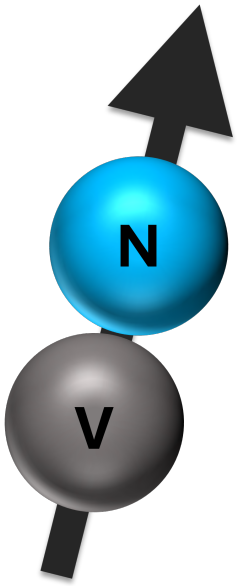
Symbol	Physical Quantity (Unit)
I_{latch}	Latching current threshold (A)
ΔR_x, ΔR_y	Lateral straggle (nm)
a	Lattice constant (Å)
ΔR_z	Longitudinal straggle (nm)
$\vec{\mu}_m$	Magnetic dipole moment ($\mathrm{A\,m^2}$)
m	Magnetic quantum number (unitless)
Δf	Magnetic resonance frequency shift (Hz)
f_{MW}	Microwave frequency (Hz)
V_n	Normalization voltage (V)
$\vec{I}$	Nuclear spin operator (unitless)
C_{ODMR}	ODMR contrast (%)
$\vec{L}$	Orbital angular momentum operator (unitless)
C	Photon collection efficiency (unitless)
R	Photon detection rate (counts/s)
E_{ph}	Photon energy (eV)
p	Pixel pitch (µm)
h	Planck's constant (J s)
$P(E \geq \varepsilon_b)$	Probability of thermal excitation (unitless)
t_q, t_r	Quenching/recharge times (s)
I_s	Quiescent saturation current (A)
n	Refractive index (unitless)
R	Resistance (Ω)
ρ	Resistivity (Ω cm)
P_{MW}	Resonant microwave power (W)
M_{xy}	Shear strain amplitude (MHz)
C_{SPAD}	SPAD chip capacitance (F)
T_2	Spin coherence time (s)
T_2^*	Spin dephasing time (s)
$\hat{H}$	Spin–Hamiltonian (J)
T_1	Spin–lattice relaxation time (s)
λ	Spin–orbit coupling constant (GHz)
m_s	Spin projection quantum number (unitless)
S	Spin quantum number (unitless)
D_{ij}	Spin–spin interaction tensor (GHz)
h_{ij}	Strain-coupling parameters (MHz per unit strain)

Symbol	Physical Quantity (Unit)
$d^{(\text{strain})}$	Strain-coupling tensor (MHz per unit strain)
ε_{ij}	Strain tensor (unitless)
V_{dd}	Supply voltage (V)
T	Temperature (K)
l_d	Thermal diffusion length (m)
D_{th}	Thermal diffusivity ($\text{m}^2\,\text{s}^{-1}$)
E	Transverse ZFS (GHz)
V	Voltage (V)
M_z	Volumetric strain amplitude (MHz)
λ	Wavelength (nm)
d_{WD}	Working distance of objective (µm)
E_{ZPL}	ZPL energy (eV)
λ_{ZPL}	ZPL wavelength (nm)

1

INTRODUCTION

Quantum sensing and quantum computing are two of the most pivotal fields of quantum technology. The emergence of color centers in diamond has been vital to groundbreaking developments. On one hand, nitrogen-vacancy (NV) centers can provide unparalleled sub-nanoscale sensitivity, most commonly as magnetometers. The ability to perform non-invasive and highly precise diagnostic imaging of cells and tissues makes the realization of an integrated, compact diamond magnetometer all the more beneficial to society. On the other hand, tin-vacancy (SnV) centers represent a leading class of emerging solid-state qubits for quantum computing, positioning themselves among the most promising platforms under active development. In this research, we explore the on-chip integration of a diamond containing NV centers with single-photon avalanche detectors (SPADs) to perform fast, precise and high resolution biosensing, while also delving deep into the experimental and fabrication techniques required to develop this platform.



1

1.1. QUANTUM BIOSENSING: A BRIEF INTRODUCTION

Quantum biosensing refers to the harnessing of quantum phenomena, such as superposition, spin coherence or entanglement, for the detection and analysis of biological targets with enhanced sensitivity, spatial resolution, and selectivity, compared to classical sensors. Early quantum biosensing technology involved superconducting quantum interference devices (SQUIDs), which enables detection of magnetic fields down to femtotesla levels [1, 2], and atomic magnetometers based on alkali vapor cells [3], which operated near the quantum noise limit for biomagnetic signal acquisition. However, these platforms often require cryogenic cooling or bulky shielding setups, limiting their applicability in practical biomedical settings [4].

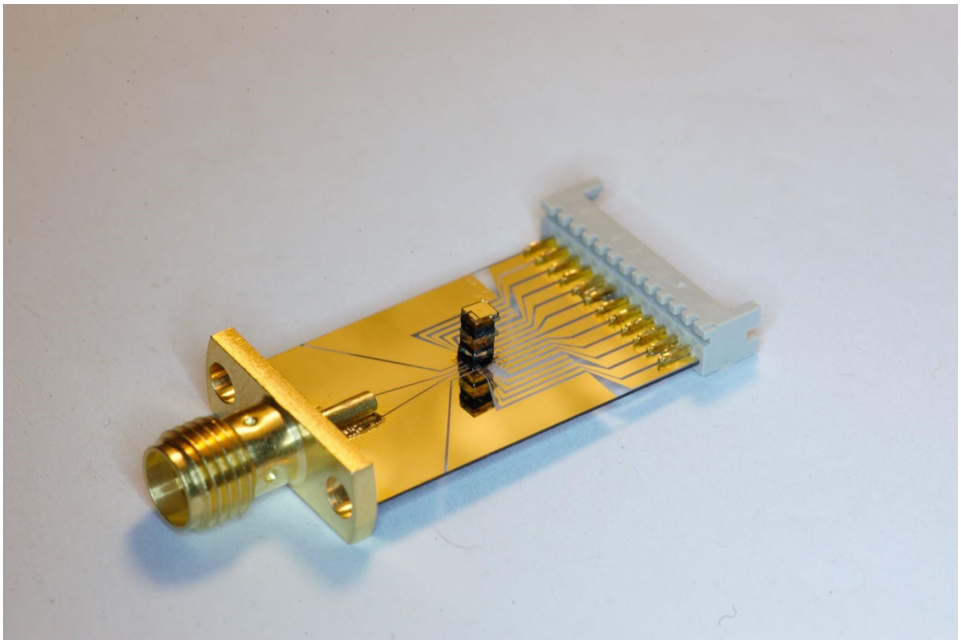


Figure 1.1: Photograph of a chip-scale atomic magnetometer, a miniaturized alkali-vapor-based device capable of highly sensitive magnetic field measurements. Image courtesy of J. Kitching, NIST (2021) [5].

In parallel, other quantum platforms, such as quantum dots, have also been explored. Quantum dots are semiconductor nanocrystals that exhibit size-tunable fluorescence, making them valuable for high resolution bioimaging and biosensing applications. Nevertheless, they do come with challenges such as photobleaching [6], blinking [7], and toxicity [8].

More recently, nitrogen-vacancy (NV) centers in diamond have emerged as a uniquely powerful biosensing tool [9]. In contrast to previous quantum sensors, NV-based systems offer several practical advantages: they are operable in ambient conditions, compatible with live-cell imaging, and capable of non-invasive, label-free detection of subcellular dynamics [10, 11]. These properties have led to rapid adoption of NV-based magnetometry and thermometry in fields ranging from single-neuron activity mapping [10] to single-molecule nuclear magnetic resonance (NMR) [12].

1.1.1. NV CENTER-BASED QUANTUM BIOSENSING OVERVIEW

Studies on the nitrogen-vacancy (NV) center in diamond started as early as 1965, by the pioneering work of du Preez *et al.* [13], culminating into a thorough study by Davies *et al.* in 1976 [14] and Loubser *et al.* in 1977 and 1978 [15]. However, it was not until 1997 [16] that negatively charged *single* NV centers were detected by Gruber *et al.* This marked the beginning of even more extensive research on this color center and discovery of its potential in both quantum information [17] and quantum metrology [18].

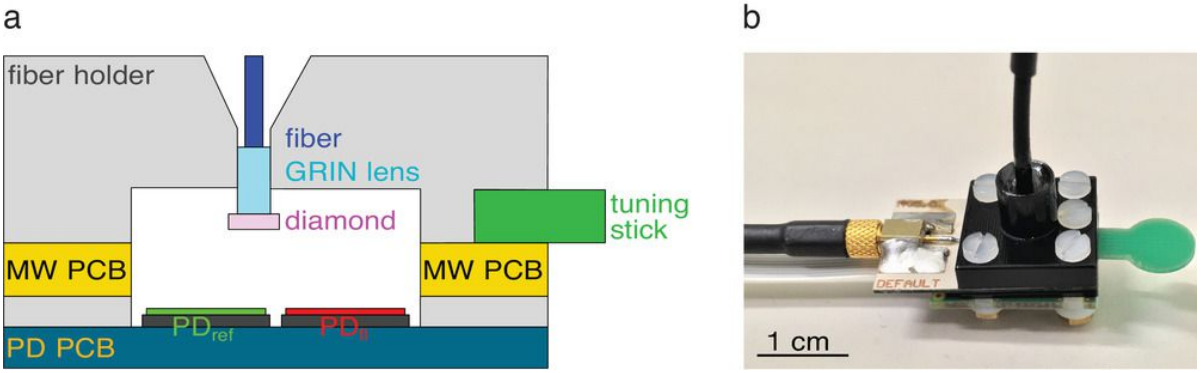


Figure 1.2: Example of an integrated, portable NV center-based magnetometer. Image courtesy of Stürner *et al.* (2021) [19].

Building upon the sensing capabilities of the NV center, Maletinsky *et al.* (2012) managed to demonstrate magnetic field detection at the nanoscale [20], while, in the same period, Sage *et al.* (2012) employed a different photon collection technique, to measure an AC magnetic field sensitivity in the order of hundreds of picotesla [21]. Ever since, NV centers have gathered increasing interest due to their exceptional sensitivity to magnetic [22] and electric fields [23], temperature [24] and strain [23, 25]. One of the most prominent reviews of the properties of NV centers in diamond was published in 2013 [26] by Doherty *et al.*

The combination of such sensitivity and the appealing properties of NV centers, that allow real-time, biocompatible, non-invasive, room temperature imaging of biological systems, have resulted in more and more NV-based quantum biosensors being developed in the last decade [27, 28, 29, 30]. Medical diagnostics is the field which stands to benefit the most out of such a biosensor. By utilizing this radiation-free, non-destructive, three-dimensional, nanoscale imaging tool that is the NV center, magnetic resonance imaging (MRI) of biomolecules can be enhanced in both contrast and resolution [31, 32, 33]. Moreover, biomarker detection such as microRNA's is considerably improved using NV centers, owing to the unnecessariness of measuring intrinsic biomolecule charges and subsequently avoiding the effect of Debye screening [30]. Thus, the positive societal impact of the production of such an efficient biosensor is unquestionable.

1

1.2. WHAT IS AN NV CENTER?

Before delving into quantum biosensing with NV centers, it is essential to first understand their formation mechanisms and the properties that make them great candidates for sensing applications. They are one of many point defects in diamond, comprised of a nitrogen (N) atom and an adjacent vacancy (V) in the diamond's crystal lattice. The nitrogen atom substitutes one of the carbon (C) atoms in the lattice, leaving behind an "empty" site called a vacancy [14, 34]. The NV center exhibits unique optical and spin properties, which can be manipulated and read out at room temperature.

Although natural diamonds might still contain some N impurities, their controlled fabrication is typically achieved through chemical vapor deposition (CVD) [35, 36, 37, 38, 39] and ion implantation techniques [40, 41]. These processes allow precise tuning of nitrogen concentration and NV center distribution, depending on the intended application.

In the NV structure, optical excitation is achieved usually by green light illumination, most often with a 515 nm or a 532 nm laser source. The relaxation back to the ground state can happen via radiative and non-radiative mechanisms [42]. Applying a resonant microwave (MW) field can drive transitions between the spin sublevels ($|0\rangle$, $|\pm1\rangle$) of the ground state triplet. The emission is dependent on the spin states, with the photoluminescence (PL) intensity associated with the "bright" $|0\rangle$ state being significantly higher than relaxation through the "dark" $|\pm1\rangle$ states. The key factor here is emission through the zero-phonon line (ZPL) that occurs in $|0\rangle$ state emissions, versus phonon-assisted relaxation that are prevalent in the $|\pm1\rangle$ states.

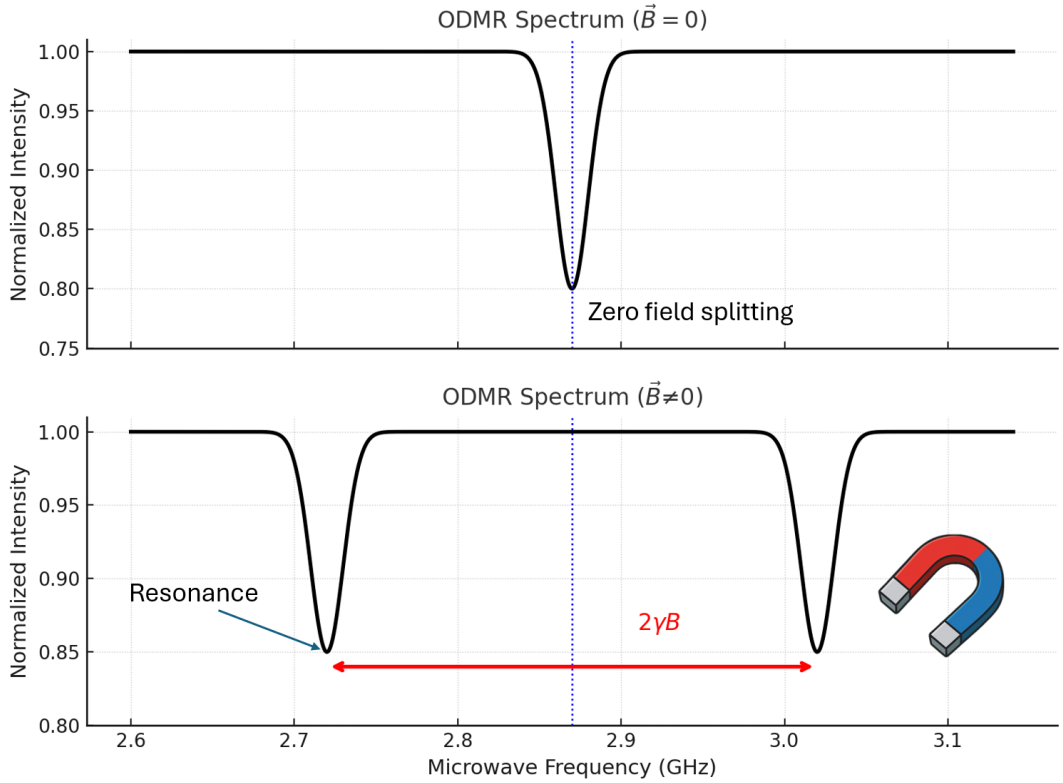


Figure 1.3: Indicative NV center ODMR spectra, demonstrating the peak splitting due to application of a magnetic field.

Manipulation of these spin states allows us to very accurately measure external magnetic fields, by making use of a technique called Optically Detected Magnetic Resonance (ODMR). The principle of ODMR is sweeping over a certain microwave frequency range, while simultaneously observing the PL intensity. When the MW frequency is resonant (matching the energy difference between the spin states), then the population of the spin states is redistributed, with a portion of it being driven to the $|\pm 1\rangle$ states, meaning that the subsequent relaxation is more likely to happen in non-ZPL emission. Hence, a contrast between resonant and non-resonant PL emission can be discerned, indicated by a single PL dip in the graph of PL intensity vs MW frequency.

However, in the presence of a magnetic field, and due to the Zeeman effect, the degeneracy of the $|\pm 1\rangle$ spin states is lifted, resulting in distinct $|+1\rangle$ and $|-1\rangle$ states, as seen in Figure 1.3. This splitting also affects the corresponding resonant frequencies. Now, when sweeping the MW frequency and collecting PL emission, two (or more) dips can be observed, indicative of the different spin states and the transitions between the $|G_0\rangle$ and $|G_1\rangle$ states. Finally, by calculating the difference in resonance frequency between these peaks, the magnetic field strength can be determined [43, 44, 45]. Utilizing ODMR techniques with NV centers in diamond has proven to be an extremely powerful tool for nanoscale magnetometry [46, 9].

1

1.3. CMOS TECHNOLOGY INTEGRATION: STATE-OF-THE-ART

Having discussed the benefits of using NV centers in diamond as biosensors, the next step is to integrate them with Complementary Metal-Oxide-Semiconductor (CMOS) technology. The goal here is to create a small, but compact, stable, and highly sensitive sensing platform. Making use of an NV-based magnetometer often goes hand in hand with large, bulky, stationary lab setups and equipment. For such sensors to really shine in their intended field, especially in biodiagnostics, it is evident that scaling down needs to take place and production costs as well as power consumption need to be limited [19].

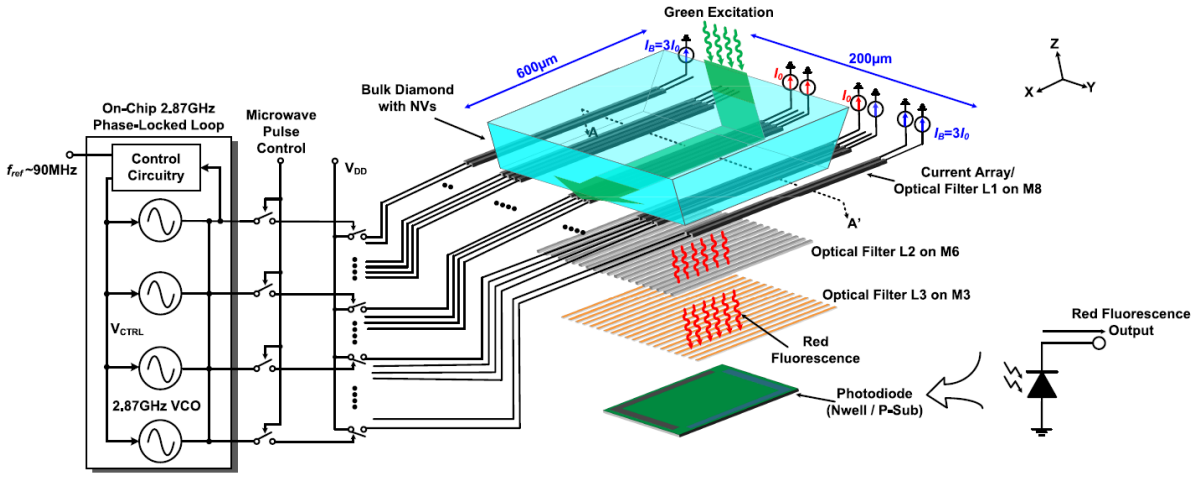


Figure 1.4: Overall schematic of a high scalability CMOS quantum magnetometer. Image courtesy of with Ibrahim *et al.* [47]

A compact CMOS sensor promises to take care of these concerns. Only a few years ago, the first compact NV-based magnetometers emerged, with the efforts of Webb *et al.* (2019) [48], Kuwahata *et al.* (2020) [49], Stürner *et al.* (2021) [19] and Wang *et al.* (2022) [50] paving the way. One of the most novel approaches was the design of a compact, USB-operated diamond sensor by Deguchi *et al.* (2023). By using a corner cube cut diamond, they report drastically enhanced collection efficiency, among others [51]. The most recent work belongs to Pogorzelski *et al.*, who published a paper on a fully integrated sensor, using LED as excitation medium [52]. Most of these researchers demonstrated magnetic field sensitivity down to a few nanotesla and made use of innovative, custom component integration to build portable quantum magnetometers. Meanwhile, in 2019, Kim *et al.* published one of the first works on CMOS integrated NV-based quantum sensors [53], followed by a significantly improved version in 2021 by Ibrahim *et al.* [47] (see Figure 1.4). These innovations are nothing short of inspiring and contribute a great deal towards the realization of the ultimate quantum diamond biosensor.

1.4. NV-BASED STRAIN SENSING FOR 3D QUANTUM HARDWARE INTEGRATION

The integration of color centers in diamond into compact, scalable quantum computing platforms is one of the major objectives of current solid-state quantum technology. Among the most promising approaches toward realizing this goal is the design of a three-dimensional (3D) chip architecture, wherein individual functional layers, hosting spin qubits, integrated photonics, and control electronics, are vertically stacked to create a modular, high-density quantum processor. This design enables increased connectivity, low crosstalk, and local control of each module, which is essential for scaling the number of qubits while maintaining system coherence and fidelity. As proposed by Ishihara *et al.* [54], this architecture utilizes direct bonding of diamond onto silicon substrates to form a diamond-on-insulator (DOI) platform [55, 56, 57], which supports monolithic integration of photonic circuits, waveguide-coupled detectors, and local magnetic field generators, in conjunction with flip-chip bonded cryo-CMOS electronics.

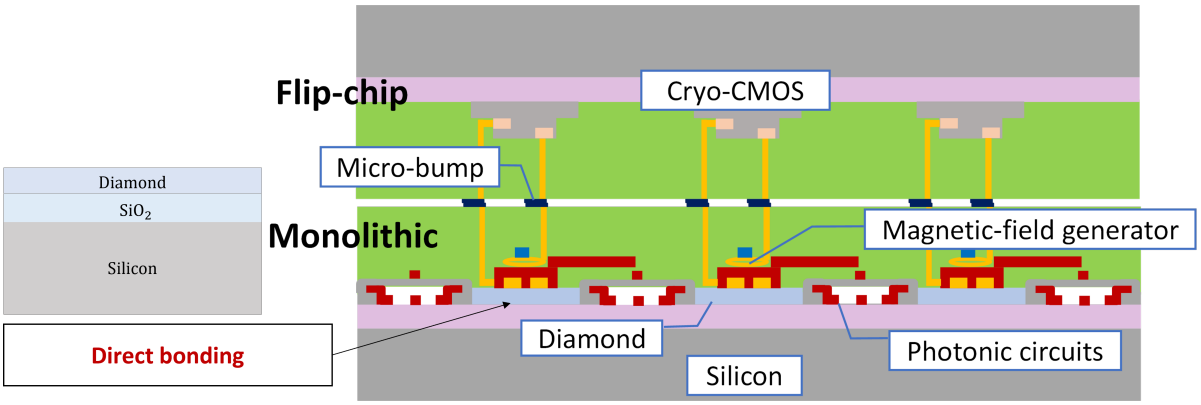


Figure 1.5: 3D integration of a modular quantum computer chip with spins in diamond. Image courtesy of Ishihara *et al.* (2021) [54].

However, for this vision to be realized, it is imperative to ensure that the optical and spin properties of the color centers embedded in the diamond remain unaffected by the mechanical and thermal steps required for integration. One critical factor in this regard is strain. The direct bonding process, which is typically carried out at elevated temperatures [56, 57], inherently introduces mechanical stress at the diamond–silicon interface due to the mismatch in thermal expansion coefficients. This stress propagates into the diamond layer, causing local crystal deformations. These deformations —referred to as strain— can shift the energy levels of the NV or SnV centers and degrade coherence times, spectral stability, and quantum gate fidelity. Given the sensitivity of spin qubits to their local environment, characterization of this strain is not only beneficial, but necessary.

Apart from its capabilities at measuring temperature and external magnetic or electric fields, the NV center in diamond can determine minor crystal lattice deformations within the diamond itself, with rather good precision. These deformations are quantified as strain and can be characterized in a similar manner to magnetic fields. This not only provides a picture of the intrinsic lattice properties of the diamond samples, but also allows scientists to monitor any strain-inducing effects. These effects may arise during

temperature or pressure treatments [58], chemical reactions, or mechanical contact with other surfaces, and can heavily affect the optical and spin properties of the color centers.

Therefore, the ability to map strain in diamond plays a dual role that is central to the advancement of integrated quantum technologies. First, it acts as a diagnostic tool to evaluate the mechanical integrity of bonded substrates, revealing whether bonding-induced stress compromises the host lattice. Second, it provides critical feedback for optimizing fabrication parameters such as bonding temperature, annealing conditions, and material interfaces. In this project, ODMR-based measurements are used to obtain spatially resolved strain profiles across diamond-on-insulator (DOI) substrates, enabling the detection of localized stress concentrations, depth-dependent variations, and correlations with processing conditions. These insights are not only instrumental in improving the reproducibility and performance of CMOS-integrated quantum sensors but also directly support the broader objective of 3D-integrated quantum computing based on color centers in diamond. Maintaining mechanical and optical stability of the qubit-hosting diamond layer is essential to preserving coherence and ensuring device scalability. As such, this work bridges quantum sensing and hardware integration, supporting the development of scalable, high-performance quantum processors.

1.5. EVALUATING SNV CENTERS FOR QUANTUM SENSING AND 3D-INTEGRATED QUANTUM COMPUTING

Despite the proven effectiveness of NV centers in biological imaging and sensing applications, it is reasonable to explore alternative defects in diamond, particularly the tin-vacancy (SnV) centers, given their superior optical coherence properties and strong zero-phonon line (ZPL) emission. SnV centers exhibit narrow linewidths [59], minimal phonon coupling, and high photon indistinguishability, making them promising candidates for quantum communication applications [60].

However, despite these advantageous optical properties, employing SnV centers directly as quantum sensors for bioimaging presents substantial challenges. Firstly, practical SnV-based sensors suitable for magnetic resonance imaging or biosensing have not yet been realized, primarily due to the complexity involved in reliably controlling and manipulating SnV spin states at room temperature. Unlike NV centers, which have a spin-1 ground state and exhibit strong coupling to external magnetic, electric, and strain fields via their electric dipole moment, SnV centers possess an inversion-symmetric structure that significantly suppresses their dipole coupling. While this symmetry leads to enhanced spectral stability and reduced spectral diffusion (key for quantum communication) it also results in weaker interactions with environmental perturbations, limiting their utility in sensing. Moreover, the strong spin–orbit coupling inherent to SnV centers leads to rapid spin decoherence at elevated temperatures, making spin readout and control feasible only under cryogenic conditions [61]. In contrast, NV centers retain long coherence times and allow full optical and microwave spin manipulation at room temperature, making them far more suitable for practical biosensing and imaging applications.

Having said that, and while NV centers are among the most researched and well-documented solid state defects [62], SnV centers [63] are currently at the forefront of

quantum computing research, along with silicon-vacancy centers (SiV) [64], silicon carbide (SiC) [65], and others. As mentioned above, light emission without phonon assistance (ZPL) is desirable [66]. The importance of this is greatly magnified, when it comes to quantum computing and quantum communication applications, where high quality qubit entanglement generation is mandatory. High ZPL emission leads to reduced spectral noise and enables indistinguishable single photon emission, substantially boosting quantum state fidelity [67, 68]. Thankfully, SnV centers in diamond (which belong in group-IV color centers) show extremely strong ZPL emission, an order of magnitude or more higher than that of the NV center, making them excellent contenders for the aforementioned applications [67, 69, 70, 71].

Nevertheless, creation of good quality quantum emitters is not trivial. In this research, multiple fabrication methods are being explored, with the combined goal of precise and deterministic generation of single SnV centers in diamond [70, 72, 73, 74]. This is essential for 3D-integrated quantum chips, where scalable architectures demand high-yield, site-controlled implantation to ensure efficient spin-photon coupling, spectral uniformity, and integration with photonic and cryo-CMOS layers [54].

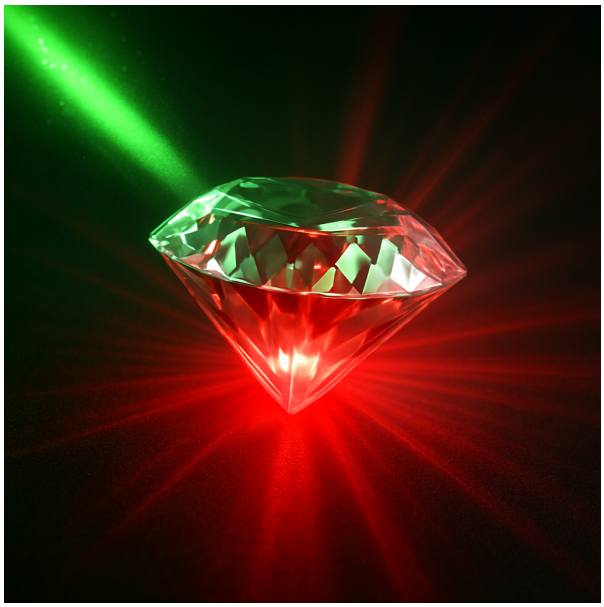


Figure 1.6: Concept image of a diamond containing NV centers being illuminated by green light and emitting red fluorescence. Image generated using ChatGPT (OpenAI, 2025).

1

1.6. RESEARCH GOALS

The primary goal of this research is to develop a proof-of-concept for a compact, highly-sensitive, CMOS-integrated quantum biosensor. As seen in section 1.3, there have been various different approaches to building NV center-based biosensors and magnetometers over the years. Some of these excel in compactness and portability, whereas others exhibit very high sensitivity. Our approach of this project involves:

- Design and characterization of a novel 40 nm CMOS array of single-photon avalanche diodes (SPADs),
- Fabrication of the related color centers for quantum sensing and use with the designed SPADs:
  - Single and ensembles of NV centers
  - Single and ensembles of SnV centers
- Integration of the SPADs with a diamond containing NV centers and, finally,
- Recommendations for enhanced optical excitation, through the use of photonic structures.

By utilizing the confocal ODMR setup that is developed for characterization as part of this research, additional objectives include:

- Characterization of strain effects on diamond-on-insulator (DOI) substrates, induced during direct bonding, and also:
- Biosample labeling research and measurements using ODMR

A concept image of the final, fully-integrated diamond-on-chip NV-based sensor is shown in Figure 1.7. The main research goals are elaborated on below.

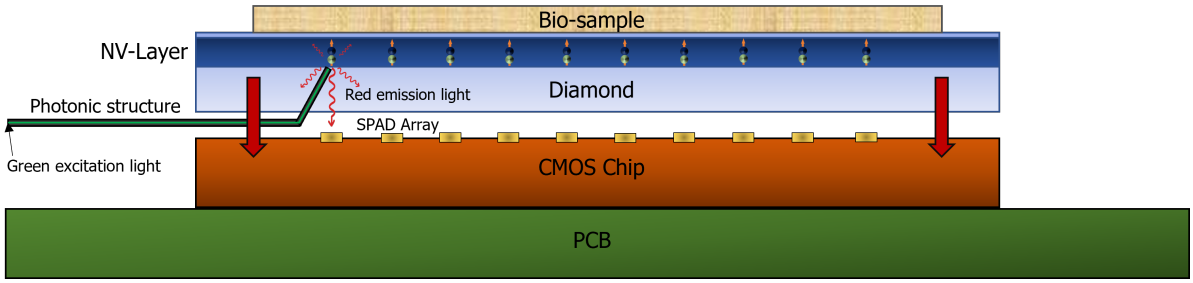


Figure 1.7: Concept design of a fully-integrated diamond-on-chip NV-based quantum biosensor. Photonic structures are also visible, which can efficiently guide the excitation light to the corresponding NV layer.

Fabrication of CMOS chip containing a SPAD array and integration with diamond

As a first step toward the integration of an on-chip quantum biosensor system, this project aims to fabricate a 16×16 array of SPADs in 40 nm CMOS technology and integrate it with the diamond sample, while making use of necessary optics in between.

Such an integration scheme utilizes widefield ODMR with NV centers in diamond, in order to perform static imaging of biological cells with magnetic properties (labeled via use of magnetic nanoparticles). Our proposed design facilitates compactness by eliminating the need for bulky optics and photodetectors for the collection of the emitted light. Moreover, by employing simultaneous ODMR data collection from each individual SPAD, the imaging process can (theoretically) be sped up $16^2 = 256$ times (proportionally to the total number of pixels/detectors). The imaging speed can be further improved by scaling up the number of available detectors. This is a stark contrast compared to point-by-point confocal ODMR measurements. Meanwhile, all necessary readout circuits are located on-chip, and the corresponding software can be easily managed through the communication of the chip with a Field-Programmable Gate Array device (FPGA) and a computer. And, although commercially available cameras/imagers do exist, the SPADs' high-sensitivity single-photon detection capabilities, coupled with their high temporal resolution, imaging speed, and scalability, make for an undeniably powerful sensing tool.

Fabrication of color centers in diamond

Besides the CMOS integration part of the research goal, the sensor itself (i.e. the NV centers in diamond) is of crucial importance. There are three different approaches, two of which are investigated for their enhanced sensing potential. A strategically fabricated layer of an ensemble of NV centers can significantly improve signal-to-noise ratio and sensitivity. On the other hand, an array of single NV centers that directly couple their emitted fluorescence light to the corresponding SPADs below them can offer unparalleled spatial resolution, in scenarios where this is required. For this purpose, this research examines two different fabrication techniques for the creation of both single color centers and ensembles.

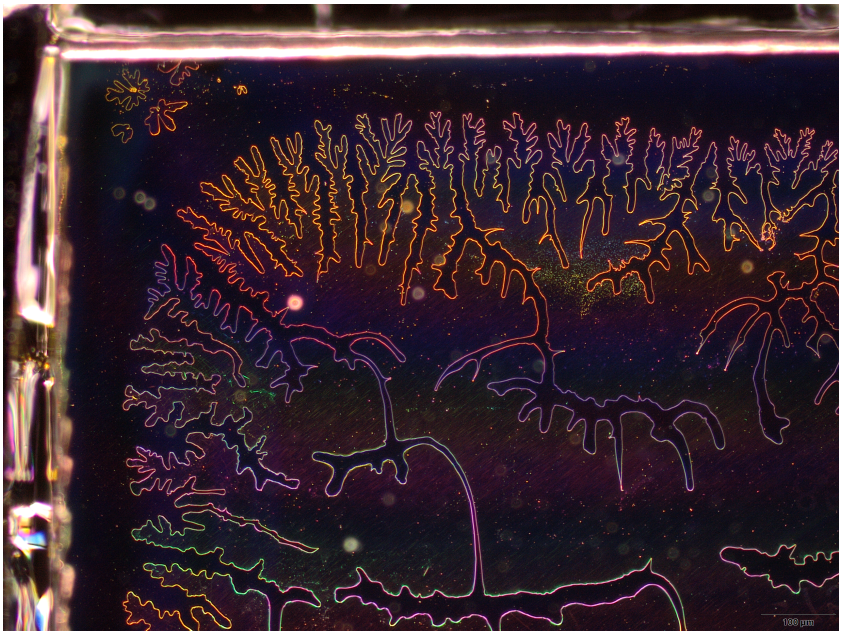


Figure 1.8: Microscope image of a diamond substrate, after an unsuccessful spin-coating process in the cleanroom.

The first of these techniques makes use of a cleanroom-fabricated resist mask to implant ions through carefully designed apertures, in order to create deterministically placed color centers. While research was done on the implantation of both nitrogen and tin ions, only the tin ion implantation process was carried out in the end. This was done as part of a side-project under Fujitsu, which looked into the fabrication efficiency of color centers in diamond for use in quantum computing applications. The goal set for this was reproducible fabrication of sub-50 nm apertures in the resist that acted as a mask during ion implantation.

The second implantation technique investigated in this project was direct single ion implantation using a focused ion beam (FIB) for the generation of both NV and SnV color centers in diamond, with the goal of comparing the efficiency of different implantation techniques in mind.

Characterization of strain-induced effects in a diamond-on-insulator substrate

Finally, since this project entailed the full design and installation of a completely new lab and setup, the confocal version of the ODMR setup was first built. This setup allowed not only for optimization and characterization of NV-based sensing platforms, but also enabled a focused investigation into strain-induced effects in diamond-on-insulator (DOI) substrates—effects that are directly relevant to 3D-integrated quantum hardware. Specifically, the study targeted strain arising from thermal expansion mismatch between diamond and the underlying SiO_2/Si substrate during the direct bonding process.

By performing spatial and depth-resolved ODMR measurements across both bonded and unbonded regions, we aim to quantify how strain propagates through the diamond lattice and evaluate its impact on the optical and spin coherence properties of embedded color centers. Strain mapping not only serves as a diagnostic tool for bonding quality, but also provides critical feedback for integration processes in future quantum devices. To address the influence of strain on color center performance and DOI fabrication, this research focuses on the following key points:

- Development of a methodology for depth-resolved ODMR measurements to characterize strain fields near the diamond–SiO_2/Si interface.
- Exploration of thermally induced strain resulting from mismatched thermal expansion coefficients during the bonding process.
- Use of 2D ODMR mapping to spatially resolve variations in volumetric and shear strain across bonded and unbonded regions.
- Integration of photoluminescence (PL) mapping as a complementary tool to identify bonding irregularities and correlate them with local strain signatures.
- Evaluation of how strain affects NV center optical properties, including linewidth, contrast, and signal stability, in support of future integration in scalable quantum devices.

1.7. DISSERTATION OVERVIEW

This dissertation investigates advances in NV centers in diamond, focusing on their integration into quantum sensing and compact imaging systems, and their potential applications in biosensing, and strain mapping. The research entails the development of optical setups, and the integration of CMOS-fabricated Single-Photon Avalanche Diode (SPAD) arrays with diamond, for high-speed photon detection. In parallel, different methods of fabricating NV and SnV color centers are examined, supported by simulations.

The dissertation is organized as follows:

- **Chapter 2** introduces NV centers in diamond, as well as the theory behind their unique optical properties and their potential in quantum sensing. SnV centers in diamond are also examined for their quantum computing capabilities. It also provides an overview of the ODMR characterization setup that is built from scratch inside our research group's lab facility. Its individual components are described, along with considerations that shaped our choices and the final configuration. Additionally, biosample magnetic labeling is investigated and measurements are attempted on said biosamples.

- In **chapter 3**, a background on diamond and color center fabrication is established, followed by thorough simulations that help validate fabrication-specific parameters. The simulation results allow cleanroom processing of diamonds for optimized ion implantation of color center. Meanwhile, different implantation and post-implantation techniques (overgrowth, annealing) are also explored.

- **Chapter 4** presents experimental investigations into strain mapping of diamond-on-insulator (DOI) substrates. The influence of fabrication-induced and intrinsic strain on NV center performance is studied, providing insight into the degree to which optical properties may deteriorate after direct bonding.

- **Chapter 5** focuses on the CMOS design of chips containing SPAD arrays and the electrical characterization of their properties. Subsequently, integration of the fabricated SPAD array chip with diamond containing NV centers is investigated, for high-sensitivity high-speed quantum imaging. An alternate SPAD chip is also examined as a replacement, to provide proof-of-concept.

- Finally, the **conclusion** chapter summarizes the findings and contributions to NV-based sensing, to SPAD design and characterization in 40 nm CMOS technology, to the integration and design of a compact widefield imaging setup, as well as to color center fabrication techniques. It also discusses challenges encountered along the way and provides recommendations on how to improve the conceptualized biosensor.

BIBLIOGRAPHY

[1] I. Sochnikov, D. Davino, and B. Kalisky. "dc SQUID Design with Femtotesla Sensitivity for Quantum-Ready Readouts". In: *Phys. Rev. Appl.* 14 (1 July 2020), p. 014020. DOI: 10.1103/PhysRevApplied.14.014020.

[2] Yijin Xie et al. "A hybrid magnetometer towards femtotesla sensitivity under ambient conditions". In: *Science Bulletin* 66.2 (2021), pp. 127–132. ISSN: 2095-9273. DOI: https://doi.org/10.1016/j.scib.2020.08.001.

[3] Guzhi Bao et al. "Suppression of the Nonlinear Zeeman Effect and Heading Error in Earth-Field-Range Alkali-Vapor Magnetometers". In: *Phys. Rev. Lett.* 120 (3 Jan. 2018), p. 033202. DOI: 10.1103/PhysRevLett.120.033202.

[4] Robert Wyllie et al. "Magnetocardiography with a modular spin-exchange relaxation-free atomic magnetometer array". In: *Physics in Medicine and Biology* 57.9 (May 2012). Epub 2012 Apr 13, pp. 2619–2632. DOI: 10.1088/0031-9155/57/9/2619.

[5] J. Kitching. *Chip-scale atomic magnetometers*. Accessed: 2025-06-11. 2021. URL: https://www.nist.gov/noac/technology/magnetic-and-electric-fields/chip-scale-atomic-magnetometers.

[6] Bradley A. Kairdolf et al. "Semiconductor quantum dots for bioimaging and biodiagnostic applications". In: *Annual Review of Analytical Chemistry (Palo Alto, Calif.)* 6.1 (2013), pp. 143–162. DOI: 10.1146/annurev-anchem-060908-155136.

[7] Verena Rombach-Riegraf et al. "Blinking effect and the use of quantum dots in single molecule spectroscopy". In: *Biochemical and Biophysical Research Communications* 430.1 (2013), pp. 260–264. ISSN: 0006-291X. DOI: https://doi.org/10.1016/j.bbrc.2012.10.140.

[8] Yali Lv, Lin Zhang, Ruyi Wu, et al. "Recent progress on eco-friendly quantum dots for bioimaging and diagnostics". In: *Nano Research* 17.12 (2024), pp. 10309–10331. DOI: 10.1007/s12274-024-6926-5.

[9] Romana Schirhagl et al. "Nitrogen-Vacancy Centers in Diamond: Nanoscale Sensors for Physics and Biology". In: *Annual Review of Physical Chemistry* 65.Volume 65, 2014 (2014), pp. 83–105. ISSN: 1545-1593. DOI: https://doi.org/10.1146/annurev-physchem-040513-103659.

[10] John F. Barry et al. "Optical magnetic detection of single-neuron action potentials using quantum defects in diamond". In: *Proceedings of the National Academy of Sciences of the United States of America* 113.49 (2016). Epub 2016 Nov 22; Erratum in: Proc Natl Acad Sci U S A. 2017 Aug 8;114(32):E6730. doi:10.1073/pnas.1712523114, pp. 14133–14138. DOI: 10.1073/pnas.1601513113.

[11] Tongtong Zhang et al. “Toward Quantitative Bio-sensing with Nitrogen–Vacancy Center in Diamond”. In: *ACS Sensors* 6.6 (2021). PMID: 34038091, pp. 2077–2107. DOI: 10.1021/acssensors.1c00415.

[12] Matthias Kost, Jianming Cai, and Martin B. Plenio. “Resolving single molecule structures with Nitrogen-vacancy centers in diamond”. In: *Scientific Reports* 5 (2015), p. 11007. DOI: 10.1038/srep11007.

[13] L Du Preez. “Electron paramagnetic resonance and optical investigations of defect centres in diamond”. In: (1965). URL: https://wiredspace.wits.ac.za/server/api/core/bitstreams/974855d1-6b1f-4467-8264-eb40c946f716/content.

[14] G. Davies and M. F. Hamer. “Optical Studies of the 1.945 eV Vibronic Band in Diamond”. In: *Proceedings of the Royal Society of London. Series A, Mathematical and Physical Sciences* 348.1653 (1976), pp. 285–298. DOI: 10.1098/rspa.1976.0039.

[15] J. H. N. Loubser and J. A. van Wyk. “Electron spin resonance in the study of diamond”. In: *Reports on Progress in Physics* 41.8 (Aug. 1978), p. 1201. DOI: 10.1088/0034-4885/41/8/002.

[16] A. Gruber et al. “Scanning confocal optical microscopy and magnetic resonance on single defect centers”. In: *Science* 276 (1997), pp. 2012–2014. DOI: 10.1126/science.276.5321.2012.

[17] F. Jelezko and H. B. et al. “Observation of coherent oscillations in a single electron spin”. In: *Physical Review Letters* 92.7 (2004), p. 076401. DOI: 10.1103/PhysRevLett.92.076401.

[18] J. M. Taylor and et al. “High-sensitivity diamond magnetometer with nanoscale resolution”. In: *Nature Physics* 4.10 (2008), pp. 810–816. DOI: 10.1038/nphys1075.

[19] Felix M. Stürner et al. “Integrated and Portable Magnetometer Based on Nitrogen-Vacancy Ensembles in Diamond”. In: *Advanced Quantum Technologies* 4.4 (2021), p. 2000111. DOI: https://doi.org/10.1002/qute.202000111.

[20] P. Maletinsky et al. “A robust scanning diamond sensor for nanoscale imaging with single nitrogen-vacancy centres”. In: *Nature Nanotechnology* 7.5 (2012), pp. 320–324. ISSN: 1748-3395. DOI: 10.1038/nnano.2012.50.

[21] D. Le Sage et al. “Efficient photon detection from color centers in a diamond optical waveguide”. In: *Phys. Rev. B* 85 (12 Mar. 2012), p. 121202. DOI: 10.1103/PhysRevB.85.121202.

[22] H. J. Mamin et al. “Nanoscale Nuclear Magnetic Resonance with a Nitrogen-Vacancy Spin Sensor”. In: *Science* 339.6119 (2013), pp. 557–560. DOI: 10.1126/science.1231540.

[23] F. Dolde et al. “Electric-field sensing using single diamond spins”. In: *Nature Physics* 7.6 (2011), pp. 459–463. ISSN: 1745-2473 1745-2481. DOI: 10.1038/nphys1969.

[24] P. Neumann et al. “High-Precision Nanoscale Temperature Sensing Using Single Defects in Diamond”. In: *Nano Letters* 13.6 (2013), pp. 2738–2742. ISSN: 1530-6984. DOI: 10.1021/nl401216y.

[25] J. R. Maze et al. “Properties of nitrogen-vacancy centers in diamond: the group theoretic approach”. In: *New Journal of Physics* 13.2 (2011). ISSN: 1367-2630. DOI: 10.1088/1367-2630/13/2/025025.

[26] Marcus W. Doherty et al. “The nitrogen-vacancy colour centre in diamond”. In: *Physics Reports* 528.1 (2013), pp. 1–45. DOI: 10.1016/j.physrep.2013.02.001.

[27] Gopalakrishnan Balasubramanian et al. “Nitrogen-Vacancy color center in diamond—emerging nanoscale applications in bioimaging and biosensing”. In: *Current Opinion in Chemical Biology* 20 (2014). Molecular imaging, pp. 69–77. ISSN: 1367-5931. DOI: https://doi.org/10.1016/j.cbpa.2014.04.014.

[28] Giulia Petrini et al. “Is a Quantum Biosensing Revolution Approaching? Perspectives in NV-Assisted Current and Thermal Biosensing in Living Cells”. In: *Advanced Quantum Technologies* 3.12 (2020), p. 2000066. DOI: https://doi.org/10.1002/qute.202000066.

[29] Nabeel Aslam et al. “Quantum sensors for biomedical applications”. In: *Nature Reviews Physics* 5.3 (2023), pp. 157–169. ISSN: 2522-5820. DOI: 10.1038/s42254-023-00558-3. URL: https://doi.org/10.1038/s42254-023-00558-3.

[30] Justas Zalieckas et al. “Quantum sensing of microRNAs with nitrogen-vacancy centers in diamond”. In: *Communications Chemistry* 7.1 (2024), p. 101. ISSN: 2399-3669. DOI: 10.1038/s42004-024-01182-7.

[31] D. Rugar et al. “Proton magnetic resonance imaging using a nitrogen-vacancy spin sensor”. In: *Nat Nanotechnol* 10.2 (2015), pp. 120–4. ISSN: 1748-3387. DOI: 10.1038/nnano.2014.288.

[32] G. Balasubramanian et al. “Nanoscale imaging magnetometry with diamond spins under ambient conditions”. In: *Nature* 455.7213 (2008), pp. 648–51. ISSN: 0028-0836. DOI: 10.1038/nature07278.

[33] A. Boretti, L. Rosa, and S. Castelletto. “Towards Single Biomolecule Imaging via Optical Nanoscale Magnetic Resonance Imaging”. In: *Small* 11.34 (2015), pp. 4229–36. ISSN: 1613-6810. DOI: 10.1002/smll.201500764.

[34] N. B. Manson, J. P. Harrison, and M. J. Sellars. “Nitrogen-vacancy center in diamond: Model of the electronic structure and associated dynamics”. In: *Phys. Rev. B* 74 (10 Sept. 2006), p. 104303. DOI: 10.1103/PhysRevB.74.104303.

[35] Alix Gicquel et al. “CVD diamond films: from growth to applications”. In: *Current Applied Physics* 1.6 (2001), pp. 479–496. ISSN: 1567-1739. DOI: https://doi.org/10.1016/S1567-1739(01)00061-X.

[36] Robert J. Nemanich et al. “CVD diamond—Research, applications, and challenges”. In: *MRS Bulletin* 39.6 (2014), pp. 490–494. DOI: 10.1557/mrs.2014.97.

[37] Qi Liang et al. “Recent advances in high-growth rate single-crystal CVD diamond”. In: *Diamond and Related Materials* 18.5 (2009). Proceedings of Diamond 2008, the 19th European Conference on Diamond, Diamond-Like Materials, Carbon Nanotubes, Nitrides and Silicon Carbide, pp. 698–703. ISSN: 0925-9635. DOI: https://doi.org/10.1016/j.diamond.2008.12.002.

[38] Jocelyn Achard et al. “The control of growth parameters in the synthesis of high-quality single crystalline diamond by CVD”. In: *Journal of Crystal Growth* 284.3 (2005), pp. 396–405. ISSN: 0022-0248. DOI: https://doi.org/10.1016/j.jcrysgro.2005.07.046.

[39] Michael N. R. Ashfold et al. “Nitrogen in Diamond”. In: *Chemical Reviews* 120.12 (2020). PMID: 32048841, pp. 5745–5794. DOI: 10.1021/acs.chemrev.9b00518.

[40] J. O. Orwa et al. “Engineering of nitrogen-vacancy color centers in high purity diamond by ion implantation and annealing”. In: *Journal of Applied Physics* 109.8 (Apr. 2011), p. 083530. ISSN: 0021-8979. DOI: 10.1063/1.3573768.

[41] S. Sangtawesin et al. “Highly tunable formation of nitrogen-vacancy centers via ion implantation”. In: *Applied Physics Letters* 105.6 (Aug. 2014), p. 063107. ISSN: 0003-6951. DOI: 10.1063/1.4892971.

[42] K Iakoubovskii, G J Adriaenssens, and M Nesladek. “Photochromism of vacancy-related centres in diamond”. In: *Journal of Physics: Condensed Matter* 12.2 (Jan. 2000), p. 189. DOI: 10.1088/0953-8984/12/2/308.

[43] Ádám Gali. In: *Nanophotonics* 8.11 (2019), pp. 1907–1943. DOI: doi:10.1515/nanoph-2019-0154. URL: https://doi.org/10.1515/nanoph-2019-0154.

[44] C. L. Degen, F. Reinhard, and P. Cappellaro. “Quantum sensing”. In: *Rev. Mod. Phys.* 89 (3 July 2017), p. 035002. DOI: 10.1103/RevModPhys.89.035002.

[45] Victor Acosta and Philip Hemmer. “Nitrogen-vacancy centers: Physics and applications”. In: *MRS Bulletin* 38.2 (2013), pp. 127–130. DOI: 10.1557/mrs.2013.18.

[46] Taras Plakhotnik and Haroon Aman. “NV-centers in nanodiamonds: How good they are”. In: *Diamond and Related Materials* 82 (2018), pp. 87–95. ISSN: 0925-9635. DOI: https://doi.org/10.1016/j.diamond.2017.12.004.

[47] Mohamed I. Ibrahim et al. “High-Scalability CMOS Quantum Magnetometer With Spin-State Excitation and Detection of Diamond Color Centers”. In: *IEEE Journal of Solid-State Circuits* 56.3 (2021), pp. 1001–1014. DOI: 10.1109/JSSC.2020.3027056.

[48] James L. Webb et al. “Nanotesla sensitivity magnetic field sensing using a compact diamond nitrogen-vacancy magnetometer”. In: *Applied Physics Letters* 114.23 (June 2019), p. 231103. ISSN: 0003-6951. DOI: 10.1063/1.5095241.

[49] Akihiro Kuwahata et al. “Magnetometer with nitrogen-vacancy center in a bulk diamond for detecting magnetic nanoparticles in biomedical applications”. In: *Scientific Reports* 10.1 (2020), p. 2483. DOI: 10.1038/s41598-020-59374-2.

[50] Xuemin Wang et al. “Portable Diamond NV Magnetometer Head Integrated With 520 nm Diode Laser”. In: *IEEE Sensors Journal* 22.6 (2022), pp. 5580–5587. DOI: 10.1109/JSEN.2022.3147775.

[51] Hiroshige Deguchi et al. “Compact and portable quantum sensor module using diamond NV centers”. In: *Applied Physics Express* 16.6 (June 2023), p. 062004. DOI: 10.35848/1882-0786/acd836.

[52] Jens Pogorzelski et al. “Compact and Fully Integrated LED Quantum Sensor Based on NV Centers in Diamond”. In: *Sensors* 24.3 (2024). ISSN: 1424-8220. DOI: 10.3390/s24030743.

[53] Donggyu Kim et al. “A CMOS-integrated quantum sensor based on nitrogen–vacancy centres”. In: *Nature Electronics* 2.7 (July 2019), pp. 284–289. ISSN: 2520-1131. DOI: 10.1038/s41928-019-0275-5.

[54] R. Ishihara et al. “3D Integration Technology for Quantum Computer based on Diamond Spin Qubits”. In: *2021 IEEE International Electron Devices Meeting (IEDM)*. 2021, pp. 14.5.1–14.5.4. DOI: 10.1109/IEDM19574.2021.9720552.

[55] T. Matsumae et al. “Hydrophilic direct bonding of monocrystalline (111) diamond substrate onto Si wafer”. In: *2019 6th International Workshop on Low Temperature Bonding for 3D Integration (LTB-3D)*. 2019, pp. 70–70. DOI: 10.23919/LTB-3D.2019.8735180.

[56] Takashi Matsumae et al. “Low-temperature direct bonding of diamond (100) substrate on Si wafer under atmospheric conditions”. In: *Scripta Materialia* 191 (2021), pp. 52–55. ISSN: 1359-6462. DOI: https://doi.org/10.1016/j.scriptamat.2020.09.006.

[57] Tianyin Chen et al. *Hydrophilic direct bonding of (100) diamond and deposited SiO_2 substrates*. 2025. DOI: https://arxiv.org/abs/2501.12831. arXiv: 2501.12831 [cond-mat.mtrl-sci].

[58] Todd Karin, Scott Dunham, and Kai-Mei Fu. “Alignment of the diamond nitrogen vacancy center by strain engineering”. In: *Applied Physics Letters* 105.5 (Aug. 2014), p. 053106. ISSN: 0003-6951. DOI: 10.1063/1.4892544.

[59] Xinghan Guo et al. “Microwave-Based Quantum Control and Coherence Protection of Tin-Vacancy Spin Qubits in a Strain-Tuned Diamond-Membrane Heterostructure”. In: *Phys. Rev. X* 13 (4 Nov. 2023), p. 041037. DOI: 10.1103/PhysRevX.13.041037.

[60] Ioannis Karapatzakis et al. *Microwave Control of the Tin-Vacancy Spin Qubit in Diamond with a Superconducting Waveguide*. 2024. arXiv: 2403.00521 [quant-ph].

[61] Matthew E. Trusheim et al. “Transform-Limited Photons From a Coherent Tin-Vacancy Spin in Diamond”. In: *Phys. Rev. Lett.* 124 (2 Jan. 2020), p. 023602. DOI: 10.1103/PhysRevLett.124.023602.

[62] F. Jelezko and J. Wrachtrup. “Single defect centres in diamond: A review”. In: *physica status solidi (a)* 203.13 (2006), pp. 3207–3225. DOI: https://doi.org/10.1002/pssa.200671403.

[63] Takayuki Iwasaki et al. “Tin-Vacancy Quantum Emitters in Diamond”. In: *Phys. Rev. Lett.* 119 (25 Dec. 2017), p. 253601. DOI: 10.1103/PhysRevLett.119.253601.

[64] Lachlan J. Rogers et al. “Electronic structure of the negatively charged silicon-vacancy center in diamond”. In: *Phys. Rev. B* 89 (23 Jan. 2014), p. 235101. DOI: 10.1103/PhysRevB.89.235101.

[65] Abram L. Falk et al. “Polytype control of spin qubits in silicon carbide”. In: *Nature Communications* 4.1 (2013), p. 1819. ISSN: 2041-1723. DOI: 10.1038/ncomms2854.

[66] A.A. Razgulov et al. “Low-temperature photoluminescence study of SnV centers in HPHT diamond”. In: *Diamond and Related Materials* 116 (2021), p. 108379. ISSN: 0925-9635. DOI: https://doi.org/10.1016/j.diamond.2021.108379.

[67] Jesús Arjona Martínez et al. “Photonic Indistinguishability of the Tin-Vacancy Center in Nanostructured Diamond”. In: *Phys. Rev. Lett.* 129 (17 Oct. 2022), p. 173603. DOI: 10.1103/PhysRevLett.129.173603.

[68] Abigail Stein et al. “Coherent Spin Control of a Tin Vacancy Center in Diamond”. In: *2023 Conference on Lasers and Electro-Optics (CLEO)*. 2023, pp. 1–2. URL: https://ieeexplore-ieee-org.tudelft.idm.oclc.org/document/10259760.

[69] Emilio Corte et al. “Spectral Emission Dependence of Tin-Vacancy Centers in Diamond from Thermal Processing and Chemical Functionalization”. In: *Advanced Photonics Research* 3.1 (2021). DOI: 10.1002/adpr.202100148.

[70] Tobias Lühmann et al. “Charge-State Tuning of Single SnV Centers in Diamond”. In: *ACS Photonics* 7.12 (2020). doi: 10.1021/acsphotonics.0c01123, pp. 3376–3385. DOI: 10.1021/acsphotonics.0c01123.

[71] Romain Debroux et al. “Quantum Control of the Tin-Vacancy Spin Qubit in Diamond”. In: *Phys. Rev. X* 11 (4 Nov. 2021), p. 041041. DOI: 10.1103/PhysRevX.11.041041.

[72] Alison E. Rugar et al. “Generation of Tin-Vacancy Centers in Diamond via Shallow Ion Implantation and Subsequent Diamond Overgrowth”. In: *Nano Letters* 20.3 (2020). doi: 10.1021/acs.nanolett.9b04495, pp. 1614–1619. ISSN: 1530-6984. DOI: 10.1021/acs.nanolett.9b04495.

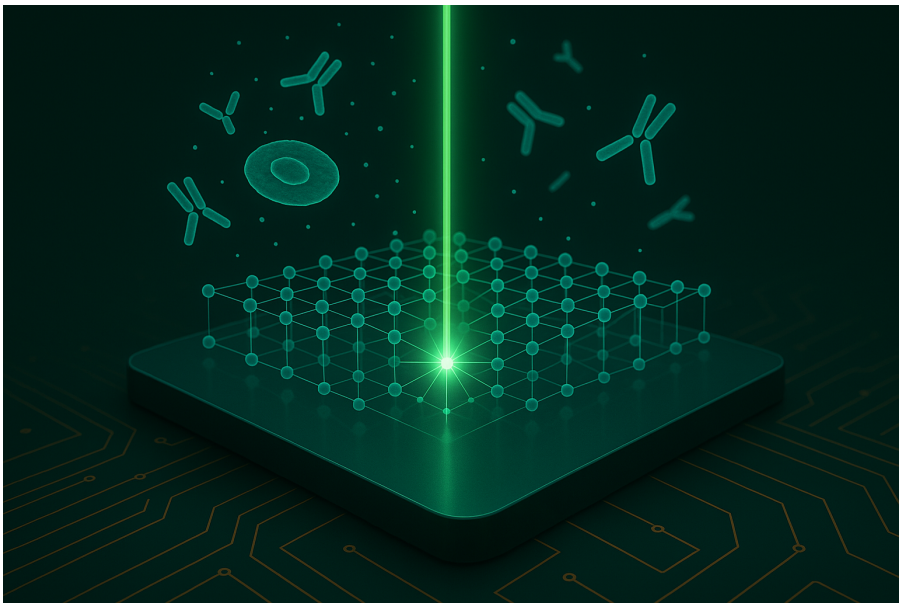
[73] Alison E. Rugar et al. “Narrow-Linewidth Tin-Vacancy Centers in a Diamond Waveguide”. In: *ACS Photonics* 7.9 (2020). doi: 10.1021/acsphotonics.0c00833, pp. 2356–2361. DOI: 10.1021/acsphotonics.0c00833.

[74] Alison E. Rugar et al. “Quantum Photonic Interface for Tin-Vacancy Centers in Diamond”. In: *Phys. Rev. X* 11 (3 July 2021), p. 031021. DOI: 10.1103/PhysRevX.11.031021.

2

COLOR CENTERS IN DIAMOND: THEORY, ODMR & BIOSENSING

This chapter introduces the fundamental concepts of color centers in diamond, focusing primarily on the nitrogen-vacancy (NV) and tin-vacancy (SnV) centers. It begins with a theoretical overview of their electronic structure, physical properties, and quantum behavior, that make these color centers pivotal in advancing quantum technologies, sensing applications, and materials science. The second part of the chapter covers the principles of Optically Detected Magnetic Resonance (ODMR) using NV centers, focusing on its applications in quantum magnetometry and biosensing. The experimental setup employed in this work is described in detail, followed by a description of the concept and the method of culturing cells and injecting them with magnetic nanoparticles, in order to emulate magnetic properties and measure them with the ODMR setup.



2.1. DIAMONDS: AN INTRODUCTION

Carbon (C) is one of the most fascinating elements in nature. Not only is it one of the building blocks of life (at least as we know it), but it is also responsible for some of the most commonly used or innovative materials (graphite, graphene [1], carbon fibers and carbon nanotubes [2] to name a few). Among these, diamond is a material that can function as either jewelry or scientific research tool, depending on the user.

Diamonds can be found in two forms, either natural or manufactured. Natural diamonds form deep beneath the Earth's surface, in high temperature and high pressure conditions, that allow crystallization of carbon. They are then brought to the surface via volcanic eruptions and mined by mineralogists and geologists. Throughout history, many civilizations have used diamonds as symbols of power and wealth. De Beers group has led the diamond mining and exploitation business since 1888 and until recently, popularizing diamonds to consumer markets.

Synthetic diamonds can be fabricated via a number of different techniques, each with its own advantages and disadvantages. Among these, Chemical Vapor Deposition (CVD) and High-Pressure High-Temperature (HPHT) are the most popular ones. These techniques will be discussed in more depth in chapter 3.

2.1.1. DIAMOND CLASSIFICATION

Diamonds can be divided into two main categories, depending on the type and concentration of impurities present in them. This classification was introduced in 1934 by Robertson *et al.* [3] and became standardized during the following decades [4]. In general, diamonds with a nitrogen concentration that is high enough to alter optical absorption properties are classified as *Type I*. The most commonly found natural diamonds belong to this category. Within this class, a further distinction is possible, based on whether the N impurities are aggregated (*Type Ia*) or not (*Type Ib*).

The second main category is called *Type II*. Although such diamonds are rare in nature ($< 0.1\%$ [4]), they can be fabricated through common synthesis procedures. The criterion upon which Type II is assigned to a diamond is nitrogen concentration of < 5 ppb. These are the so-called "electronic grade" diamonds and are invaluable assets to modern scientific research. Once again, within the Type II class, another categorization can be made. This time, it depends on the boron (B) concentration; none or minuscule boron impurities result in *Type IIa* diamonds, while considerable B concentration results in *Type IIb* diamonds [3, 4, 5].

2.1.2. DIAMOND COLORATION

Natural diamonds actually come in all sorts of colors. Although the most valuable diamonds (according to today's societal standards) have usually been transparent, there is increasing demand for non-colorless diamonds among commercial users. The factors that affect diamond coloration are mainly impurities, defects and radiation, temperature or pressure.



Figure 2.1: Overview of different potential diamond colors [6].

As can be seen in Figure 2.1, there is a strong correlation between diamond type and color, which, as mentioned above, has to do with the type and concentration of different impurities. Type Ia diamonds can often have various yellow tints, due to the different concentrations of nitrogen in them, while Type Ib diamonds exhibit a slightly more intense yellow or brown tint, because of the lack of aggregated nitrogen. On the other hand, most Type IIa diamonds are usually transparent or have more faint colors, having very low N concentration. Finally, Type IIb diamonds are typically blue, since they contain boron impurities. Nevertheless, it is worth noting that HPHT treatment is able to remove brown color in Ia diamonds or create pink or blue colors in IIa diamonds. At the same time, irradiation processing could again modify the diamond's color, by creating color centers (more about color centers in subsection 2.1.4) [4, 7, 8, 9]. In the research being conducted in the field of quantum sensing and quantum computing, transparent diamonds of Type Ib or IIa (further doped with N atoms) are generally used, depending on the conditions of a given experiment.

2.1.3. THE DIAMOND CRYSTAL STRUCTURE

The crystal structure of diamond (see Figure 2.2) was first described in 1913, by W. Henry Bragg and W. Lawrence Bragg [10]. It can be characterized by a Face-Centered Cubic (FCC) lattice structure with a basis consisting of two distinct carbon atoms, instead of a single one. It may, thus, be classified as a Zinc Blende structure, having two identical atoms in its basis. More specifically, the first carbon atom is located at $(0,0,0)$, being the origin of the unit cell, while the second carbon atom is positioned at $\left(\frac{1}{4},\frac{1}{4},\frac{1}{4}\right)$, creating a tetrahedral formation.

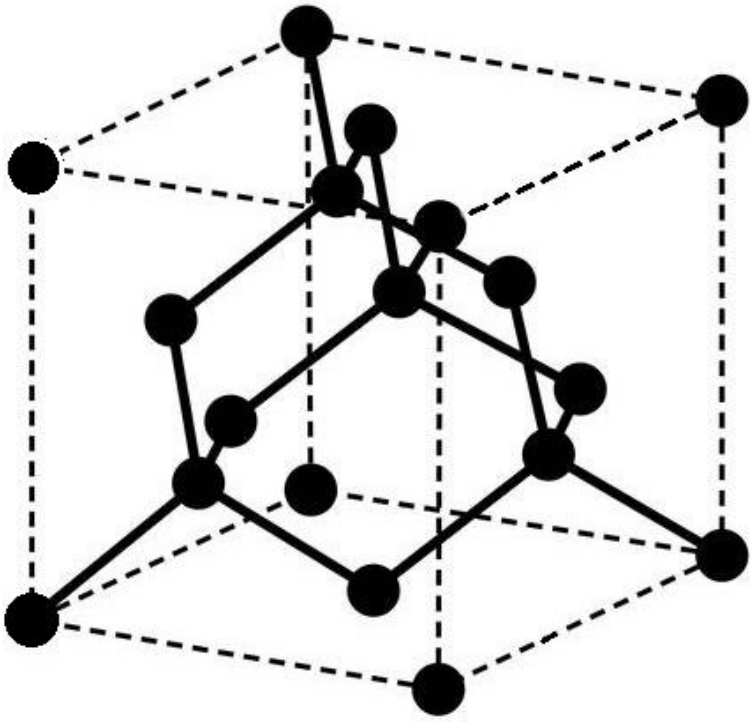


Figure 2.2: Diamond's crystal structure.

In this arrangement, there are four (sp^3 hybridized) covalent bonds, created by the valence electrons of each carbon atom and the neighboring carbon atoms, at an angle of $\approx 109.5°$. The bond length can be calculated as the distance d between two carbon atoms in the unit cell:

$$d = \sqrt{(x_2 - x_1)^2 + (y_2 - y_1)^2 + (z_2 - z_1)^2} \approx 1.54\,\text{Å} \tag{2.1}$$

Meanwhile, the lattice constant a (distance between two adjacent points in the unit cell) has a value of $a \approx 3.566\,\text{Å}$ [10, 11, 12].

Diamonds are well-known for their exceptional hardness (10,000 kg/mm^2 [13]), rated 10 out of 10 in the Mohs scale [14]. As described by Petrescu *et al.*, diamond hardness is attributed mainly to its strong covalent bonding with short bond lengths, its cubic structure that maximizes atomic packing and its sp^3 hybridization. This hardness enables the use of diamonds in various industrial applications [15, 10, 16, 17, 18].

2.1.4. COLOR CENTERS IN DIAMOND

There exist multiple different possible types of defects in a given material. Such defects may form on the surface after a chemical treatment [19], or in grain boundaries of polycrystalline materials [20, 21, 22]. They could be atom or vacancy aggregates (clusters) [23, 24, 25]. Or they could be point defects, which refer to localized lattice disruptions, and include interstitial atoms, substitutional impurities, or vacancies [26, 27, 23, 28].

In diamond, a color center is a type of point defect, which may not only alter the optical properties, like absorption and emission, but also the electrical, mechanical, magnetic and spin properties. Therefore, diamonds have exceptional versatility and can find uses in multiple different scientific fields. The image below depicts the periodic table, with the most studied and used elements related color centers colored red, blue and yellow, depending on their significance (see Figure 2.3).

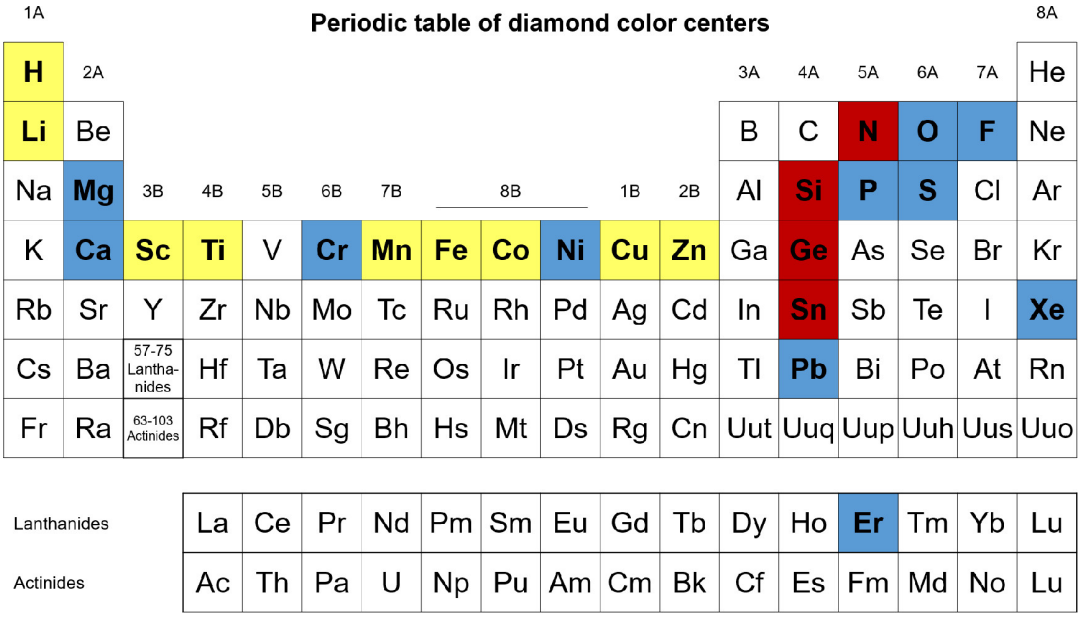


Figure 2.3: Periodic table demonstrating potential color centers in diamond. Image by Mzyk *et al.* [29]. Most popular and promising color centers are in red, theoretically studied color centers are in yellow and others in blue.

The elements need to fulfill a few criteria in order to be able to form stable and useful color centers. To start with, they need to be able to form stable bonds with the rest of the atoms in the diamond lattice. Moreover, their size needs to be comparable to that of carbon. Thus, lighter atoms are preferred, since they do not cause excessive strain in the lattice. In contrast, heavier and bigger atoms could damage the diamond during their implantation processes and result in graphitization [29].

Despite the fact that such a plethora of color centers exists, only few possess features that make them prominent in either quantum sensing, quantum computing, or quantum communication. These are the nitrogen-vacancy (NV) center and the group-IV color centers. This group includes the tin-vacancy (SnV) [30, 31, 32], the silicon-vacancy (SiV) [33, 34, 35], the germanium-vacancy (GeV) [36, 37], and the lead-vacancy (PbV) [38, 39] centers. In this chapter, however, and for the rest of this dissertation, we are only going to discuss and investigate NV and SnV centers in diamond.

2.2. NV CENTERS IN DIAMOND

Starting with the NV center, its atomic structure is going to be examined, as well as its charge states and its emerging electronic, optical and magnetic properties. Finally, a brief overview of its coherence and relaxation times will be provided, along with a basic analysis of its Hamiltonian terms.

2.2.1. ATOMIC STRUCTURE

An NV center consists of one nitrogen atom and one adjacent vacancy. This nitrogen atom substituting for a former carbon atom at the same location, whereas vacancy refers to a missing carbon atom. As mentioned in subsection 2.1.3, diamond can be described as a zinc blende structure, with identical (carbon) atoms as the basis. Each carbon atom has six electrons, four of which are valence electrons and are key to the electronic properties of the NV center [40]. The distribution is as follows (see Figure 2.4), based on Hund's rule of lowest-energy electron configuration:

$$[\mathrm{C}]\ 1s^2\,2s^2\,2p^2 \tag{2.2}$$

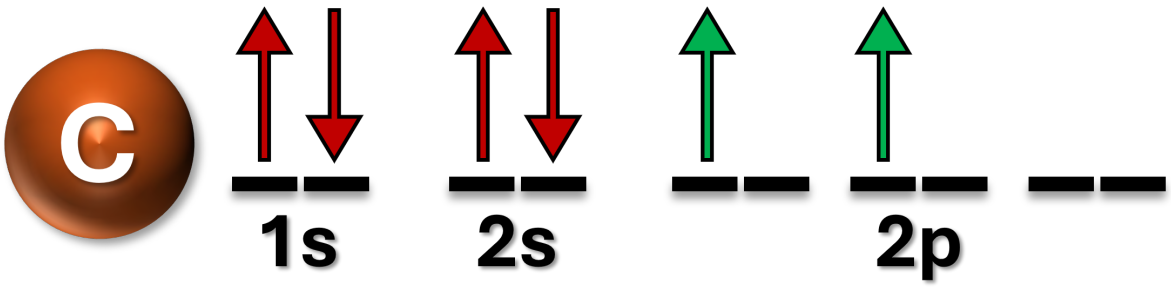


Figure 2.4: Electron configuration of a carbon atom.

The valence electrons occupy the 2s and 2p orbitals. Each of these electrons forms covalent bonds with four neighboring carbon atoms. In order to form these bonds, however, there need to be four available orbitals. Hence, the need for hybridization arises, and four sp^3 hybrid orbitals are created by utilizing one 2s and three 2p orbitals. These are strong σ bonds.

In the case of a nitrogen-vacancy center, a nitrogen atom replaces a carbon atom, to then form three covalent σ bonds with three neighboring carbon atoms. From the remaining two electrons (out of the initial five valence electrons of nitrogen), one contributes to the creation of a lone pair in the fourth sp^3 hybrid orbital, and one remains unpaired. This lone pair does not participate in bonding, but does affect the overall electronic structure.

The electron configuration of a nitrogen atom is as seen in Figure 2.5 below:

$$[\mathrm{N}]\ 1s^2\,2s^2\,2p^3 \tag{2.3}$$

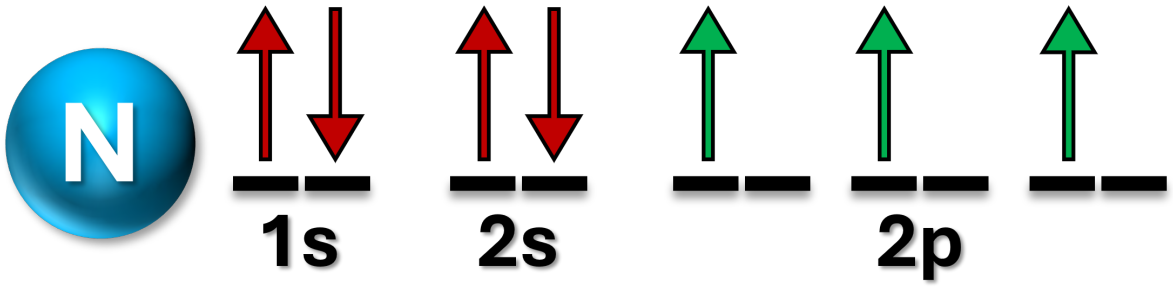


Figure 2.5: Electron configuration of a nitrogen atom.

The role of the vacancy is also critical to the function of an NV center. A vacancy indicates the absence of (in this case) a carbon atom in the lattice (see Figure 2.6). It is formed either naturally or after processing, during which the carbon atoms are displaced. While it does not "carry" any electrons by itself, it creates localized electronic states, which can trap electrons that are optically excited to the conduction band [40, 41, 42, 43].

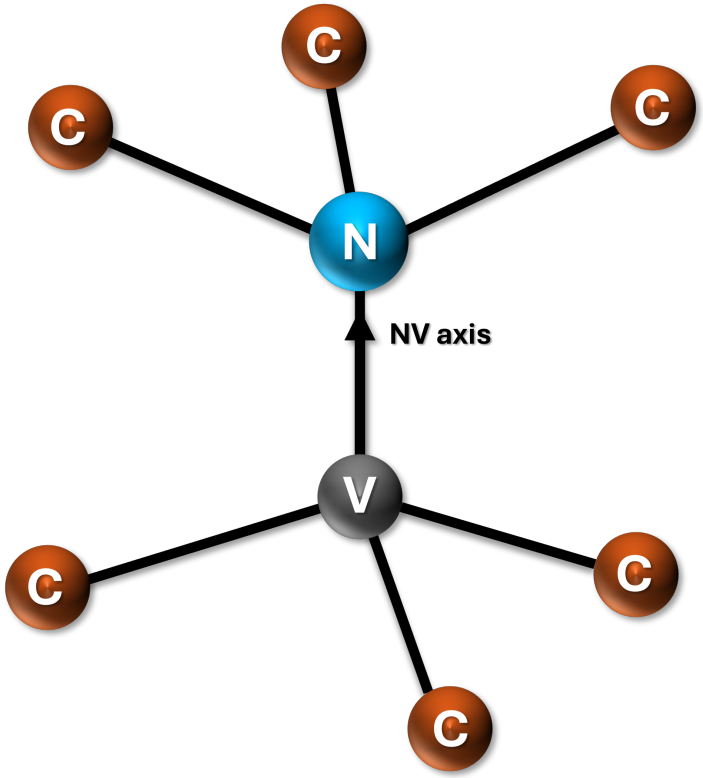


Figure 2.6: The structure of an NV center.

2.2.2. A QUICK OVERVIEW OF THE NEUTRAL STATE NV^0

If an additional electron does not occupy an available state, the NV center is then in a neutral state, known as NV^0. Contrary to the NV^-, it is primarily characterized by a doublet state with spin $S = 1/2$, which is made more energetically favorable due to the Jahn-Teller effect. The distortion caused by this effect also leads to a reduced symmetry, from C_{3v} to C_S.

Employing IR and Raman spectroscopy results in distinct spectra, due to the unique electronic configuration of the NV^0 state. As seen in Figure 2.7, the NV^0 exhibits a wide emission spectrum, with a Zero-Phonon Line (ZPL) emission at ≈ 575 nm [40, 44, 45, 46, 47].

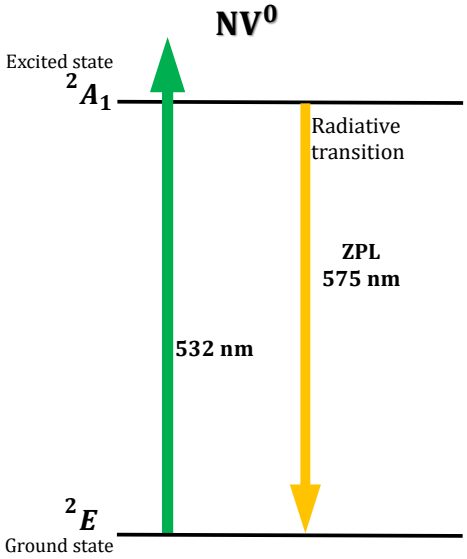


Figure 2.7: Energy level diagram of the neutral NV^0 state.

It is worth mentioning that charge conversion of the NV center is possible. Optical excitation (in both NV^0 and NV^- is usually achieved with a green laser of 532 nm or less. However, the energy of such a laser beam can ionize the negative NV^- state and convert it to NV^0. This effect is even more pronounced when using higher laser excitation powers and can take place even when below saturation intensity levels. Excitation of the NV^- from its ground ($^3A_2$) state to its excited (^3E) states can end in intersystem crossing (ISC) to the singlet states $^1A_1$ and ^1E. This may come with a change in spin and can, due to the Jahn-Teller effect, lead the system to decay into the energetically favorable NV^0 state.

Similarly, an NV^0 is able to be converted an NV^- state, via a recharge process that takes place in the dark (under no illumination). Such a process occurs when an electron from the environment successfully recombines with the NV^0 center, turning it back into an NV^-, and is facilitated by vacancies, or electronegative surface groups that exist on the surface of the diamond [47].

2.2.3. THE NEGATIVELY CHARGED STATE NV^-

Whenever an electron occupies such an electronic state created by the vacancy, then the NV center goes into its negatively charged state, NV^-, having a total of two unpaired electrons. This is the NV state that is going to be studied in this investigation hereafter and what should be implied when referred to as simply NV. In this state, there exists a spin triplet ground state (with spin $S = 1$) [42]. The energy difference between the $|\pm1\rangle$ states and the ground $|0\rangle$ state is given by:

$$\Delta E_m = E_{|m\rangle} - E_{|0\rangle} = D_m + \gamma B \quad (m = +1, 0, -1) \tag{2.4}$$

where E_m is the energy of the spin state $|m\rangle$, E_0 is the energy of the ground state $|0\rangle$, m is the magnetic quantum number, D_m is the zero-field splitting (ZFS) parameter, γ is the gyromagnetic ratio, which relates the magnetic moment of the NV center to its angular momentum, and B is the magnitude of an external magnetic field. The values for the above parameters are:

$$D_m \approx 2.87\,\text{GHz, for the ground triplet state} \tag{2.5}$$

$$\gamma \approx 28\,\text{GHz/T} \tag{2.6}$$

The zero-field splitting (ZFS) is of major significance. It originates from spin-spin interactions (primarily in the case of the ground state) or spin-orbit coupling and results in discrete energy separation between the $|0\rangle$ and $|\pm1\rangle$ states [40, 43, 48]. Further on in this chapter, the notations $m_s = 0$ and $m_s = \pm1$ are going to be predominantly used instead.

2.2.4. ELECTRONIC AND OPTICAL PROPERTIES

The NV center adheres to the symmetry of the C_{3v} point group. It can, thus, be described by three principal axes, consisting of the z-axis (serving as the axis of symmetry along the [111] direction) and two perpendicular axes (x and y). This symmetry allows rotations of 120° and 240° around the principal z-axis, and reflections across three vertical reflection planes that intersect the z-axis [49].

GROUND STATE

Based on this symmetry, the NV center assumes the following ground state configuration, consisting of four electrons:

$$(a_1^2)(e^2) \equiv |a_1(1)\rangle, |a_1(2)\rangle, |e_x\rangle, |e_y\rangle \tag{2.7}$$

In this configuration, the $|a_1(1)\rangle$ and $|a_1(2)\rangle$ orbitals are less mobile and serve to stabilize the ground state, whereas the electrons in the degenerate $|e_x\rangle$ and $|e_y\rangle$ orbitals are mainly involved in excitation dynamics.

More specifically, the NV center consists of a triplet ground state ${}^3A_2$ and two singlet ($S = 0$) states, ${}^1E$ and ${}^1A_1$. The ${}^3A_2$ state is characterized by a symmetric spatial wave function and antisymmetric spin states, according to the Pauli exclusion principle [48]. The total wave function for this state is the following:

The total wave function for the triplet state $^3A_2$ can be written as:

$$\Psi_{^3A_2} = \psi_s(\mathbf{r}_1, \mathbf{r}_2) \otimes \chi_a(s_1, s_2) \tag{2.8}$$

where ψ_s is the spatial wave function, r_1, r_2 are the spatial coordinates of the electrons, s_1, s_2 their spin states, and χ_a is the spin wave function, resulting in:

$$\Psi_{^3A_2} = \frac{1}{\sqrt{2}}\left(|e_x\rangle|e_y\rangle + |e_y\rangle|e_x\rangle\right) \otimes \frac{1}{\sqrt{2}}\left(|\uparrow\downarrow\rangle - |\downarrow\uparrow\rangle\right) \tag{2.9}$$

Due to the nature of this symmetry, the $^3A_2$ is assigned as the lowest energy state.

Regarding the singlet states, they rely on the electrons of lower energy levels being excited to these states. The doubly degenerate state ^1E is formed when the $|e_x\rangle$ and $|e_y\rangle$ states couple into an antisymmetric spin state. Meanwhile, the $^1A_1$ state has a completely symmetric spatial and spin configuration, as a result of the symmetric coupling of the two electrons in the same, a_1, orbital [48].

For the singlet state ^1E, the total wave function is:

$$\Psi_{^1E} = \psi_a(\mathbf{r}_1, \mathbf{r}_2) \otimes \chi_s(s_1, s_2) \tag{2.10}$$

Similarly for the singlet state $^1A_1$:

$$\Psi_{^1A_1} = \psi_s(\mathbf{r}_1, \mathbf{r}_2) \otimes \chi_a(s_1, s_2) \tag{2.11}$$

These singlet states are heavily influenced by Coulomb interaction (see Appendix A.1). In the $^1A_1$ state, there is increased electron spatial proximity, due to the presence of electrons in the same orbital, leading to increased electron-electron interaction energy and increased Coulomb repulsion. Likewise, the ^1E state experiences Coulomb repulsion, although several other factors contribute to its increased energy level, such as its lower symmetry compared to the $^1A_1$ state [48, 50, 43, 51]. Overall, the energy hierarchy of the ground state and the higher-energy singlet states can be summarized as follows:

$$E_{^3A_2} < E_{^1E} < E_{^1A_1} \tag{2.12}$$

EXCITED STATE

The excited state of the NV center is another spin triplet state with spin $S = 1$ and three possible spin projections along the z-axis. It is denoted as ^3E. Excitation to the ^3E state is done by absorption of a photon, resulting in the transition of one of the electrons from the low-energy a_1 orbital to a higher-energy, degenerate e_x or e_y orbital.

The excited ^3E state is also governed by ZFS of about 1.42 GHz. This splitting is, this time, in contrast to the ZFS in the ground state, mainly caused by the degenerate e_x and e_y orbitals, which introduce additional degrees of freedom. The degeneracy of these orbitals gives rise to more delocalized electrons with less intense spin-spin interactions, but makes the state more prone to spin-orbit coupling and strain effects. Averaging out these effects results in a reduction in spin-spin interactions and, therefore, a lower ZFS value than the $^3A_2$ ground state [48, 51, 43, 52].

OPTICAL EXCITATION AND EMISSION

Diamond has a wide bandgap of ≈ 5.5 eV. Yet, the NV centers introduce localized and discrete energy levels within this bandgap, making optical excitation and emission possible while still in the visible wavelength, with both the ground $^3A_2$ and the excited ^3E states lying below the diamond's conduction band. Therefore, a purely optical, non-phonon related optical transition requires an energy of ≈ 1.95 eV, which corresponds to a wavelength of 637 nm (see Appendix A.2). This also represents the direct $^3A_2$ to ^3E electronic transition and defines the zero-phonon line (ZPL), meaning that emission occurs without the involvement of any phonons [40, 41, 50].

Nonetheless, in most sensing setup configurations utilizing NV centers in diamond, a green wavelength of (most often) 532 nm is used. A wavelength in this range can drive transitions that include phonon sidebands, and is beneficial, since it allows a broader absorption spectrum and more efficient NV center excitation. The reason behind this is that there exist multiple imperfections within the lattice, be it strain or temperature variations, that may impact and shift the ZPL [51, 50, 53].

The transition from the $^3A_2$ ground triplet state to the ^3E excited triplet state is an electric dipole transition, that comes with conservation of the spin and the orbital angular momentum, $\Delta S = 0$. As just mentioned above, it is connected to photons with wavelength of $\lambda = 637$ nm. Excitation with lower wavelength (meaning higher energy) will result in excess energy being absorbed by the lattice, in the form of vibrational phonons. This is a momentum-conserving transition.

When relaxation from the ^3E to the $^3A_2$ state takes place, a great deal of this comes in the form of phonon-sideband emission, owing to phonon interactions. Those emitted photons carry lower energies, or, in other words, have a higher wavelength, with a broad range reaching till the near-infrared (NIR) part of the spectrum. The majority of emission happens in this regime between the ZPL and roughly 800 nm, while only about 4% occurs in the ZPL, registering the NV as a color center with very small Debye-Waller factor (see Appendix A.3).

Finally, there are a few forbidden transitions. These include transitions between the triplet (^3E, $^3A_2$) and the singlet (^1E, $^1A_1$) states, which do not preserve the total spin ($\Delta S \neq 0$). Nevertheless, they may still happen in a non-radiative manner, through intersystem crossing (ISC) (see Appendix A.4). They are enabled by spin-orbit coupling and magnetic dipole or phonon interactions, that allow mixing of the triplet and singlet states [48, 51, 50, 43, 54].

The lifetime of NV centers is based on several factors, including but not limited to the presence of nearby impurities, external fields, spin and orbital interactions, the Purcell effect and temperature. Single NV centers in nanodiamonds have a fluorescence lifetime between 15 ns and 30 ns at RT [55, 56]. Meanwhile, single NV centers in bulk diamond have a lifetime of ≈ 30 ns [57] and ensemble NV centers exhibit reduced lifetimes, around 10 ns to 20 ns, due to increased dipole-dipole interactions [56].

2.2.5. MICROWAVE DRIVING AND MAGNETIC PROPERTIES

From subsection 2.2.3, it is understood that the ground triplet state $^3A_2$ is split into its $m_s = 0$ and $m_s = \pm 1$ states with a ZFS of 2.87 GHz. A microwave (MW) field with a frequency of the same value induces resonant oscillations (Rabi oscillations), that constantly and coherently drive the spin population between these sublevels, as seen in Figure 2.9. The $m_s = \pm 1$ states, however, are mainly responsible for non-radiative transitions through ISC, resulting in reduced fluorescence, compared to the $m_s = 0$ state [43].

The application of an external magnetic field $\vec{B}$ leads to the separation of the $m_s = \pm 1$ states and the negation of their degeneracy, relative to the $m_s = 0$ state. This, in turn, affects the energy difference (or splitting) between the $m_s = 0$ and each of the $m_s = -1$ and $m_s = +1$ states, altering the resonance conditions (see Figure 2.8). This is a phenomenon that is referred to as Zeeman splitting and results in discrete energy for each sublevel, which scales linearly with the applied magnetic field. The corresponding resonance frequency difference Δf is given by:

$$\Delta f = \frac{\Delta E}{h} = \frac{g_e \mu_B B}{h} \tag{2.13}$$

where ΔE is the energy difference between $m_s = 0$ and $m_s = +1$, h is Planck's constant, g_e is the electron g-factor, μ_B Bohr's magneton, and B is the magnetic field strength.

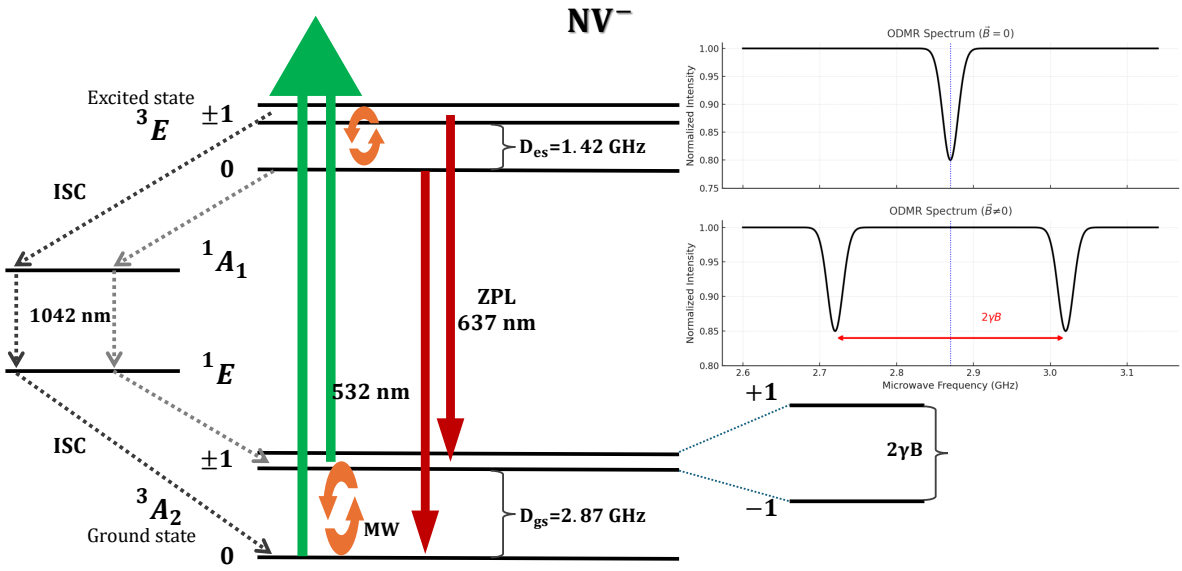


Figure 2.8: Energy level diagram of the negatively charged NV^- state.

There is a magnetic moment associated with each spin triplet state of the NV center, due to its $S = 1$ spin. This renders the interaction with external magnetic fields possible. Furthermore, the NV center's unpaired electron acts as a permanent magnetic dipole, making it highly susceptible to such interactions. Its sensitivity is enhanced by the presence of ZFS and is subsequently modified when an external magnetic field is applied. The aforementioned characteristics combine to make the NV center an excellent magnetic field sensor [40, 43, 50, 52].

2.2.6. SPIN RELAXATION AND DECOHERENCE TIMES

When describing the properties and qualities of NV centers, a few parameters come to mind. These parameters describe spin relaxation and coherence times, providing a quantifiable metric for their stability and sensitivity. They are dependent not only on the impurities present (both in concentration and type), but also on any local magnetic, strain or electric fields and even temperature or electron-phonon interactions. They drastically affect spin dynamics and are relevant to any kind of experimental measurement or application involving NV centers. Therefore, their extensive study has been ongoing for several years [58, 59, 52].

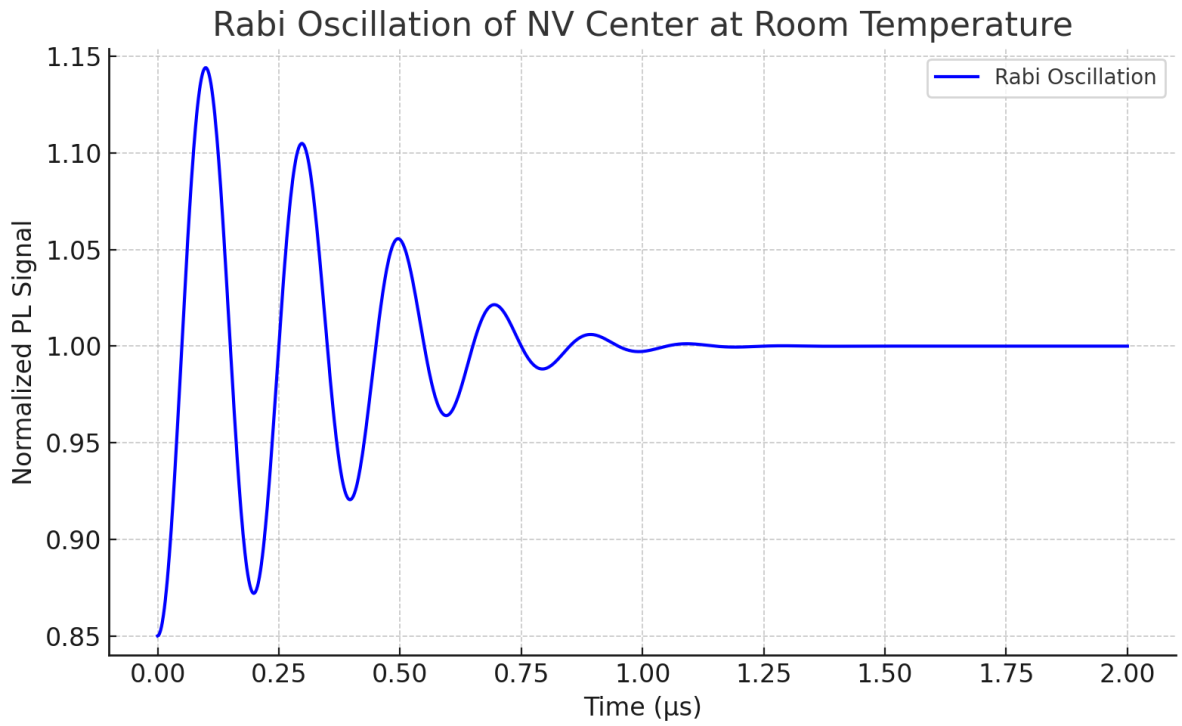


Figure 2.9: Simulated Rabi oscillation of an NV center at room temperature. The normalized PL signal is plotted as a function of microwave pulse duration. The simulation assumes a Rabi frequency of $\Omega_R = 2\pi \cdot 5\,\text{MHz}$, a Gaussian dephasing envelope with $T_2^* = 0.5\,\mu\text{s}$, and a fluorescence contrast of 15%. The observed oscillation decay reflects the loss of spin coherence due to inhomogeneous broadening in the diamond environment.

SPIN-LATTICE RELAXATION TIME T_1

The first parameter of interest is the one referred to as spin-lattice relaxation time (or longitudinal relaxation time), denoted as T_1. This parameter is an indicator of the time it takes an NV center's spin to fall back into a thermal equilibrium state following excitation to higher spin levels. It is also used as a measure of energy dissipation into phonons, closely related to non-radiative relaxation mechanisms. Application-wise, it is most important in quantum sensing, since it affects the effectiveness with which magnetic or electric fields are detected, by being correlated with environmental noise and influencing spin coherence [60, 61]. Therefore, high values T_1 are desirable. Values of T_1 range from milliseconds in room temperature up to tens of seconds in cryogenic temperatures [60, 62].

Surface impurities may cause the NV centers to experience strong, random magnetic field fluctuations that drive $m_s = 0$ to $m_s = \pm 1$ transitions, significantly reducing the spin relaxation time. When investigating nanodiamonds, where thermal noise is more prominent closer to the surface, it is possible to model the relaxation rate $\Gamma_1 = 1/T_1$ as a Lorentzian function of temperature, expressing the impact of temperature-dependent magnetic noise. Based on this, de Guillebon *et al.* (2020) [60] derive the following expression:

$$\Gamma_1 = \Delta \left(\frac{\Gamma_\infty e^{-T_a/T}}{\left(\Gamma_\infty e^{-T_a/T}\right)^2 + \omega_0^2} \right) \tag{2.14}$$

where Δ is an empirical fitting parameter, Γ_∞ is the high-temperature fluctuation limit, T_a is the activation temperature related to thermal noise, T is the temperature, and $\omega_0 = 2.87\,\text{GHz}$ is the resonance frequency of the NV center.

Another factor that heavily influences the spin relaxation time is the NV center concentration and external magnetic fields. In the presence of dense NV concentrations, there is heightened spin dipole-dipole coupling that enables faster energy transfer between spins and diminishes T_1. A study by Jarmola *et al.* (2015) [61] modeled the fluorescence intensity $I(s)$ as a function of time s, using the exponential function seen below:

$$I(s) = \exp\left(-\frac{s}{T_1}\right)^\beta \tag{2.15}$$

where β is a parameter between zero and one, indicative of the different relaxation times in an ensemble of NV^- centers, due to elevated spin-spin interactions. This model showcases the strong dependence of fluorescence on T_1 and hints towards a non-uniform distribution of relaxation times across the NV ensemble.

SPIN DEPHASING TIME T_2

Spin dephasing time, also known as spin coherence time, spin-spin relaxation time or transverse relaxation time, T_2 is another crucial parameter for the NV center. As the name suggests, it provides a value for how fast a spin state loses its phase coherence. It can easily be inferred that a higher T_2 is advantageous, as plenty of quantum-based application rely on maintaining long-lived coherent superpositions of quantum states.

Similarly to T_1, increased concentration of paramagnetic impurities results in fluctuating magnetic fields in the vicinity of the NV centers, leading to dephasing and degrading T_2. Nearby nuclear spins, and especially ^{13}C nuclei cause dipolar coupling and lead to decoherence [63, 43, 64]. There have been numerous studies on the impact that high ^{13}C concentration has on the T_2 coherence time, finding, empirically, that T_2 scales inversely with said concentration. This relationship is shown below, with n being the nuclear spin concentration [65, 66]:

$$T_2 \propto \frac{1}{\sqrt{n}} \tag{2.16}$$

Typical values for the spin dephasing time T_2 for NV centers in diamonds with high concentrations of ^{13}C (~ 20%) or nitrogen are in the order of tens of µs, while those with low

^{13}C concentration (~ 0.03%) can reach up to 1.8 ms [59, 65]. NV ensembles with nitrogen density in the order of 0.01 to 300 ppm usually exhibit T_2 of up to 700 µs, according to Bauch *et al.* (2020) [66]. Meanwhile, de Lange *et al.* (2010) employed dynamical decoupling (see Appendix A.5) with single NV spins to extend T_2 25-fold, from initial values of a couple µs [67]. On top of that, it was demonstrated by Bar-Gill *et al.* (2013) that T_2 times reaching 1 second are possible, for single NV centers in isotopically purified diamond [68].

Single NV spin decay model

Modeling the T_2 decay has to take into account whether a diamond with single NV spins or ensemble of NV centers is investigated. In the single NV spin decay model, an isolated NV center in a diamond lattice is assumed to have individual dipolar interactions with each nuclear spin located nearby. The following stretched exponential function is inferred [67, 65]:

$$S(t) \propto \exp\left(-\left(\frac{t}{T_2}\right)^q\right) \tag{2.17}$$

where $S(t)$ is the coherence as a function of time, t, and $q \approx 2$ is the (Gaussian) decay parameter.

Ensemble NV spin decay model

The decay model of an NV center ensemble requires a somewhat different function. This is due to multiple NV centers experiencing different local fields, both in density and spatially, thus averaging the interaction with nearby nuclear spin baths. Putting this into mathematical terms would look like the relationship below:

$$S(t) \propto \exp\left(-\left(\frac{t}{T_2}\right)^{3/2}\right) \tag{2.18}$$

Once again here, an exponential decay function is made use of [66, 67].

Inhomogeneous dephasing time T_2^*

The inhomogeneous dephasing time T_2^*, otherwise known as free induction decay (FID) time, is a parameter which reflects the decay of a spin system's coherence, because of inhomogeneous broadening. The cause of this inhomogeneous broadening is, this time, slowly fluctuating or static fields, in contrast with the homogeneous dephasing time T_2, which is related to more dynamic interactions.

As mentioned in Equation 2.2.6, the presence of electron or nuclear spins within the diamond's lattice in proximity to the NV centers creates fluctuating local fields. The NV centers respond to those field variations, and so their resonance frequencies shift by different, non-standardized amounts, based on their random spatial distribution and spin interaction strengths. This leads to inhomogeneous broadening of the resonant peaks and causes coherence decay during Ramsey measurements (see Appendix A.6) [59, 69]. Building on top of this, variations in either applied or intrinsic magnetic fields, such as ones usually found in ensembles of NV centers, further exacerbate the dephasing of T_2^*.

In a similar way, strain variations are also responsible for shifting the energy levels of the NV center and altering its resonance frequencies, causing additional inhomogeneous broadening [70]. Temperature fluctuations are another factor to consider for impacting T_2^*, as they affect ZFS and, therefore, contribute to phase decoherence [52].

Values of T_2^* can be acquired by performing Ramsey fringe measurements, in which the static nature of local fields creates a Gaussian coherence decay [71, 59]. Bauch *et al.* (2018) present an equation summarizing the aforementioned, independent spin dephasing mechanisms in an ensemble of NV centers [70]:

$$\frac{1}{T_2^*} \approx \frac{1}{T_2^{*\,\{\text{NV-}^{13}\text{C}\}}} + \frac{1}{T_2^{*\,\{\text{NV-N}\}}} + \frac{1}{T_2^{*\,\{\text{other spins}\}}} + \frac{1}{T_2^{*\,\{\text{strain grad.}\}}} + \frac{1}{T_2^{*\,\{\text{B-field grad.}\}}} + \frac{1}{T_2^{*\,\{\text{temp. fluctuations}\}}} + \dots \tag{2.19}$$

The inhomogeneous dephasing time T_2^* is, by definition, shorter than (in most cases) or equal to T_2. It is, like T_2, strongly correlated to ^{13}C concentration. Hence, while diamonds with natural isotopic abundance of ^{13}C exhibit T_2^* times of barely a few microseconds, isotopically purified diamonds show significantly (but still not greatly) improved T_2^* in the order of tens of µs. However, utilizing advanced quantum control techniques, such as spin-bath driving or double quantum coherence magnetometry, has the potential to further increase the inhomogeneous spin dephasing time (see Appendices A.7 & A.8) [70, 69, 59, 52].

2.2.7. NV HAMILTONIAN

In order to represent the energy of a system in quantum mechanics, the operator known as Hamiltonian ($\hat{H}$) is used. It is equal to the sum of the kinetic and potential energy of the system's particles and can be either time-dependent or time-independent. For a given quantum state or wavefunction $|\psi\rangle$, the corresponding Schrödinger equation is used:

Time-dependent Schrödinger equation:

$$\hat{H}|\psi(t)\rangle = i\hbar\frac{\partial}{\partial t}|\psi(t)\rangle \tag{2.20}$$

where $\hbar$ is the reduced Planck's constant, and

Time-independent Schrödinger equation:

$$\hat{H}|\psi\rangle = E|\psi\rangle \tag{2.21}$$

where E is the $|\psi\rangle$ state's energy eigenvalue.

In the context of the NV center, the Hamiltonian can, most of the time - and at least for this dissertation, be considered time-independent. There are multiple terms that are in play and contribute to the overall Hamiltonian, although each to a different degree. The full Hamiltonian can be written in the following form:

$$\hat{H}_{\text{NV}} = \hat{H}_{\text{ZFS}} + \hat{H}_{\text{Zeeman}} + \hat{H}_{\text{Hyperfine}} + \hat{H}_{\text{Spin-Orbit}} + \hat{H}_{\text{Strain}} + \hat{H}_{\text{Electric}} + \hat{H}_{\text{MW}} - i\hbar\Gamma_{\text{ISC}} \tag{2.22}$$

Now, the individual terms shall be further investigated.

ZFS TERM

To begin with, the most dominant term in the Hamiltonian of the NV center is that of zero field splitting (ZFS), $\hat{H}_{\text{ZFS}}$. As mentioned earlier, there are two unpaired electrons, which are subject to spin-spin interactions, giving rise to the Hamiltonian below:

$$\hat{H}_{\text{SS}} = \sum_{i,j} D_{ij}\hat{S}_i\hat{S}_j \tag{2.23}$$

where D_{ij} is the ZFS tensor and $\hat{S}_i$, $\hat{S}_j$ are the spin operators, with $(i,j) = (x,y,z)$. Due to symmetry along the NV axis, the term can be simplified to

$$\hat{H}_{\text{SS}} = D\left(\hat{S}_z^2 - \frac{1}{3}S(S+1)\right) + E\left(\hat{S}_x^2 - \hat{S}_y^2\right) \tag{2.24}$$

where D is the axial ZFS parameter, originating from the magnetic dipole-dipole interaction and responsible for the splitting into $m_s = 0$ and $m_s = \pm 1$, while E is the less prominent, transverse term, responsible for lifting the degeneracy of the $m_s = \pm 1$ states

when asymmetries are present [58, 52, 72]. Given that $S = 1$, and neglecting the constant energy offset, the expression is simplified to:

$$\hat{H}_{\text{ZFS}} = D\hat{S}_z^2 + E\left(\hat{S}_x^2 - \hat{S}_y^2\right) \tag{2.25}$$

2

ZEEMAN TERM

Next in terms of importance is the Zeeman term, $\hat{H}_{\text{Zeeman}}$, which is the cause of lifting of the degeneracy of the $m_s = \pm 1$ states, and energy level shift, when a magnetic field is present. It stems from coupling between the NV center's magnetic moment related to its spin and the magnetic field. It is known that

$$\vec{\mu} = -g\mu_B \hat{S} \tag{2.26}$$

where $\vec{\mu}$ is the magnetic moment of an electron and $\hat{S}$ its spin operator, with the Landé electronic g-factor being $g = 2.0028 \pm 0.003$ [58] and μ_B the Bohr magneton. From there, the resulting interaction energy with a magnetic field $\vec{B}$ is given by

$$\hat{H}_{\text{Zeeman}} = -\vec{\mu} \cdot \vec{B} \tag{2.27}$$

$$= g\mu_B \hat{S} \cdot \vec{B} \tag{2.28}$$

leading to a linear splitting, dependent on the applied magnetic field strength [73, 52, 43].

HYPERFINE INTERACTION TERM

Following the Zeeman term is the hyperfine interaction term. It describes the coupling between the electron spin of an NV center and nearby nuclear spin. That nuclear spin could belong to either a ^{14}N nucleus or a ^{13}C atom. This interaction corresponds to both isotropic (Fermi contact) interaction and also anisotropic (magnetic dipole-dipole) interaction between the electron spin and the nuclear spin. This term is written as:

$$\hat{H}_{\text{Hyperfine}} = \hat{S} \cdot \mathbf{A} \cdot \vec{I} \tag{2.29}$$

where $\hat{S}$ is once again the electron spin operator, $\mathbf{A}$ is the hyperfine coupling tensor and $\vec{I}$ is the nuclear spin operator. Note that $I = 1$ in the case of a ^{14}N nucleus, and $I = \frac{1}{2}$ in the case of a ^{15}N or ^{13}C nucleus. The hyperfine tensor $\mathbf{A}$ may be reduced to axial, $A_\parallel$ and perpendicular, $A_\perp$, components, as long as axial symmetry exists within an NV center. This makes it possible for the hyperfine Hamiltonian term to be simplified as:

$$\hat{H}_{\text{Hyperfine}} = A_\parallel \hat{S}_z \hat{I}_z + A_\perp (\hat{S}_x \hat{I}_x + \hat{S}_y \hat{I}_y) \tag{2.30}$$

Here, the axial (or parallel) term $A_{\parallel}\hat{S}_z\hat{I}_z$ is related to the nuclear spin alignment along the z-axis, whereas the perpendicular term $A_{\perp}(\hat{S}_x\hat{I}_x+\hat{S}_y\hat{I}_y)$ may cause spin state mixing, thus affecting the stability of the NV center. To be more specific, the inhomogeneous dephasing time T_2^* is more severely impacted by the presence of ^{13}C atoms, owing to increased sensitivity to static field inhomogeneities caused by the surrounding spins. In addition to that, the hyperfine interaction increases environmental noise sensitivity and accelerated dephasing of the spin states, causing the spin-spin relaxation time (or coherence time) T_2 to be reduced. Finally, the longitudinal relaxation time T_1 is also degraded, albeit to a lesser extent, as the perpendicular term enhances the likelihood of spin-flip transitions induced by interactions with fluctuating magnetic fields from nearby nuclear spins [58, 43, 74, 75].

SPIN-ORBIT COUPLING TERM

Spin-orbit coupling introduces splitting between the excited triplet (^3E) state sublevels, as a result of the orbital motion of an electron spin. It can be ignored when talking about the ground state $^3A_2$, which does not have an orbital angular momentum. Such an effect may cause dephasing, ultimately leading to linewidth broadening. The spin-orbit coupling term $\hat{H}_{\text{Spin-Orbit}}$ (or $\hat{H}_{\text{SOC}}$) is formulated as:

$$\hat{H}_{\text{Spin-Orbit}} = \lambda\vec{L}\cdot\hat{S} \tag{2.31}$$

where λ is the spin-orbit coupling constant, $\vec{L}$ is the orbital angular momentum operator and $\hat{S}$ (once again) is the spin operator [48, 52].

STRAIN AND ELECTRIC FIELD INTERACTION TERM

Strain refers to displacements Δu of the atoms, under stretch Δx of the diamond crystal lattice and has the power to lower the symmetry of the crystal field around the NV axis. While it is a dimensionless tensor, it may be produced when either stress or electric field is applied, or even temperature variations take place. It is often difficult to distinguish between strain and electric fields, as they can both introduce a similar anisotropic potential, which can split the $m_s = \pm 1$ states or cause their energy levels to shift. The Hamiltonian term for strain can be represented as:

$$\hat{H}_{\text{Strain}} = \hat{S}\cdot d^{(\text{strain})}\cdot\vec{\epsilon} \tag{2.32}$$

where $\vec{\epsilon}$ is the dimensionless strain tensor, $d^{(\text{strain})}$ is the tensor describing the coupling of strain to the spin operators of the NV center, and $\vec{S}$ is the electron spin operator.

Similarly, the Hamiltonian describing the Stark effect due to an applied electric field [43] is given by:

$$\hat{H}_{\text{Electric}} = \hat{S}\cdot d^{(\text{electric})}\cdot\vec{E} \tag{2.33}$$

where $\vec{E}$ is the applied electric field vector, $d^{(\text{electric})}$ is the electric dipole coupling tensor, and $\vec{S}$ is the electron spin operator.

The axial component $d_z^{(\text{strain})}\epsilon_z$ is aligned with the NV center's symmetry axis. Its role is similar to that of the first ZFS component (see Equation 2.25), preserving the C_{3v} symmetry and being able to increase or decrease the energy difference between the $m_s = 0$ and $m_s = \pm 1$ states. On the other hand, the perpendicular strain component lies on the x-y plane, orthogonal to the z-axis and causes symmetry break. This can, in a manner similar to the second term of the ZFS splitting, contribute to lifting the degeneracy of the $m_s = -1$ and $m_s = +1$ states [48].

MICROWAVE INTERACTION TERM

The effect of applying a microwave field on the NV center has already been described in subsection 2.2.5. The Hamiltonian representation of the effect that the magnetic component of the applied MW field has on the NV center, when coupled to its spin is given by the expression:

$$\hat{H}_{\text{MW}} = \gamma_e \vec{B}_{\text{MW}} \cdot \hat{S} \tag{2.34}$$

where $\gamma_e = g_e \mu_B / \hbar$ is the electron's gyromagnetic ratio, $\vec{B}_{\text{MW}}$ is the vector of the magnetic field caused by MW radiation, and (for the last time in this section) $\hat{S}$ is the spin operator [76, 77, 78].

ISC TERM

Closely related to the spin-orbit coupling term is the intersystem crossing (ISC) effect. Physically, ISC refers to non-radiative, spin-dependent transitions between the triplet and singlet states of the NV center. These transitions are typically facilitated by spin-orbit coupling and result in population loss from the excited triplet manifold.

To model this decay mechanism within the Hamiltonian formalism, a non-Hermitian term is introduced. This accounts for the effective loss of population from the system and takes the form of an imaginary energy term. The resulting effective Hamiltonian is given by [79]:

$$\hat{H}_{\text{NV, eff}} = \hat{H}_0 - \frac{i\hbar}{2}\Gamma_{\text{ISC}} \tag{2.35}$$

Here, $\hat{H}_0$ includes the previously discussed Hermitian Hamiltonian terms, and Γ_{ISC} is the effective decay rate associated with ISC processes. This includes not only the transition probability between triplet and singlet states, but also other non-radiative decay pathways that contribute to the overall loss from the triplet system [63, 80, 81].

THE FULL HAMILTONIAN

Inserting all these terms into the full Hamiltonian results in an expression such as the following:

$$
\begin{aligned}
\hat{H}_{\mathrm{NV}} = {} & D\hat{S}_z^2 && \text{(ZFS axial term)} \\
& + E(\hat{S}_x^2 - \hat{S}_y^2) && \text{(ZFS transverse term)} \\
& + g_e \mu_B \vec{B} \cdot \hat{S} && \text{(Zeeman interaction)} \\
& + \hat{S} \cdot \mathbf{A} \cdot \vec{I} && \text{(Hyperfine interaction)} \\
& + \lambda \vec{L} \cdot \hat{S} && \text{(Spin-orbit coupling)} \\
& + \hat{S} \cdot d^{(\mathrm{strain})} \cdot \vec{\epsilon} && \text{(Strain interaction)} \\
& + \hat{S} \cdot d^{(\mathrm{electric})} \cdot \vec{E} && \text{(Electric field interaction)} \\
& + \gamma_e \vec{B}_{\mathrm{MW}} \cdot \hat{S} && \text{(Microwave interaction)} \\
& - \frac{i\hbar}{2} \Gamma_{\mathrm{ISC}} && \text{(ISC decay term)}
\end{aligned}
\tag{2.36}
$$

Additional modifications may be made on the Hamiltonian, depending on the nature of the measurement and the environmental or experimental conditions.

2.3. SnV CENTERS IN DIAMOND

Following the NV center, the SnV center in diamond is described, starting with its atomic structure, its electronic states, and its optical properties, and then continuing with a brief analysis of its magnetic properties and relevant coherence parameters. In discussing this, the most stable and abundant ^{120}Sn isotope is primarily taken into account. Within the scope of this dissertation, the SnV center serves a secondary investigation role and, therefore, the theoretical examination of its properties will not be as detailed as that of the NV center.

2.3.1. ATOMIC STRUCTURE

The tin-vacancy (SnV) center in diamond belongs to the group-IV color centers. It is formed when a tin (Sn) atom is positioned in between two adjacent carbon vacancies in the diamond lattice (see Figure 2.11), thus adopting the title of a "split-vacancy" configuration. This is in part due to the sheer size of a Sn atom that makes it unable to fit in a single substitutional site. Its position would formerly correspond to a bond-centered (BC) site. This interstitial placement gives rise to a D_{3d} inversion symmetry, opposed to the NV center's C_{3v} symmetry. Their superiority in terms of optical properties that are useful in quantum technologies arises primarily as a consequence of this type of symmetry [82]. The electronic configuration of an Sn atom can be seen in Figure 2.10 below:

$$[\mathrm{Sn}]1s^2 2s^2 2p^6 3s^2 3p^6 4s^2 3d^{10} 4p^6 5s^2 4d^{10} 5p^2 \tag{2.37}$$

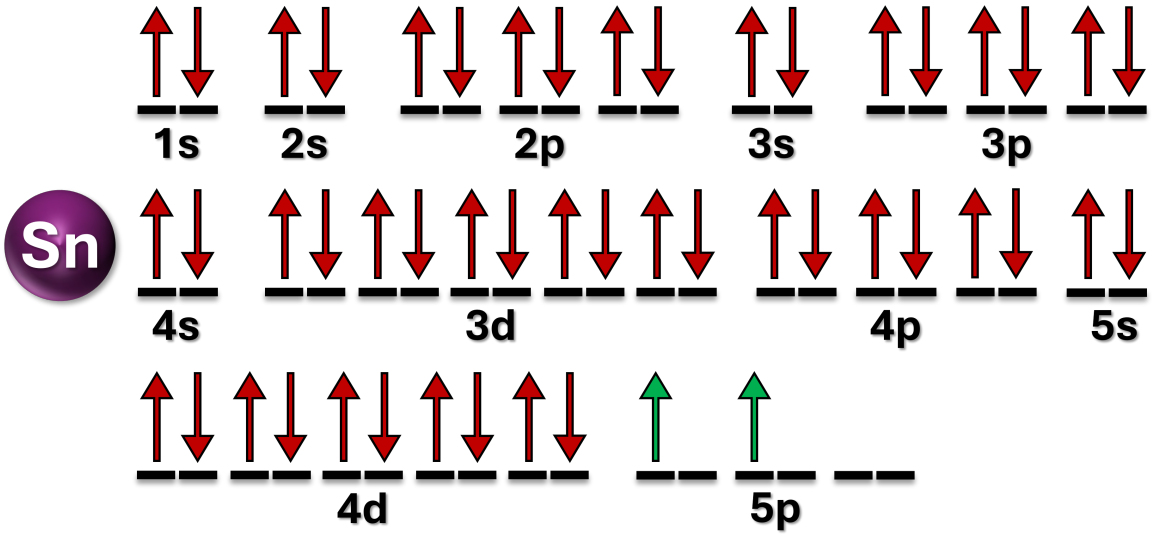


Figure 2.10: Electron configuration of a tin atom.

While there is interaction between the Sn's two valence electrons in the $5p$ orbital and the surrounding carbon atoms, it is not as prominent as in the case of the NV center. This results in a lack of hybridization and more discrete and localized electronic states. Moreover, because of its atomic radius, Sn causes disruptions in the diamond lattice itself, in the form of mid-gap states, which enhance its optical properties [83].

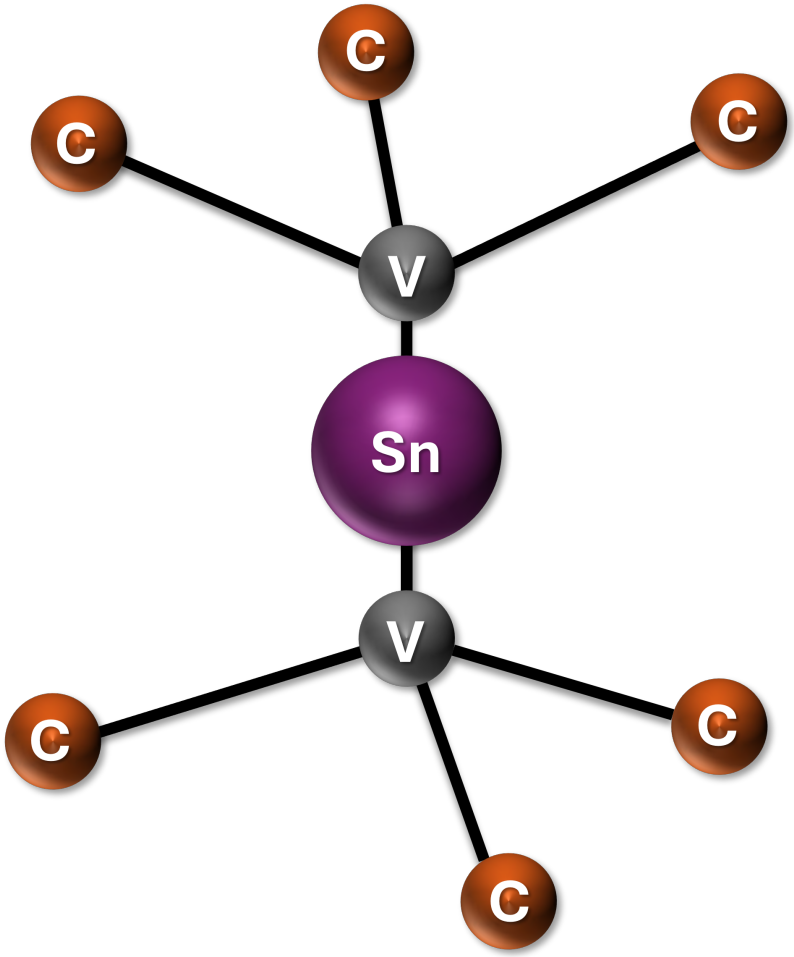


Figure 2.11: The structure of an SnV center.

2.3.2. Electronic and Optical Properties

The SnV center in diamond belongs to the D_{3d} symmetry point group, which has a higher symmetry than that of the NV center (C_{3v}). Its symmetry can be defined by three principal axes: the symmetry axis (z-axis) along the [111] direction and the perpendicular axes, x and y. The D_{3d} symmetry allows 120° and 240° rotations around the symmetry axis. It also contains twofold rotational symmetries, enabling 180° rotations about the x and y axes (perpendicular to the [111] axis). Finally, it has reflections across the three vertical planes intersecting the z-axis and consists of an inversion point halfway between the Sn atom and the vacancies [84].

While the neutral charge state of the SnV center (SnV^0) might have a spin quantum number $S = 1$, it is most commonly used and studied in its negatively charged state SnV^-, which is a $S = 1/2$ system. In Figure 2.12, it is seen that its ground state is split into two orbital levels, mostly due to spin-orbit coupling. Let those be arbitrarily called $|G_1\rangle$ and $|G_2\rangle$. This splitting is equivalent to $\Delta_{gs} = 850\,\text{GHz}$ in unstrained samples and can reach up to $\approx 1500\,\text{GHz}$ when strain is present in the lattice [85]. An external magnetic field can cause Zeeman splitting of each of these two energy states, into two distinct, spin-based sublevels, allowing selective tuning of the transitions.

Moving away from the group symmetry notation that was used for the NV center, the split levels introduced above can be labeled as $|1\rangle$ and $|2\rangle$ (lower-energy ground state sublevels), and $|3\rangle$ and $|4\rangle$ (higher-energy ground state sublevels). The excited state obeys the same concepts. It is, first, split into two orbital levels, separated by $\Delta_{es} = 3\,\text{THz}$ in unstrained samples and around $\approx 4\,\text{THz}$ under strain [85]. Let those be arbitrarily called $|E_1\rangle$ and $|E_2\rangle$. Next, the Zeeman effect can cause each of these to split further into two discrete energy states, hereby labeled $|A\rangle$ and $|B\rangle$ (lower-energy excited state sublevels), and $|C\rangle$ and $|D\rangle$ (higher-energy excited state sublevels) [86, 87, 85].

The ZPL of the SnV center corresponds to transitions between the $|G_1\rangle \rightarrow |E_1\rangle$ and $|G_2\rangle \rightarrow |E_2\rangle$ levels. It is tied to a wavelength of $\approx 619\,\text{nm}$. These are nearly lifetime-limited transitions, indicating the potential for high optical coherence [85]. In addition to the ZPL emission, there are both spin-conserving and spin-flipping transitions. The spin-conserving transitions include those between the excited state $|A\rangle$ and the ground state $|1\rangle$, labeled as $|A1\rangle$, and between the excited state $|B\rangle$ and the ground state $|2\rangle$, labeled as $|B2\rangle$. Using the same annotation, the spin-flipping transitions are hereafter called $|A2\rangle$ and $|B1\rangle$ [87].

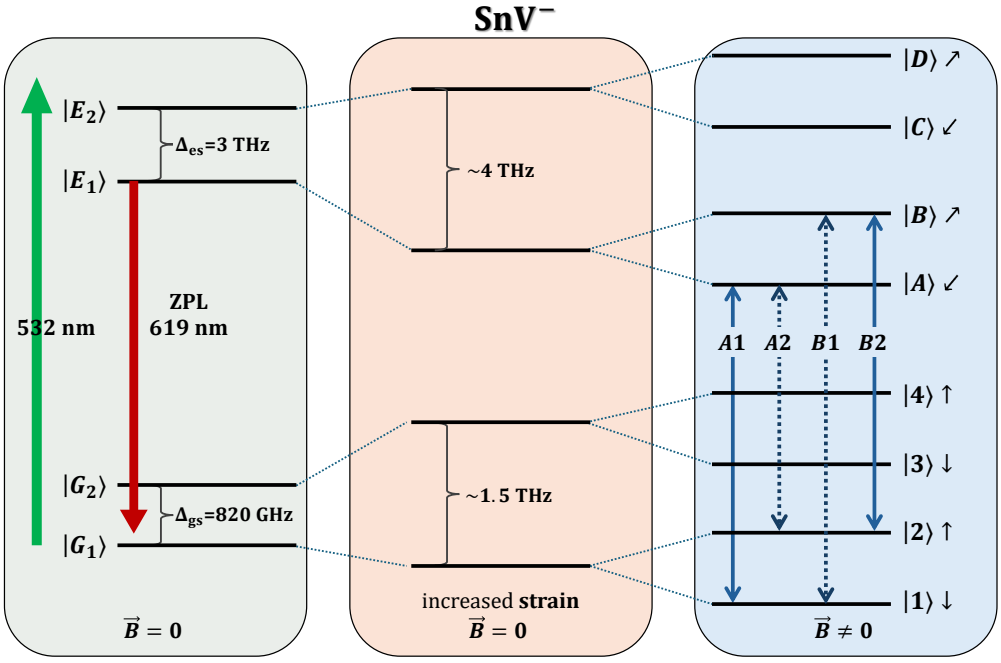


Figure 2.12: Energy level diagram of the negatively charged SnV^- state.

2.3.3. EFFECT OF MAGNETIC FIELD AND MICROWAVE DRIVING IN SPIN STATE MANIPULATION

By applying microwave frequencies on the SnV center, it is possible to achieve coherent manipulation of its quantum states. Resonant microwave driving usually occurs in the spin-conserving transitions $A1$ and $B2$, which are the primary focus of quantum operations. This is made possible with added strain-induced splitting present, with strength similar to that of spin-orbit coupling. This strain relaxes the orthogonality between the orbitals, reduces the energy gap between them and allows transitions at lower mi-

crowave field intensities. Such microwave driving between the Zeeman-split spin sublevels was demonstrated by Rosenthal *et al.* (2023), who applied a MW field in the range of less than ≈ 4 GHz [87].

Except for the strain and magnetic field strength, the orientation of the magnetic field is another crucial parameter. It has been discovered that a magnetic field parallel to the SnV (symmetry) axis yields higher T_2 coherence times of more than an order of magnitude, as opposed to a perpendicular field, due to enhanced decoupling from the electron spin bath. The integration of the SnV center spin qubits with a superconducting waveguide [88], along with dynamical decoupling techniques has the ability to enhance fidelity and coherence under microwave driving [85, 87, 88] Fidelity here refers to the quantifiable effectiveness and accuracy of quantum operations, as a comparison of the resulting quantum state of a system versus its ideal (or theoretical) state.

2.3.4. EMISSION, COHERENCE, SENSITIVITY

The tin-vacancy, being part of the group-IV color centers, has strong spin-orbit coupling and, thus, large orbital splitting. Because of this, it is much less susceptible to external fields, including magnetic fields, electric fields, and strain-induced perturbations. Nonetheless, while this might be a drawback for its sensing capabilities, it is a huge benefit for achieving improved coherence rates and quantum state stability. Lower sensitivity to external fields directly translates into fewer perturbations and reduced environmental noise sensitivity. This effect is especially pronounced in lower temperatures [85, 87, 88, 89].

Another consequence of the tin-vacancy center's D_{3d} inversion symmetry (meaning the absence of a permanent electric dipole), and its strong spin-orbit coupling, is a very high ZPL emission efficiency of around 70%, which is almost twenty times higher than that of the NV center and may be enhanced even more. The result of such high ZPL emission efficiency is limited phonon involvement, that implies not only improved coherence but also allows reliable entanglement and better coupling to optical cavities, for use in quantum computing or quantum communication applications [31, 90, 85, 87, 88, 89, 91].

In SnV centers, temperature plays a bigger role than in NV centers in terms of coherence times. While NV centers maintain very good coherence and relaxation times even at room temperature (RT), largely due to their less intricate electronic structure, SnV centers require cooling down to cryogenic temperatures, below 4 K [85, 89].

Therefore, and since the properties of tin-vacancy centers actually require very low temperatures in order to really shine, the relaxation and coherence times are usually studied under cryogenic conditions and making use of strain effects and dynamical decoupling techniques. To be more precise, in such conditions, the spin-lattice relaxation time T_1 in SnV centers can range from hundreds of microseconds up to ≈ 20 ms [88, 89, 87]. Similarly, the spin coherence time T_2 may vary from hundreds of microseconds up to ≈ 10 ms [88], and, finally, the inhomogeneous dephasing time T_2^* can be somewhere between tens or hundreds of nanoseconds [31] and a couple of microseconds [85, 86].

Concerning the fluorescence lifetime of SnV centers, it is around 5 ns in ensembles and it can vary between 7 ns and 25 ns for single emitters, depending on their proximity from the diamond surface and a potentially damaged environment [92, 90, 31].

2.3.5. SnV HAMILTONIAN

Based on the paper from Karapatzakis *et al.* (2024) [88], we can derive the following, simplified Hamiltonian for the SnV^- center in diamond:

$$\hat{H}_{SnV} = \hat{H}_{SOC} + \hat{H}_{Ze} + \hat{H}_{ZL} + \hat{H}_{JT} \tag{2.38}$$

It is comprised of four main terms, first of which is the spin-orbit coupling contribution $\hat{H}_{SOC}$, describing how an electron spin interacts with its orbital angular momentum, an important factor for its overall structure and energy splitting. Next is the spin-Zeeman term $\hat{H}_{Ze}$, which describes the splitting of the spin states due to the interaction of an electron's spin with an external magnetic field. Following that is the orbital-Zeeman term $\hat{H}_{ZL}$, which affects the electron's orbital motion and is responsible for causing orbital state splitting.

Finally, the $\hat{H}_{JT}$ is a combined Hamiltonian contribution. It consists of the Jahn-Teller effect, along with the effect of strain, and involves parameters that describe the strain field and cause distortions in the lattice, altering the electronic properties of the SnV center and modifying the orbital levels [31, 88].



2.4. INTRODUCTION TO ODMR

2.4.1. FUNDAMENTALS OF ODMR

Optically Detected Magnetic Resonance (ODMR) is an experimental technique that is utilized to extract information from color centers and perform magnetic field measurements. It consists of excitation of the diamond containing NV centers by green light illumination, microwave driving (MW) of the NV spin populations, and collection of the emission in the form of photoluminescence (PL), in order to detect disturbances caused by magnetic field perturbations. Depending on the application and the type of sensing required, variations of either confocal or widefield imaging setups may be used.

EXCITATION

Optical excitation is done with a green light source, ideally a laser, usually at a wavelength of 532 nm, since this where the most common solid-state green lasers operate. The laser power used to excite NV centers depends on whether these are in nanodiamonds, ensemble NV centers or single color centers in bulk diamond, and whether a continuous-wave (CW) or pulsed ODMR scheme is used. The values can range from a few microwatts (μW) to milliwatts (mW). Green laser light not only initializes the NV^- center into its $m_s = 0$ ground spin state, but it is able to introduce interconversions between the neutral and the negative charge states, as well [93, 94, 47].

MW DRIVING

The role of microwave driving has already been explained in subsection 2.2.5. The small ZFS of the NV center, that sits, by default, at around 2.87 GHz, makes the application of a microwave field feasible, without any added hassles (e.g., strain required in the case of the SnV center). This MW frequency is also well within the range of modern and affordable electronic equipment, like MW generators. When the applied MW field is resonant to the ZFS frequency, there is redistribution of the spin population between the $m_s = 0$ and $m_s = \pm 1$ states, resulting in fluorescence being increasingly emitted through non-radiative relaxation paths and, thus, being observably decreased [95, 43].

EMISSION AND COLLECTION

Following excitation, the NV center relaxes back to its ground state through multiple possible paths. These relaxations are either radiative, emitting photons in the visible spectrum, mostly between 600-800 nm with a distinct peak around 637 nm associated with the ZPL emission, in a process called photoluminescence (PL), or non-radiative, in the form of lattice vibrations (phonons), and usually occur when relaxation takes place through the metastable states [58, 52].

With the help of a light collection device, such as a photodiode or a single-photon counting module (SPCM), that is sensitive in the wavelength range mentioned above, it is possible to capture the emitted photons and record them, after turning them into a digital/electrical signal. This signal can be used to monitor the PL intensity under different experimental conditions, be it over time or across a range of applied microwave frequencies [96, 97].

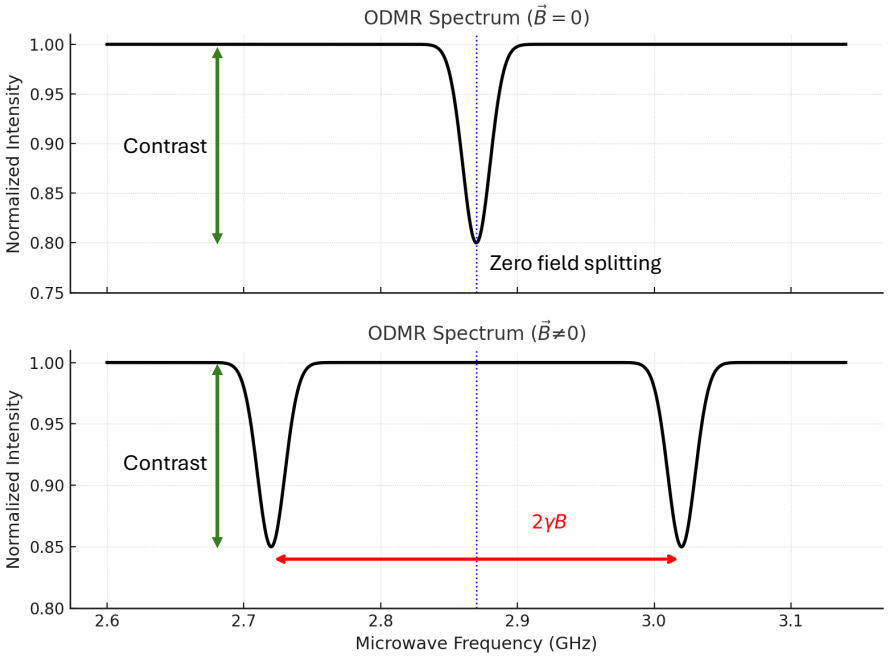


Figure 2.13: Indicative ODMR spectra of NV centers in diamond, showcasing the peak splitting due to the presence of an external magnetic field.

MAGNETIC FIELD SENSING

Finally, making use of the Zeeman splitting effect is of utmost importance when it comes down to magnetic field sensing with the ODMR technique. The key concept is that an external magnetic field is able to split the $m_s = \pm 1$ state into two distinguishable sublevels, as illustrated in Figure 2.13. These sublevels are energetically differentiated by $g_e \mu_B B$ (although not always symmetrically), which can be transformed into a frequency difference by dividing by h (Planck's constant).

It is the essence of an ODMR experiment to record photoluminescence intensity as a function of microwave frequency, determine the resonant frequencies for each of the -now split under a magnetic field- spin substates, and then solve for B, in order to calculate the strength of a given magnetic field [96, 97].

2.4.2. CONTINUOUS-WAVE (CW) VS. PULSED ODMR

There are two main ODMR measurement schemes, continuous-wave (CW) ODMR and pulsed ODMR, both with their advantages and disadvantages. CW ODMR refers to continuous pumping with the excitation laser and constant application of a MW field, while, on the other hand, pulsed ODMR is done by precise timing of both laser and pulse sequences. Sensing with ODMR can also be categorized, based on the type of magnetic fields being measured, into two regimes: the low frequency ($< 10\,\text{kHz}$), or DC (static fields), regime, and the higher frequency, AC regime (for time-varying fields). The measurement scheme employed in this dissertation is CW ODMR, targeting DC magnetic fields.

CW ODMR outshines pulsed ODMR when it comes down to simplicity and ease of use and implementation. The DC regime is of particular interest for biosensing applications. Furthermore, the use of ensembles of NV centers or nanodiamonds is usually

prevalent in biosensing. Ensembles of NV centers, like the ones used throughout most of the experiments described hereafter, also show increased inhomogeneous broadening. Taking into account the MW field, CW ODMR is more suitable when there are high MW field drive amplitude variations, whereas pulsed ODMR outperforms in low driving variations and whenever inhomogeneous broadening is not as extensive. Finally, CW ODMR also provides high sensitivity when used in widefield imaging [98, 99, 100], as well as in the type of confocal imaging measurements carried out with the setup described later, in section 2.5.

2.5. ODMR EXPERIMENTAL SETUP

In Figure 2.14, the full ODMR setup is shown, located inside the Diamond Lattice (DL) lab of the Quantum Integration Technology (QIT) research group. The setup was not built using off-the-shelf components. Rather, it was designed from scratch, with its initial purpose being continuous wave (CW) ODMR measurements and, further down the line, integration with a chip containing an array of single-photon avalanche diodes (SPADs). The design and installation of this setup started as one of the first projects in a newly formed research group and in a brand new lab area. Therefore, all necessary components had to be ordered and installed manually, piece by piece.

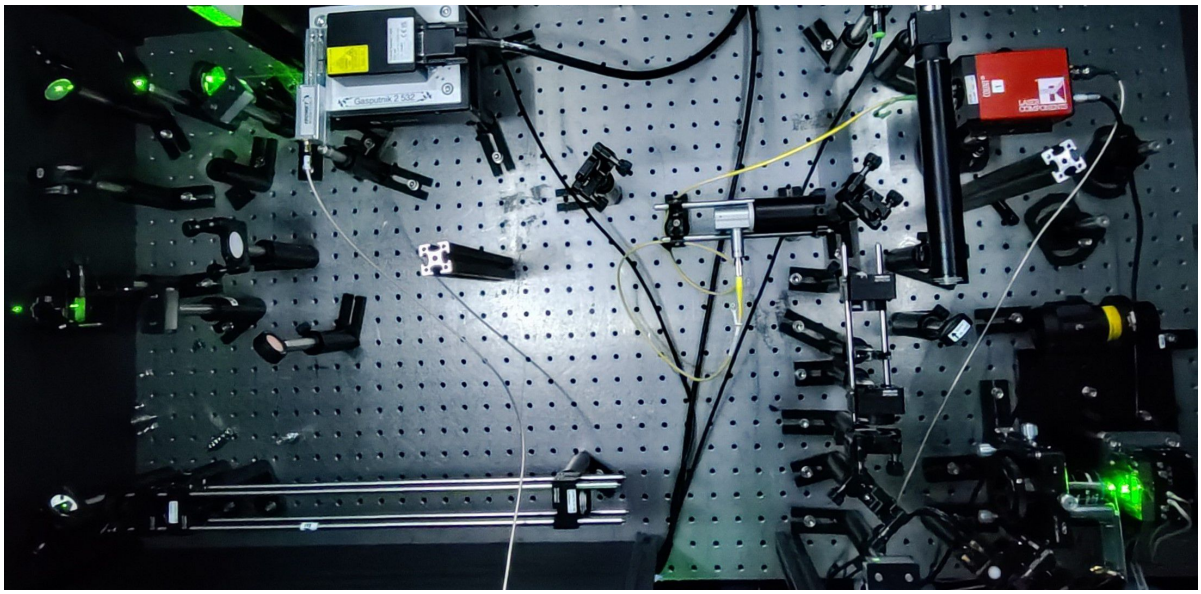


Figure 2.14: Photo of the Optically Detected Magnetic Resonance (ODMR) setup, that was built as part of this PhD project. It is located inside the QIT DL lab.

Subsequently, the first version of the room-temperature ODMR setup (and what is essentially a confocal microscopy setup) shall be described, along with the components that comprise it.

2.5.1. EXCITATION LASER

The initial goal of the ODMR setup was to perform CW-ODMR measurements. Thus, a green laser with CW functionality was acquired, to serve as excitation source. That is the Cobolt Samba 04-051, with a wavelength of 532 nm. It is a diode-pumped solid-state (DPSS) laser and also operates in a Single Longitudinal Mode (SLM), meaning that it emits a very narrow, coherent and stable beam. It produces a linearly polarized beam with a diameter of $\simeq$ 700 µm, at a power of 400 mW, with a Class 3B classification. A heatsink is placed underneath the laser source, to provide cooling and thermal stability.

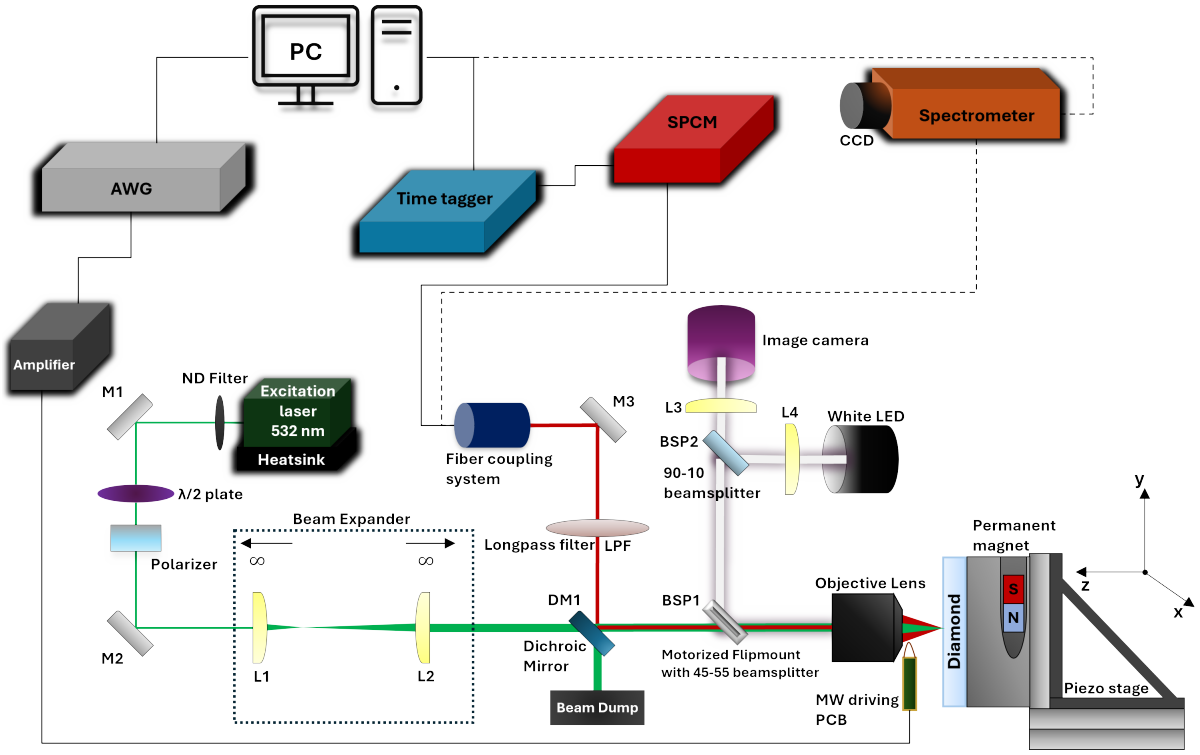


Figure 2.15: Schematic of the ODMR setup, illustrating its individual components and the pathways of the excitation laser, the emitted red fluorescence, and the white light used to image the sample before the measurements. The excitation source is a 400 mW green laser with a wavelength of 532 nm (Cobolt Samba 04-051). The beam exiting the laser is immediately attenuated using an ND filter, followed by an attenuation system composed of a $\lambda/2$ plate and a polarizing beamsplitter. Mirrors M_1 and M_2 are used to steer and align the excitation beam. Next is a beam expander system, allowing us to increase the beam's diameter to better match the objective lens' NA. The green laser passes through a dichroic mirror DM_1 and then through the objective lens, creating a focused spot on the diamond sample containing NV centers. The sample is mounted on a custom detachable aluminum plate, which is in turn screwed on top of another custom plate, with a pocket for a bias magnet. This plate is mounted on top of a piezo stage, that allows controlled movement in the x, y and z-axes, with nanoscale precision. A PCB that carries the MW signals is fixed on the mount of the objective lens, enabling MW driving of the NV centers. The emitted red fluorescence light is collected by the same objective lens and sent to the dichroic mirror, which reflects it towards the collection path. This light is further filtered when it passes through the longpass filter LPF, which blocks any wavelengths below 633 nm. afterward, a mirror (M_3) sends the beam into the fiber-coupling system. Through the P5-630A-PCAPC-1 single mode fiber cable, it is guided to the SPCM (COUNT-10C-FC), whose data is then processed and handled by a time-to-digital converter module (Time Tagger X), connected to a computer. By swapping the fiber connected to the fiber-coupling system, it is possible to instead send the collected light into a spectrometer (SpectraPro HRS-750), for a thorough spectral analysis. The M_3 mirror may also be easily (magnetically) detached, allowing free-space collection of the fluorescent light, in case that is desired. Before measurements start, the sample may be digitally viewed and focused on using a white LED source (MWUVL1) and an imaging camera (Blackfly S GigE BFS-PGE-31S4M-C). For this purpose, a motorized flip mount is placed between the dichroic mirror and the objective lens, enabling quick swap of a 45-55 beamsplitter (BSP_1) mounted on it. This also allows imaging of the laser beam, for alignment and beam quality tests. Creation of the MW signal is done by an arbitrary waveform generator (SHFSG+ 8.5 GHz) and amplified by a ZHL-15W-422-S+ amplifier. Control of the electronic devices is handled via a Linux computer, with custom-developed software (provided partly by TNO and adapted to this setup).

2.5.2. NEUTRAL-DENSITY FILTER

The output beam is immediately attenuated with the use of neutral-density (ND) filter. Each filter comes with a specific optical density (OD), which reduces transmission T based on the following equation:

$$\mathrm{OD} = \log_{10}\left(\frac{1}{T}\right) \Leftrightarrow T = 10^{-\mathrm{OD}} \tag{2.39}$$

An ND filter can be absorptive or reflective, depending on the needs of the experiment, and also multiple ND filters may be used one after another for multiplicative attenuation. This results in reduction in laser power, right at the start of the laser beam path. The role of this filter is extremely important, as it not only helps mitigate potential hazards, but also regulates the energy that the NV centers are illuminated with. Such high laser power could result in photoionization into the NV^0 state, as well as graphitization, damaging the diamond substrate [101].

2.5.3. STEERING MIRRORS AND ALIGNMENT IRISES

The laser beam coming out of the laser source requires manual steering in order to ensure proper propagation through the optics that are placed in its path. For this purpose, a set of broadband dielectric steering mirrors is used, with very high reflectivity in the range of 400-750 nm. Specifically, their reflectance values are above 99%, or nearing 100% depending on the incident wavelength, which is essential for minimizing power losses. These mirrors, in conjunction with irises (small apertures) which serve as alignment references along the beam path, are used to steer the light onto the diamond sample. This is achieved with the help of kinematic mounts, on which the mirrors are mounted, that provide precise angular adjustments, allowing fine-tuning of the laser beam while it propagates in the x and y planes.

2.5.4. VARIABLE ATTENUATION OPTICS SYSTEM

Even though ND filters can reduce the incoming laser power by an order of magnitude or more, it is still useful to be able to precisely adjust its power, sometimes down to the μW scale. This is achieved by using a half-wave plate ($\lambda/2$ plate), followed by a polarizer. First, the already polarized laser beam experiences a phase shift of 180° between the fast and slow axes of its electric field, thus rotating its polarization vector. Meanwhile, rotations of the $\lambda/2$ plate by an angle θ (relative to the initial polarization axis and the fast axis) cause rotations of the polarization direction by 2θ [102]. afterward, the (still linearly polarized) light beam enters the polarizer. The polarizer's operating principle is based on allowing only the light component that is aligned with its transmission axis to pass through. Going through the polarizer, the light is then filtered according to Malus' law:

$$I = I_0 \cos^2(\phi) \tag{2.40}$$

where I is the final intensity, I_0 is the initial intensity and ϕ is the angle between the

polarization direction and the polarizer's transmission axis. Therefore, an angle of $\phi = 90°$ results in the intensity being completely blocked [103].

2.5.5. DICHROIC MIRROR

A fundamental optical component in an ODMR setup is the dichroic mirror. It allows the separation of the excitation light from the fluorescent light emitted by the NV centers. It consists of dielectric layers, each with different refractive index, that allow constructive or destructive interference, depending on the incident wavelength. In this setup, a short-pass dichroic mirror with a cutoff wavelength of 567 nm is used. This dichroic is highly transmissive below 567 nm and highly reflective above that, meaning that the green excitation light freely passes through the dichroic and onto the sample, while the emitted red light is instead reflected at an angle of 45°.

2.5.6. OBJECTIVE LENS

An objective lens is used to focus the incoming excitation light onto the diamond sample, and also collected the emitted fluorescence. In this particular setup, use was made of the MPLAPON60x objective lens, provided by Evident. This objective has 60x magnification, numerical aperture (NA) of 0.90, working distance (WD) of 0.4 mm (or 400 µm) and a maximum field of view of 0.43 mm. The objective lens is fixed on an objective mount by Newport, allowing fine adjustment in the x and y plane, as well as rotational adjustment around these two axes.

CONSIDERATION #1

A high NA is usually desired in a confocal ODMR system, for a few reasons. First, it creates a smaller focal spot size, which in turn enhances the excitation intensity and the spatial resolution when performing PL scans or magnetic field mapping. Moreover, high NA means larger collection angle, allowing more emitted photons to travel to and be captured by the photodetector. Hence, a laser beam size that matches the back aperture of this objective lens would be ideal, in order to maximize the focus quality. This can be done with a beam expander system, which is described later in subsection 2.5.16.

2.5.7. MICROWAVE DELIVERY SYSTEM

Applying a microwave field to the NV centers is of vital importance. The whole concept of measuring magnetic fields with them revolves around resonance between the MW field frequencies and the NV center's spin states, causing changes in spin population between the energy levels, and resulting in measurable PL dips via the ODMR technique. There are various MW driving approaches, all of which come with their advantages and drawbacks, depending on the type of measurements taking place. These include coil antennas, generally used for broad fields, wire and stripline antennas, more often used for localized fields, and resonators, which provide high precision driving. Additional considerations are whether single NV centers or an ensemble is used, whether physical restrictions are imposed by the setup itself, whether the goal is biosensing or other types of magnetometry, etc.[104, 105].

For the majority of the experiments carried out in this dissertation, an ensemble of NV centers in a confocal-type configuration is used. This requires the application of a

MW field with high spatial homogeneity and uniformity, as well as minimal space occupation, in order to avoid interference with the movements of the piezo scanning stage (see subsection 2.5.8) or obstruction of the collection volume. For this purpose, the optimal MW driving configuration consists of a microstripline-based Ω-shaped antenna, along with careful parameter design [105, 106]. As part of a collaboration between our research group and TNO, a custom design PCB was provided for use and testing of the room temperature ODMR setup. This is a planar PCB, with pads for soldering a copper wire at its edges. It also contains two SMP sockets, for connection to the microwave waveform generator (see subsection 2.5.15) and signal termination with a 50 Ω terminator. The copper wire soldered on it has a diameter of 100 µm. Note that an Ω-shaped copper wire design was also attempted, however yielding worse results compared to the simple curve design shown in Figure 2.16.

CONSIDERATION #2

A couple of factors need to be considered when applying a microwave field. These include local heating of the sample and signal distortion. While higher MW driving power may result in better PL contrast between the different spin transitions, it ultimately comes with considerable broadening of the resonance peaks. Combining this fact with how higher laser excitation powers affect the ODMR signal and contrast, it is clear that fine-tuning of both sources is required to achieve optimal ODMR measurement conditions [95, 107].

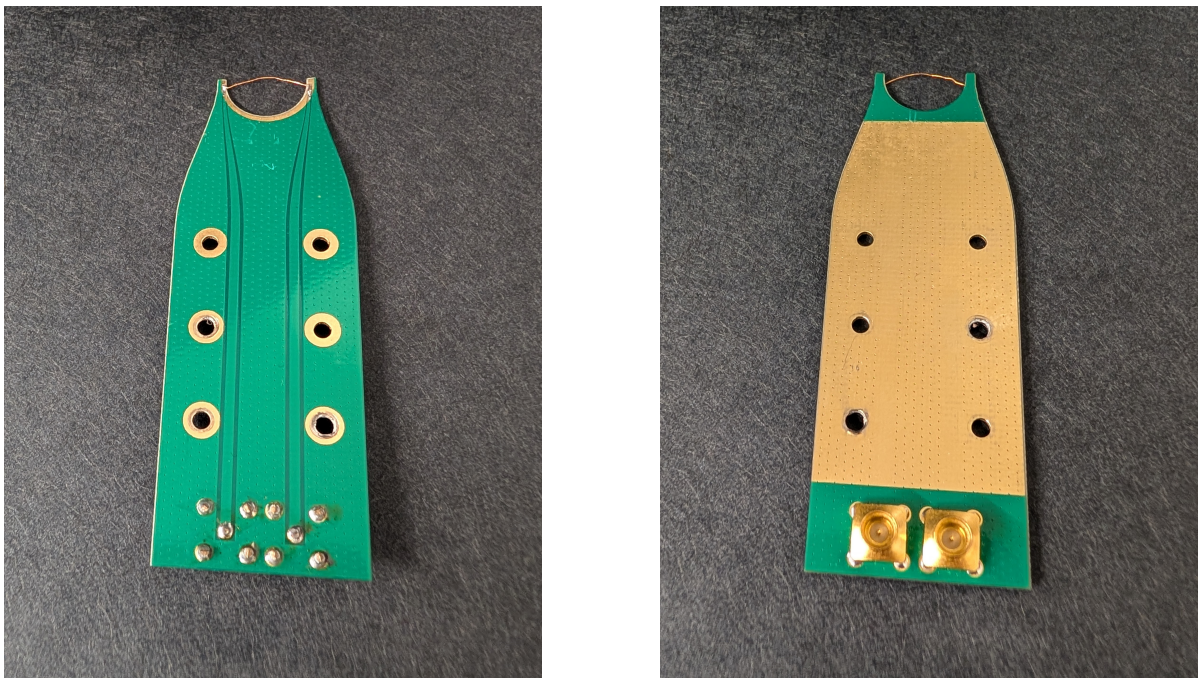


Figure 2.16: Front and back side of the custom planar PCB with a copper wire, used for applying a microwave field to the NV centers in the diamond sample. PCB designed and fabricated by TNO. Soldering of the copper wire was done by Yannick van der Linden and Lars Leenheer, from DEMO.

2.5.8. PIEZOELECTRIC SCANNING STAGE

In order to accurately scan a layer of the diamond sample and create a two-dimensional (2D) map of the effect of an external magnetic field on it, precise, step-by-step movement is required. To achieve this, a piezoelectric scanning stage is employed (simply referred to as piezo stage from now on). The operating principle of a piezo stage is based on the piezoelectric effect. Piezoelectric actuators exploit this to contract or expand, causing controllable (often sub-nanometer) mechanical movements, depending on the polarity and magnitude of the voltage applied.

The specific piezo stage model used in this research is Q-545.140, by Physik Instrumente (PI). In particular, three of these stages are used, along with three E-873 servo controllers. Two of the stages are mounted on top of each other, enabling movement in the x-y plane, with the third one mounted vertically using the Q-145 adapter bracket, enabling movement in the z-axis. This configuration allows three-dimensional (3D) movement control of the diamond sample placed on the piezo stage system. This stage is able to move in a $13 \times 13\,\text{mm}^2$ area, which is often more than enough when measuring diamond samples. It also has a minimum (theoretical) incremental motion of 6 nm, thus allowing extremely precise and fine positioning when scanning over an area.

2.5.9. MAGNET-HOUSING PLATE & DETACHABLE SAMPLE MOUNTING PLATE

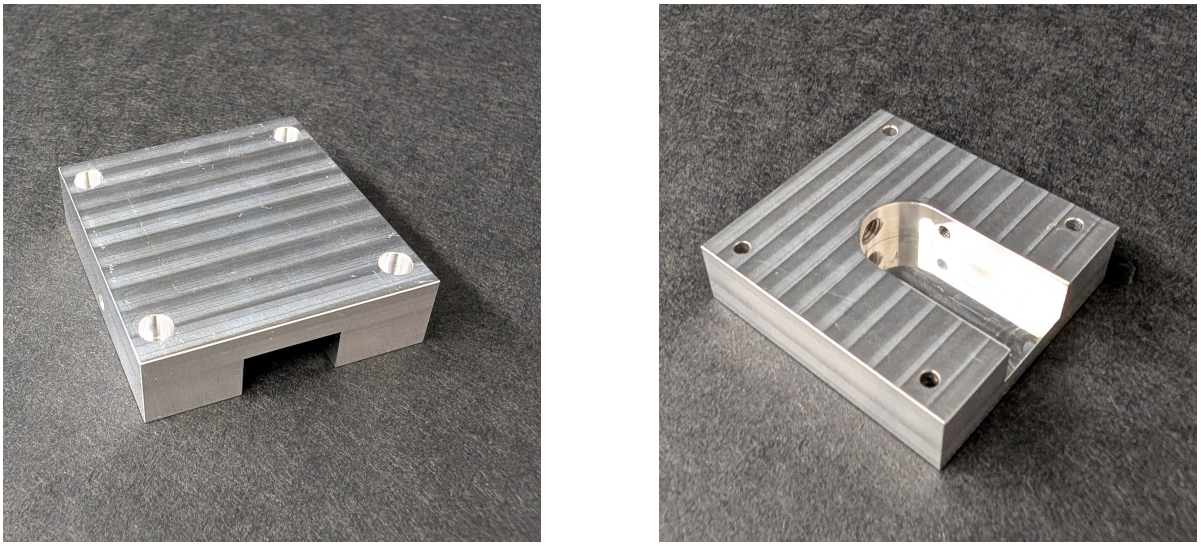
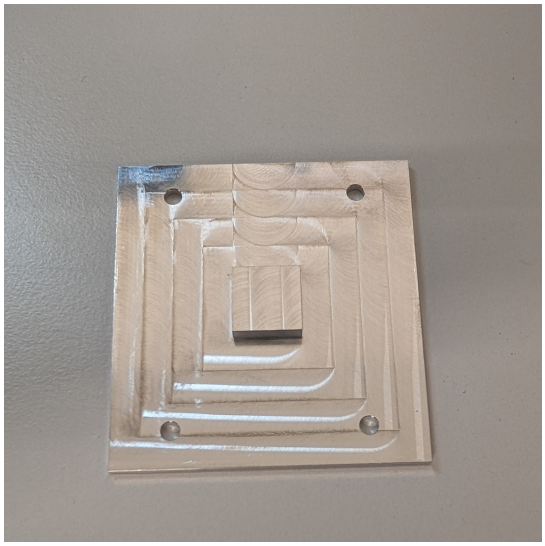


Figure 2.17: Custom design of a mounting adapter plate, made out of aluminum, by Tim Hiep (QuTech workshop). The pocket designed to house a magnet can be seen.

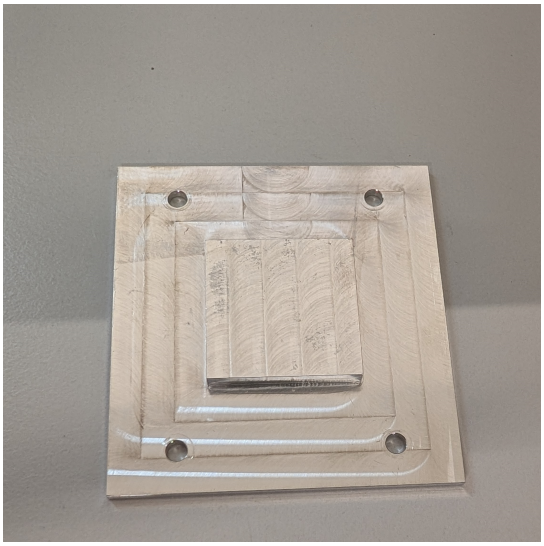
The diamond sample needs to be fixed on the piezo scanning stage. This cannot be done directly on the piezo stage (method of attaching the sample explained in subsection 2.7.1), so a custom design of a mounting adapter plate is used, in combination with thin detachable sample mounting plates (see Figure 2.17). The adapter plate has the same length and width as the piezo stage, and serves as an intermediate adapter between the thin sample mounting plates and the piezo stage. However, its main purpose it to house a permanent magnet, often required to create an external magnetic field in ODMR measurements. The magnet may be inserted from the top opening of the plate,

sliding down into a pocket, from where it produces an approximately uniform magnetic field. Therefore, the adapter plate is made as thin as possible, while having enough space for a cylindrical magnet to fit in it.

Next, two variations of custom aluminum plates (with the same length and width as the piezo stage and the adapter plate) are designed, that function as detachable sample mounting plates, so that each individual sample being measured may be fixed on a separate plate, for convenience. The first variation is a thin aluminum piece, with a protrusion with an area of 1×1 mm^2, which allows fixing of smaller diamond substrates on it. The second variation, instead, has a protrusion with an area of 2×2 mm^2, designed to host larger diamond samples or even diamond-on-silicon chips. These plates are shown below, in Figure 2.18.



(a) First variation of the detachable sample mounting plate, with a protrusion of with an area of 1×1 mm^2.



(b) Second variation of the detachable sample mounting plate, with a protrusion with an area of 2×2 mm^2.

Figure 2.18: Two variations of the detachable sample mounting plates, made out of aluminum, by Tim Hiep (QuTech workshop).

CONSIDERATION #3

When performing 2D ODMR scans of a sample, attention needs to be paid to the proximity of the sample to the objective lens. As mentioned above, the objective lens used has a WD of 400 µm. Given the unavoidable minimum thickness of the microwave wire (which at best is tens to hundreds of µm) located in front of the objective (and in between the objective and the sample), a problem arises regarding the possible distance from the objective that the diamond may have (in the z direction), so that any desired layer of the diamond may be focused on, without fear of crashing into the MW wire and the objective. Moreover, owing also to the potential tilt of the objective lens and the piezo stage, as well as the variations in diamond surface thickness, it has been noticed before that whenever such a collision takes place, the MW wire may be displaced, thus preventing further measurements.

The reason the protrusions on the detachable sample mounting plates were designed was so that there is less of a chance for the mounted sample or the plate itself to accidentally collide with the wire and the objective, whilst allowing undeterred movement

in the x and y directions. Figure 2.19 shows how the microwave driving PCB is mounted in front of the objective.

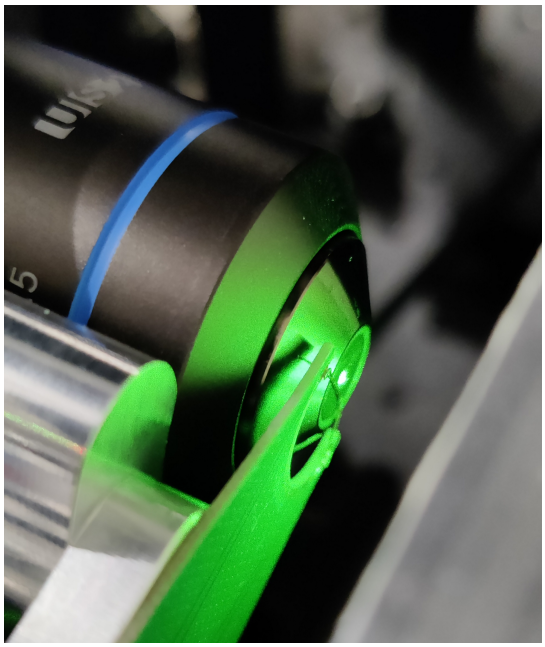


Figure 2.19: The MW driving PCB is mounted in front of the objective. During ODMR measurements, the piezo stage is brought in very close proximity to the copper wire of the PCB.

2.5.10. EXTERNAL MAGNETIC FIELD CONTROL AND APPLICATION

Often, an external permanent magnet is used in ODMR experiments, besides the smaller magnetic field perturbations that are being investigated. If the magnetic field being measured is considerably small, there is a chance that there is not enough peak splitting in the observed PL dips of an ODMR spectrum. This makes it hard to distinguish between individual peaks and calculate the magnetic field under question. Therefore, using an external magnet provides a bias magnetic field, which creates a certain peak splitting and allows easier determination of the measured magnetic field.

The adapter plate custom design from subsection 2.5.9 features a pocket intended to house a permanent bias magnet. This is a cylindrical, nickel-plated neodymium (NdFeB) magnet, with a diameter of 8 mm and a height (thickness) of 2 mm. It is N42 grade, which results in a magnetic field of roughly ~ 3000 Gauss at a distance of 1 mm from the center of its disc base (see Figure 2.20).



Figure 2.20: Neodymium N42 disc magnet, used occasionally for applying an external bias magnetic field during ODMR measurements.

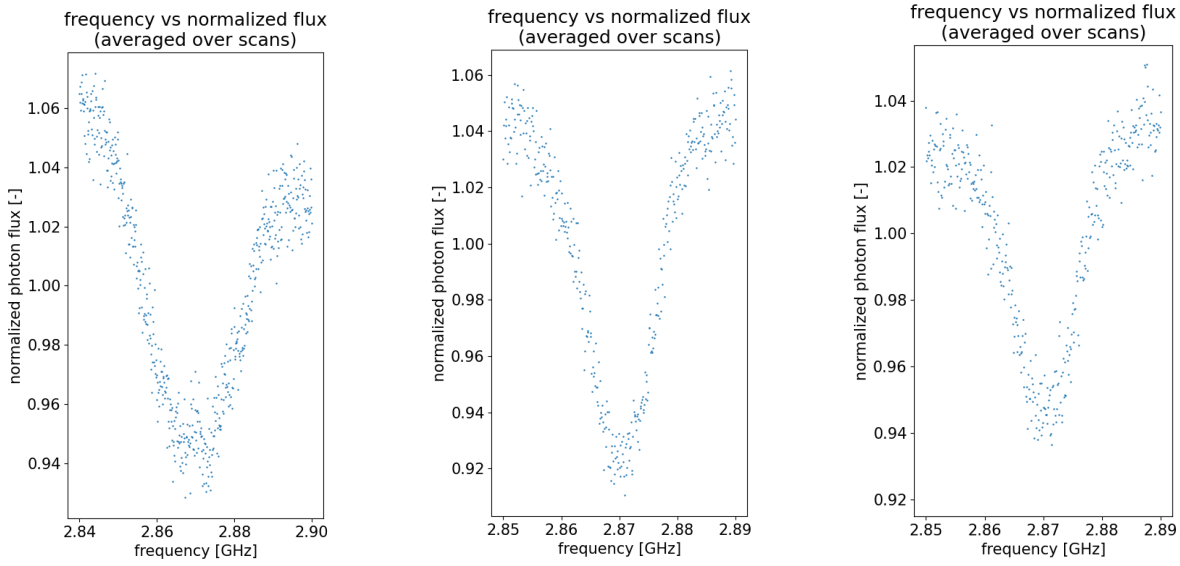
2.5.11. MAGNETIC SHIELDING METAL PLATES

While an external, bias magnetic field is often beneficial to performing ODMR measurements, there are multiple stray magnetic fields generated by electronics, optics mounting equipment and even the piezo stage itself (causing a significant peak splitting of roughly 10-15 MHz). Such inconsistent fields are unwanted and, thus, shielding of the diamond sample against them is required. For this reason, two magnetic shielding metal plates were employed, made by Tim Hiep from the QuTech workshop, to determine the most effective shielding material. The first one is a 3 mm thick steel plate, whereas the second one is a mu-metal plate, 3.1 mm thick. Both metal plates can be screwed directly on the magnet-housing adapter plate, allowing the detachable sample-mounting plates to also be mounted on top of it, as seen in Figure 2.21. Tests shown in Figure 2.22 reveal that both are reasonably effective in blocking stray magnetic fields, resulting in but a 2-3 MHz peak splitting.



(a) (b)

Figure 2.21: The two magnetic shielding metal plates used to minimize stray magnetic fields. **(a)** Steel plate. **(b)** Mu-metal plate.



(a) (b) (c)

Figure 2.22: Three ODMR measurements, demonstrating the effect of magnetic shielding against unwanted fields with a metal plate: **(a)** without magnetic shielding, **(b)** using a steel plate, **(c)** using a mu-metal plate. The ODMR peak splitting is reduced from 11 MHz in **(a)** down to only 2-3 MHz in **(b)**, and **(c)**.

2.5.12. LONGPASS FILTER

Before the emitted red light travels to the photodetector, a longpass filter is placed in its path. This filter has a cut-on wavelength of 633 nm (in the case of NV centers) and allows only wavelengths above this threshold to pass through and enter the photodetector, blocking any unwanted (stray) light or residual excitation light, thereby increasing the signal-to-noise ratio (SNR). In the case of SnV centers, this filter is replaced with one that has a cut-on wavelength of about 610 nm, since the ZPL emission of tin-vacancy centers is typically the most relevant signal and occurs at ≈ 619 nm.

2.5.13. FIBER-COUPLING SYSTEM

For the emitted light to travel to the photodetector, it first has to be fiber-coupled. Hence, a fiber-coupling system is used, which, instead of lenses, uses off-axis parabolic, metallic (silver) mirrors to efficiently focus the incoming light beam onto the optical fiber. The fiber cable used is the P5-630A-PCAPC-1 single mode patch cable from Thorlabs, with an operating wavelength of 633-780 nm. The alignment of the fluorescence emission light into this fiber-coupling system is achieved by precisely adjusting the position and angle of a mirror placed before it, which reflects the light into it.

2.5.14. PHOTODETECTION AND TIME-TAGGING

For efficient collection of the photons emitted by the NV centers after illumination, a Single-Photon Counting Module (SPCM) is employed. This is the COUNT-10C-FC model from Laser Components, to be precise. It has a typical detection efficiency exceeding 60% in the 600-800 nm range, dark count rate of 10 counts/s, typical dead time of 45 ns, and timing resolution of 1 ns. To operate the SPCM, the DSN 102 Dual SPAD Power Supply is used, which also has an integrated counter for a quick count rate check.

After the incoming photons have been converted to electrical signal, they need to be digitized and monitored on a computer. Therefore, connecting to the TTL socket of the power supply of the SPCM, is a time-to-digital converter module, that being the Time Tagger X, by Swabian Instruments. Using software, in combination with this time tagger, allows for efficient recording and visualization of the light emitted from the NV centers, as well as communication and synchronization with other devices, in order to accurately and confidently control an ODMR measurement.

2.5.15. ARBITRARY WAVEFORM GENERATOR (AWG) & MW POWER AMPLIFIER

The arbitrary waveform generator (AWG) is responsible for creating the microwave field that is applied to the diamond. For this purpose, the Zurich Instruments SHFSG+ 8.5 GHz Signal Generator model is used. It not only provides easy programming and application of signals from its browser-based user interface, but also allows for backend control, enabling communication and synchronization with other devices.

However, the signal generated from the AWG needs further amplification in order to properly drive the NV centers. The MW amplifier ZHL-15W-422-S+ by Mini-Circuits is used to achieve this, connected to a variable power supply. This amplifier comes with a ~ 46 dB gain and ~ 39 dBm of output power at 1 dB compression. The signal produced by the SHFSG+ is amplified by the MW amplifier, and then fed to the PCB with the cop-

per wire, that is in close proximity to the diamond. Figure 2.23 shows how the different electronic devices described above are connected to each other in the ODMR setup.

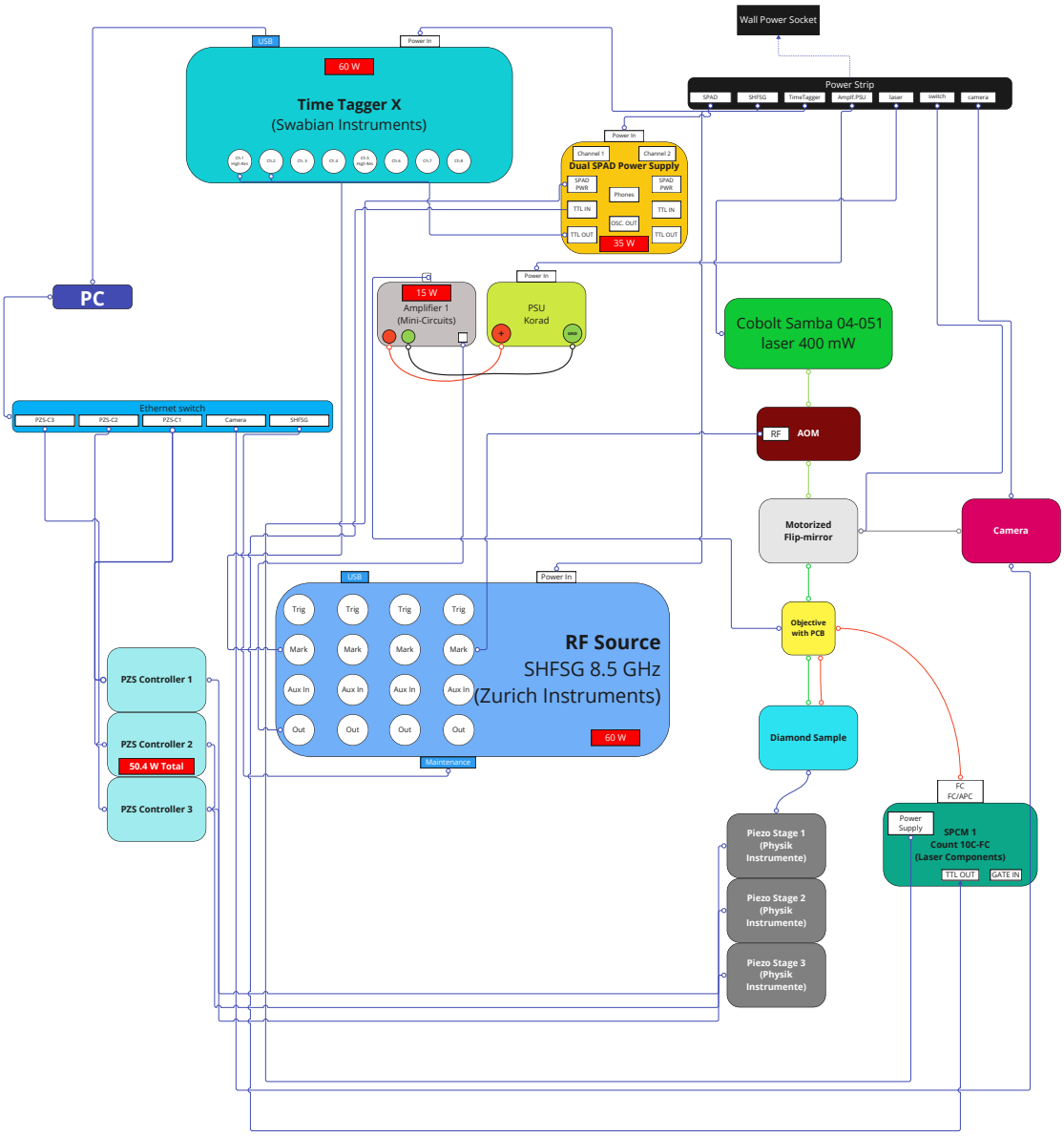


Figure 2.23: Diagram showing the components, instruments and devices used in the ODMR setup, as well as the multiple connections between them.

2.5.16. KEPLERIAN BEAM EXPANDER

As explained in Consideration #1, a Keplerian beam expander system can be situationally utilized, in order to efficiently adjust the beam diameter so that it better matches the optical requirements of the objective lens, thus creating a small and tight laser focus spot onto the sample. The principle of a beam expander relies on the use of two positive (convex) lenses. These lenses are placed at a distance equal to the sum of their focal lengths, such that the focal point of the first lens coincides with that of the second lens. The incoming collimated beam is converged onto the first lens' focal point, while the second lens recollimates the converged beam. The ratio of the focal length of the second lens f_2 to the focal length of the first lens f_1 is equal to the magnification M the beam experiences:

$$M = \frac{f_2}{f_1} \tag{2.41}$$

From Equation 2.41, it can be seen that when the expansion factor is positive, the output beam is expanded by a factor of M, and when it is negative, the output beam is instead reduced by a factor of M. In the ODMR setup described in Figure 2.15, the lenses used as part of the Keplerian beam expander have focal lengths $f_1 = 35\,\text{mm}$ and $f_2 = 500\,\text{mm}$. This results in the beam being expanded $\simeq 14.3$ times, thereby increasing the laser beam spot from 0.7 mm to $\simeq 10.1\,\text{mm}$. This does not yet fully fill the back aperture of the objective lens, which has a diameter of 16.6 mm, but does significantly improve the focal spot. The reason that a lens with even larger focal length was not used, is due to physical constraints and lack of available space on the optical table.

BEAM CHARACTERISTICS

A few calculations can be performed regarding the effective NA, NA_{eff}, of the objective lens, the spot size at focus, and the intensity at focus, depending on the beam diameter of the laser entering the objective. There are two cases to be dealt with; with or without the beam expander system.

Using the beam expander

In this case, the beam entering the objective lens has a diameter $d_{\text{BE}} = 6\,\text{mm}$, which is still smaller than its back aperture, with a diameter equal to $d_{\text{obj}} = 16.6\,\text{mm}$. The effective NA can be calculated by:

$$\text{NA}_{\text{eff}_1} = \text{NA}\frac{d_{\text{BE}}}{d_{\text{obj}}} = 0.90\frac{10.01}{16.6} \simeq 0.543 \tag{2.42}$$

The diffraction-limited lateral spot size w_0 is then given by:

$$w_0 = \frac{\lambda}{2\pi\,\text{NA}_{\text{eff}_1}} = \frac{532\times10^{-9}}{2\pi\times0.543} \simeq 155.9\,\text{nm} \tag{2.43}$$

where λ is the wavelength of the green laser. The axial range (spot size in the z-axis), can be calculated as:

$$z_R = \frac{\pi w_0^2}{\lambda} \simeq 143\,\text{nm} \tag{2.44}$$

Due to the nature of the Gaussian beam profile, the collection volume V_c can be approximated as an ellipsoid:

$$V_c = \frac{4}{3}\pi w_0^2 z_R \simeq 0.0145\,\mu\text{m}^3 \tag{2.45}$$

The intensity I at focus is obtained by dividing the laser power (after taking into account a certain amount of attenuation while traveling through the different optics - usually around 10%) with the area A of the focused spot:

$$I = \frac{P_{\text{focus}}}{A} = \frac{\eta P_0}{A} = \frac{\eta P_0}{\pi {w_0}^2} \tag{2.46}$$

where P_0 is the initial laser power, P_{focus} is the power at the focus, and η is the (collective) transmission efficiency of the optics.

Without using the beam expander

In the case where no beam expander is present, the beam entering the objective lens has a diameter $d_{\text{laser}} = 0.7\,\text{mm}$, which is much smaller than its back aperture. The effective NA is then given by:

$$\text{NA}_{\text{eff}_2} = \text{NA}\frac{d_{\text{laser}}}{d_{\text{obj}}} = 0.90\frac{0.7}{16.6} \simeq 0.038 \tag{2.47}$$

Similarly, the diffraction-limited lateral spot size w_0 is calculated by:

$$w_0 = \frac{\lambda}{2\pi\,\text{NA}_{\text{eff}_2}} = \frac{532\times10^{-9}}{2\pi\times0.038} \simeq 2.228\,\mu\text{m} \tag{2.48}$$

where λ is the wavelength of the green laser. The axial range can be calculated as:

$$z_R = \frac{\pi w_0^2}{\lambda} \simeq 29.3\,\mu\text{m} \tag{2.49}$$

The collection volume V_c is given by:

$$V_c = \frac{4}{3}\pi w_0^2 z_R \simeq 609\,\mu\text{m}^3 \tag{2.50}$$

The intensity I at focus can be obtained in the same manner as earlier.

2.5.17. DIGITAL CAMERA & WHITE LED

Before starting any measurement, the laser beam has to be precisely aligned onto the diamond sample through the objective lens. Moreover, the surface of the diamond has to be determined, so that accurate scanning parameters are in place. This imaging system consists of a white LED (MWUVL1, by Thorlabs) accompanied by a convex lens (M_4), an imaging camera (Blackfly S GigE BFS-PGE-31S4M-C, by Teledyne Vision Solutions) with another convex lens (M_5), a 90-10 beamsplitter (BSP_2) at a 45° angle between them, and a 45-55 pellicle beamsplitter (BSP_1), mounted on a motorized flip mount. When the laser is on, this configuration allows monitoring of the laser beam focus, alignment and uniformity. Turning the laser off and using the white LED source (which can be controlled with software) allows for direct viewing of the sample and its characteristics. This aids in defining the coordinates of the sample's corners, identifying areas of interest, and focusing on specific layers, as seen in Figure 2.24.

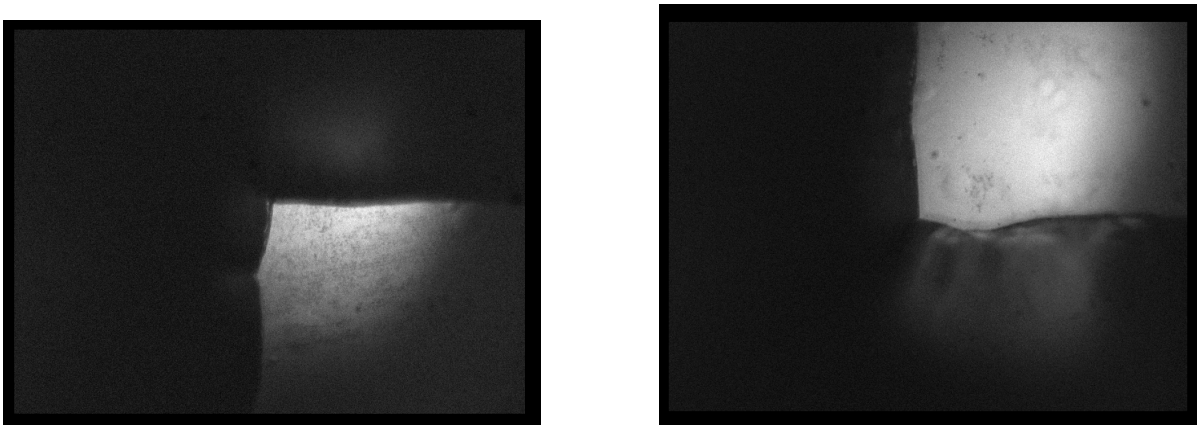


Figure 2.24: Images of a random diamond sample's corners, as viewed on the computer screen. This check (along with other surface checks) is performed before every experiment, to ensure proper focusing and define the coordinates of the corners of the diamond sample.

2.5.18. SPECTROMETER

As described briefly in Figure 2.15, by simply attaching a different fiber cable to the fiber-coupling system, it is possible to instead send the emitted light into a spectrometer (SpectraPro HRS-750, by Teledyne Princeton Instruments). Attached to it is a charge-coupled device (CCD) camera (PIXIS 100B, also by Teledyne Princeton Instruments). When light enters the spectrometer, it is dispersed into its component wavelengths by a diffraction grating. Three different diffraction gratings are available for use, depending on how broad the range of the wavelengths being analyzed is. After being dispersed, the light is focused on the CCD detector, which contains photo-sensitive pixels that convert incoming light into an electric charge. Finally, the signal is digitized and analyzed through the LightField software, in order to generate a spectrum, in the form of intensity versus wavelength.

2.6. SOFTWARE IMPLEMENTATIONS OVERVIEW

Initialization, control and communication of the devices, as well as monitoring, recording and analysis of the data is done using custom-developed software, part of which was provided by TNO. From then on, several improvements and adjustments have been made, in order to better accommodate the specific electronics and optical components of this setup. The code for the ODMR experiments is provided in Appendix B.

2.6.1. SERPENTINE SCAN

To start with, a serpentine scan pattern was implemented for the piezo scanning stage. This allows uninterrupted, continuous movement between pixels, thereby reducing unnecessary intermediate steps. In this configuration, instead of scanning row-by-row, left-to-right, the stage moves in a "snake-like" pattern, from the last pixel of a row, directly to the pixel above it in the next row. Switching to this type of scan pattern resolved any discontinuities caused by large, diagonal movements of the piezo stage and also resulted in less overall measurement time.

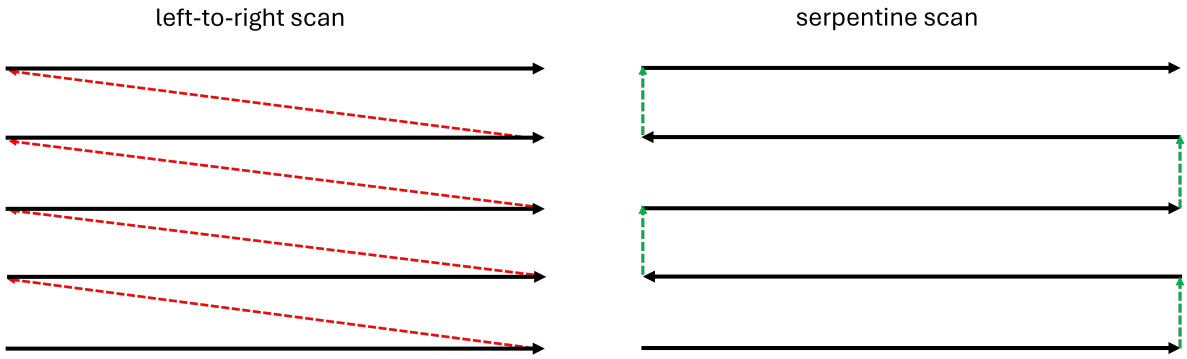


Figure 2.25: The two types of scanning patterns used in these experiments. On the left, the standard linear scan is shown. On the right, the improved, serpentine scan is depicted.

2.6.2. TILT CORRECTION

During alignment and viewing of the sample's surface on the computer, it was made evident that many of the samples being investigated had non-uniform thickness or flatness. In addition, the material used to fix a sample on the custom aluminum plate creates another factor of tilt. This resulted in the stage having to move back and forth in the z-axis, in order to properly focus, and compensate for the few micron difference between different areas of the same sample. Therefore, the decision was made to modify the software, so that it takes into account the difference in height between the corners of an area of interest. After manual inspection of the corners and their coordinates, the z-axis value is recorded, so that the image is in focus. afterward, the tilt coefficients α_x and α_y are calculated and inserted into the code:

$$\alpha_x = \frac{\Delta z}{\Delta x},\ \alpha_y = \frac{\Delta z}{\Delta y} \tag{2.51}$$

2.6.3. PERIODIC AUTO-ZEROING

Some inherent problems of the piezo stage can cause it to get stuck, especially during measurements that last many hours. This is quite a problem, not only because time is wasted, unknowingly waiting for overnight measurements to finish, but also results in inconsistencies of measurements on nearby pixels and discontinuities in the data acquired. However, it was found out that, by programming an auto-zeroing function into the software controlling the piezo stage, it would no longer randomly freeze and disobey movement commands. Auto-zeroing refers to the recalibration of the piezo stage in all of its three axes. Hence, for every thousand scanning steps, an automatic auto-zeroing was employed, resulting in roughly +5% scanning time, but getting rid of unwanted interruptions.

2.6.4. Z-SCAN

Part of the process that takes place before any measurement, is determining the location of the front and back surface of the sample. For this purpose, a "scan" is run only in the z-axis, recording the PL intensity at each location, thus providing a profile of PL intensity versus depth. From the resulting graph (see Figure 2.26 as an example), distinct PL spikes are visible whenever the focus of the objective lens coincides with either the top or back surface, likely due to increased reflections of the excitation light. Thus, a rather accurate estimation of the sample's thickness can be made and the z-axis values corresponding to the different surface planes of the diamond sample can be obtained.

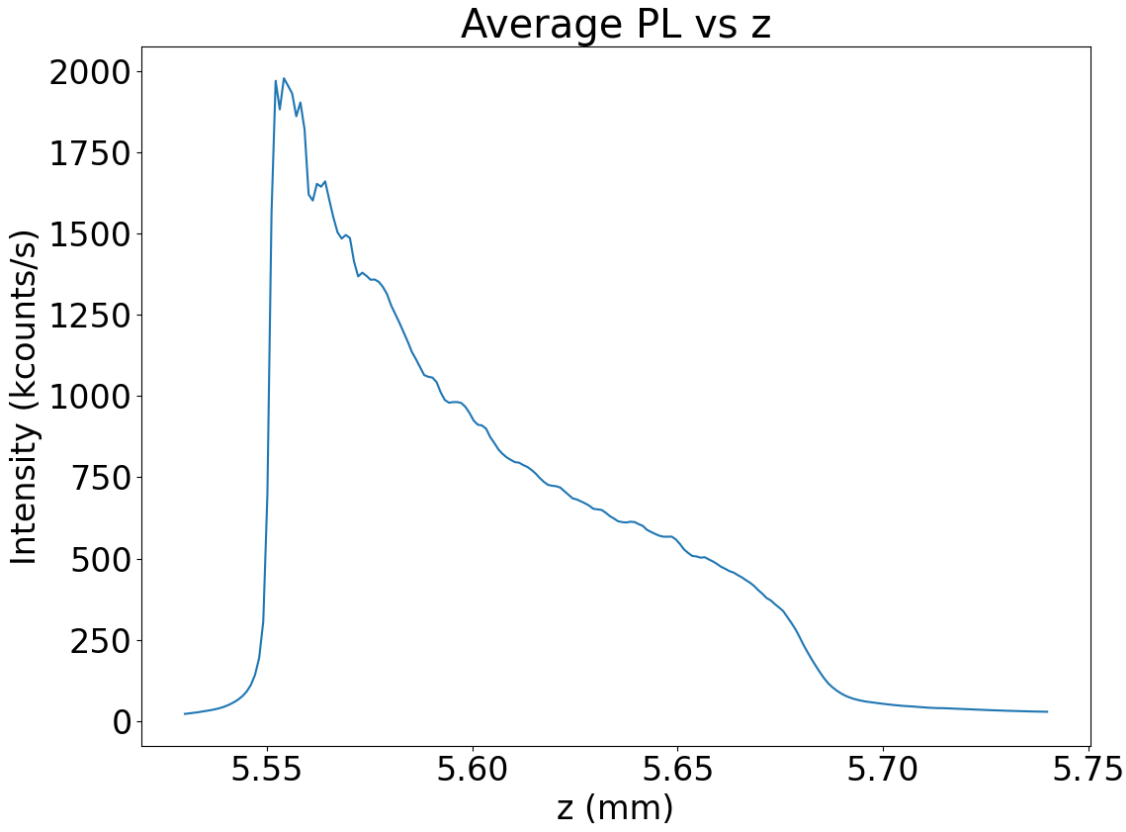


Figure 2.26: PL intensity vs. diamond sample depth/thickness, referred to as a Z-scan.

2.7. METHODS

Next, the methods of setting up an ODMR experiment shall be reviewed.

2.7.1. DIAMOND SAMPLE MOUNTING

The diamond sample has to first be mounted on the custom, detachable aluminum plate. This is done with the help of a PMMA 950k resist (950k referring to its molecular weight). Roughly a drop of PMMA is deposited on top of the aluminum plate. Subsequently, the diamond is placed on top of the plate, so that it makes good contact with the plate, and carefully so the liquid beneath does not overflow. The diamonds being investigated range from $2 \times 2\,\mathrm{mm}^2$ to $10 \times 10\,\mathrm{mm}^2$, so proper PMMA deposition is crucial. afterward, the aluminum plate with the diamond fixed on top of it is placed on a hotplate, where it is heated at 120° for 2 minutes. This plate is then labeled with a sticker that identifies the diamond in use, and screwed on top of the adapter plate and the piezo stage. Figure 2.27a and Figure 2.27b show the tools used to fix the diamond sample on the detachable aluminum plates, and Figure 2.27c shows a mounted diamond substrate ready for ODMR measurements.



(a) (b) (c)

Figure 2.27: Photos of **(a)** PMMA lithography resist (used for fixing the diamond on its mounting plate), **(b)** the hotplate used to bake the PMMA, and **(c)** a random diamond sample fixed on the detachable aluminum mounting plate.

2.7.2. MEASUREMENT PREPARATION

Assuming the setup is well aligned and the sample mounted on the piezo stage, some preparations need to be done before starting any measurement. The following steps are performed via the software's graphical user interface (GUI). The GUI is brought up by typing "`rtcs gui`" on the Ubuntu terminal. Auto-zeroing of the stage has to take place, followed by live viewing of the sample's surface. To view the sample, the pellicle beamsplitter is first flipped down. The digital camera and the white LED (at 12 mA) are turned on. Moving the piezo stage closer to the objective lens results in a reflection of the LED's sensors appearing on the screen, whenever either the top or back surface are approximately in focus.

From there, the tilt coefficients of the sample are determined, by recording the surface focus values at different, far-away points or at the corners. These values are then given as inputs to the software. Next, the laser is turned on and a check on whether its focus is also on the surface of the sample is done (within a margin of few microns). Finally, the digital camera and the white LED are turned off, and the pellicle beamsplitter is raised, to allow direct, full-power excitation of the diamond sample. The lights in the lab are also turned off and the setup is covered by black panels, to minimize and block any stray or unwanted light from traveling to the photodetector.

2.7.3. RUNNING THE MEASUREMENT

Electronics such as the AWG, the MW amplifier, and the power supply of the SPCM may now be turned on. A quick ODMR measurement can now be run as a test, before the actual scan takes place. The default command for this is "`rtcs esr-scan --show --num-sweeps 1`". In case parameters need to be changed, a help page is available by typing "`rtcs esr-scan --help`". After defining an area of interest, A, and its corresponding coordinates and tilt, a 2D ODMR scan can be initiated. This is performed through the python script "`ODMR_2D.py`", in which the area of interest can be defined, as well as the appropriate step sizes Δx, Δy (movement in the x and y-axis). For each pixel/location, an ODMR graph is obtained and then processed by the fitting function, in order to provide the values used in the corresponding maps. The frequency sweeping parameters are also set, such as initial and final frequency, and frequency step size. The amount of pixels (n_{pixels}) present in the final 2D graph is given by:

$$n_{\text{pixels}} = \frac{A}{\Delta x \times \Delta y} \tag{2.52}$$

Reducing the step size increases the number of pixels in a given area, thus resulting in higher spatial resolution, but more measurement time instead.

$$t_{\text{msr}} \propto n_{\text{pixels}} \tag{2.53}$$

The core of an ODMR measurement lies in sweeping the microwave frequency and recording the decrease in photoluminescence intensity, i.e. the MW field is resonant with the $m_s = \pm 1$ transitions. As is inferred by the term "2D scan", the usual goal of an ODMR measurement, in terms of sensing, is to end up with a map of the effect of the property in question, whether that is magnetic field, electric field, temperature, or strain. By post-processing and extracting this data, it is then possible to create different maps depicting these effects in a quantitative way. This results in multiple possible representations of the acquired data, starting with photoluminescence maps and continuing with peak splitting, frequency shift and photoluminescence contrast.

2.8. BIOSENSING WITH ODMR

On the path towards creating a fully integrated, compact NV-based quantum biosensor, the first step is determining the type of biological sample to be measured and the method to use for that. There are numerous approaches to performing biosensing with NV centers in diamond. Temperature is one of the properties that can be monitored intracellularly, providing information on inflammations or local heating [108], which could be indications of carcinogenic changes. The pH variations in a cellular environment may also be monitored, using nanodiamonds (NDs) with functionalized molecules [109]. Electric field sensing is also employed to detect and monitor cellular electrical activity, using NVs in NDs [110]. Among others, magnetic field sensing is widely applied for detecting magnetically labeled biomolecules. NV centers embedded in diamond act as quantum sensors, detecting subtle magnetic perturbations generated by cellular processes and labeling strategies, thereby offering useful insights into cell biophysics and diagnostics.

There are quite a few applications of magnetic labeling, and their nature also depends on whether real-time monitoring or static imaging (which is generally simpler) is the goal. To start with, it is possible to differentiate between multiple magnetically labeled targets [111] or perform high-resolution magnetic imaging of cells labeled with magnetic nanoparticles (MNPs) [112, 113]. In this study, the decision was made to perform static imaging of human embryonic kidney (HEK) cells, labeled with superparamagnetic iron oxide nanoparticles (SPIONs), in order to emulate magnetic field biosensing, using the ODMR technique with ensembles of NV centers in diamond. Using functionalized SPIONs in this context would allow for differentiation between cellular conditions. Although the SPIONs in this study were not functionalized to specifically target pathological markers, their random dispersion on the cell surface still provides a viable proof-of-concept for magnetic field imaging, potentially enabling the detection of subtle differences in cellular conditions and physiological states.

2.8.1. THE BIOSAMPLE: HEK CELLS

The HEK cells described here may be referred to simply as "biosample" from now on. The cell line labeled as HEK293 comes from human embryonic kidney cells, which have been subsequently transformed with human adenovirus type 5 DNA. This cell line has been further diversified into different subtypes, to match different experimental protocols and conditions. The subtype used in this project is a temperature-sensitive variant, called HEK293T, that expresses the SV40 large T antigen [114]. Historically, these cells were first isolated by Alex van der Eb in 1970s and transformed into a cell line by Frank Graham in his 293rd experiment. Hence, the name HEK293 was created. The typical diameter of HEK293 cells is on average about 13 µm and is dependent on their culturing conditions [115, 116]. Their robust characteristics make them particularly suited for controlled magnetic labeling experiments, allowing for effective differentiation of subtle variations in cellular conditions.

2.8.2. SUPERPARAMAGNETIC IRON OXIDE NANOPARTICLES (SPIONS)

Labeling of the HEK293T cells was done using biocompatible SPIONs (Fe_3O_4). In order for them to be added directly during the cell culturing process, Fe_3O_4 nanoparticles in water solution were used (by Cytodiagnostics), with a diameter of ~ 5 nm [117]. Iron ox-

ide nanoparticles of this size exhibit superparamagnetic properties [118], meaning that application of a sufficiently strong external magnetic field causes the nanoparticles to also obtain magnetization. However, upon removal of the external field, thermal effects cause random magnetic moment flipping, resulting in loss of magnetization.

All things considered, application of an external magnetic field during any measurements involving SPIONs is obligatory. The strength of that field depends on the size of the nanoparticles [119, 120]. To reach saturation magnetization [121], a field of up to 300 mT may be sufficient. At this state, these SPIONs are expected to show magnetization greater than 45 emu/g. Larger SPIONs provide greater magnetic moments, stabilizing magnetization at lower external fields but potentially reducing cellular uptake and increasing toxicity. Hence, optimal SPION sizes are usually between 10–100 nm.

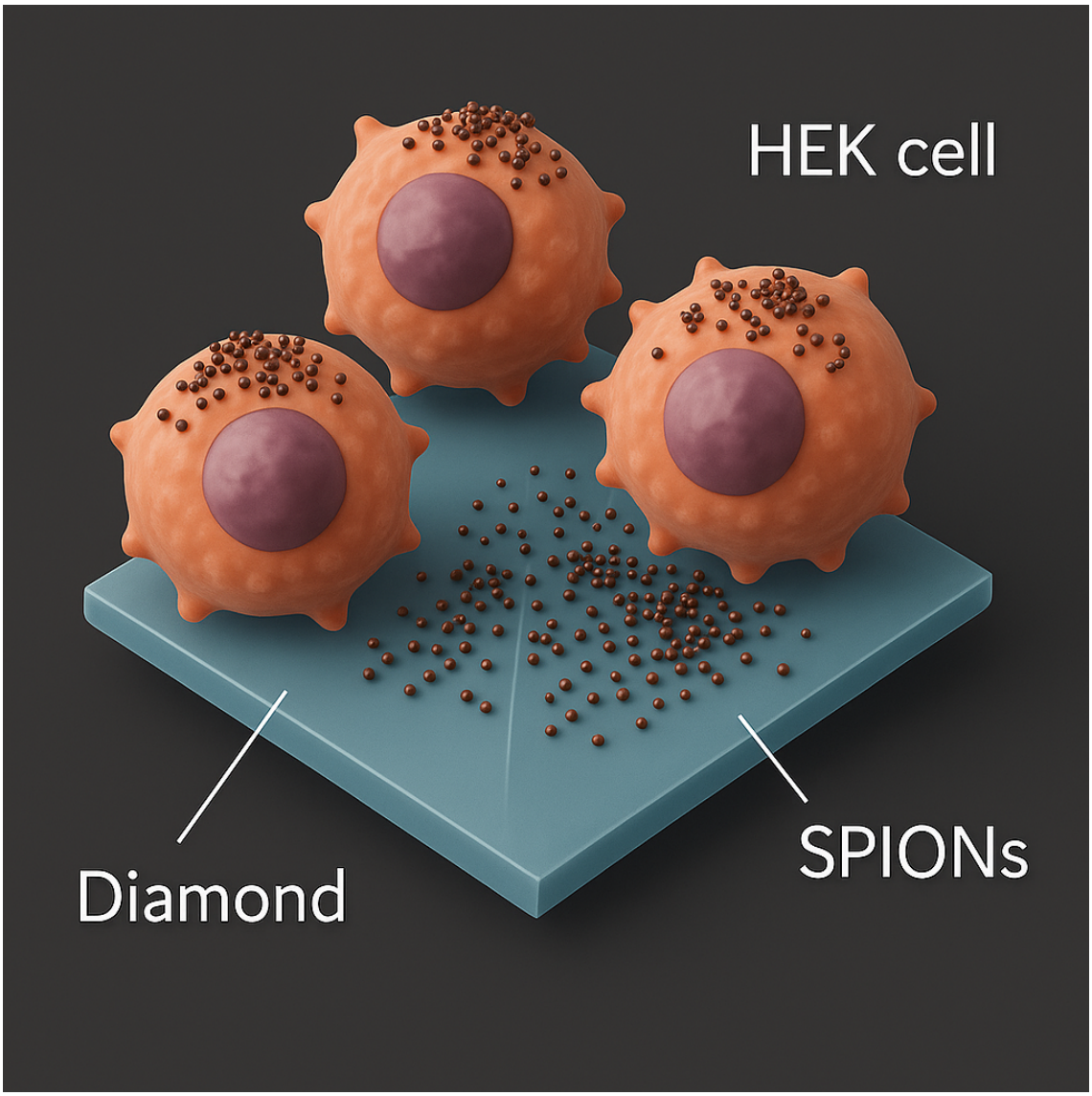


Figure 2.28: Schematic 3D illustration of HEK293T cells deposited on a flat diamond substrate, used for NV-based biosensing. The cells are labeled with superparamagnetic iron oxide nanoparticles (SPIONs), which are visible both adhered to the cell surface and dispersed across the diamond. This configuration emulates a proof-of-concept for magnetic field mapping using optically detected magnetic resonance (ODMR) with NV centers in diamond. Image generated using ChatGPT (OpenAI, 2025).

2.8.3. DIAMOND PREPARATION, CELL CULTURE & SPION INCORPORATION

Using a bulk diamond sample with an ensemble of NV centers generally comes with mostly random positioning of NV centers. For biosample measurements, a $10 \times 10\,\text{mm}^2$ diamond sample (supplied by EDP) was used, with a thickness of ~ 300 µm, cut along the {100} crystallographic plane. This is a CVD-grown substrate, with a natural N concentration between 6-8 ppm, as determined by Secondary Ion Mass Spectrometry (SIMS) measurements, resulting in an NV center concentration of roughly 15 ppb, randomly distributed throughout its volume.

Nevertheless, for optimal biosensing conditions, positioning of NV centers close to the surface of the diamond—and by extension close to the biosample—is preferred. To ensure maximum sensitivity to the —often weak— magnetic fields produced at the surface, while also minimizing surface effects (such as charge state instabilities or noise), NV centers located at shallow depths of 10-20 nm are ideal [122, 123]. More on this in chapter 3, section 3.4.

Before cell growth and injection of magnetic nanoparticles, the diamond substrate underwent a round of fuming nitric acid (HNO_3) cleaning. This process was carried out inside the cleanroom facility of Kavli Nanolab Delft. Fuming nitric acid is used because of its ability to oxidize and decompose organic residues, while the diamond itself is chemically inert to it. This provides thorough cleaning of the diamond's surface, in preparation for cell culturing. Proper cleaning of the diamond surface ensures minimal contamination, which is critical for maintaining the integrity and accuracy of subsequent ODMR biosensing measurements.

Following cleaning of the diamond surface with HNO_3, initial HEK293T cell culturing took place. Once a healthy population had been established, SPIONs were added directly to the medium, allowing them to be absorbed and incorporated into the cells via the endocytosis mechanism [124]. The concentration of deposited SPIONs was 40 µg/mL. Cell culturing and SPION incorporation was performed by Qiangrui Dong, part of the Daan Brinks group from the ImPhys department of the Technische Natuurwetenschappen (TNW) faculty of TU Delft. The selected concentration represents a balance between achieving sufficient magnetization for detection and minimizing potential nanoparticle toxicity, typically observed at concentrations exceeding 100 µg/mL.

PROOF-OF-CONCEPT EMULATION OF MAGNETIC LABELING

Because of the lack of surface coating of the SPIONs prior to this, it is assumed that the nanoparticles were not functionalized, and that, instead of being efficiently internalized, they predominantly ended up on the surface of the cell culture. Due to their non-functionalized state, SPIONs could not specifically target cancerous or unhealthy cells, which would have otherwise provided a targeted approach to magnetic labeling. Nonetheless, random dispersion of SPIONs throughout the biosample still serves as a proof-of-concept emulation of the magnetic field image that incorporation into unhealthy cells would have produced. This initial demonstration highlights the feasibility and sensitivity of NV-based magnetic biosensing for future targeted cell diagnostics.

2.8.4. ODMR BIOSAMPLE MEASUREMENT METHOD

The diamond, which now has the biosample and the SPIONs deposited on top, is then fixed on an aluminum plate and mounted on the piezo stage, in preparation for ODMR 2D mapping measurements (as described in section 2.7). Due to the superparamagnetic properties of the iron oxide nanoparticles, an external bias magnetic field is required, in order for the SPIONs to exhibit magnetization during the measurement period. Magnetic biasing is done with the neodymium magnet described in subsection 2.5.10, which is placed inside the pocket of the magnet-housing aluminum plate on the piezo stage, as seen in Figure 2.29. This magnet produces a field of ≈ 1.07 mT at the location of the biosample, resulting in a peak splitting of roughly 30 MHz during ODMR measurements (considered as the default splitting without the effect of the field generated by the SPIONs).

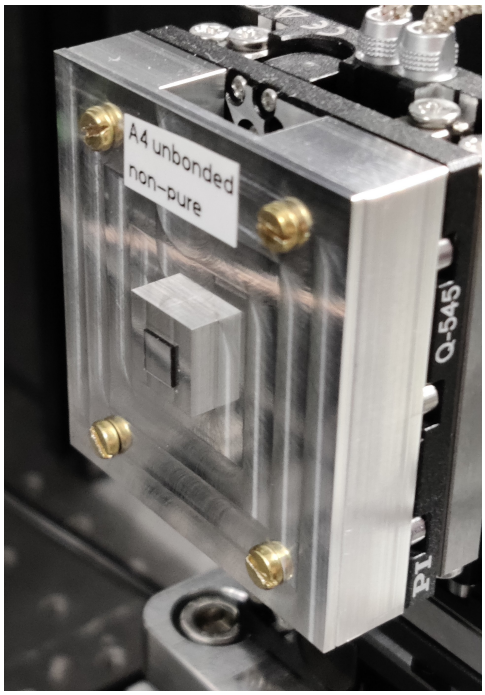


Figure 2.29: Custom magnet-housing aluminum adapter plate, with a neodymium ND42 magnet placed inside, for application of the magnetic field required to magnetize the SPIONs.

SIDE EXCITATION & TOTAL INTERNAL REFLECTION

When performing imaging of biosamples, green laser excitation from the side is commonly used in a widefield setup configuration. Doing so allows the light to enter the diamond substrate at a fixed angle, enabling total internal reflection at the diamond-biosample interface. From Snell's law, it is known how light travels and bends when it encounters materials with different refractive indices. Diamond has a refractive index (RI) $n_1 \simeq 2.4$, while HEK293 cells are assumed to have an RI of $n_2 \simeq 1.38$ (common for biological cells [125]). For reference, the refractive index of air is $n = 1$. The relationship between the angle of incidence θ_1 and the angle of refraction θ_2 is described by (Snell's law):

$$n_1 \sin\theta_1 = n_2 \sin\theta_2 \tag{2.54}$$

Total internal reflection (TIR) occurs when the refracted angle is $\theta_2 = 90°$, which means that $\sin(\theta_2)$=1. Solving for $\theta_c = \theta_1$ results in:

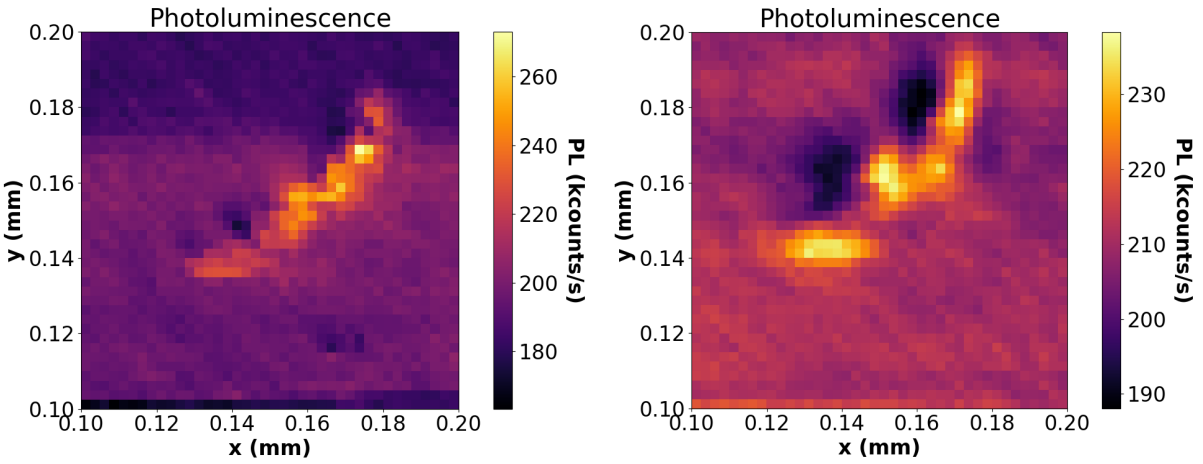
$$\theta_c = \arcsin\left(\frac{n_2}{n_1}\right) \tag{2.55}$$

Substituting n_1 and n_2 into Equation 2.55 yields $\theta_c \simeq 35°$, resulting in the angle of incidence needing to be $\theta_1 > 35°$ in order to achieve TIR inside the diamond. By utilizing this, an evanescent field is created at the diamond-biosample interface. This makes it possible to avoid direct illumination of the biosample itself, which could result in heating, potentially damaging the biosample, or even cause it to exhibit fluorescence of its own, thus introducing added noise when collecting fluorescence from NV centers.

Be that as it may, HEK293T cells do not emit a fluorescent signal (besides insignificant autofluorescence). Lastly, these cells could get damaged by local heating, but, since live imaging is not the goal, there is no substantial difference between measuring live or dead cells. Instead, they are destined for static, confocal-type imaging, as an initial demonstration of biosensing, before the diamond with the biosample on it is used in a widefield, diamond-on-chip configuration.

2.9. EXPERIMENTAL RESULTS AND ANALYSIS

For these measurements, the standard confocal version of the ODMR setup was employed. The diamond sample with the HEK293T cells and SPIONs fixed on it (as described in subsection 2.8.3) was mounted on the detachable aluminum plate, which was attached to the piezo stage. The diameter of the cells is roughly ~ 12 µm, while the SPIONs have a diameter of 5 nm. The scanning parameters were set according to subsection 2.7.3.



(a) (b)

Figure 2.30: Photoluminescence images of the diamond substrate with HEK293T cells grown on top, containing SPIONs, in the absence of an external magnetic field: **(a)** at the surface of the diamond, and **(b)** 10 µm deep.

Measurements were first taken without the presence of an external magnetic field, serving as a calibration reference for background ODMR data, both at/near the surface of the diamond (where the biological layer with SPIONs is located) and at a depth of 10 µm away from it (Figure 2.30). Next, an external magnetic field was applied, with a magnitude of $\simeq 1.07\,\text{mT}$ at the diamond's surface (converted to magnetic field strength by measuring an average peak splitting of 30 MHz). With this bias field present, measurements were taken at the surface of the diamond, and subsequently at depths of 10 µm and 50 µm. The area of interest was primarily $100 \times 100\,\mu\text{m}^2$, with an extra measurement taking place at an area of $200 \times 200\,\mu\text{m}^2$ (Figure 2.31).

Despite applying a 1.07 mT bias field, SPION magnetization may have been insufficient for clear magnetic contrast. Based on magnetic dipole modeling, the magnetic moment of a cell containing 40 µg/mL SPIONs is $m \approx 3 \cdot 10^{-15}\,\text{Am}^2$. The resulting stray field near the cell surface is estimated to lie in the range:

$$\frac{\mu_0 m}{4\pi R^3} < B < \frac{2\mu_0 m}{4\pi R^3}, \tag{2.56}$$

yielding field strengths between ~ 0.4 and 0.8 µT for $R = 9\,\mu\text{m}$. In this expression, μ_0 is the vacuum permeability ($4\pi \times 10^{-7}$ H/m), m is the magnetic dipole moment of the SPION-labeled cell (in Am^2), and R is the distance from the center of the cell to the evaluation point (in m). The inequality describes the range of magnetic field strengths B generated

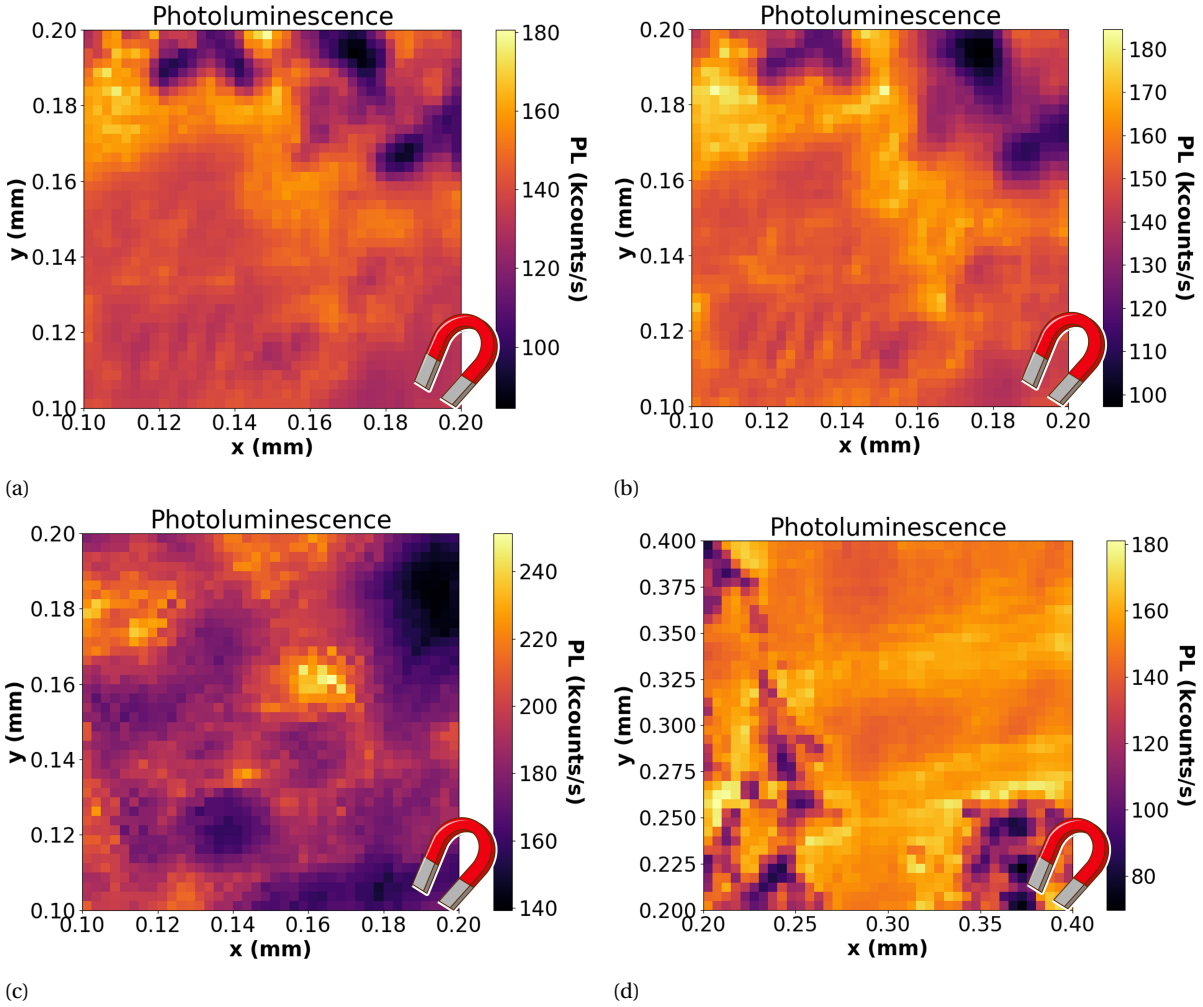


Figure 2.31: Photoluminescence images of the diamond substrate with HEK293T cells grown on top, containing SPIONs, in the presence of an external magnetic field: **(a)** at the surface of the diamond, **(b)** 10 µm deep, **(c)** 50 µm deep, and **(d)** 50 µm deep, at a different, larger ($200 \times 200\,\mu m^2$) area.

outside a magnetized sphere, such as a labeled HEK cell, where the field is weakest at the equator and strongest at the poles.

Since the NV ensemble ODMR line has a FWHM of several MHz (typically ~6 MHz), detecting such small shifts (~10-20 kHz per µT) remains at the limit of sensitivity. The magnetic sensitivity of the ODMR-based biosensing setup was estimated using the shot-noise-limited approximation (see Equation 2.57 below). Assuming an ODMR contrast of approximately 5%, a full width at half maximum (FWHM) of 6 MHz, and a photon detection rate of 180 kcounts/s, the resulting sensitivity is estimated at $\eta_B \approx 5\ \mu T/\sqrt{Hz}$. It is important to note that the system was not optimized for maximum sensitivity: the laser power was limited to 0.3 mW to avoid thermal damage to the biosample, and the confocal configuration required excitation through the biological layer, introducing additional optical losses.

$$\eta_B = \frac{4}{3\sqrt{3}} \cdot \frac{1}{\bar{\gamma}_{NV}} \cdot \frac{\Delta\nu}{C\sqrt{R}} \tag{2.57}$$

where η_B is the magnetic field sensitivity, $\bar{\gamma}_{\mathrm{NV}}$ is the NV center gyromagnetic ratio, $\Delta\nu$ is the FWHM of the ODMR resonance dip, C is the ODMR contrast, and R is the photon detection rate.

Attention was paid to the excitation and collection paths being well aligned. The laser's power was set to $P_0 = 0.3$ mW (measured right after the attenuation system), resulting in a power of $P_{\mathrm{focus}} \simeq 0.27$ mW at the focus. Assuming a beam waist size of $w_0 = 2.228$ µm (in the absence of the beam expander), the intensity at the focus (see Equation 2.46) is given by:

$$I = \frac{P_{\mathrm{focus}}}{\pi w_0^2} \simeq 1.73 \times 10^5 \frac{\mathrm{W}}{\mathrm{cm}^2} \tag{2.58}$$

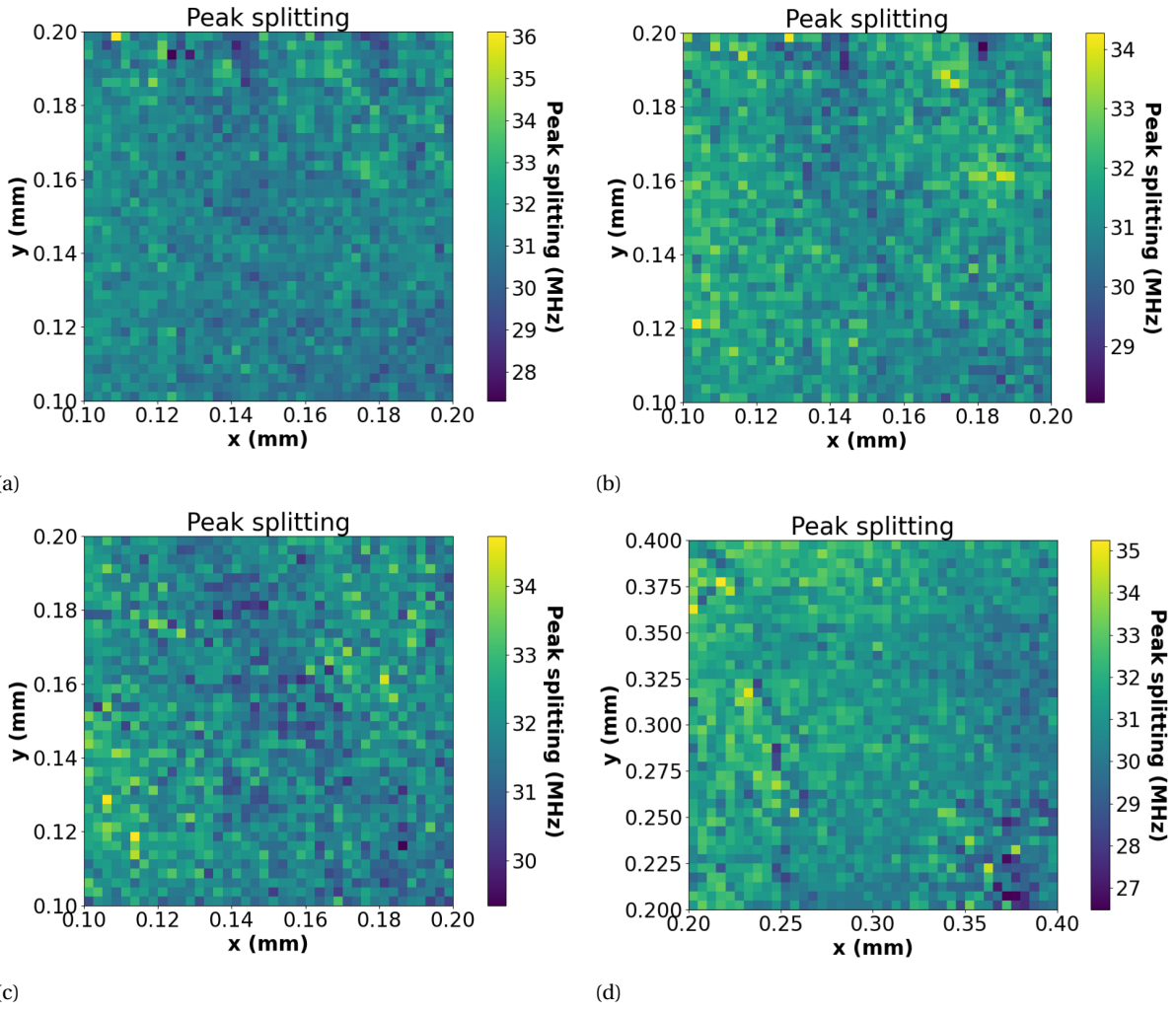


Figure 2.32: ODMR maps of the peak splitting effect of an external magnetic field on the diamond substrate with HEK293T cells grown on top, containing SPIONs: **(a)** at the surface of the diamond, **(b)** 10 µm deep, **(c)** 50 µm deep, and **(d)** 50 µm deep, at a different, larger ($200 \times 200\,\mu\mathrm{m}^2$) area.

Following careful analysis of the PL maps in Figure 2.31, clear spatial variations in intensity are revealed. Darker regions likely correspond to the presence of HEK293T cells and SPION aggregates. Given the cell diameter (~ 13 µm), these dark regions —approximately 10–20 µm across— probably result from scattering or absorption effects at the

diamond-cell interface. Single SPIONs (~ 5 nm) are too small to cause such significant localized reductions in photoluminescence intensity individually. Thus, these intensity drops suggest larger aggregates of SPIONs, potentially due to insufficient nanoparticle internalization into cells. Conversely, brighter spots (>240 kcounts/s) could indicate either locally enhanced optical conditions (due to diamond surface roughness, increased NV center density, or localized strain) or areas without significant coverage by cells or nanoparticle clusters.

After processing the ODMR data obtained while scanning these areas, color maps representing the peak splitting can be created (Figure 2.32). These images demonstrate the distribution of the magnetic field strength across the surface of the diamond. Ideally, the presence of properly magnetized SPIONs within or on the cells should lead to measurable variations in peak splitting, clearly observable in ODMR maps.

Even though some features and magnetic signatures can be seen in the ODMR maps, there does not seem to be a clear and distinguishable magnetic profile. Instead, the results here indicate limited or insufficient SPION magnetization, which likely arises due to the following factors:

1. **Inadequate magnetic bias field:** The applied external magnetic field of approximately 1.07 mT is substantially lower than the typical threshold (~ 300 mT) required to approach SPION saturation magnetization. As a result, the nanoparticles remain only weakly magnetized during measurement.

2. **Lack of SPION functionalization and inefficient cellular uptake:** In the absence of functional surface coatings, the SPIONs were not effectively internalized by the HEK293T cells. Instead, they predominantly aggregated on the cell surface, forming large clusters. This compromises both the spatial resolution and uniformity of the induced magnetic fields and limits biosensing contrast and sensitivity.

Thermal fluctuations significantly reduce the stability of SPION magnetization. For a single 5 nm SPION in an external magnetic field B, the magnetic energy is given by

$$E_B = mB,$$

where the magnetic dipole moment m can be estimated using the SPION volume, density, and saturation magnetization. Hence, for a magnetite SPION with a diameter of 5 nm, a density of 5.17 g/cm^3, and a saturation magnetization of 25 emu/g, the resulting dipole moment is approximately:

$$m \approx 8.5 \times 10^{-21}\,\mathrm{A \cdot m^2}$$

In a modest external magnetic field of $B = 1.07$ mT, this yields

$$E_B \approx 9 \times 10^{-24}\,\mathrm{J}$$

which is significantly smaller than the thermal energy scale $k_B T \approx 4 \times 10^{-21}$ J at 300 K.

This means that thermal energy dominates and destabilizes the SPION magnetic moments under such conditions. However, this highlights the critical importance of selecting an appropriate SPION size. Larger SPIONs possess a greater dipole moment and are, therefore, less susceptible to Brownian noise, improving their magnetic stability. To achieve stable magnetization, either larger SPIONs or significantly stronger external magnetic fields (in the order of Teslas) are required. This approach, however, presents a tradeoff, as larger SPIONs can negatively impact cell uptake and potentially increase cytotoxicity. Optimal SPION sizes are typically in the range of 10 to 100 nm, where external magnetic fields from a few millitesla (mT) to hundreds of mT are generally sufficient to achieve near-complete magnetization.

2.10. CONCLUSION

The measured ODMR peak splitting values provide qualitative insight into local magnetic field variations induced by SPION clusters. However, these results are not yet sufficient to draw quantitative conclusions regarding specific cellular magnetization states or successful magnetic labeling. The observed ODMR maps are influenced not only by magnetic signals but also by substantial optical effects such as surface scattering, NV density inhomogeneities, and photoluminescence artifacts.

To improve measurement fidelity, future experiments should employ fully functionalized SPIONs capable of targeted cellular uptake, which would enhance specificity and minimize aggregation artifacts. Furthermore, applying a stronger and more spatially uniform external magnetic field (approaching the SPIONs' saturation regime) is essential for ensuring stable magnetization during imaging. Instrumentally, integrating the beam expander will improve spatial resolution by reducing the focal spot size and increasing excitation intensity, thereby enhancing signal-to-noise ratio and magnetic field sensitivity.

Importantly, these measurements already demonstrate the high sensitivity of NV ensembles to magnetic fields in the sub-microtesla range. This validates the feasibility of using NV-based sensors for biosensing applications involving weak magnetic dipoles, and it establishes a clear path forward for developing widefield, chip-integrated platforms for dynamic biological field imaging with subcellular spatial resolution.

Thus, although the current results remain inconclusive in terms of functional biosensing due to limitations in SPION magnetization and targeting, they represent a critical proof-of-concept. This study confirms the potential of NV-based quantum sensing architectures in biological contexts and defines the technical and methodological improvements necessary for realizing reliable, quantitative biomagnetic imaging in future work.

BIBLIOGRAPHY

[1] A K Geim. “Graphene prehistory”. In: *Physica Scripta* 2012.T146 (Jan. 2012), p. 014003. DOI: 10.1088/0031-8949/2012/T146/014003.

[2] Sumio Iijima and Toshinari Ichihashi. “Single-shell carbon nanotubes of 1-nm diameter”. In: *Nature* 363.6430 (1993), pp. 603–605. ISSN: 1476-4687. DOI: 10.1038/363603a0.

[3] Robert Robertson, John Jacob Fox, and A. E. Martin. “Two types of diamond”. In: *Philosophical Transactions of the Royal Society of London. Series A, Containing Papers of a Mathematical or Physical Character* 232.707-720 (1933), pp. 463–535. DOI: 10.1098/rsta.1934.0013.

[4] Ben L. Green, Alan T. Collins, and Christopher M. Breeding. “Diamond Spectroscopy, Defect Centers, Color, and Treatments”. In: *Reviews in Mineralogy and Geochemistry* 88.1 (July 2022), pp. 637–688. ISSN: 1529-6466. DOI: 10.2138/rmg.2022.88.12.

[5] J.W. Harris et al. “49 - A CLASSIFICATION SCHEME FOR DIAMOND AND A COMPARATIVE STUDY OF SOUTH AFRICAN DIAMOND CHARACTERISTICS”. In: *Physics and Chemistry of the Earth*. Ed. by L.H. Ahrens et al. Pergamon, 1975, pp. 765–783. ISBN: 978-0-08-018017-5. DOI: https://doi.org/10.1016/B978-0-08-018017-5.50053-5.

[6] Christopher Breeding and James Shigley. “The "Type" Classification System of Diamonds and Its Importance in Gemology”. In: *Gems & Gemology* 45 (July 2009), pp. 96–111. DOI: 10.5741/GEMS.45.2.96.

[7] Alan T. Collins. “The detection of colour-enhanced and synthetic gem diamonds by optical spectroscopy”. In: *Diamond and Related Materials* 12.10 (2003). Proceedings of the 8th International Conference on New Diamond Science and Technology (ICNDST-8), pp. 1976–1983. ISSN: 0925-9635. DOI: 10.1016/S0925-9635(03)00262-0.

[8] Eloïse Gaillou and George R. Rossman. “Color in Natural Diamonds: The Beauty of Defects”. In: *Rocks & Minerals* 89.1 (Dec. 2013), pp. 66–75. DOI: 10.1080/00357529.2014.842839.

[9] Sally Eaton-Magaña et al. “Natural-Color Pink, Purple, Red, and Brown Diamonds: Band of Many Colors”. In: *Gems & Gemology* 54 (Feb. 2019). DOI: 10.5741/GEMS.54.4.352.

[10] William Henry Bragg and William Lawrence Bragg. “The structure of the diamond”. In: *Proceedings of the Royal Society of London. Series A, Containing Papers of a Mathematical and Physical Character* 89 (1913), pp. 277–291. DOI: 10.1098/rspa.1913.0084.

[11] V. Rajendran and A. Marikani. *Materials science*. Core engineering series. New Delhi: Tata McGraw-Hill Pub., 2004. ISBN: 0070583692; 9780070583696. DOI: 10.1098/rspa.1913.0084.

[12] Koji Kobashi. *Diamond Films: Chemical Vapor Deposition for Oriented and Heteroepitaxial Growth*. Discusses the most advanced techniques for diamond growth and assists diamond researchers in deciding on the most suitable process conditions. Elsevier, Dec. 2005, p. 336. URL: https://books.google.nl/books?vid=ISBN9780080447230.

[13] Alix Gicquel et al. "CVD diamond films: from growth to applications". In: *Current Applied Physics* 1.6 (2001), pp. 479–496. ISSN: 1567-1739. DOI: https://doi.org/10.1016/S1567-1739(01)00061-X.

[14] D Tabor. "Mohs's Hardness Scale - A Physical Interpretation". In: *Proceedings of the Physical Society. Section B* 67 (Dec. 2002), p. 249. DOI: 10.1088/0370-1301/67/3/310.

[15] Mircea Ionut Petrescu and M Fecioru. "The interatomic spacing, a key crystallochemical factor for the theoretical hardness of diamond and graphite". In: *UPB Scientific Bulletin, Series B: Chemistry and Materials Science* 64 (Jan. 2002), pp. 49–58. URL: https://www.researchgate.net/publication/261878263_The_interatomic_spacing_a_key_crystallo-chemical_factor_for_the_theoretical_hardness_of_diamond_and_graphite.

[16] Edward H. Kraus and Chester B. Slawson. "Variation of hardness in the diamond1". In: *American Mineralogist* 24.11 (Nov. 1939), pp. 661–676. ISSN: 0003-004X. eprint: https://pubs.geoscienceworld.org/msa/ammin/article-pdf/24/11/661/4233194/am-1939-661.pdf.

[17] C.A. Brookes and E.J. Brookes. "Diamond in perspective: a review of mechanical properties of natural diamond". In: *Diamond and Related Materials* 1.1 (1991), pp. 13–17. ISSN: 0925-9635. DOI: https://doi.org/10.1016/0925-9635(91)90006-V.

[18] N. Savvides and T.J. Bell. "Hardness and elastic modulus of diamond and diamond-like carbon films". In: *Thin Solid Films* 228.1 (1993), pp. 289–292. ISSN: 0040-6090. DOI: https://doi.org/10.1016/0040-6090(93)90618-Y.

[19] Yuan Hsu, Edison Yang, and Mochihiro Shimizu. "Surface treatment to reduce process defects". In: *Optical and EUV Nanolithography XXXVI*. Ed. by Anna Lio. Vol. 12494. International Society for Optics and Photonics. SPIE, 2023, 124941A. DOI: 10.1117/12.2646601.

[20] W. Zhu. "Defects in Diamond". In: *Diamond: Electronic Properties and Applications*. Ed. by Lawrence S. Pan and Don R. Kania. Boston, MA: Springer US, 1995, pp. 175–239. ISBN: 978-1-4615-2257-7. DOI: 10.1007/978-1-4615-2257-7_5.

[21] J.W. Steeds et al. "On the nature of grain boundary defects in high quality CVD diamond films and their influence on physical properties". In: *Diamond and Related Materials* 8.6 (1999), pp. 996–1005. ISSN: 0925-9635. DOI: https://doi.org/10.1016/S0925-9635(98)00425-7.

[22] Jian Han, Spencer L. Thomas, and David J. Srolovitz. "Grain-boundary kinetics: A unified approach". In: *Progress in Materials Science* 98 (2018), pp. 386–476. ISSN: 0079-6425. DOI: https://doi.org/10.1016/j.pmatsci.2018.05.004.

[23] S. Dannefaer. "Defects in diamond". In: *physica status solidi c* 4.10 (2007), pp. 3605–3613. DOI: https://doi.org/10.1002/pssc.200675790.

[24] U Bangert et al. "Vacancy clusters, dislocations and brown colouration in diamond". In: *Journal of Physics: Condensed Matter* 21.36 (Aug. 2009), p. 364208. DOI: 10.1088/0953-8984/21/36/364208.

[25] Simone Salustro et al. "Comparison between cluster and supercell approaches: the case of defects in diamond". In: *Theoretical Chemistry Accounts* 136.4 (2017), p. 42. ISSN: 1432-2234. DOI: 10.1007/s00214-017-2071-5.

[26] Alan T. Collins. "The characterisation of point defects in diamond by luminescence spectroscopy". In: *Diamond and Related Materials* 1.5 (1992). Proceedings of the Second European Conference on Diamond, Diamond-like and Related Coatings, pp. 457–469. ISSN: 0925-9635. DOI: https://doi.org/10.1016/0925-9635(92)90146-F.

[27] A. Mainwood. "Point Defects in Natural and Synthetic Diamond: What They Can Tell Us about CVD Diamond". In: *physica status solidi (a)* 172.1 (1999), pp. 25–35. DOI: https://doi.org/10.1002/(SICI)1521-396X(199903)172:1<25::AID-PSSA25>3.0.CO;2-9.

[28] Chloe Victoria Peaker. "First principles study of point defects in diamond". PhD thesis. Newcastle University, 2018. URL: http://theses.ncl.ac.uk/jspui/handle/10443/4224.

[29] Aldona Mzyk et al. "Diamond Color Centers in Diamonds for Chemical and Biochemical Analysis and Visualization". In: *Analytical Chemistry* 94.1 (2022). PMID: 34841868, pp. 225–249. DOI: 10.1021/acs.analchem.1c04536.

[30] Takayuki Iwasaki et al. "Tin-Vacancy Quantum Emitters in Diamond". In: *Phys. Rev. Lett.* 119 (25 Dec. 2017), p. 253601. DOI: 10.1103/PhysRevLett.119.253601.

[31] Matthew E. Trusheim et al. "Transform-Limited Photons From a Coherent Tin-Vacancy Spin in Diamond". In: *Phys. Rev. Lett.* 124 (2 Jan. 2020), p. 023602. DOI: 10.1103/PhysRevLett.124.023602.

[32] Shahriar Aghaeimeibodi et al. "Electrical Tuning of Tin-Vacancy Centers in Diamond". In: *Phys. Rev. Appl.* 15 (6 June 2021), p. 064010. DOI: 10.1103/PhysRevApplied.15.064010.

[33] Christian Hepp et al. "Electronic Structure of the Silicon Vacancy Color Center in Diamond". In: *Phys. Rev. Lett.* 112 (3 Jan. 2014), p. 036405. DOI: 10.1103/PhysRevLett.112.036405.

[34] Benjamin Pingault et al. "Coherent control of the silicon-vacancy spin in diamond". In: *Nature Communications* 8.1 (2017). ISSN: 2041-1723. DOI: 10.1038/ncomms15579.

[35] C. T. Nguyen et al. “An integrated nanophotonic quantum register based on silicon-vacancy spins in diamond”. In: *Phys. Rev. B* 100 (16 Oct. 2019), p. 165428. DOI: 10.1103/PhysRevB.100.165428.

[36] Takayuki Iwasaki et al. “Germanium-Vacancy Single Color Centers in Diamond”. In: *Scientific Reports* 5.1 (2015), p. 12882. ISSN: 2045-2322. DOI: 10.1038/srep12882.

[37] Petr Siyushev et al. “Optical and microwave control of germanium-vacancy center spins in diamond”. In: *Phys. Rev. B* 96 (8 Aug. 2017), p. 081201. DOI: 10.1103/PhysRevB.96.081201.

[38] Matthew E. Trusheim et al. “Lead-related quantum emitters in diamond”. In: *Phys. Rev. B* 99 (7 Feb. 2019), p. 075430. DOI: 10.1103/PhysRevB.99.075430.

[39] Peng Wang et al. “Low-Temperature Spectroscopic Investigation of Lead-Vacancy Centers in Diamond Fabricated by High-Pressure and High-Temperature Treatment”. In: *ACS Photonics* 8.10 (2021), pp. 2947–2954. DOI: 10.1021/acsphotonics.1c00840.

[40] L Du Preez. “Electron paramagnetic resonance and optical investigations of defect centres in diamond”. In: (1965). URL: https://wiredspace.wits.ac.za/server/api/core/bitstreams/974855d1-6b1f-4467-8264-eb40c946f716/content.

[41] G. Davies and M. F. Hamer. “Optical Studies of the 1.945 eV Vibronic Band in Diamond”. In: *Proceedings of the Royal Society of London. Series A, Mathematical and Physical Sciences* 348.1653 (1976), pp. 285–298. DOI: 10.1098/rspa.1976.0039.

[42] J. H. N. Loubser and J. A. van Wyk. “Electron spin resonance in the study of diamond”. In: *Reports on Progress in Physics* 41.8 (Aug. 1978), p. 1201. DOI: 10.1088/0034-4885/41/8/002.

[43] M. W. Doherty et al. “Theory of the ground-state spin of the NV^- center in diamond”. In: *Phys. Rev. B* 85 (20 May 2012), p. 205203. DOI: 10.1103/PhysRevB.85.205203.

[44] Anna Maria Ferrari et al. “The NV0 defects in diamond: A quantum mechanical characterization through its vibrational and Electron Paramagnetic Resonance spectroscopies”. In: *Journal of Physics and Chemistry of Solids* 160 (2022), p. 110304. ISSN: 0022-3697. DOI: https://doi.org/10.1016/j.jpcs.2021.110304.

[45] Wei Li et al. “Fluorescent Nanoparticles for Super-Resolution Imaging”. In: *Chemical reviews* 122 (June 2022). DOI: 10.1021/acs.chemrev.2c00050.

[46] Elisabeth Fraczek et al. “Laser spectroscopy of NV- and NV0 colour centres in synthetic diamond”. In: *Opt. Mater. Express* 7.7 (July 2017), pp. 2571–2585. DOI: 10.1364/OME.7.002571.

[47] Isabel Cardoso Barbosa, Jonas Gutsche, and Artur Widera. “Impact of charge conversion on NV-center relaxometry”. In: *Phys. Rev. B* 108 (7 Aug. 2023), p. 075411. DOI: 10.1103/PhysRevB.108.075411.

[48] J. R. Maze et al. “Properties of nitrogen-vacancy centers in diamond: the group theoretic approach”. In: *New Journal of Physics* 13.2 (2011). ISSN: 1367-2630. DOI: 10.1088/1367-2630/13/2/025025.

[49] Jack Simons. *Point Group Symmetry*. Apr. 2021. URL: https://chem.libretexts.org/Bookshelves/Physical_and_Theoretical_Chemistry_Textbook_Maps/Advanced_Theoretical_Chemistry_(Simons)/.

[50] Victor Acosta and Philip Hemmer. “Nitrogen-vacancy centers: Physics and applications”. In: *MRS Bulletin* 38.2 (2013), pp. 127–130. DOI: 10.1557/mrs.2013.18.

[51] N. B. Manson, J. P. Harrison, and M. J. Sellars. “Nitrogen-vacancy center in diamond: Model of the electronic structure and associated dynamics”. In: *Phys. Rev. B* 74 (10 Sept. 2006), p. 104303. DOI: 10.1103/PhysRevB.74.104303.

[52] Marcus W. Doherty et al. “The nitrogen-vacancy colour centre in diamond”. In: *Physics Reports* 528.1 (2013), pp. 1–45. DOI: 10.1016/j.physrep.2013.02.001.

[53] Aleksei V. Ivanov et al. “Electronic excitations of the charged nitrogen-vacancy center in diamond obtained using time-independent variational density functional calculations”. In: *SciPost Phys.* 15 (2023), p. 009. DOI: 10.21468/SciPostPhys.15.1.009.

[54] Neil Manson et al. *Optically induced spin polarisation of the NV- centre in diamond: role of electron-vibration interaction*. 2010. arXiv: 1011.2840 [cond-mat.mtrl-sci].

[55] Dinesh K. Bommidi and Andrea D. Pickel. “Temperature-dependent excited state lifetimes of nitrogen vacancy centers in individual nanodiamonds”. In: *Applied Physics Letters* 119.25 (Dec. 2021), p. 254103. ISSN: 0003-6951. DOI: 10.1063/5.0072357.

[56] Christian Laube et al. “Fluorescence Lifetime Control of Nitrogen Vacancy Centers in Nanodiamonds for Long-Term Information Storage”. In: *ACS Nano* 17.16 (2023). PMID: 37440601, pp. 15401–15410. DOI: 10.1021/acsnano.3c00328.

[57] Ryan Beams et al. “Nanoscale Fluorescence Lifetime Imaging of an Optical Antenna with a Single Diamond NV Center”. In: *Nano Letters* 13.8 (2013). PMID: 23815462, pp. 3807–3811. DOI: 10.1021/nl401791v.

[58] F. Jelezko and J. Wrachtrup. “Single defect centres in diamond: A review”. In: *physica status solidi (a)* 203.13 (2006), pp. 3207–3225. DOI: https://doi.org/10.1002/pssa.200671403.

[59] Gopalakrishnan Balasubramanian et al. “Ultralong spin coherence time in isotopically engineered diamond”. In: *Nature Materials* 8.5 (2009), pp. 383–387. ISSN: 1476-4660. DOI: 10.1038/nmat2420.

[60] T. de Guillebon et al. “Temperature dependence of the longitudinal spin relaxation time T_1 of single nitrogen-vacancy centers in nanodiamonds”. In: *Phys. Rev. B* 102 (16 Oct. 2020), p. 165427. DOI: 10.1103/PhysRevB.102.165427.

[61] A. Jarmola et al. “Longitudinal spin-relaxation in nitrogen-vacancy centers in electron irradiated diamond”. In: *Applied Physics Letters* 107.24 (Dec. 2015), p. 242403. ISSN: 0003-6951. DOI: 10.1063/1.4937489.

[62] A. Norambuena et al. “Spin-lattice relaxation of individual solid-state spins”. In: *Phys. Rev. B* 97 (9 Mar. 2018), p. 094304. DOI: 10.1103/PhysRevB.97.094304.

[63] J. -P. Tetienne et al. *Magnetic-field-dependent photodynamics of single NV defects in diamond: Application to qualitative all-optical magnetic imaging*. 2012. arXiv: 1206.1201 [cond-mat.mes-hall].

[64] T. Yamamoto et al. “Extending spin coherence times of diamond qubits by high-temperature annealing”. In: *Phys. Rev. B* 88 (7 Aug. 2013), p. 075206. DOI: 10.1103/PhysRevB.88.075206.

[65] N. Mizuochi et al. “Coherence of single spins coupled to a nuclear spin bath of varying density”. In: *Phys. Rev. B* 80 (4 July 2009), p. 041201. DOI: 10.1103/PhysRevB.80.041201.

[66] Erik Bauch et al. “Decoherence of ensembles of nitrogen-vacancy centers in diamond”. In: *Phys. Rev. B* 102 (13 Oct. 2020), p. 134210. DOI: 10.1103/PhysRevB.102.134210.

[67] G. de Lange et al. “Universal Dynamical Decoupling of a Single Solid-State Spin from a Spin Bath”. In: *Science* 330.6000 (2010), pp. 60–63. DOI: 10.1126/science.1192739.

[68] N. Bar-Gill et al. “Solid-state electronic spin coherence time approaching one second”. In: *Nature Communications* 4.1 (2013), p. 1743. ISSN: 2041-1723. DOI: 10.1038/ncomms2771.

[69] V. V. Dobrovitski et al. “Decay of Rabi Oscillations by Dipolar-Coupled Dynamical Spin Environments”. In: *Phys. Rev. Lett.* 102 (23 June 2009), p. 237601. DOI: 10.1103/PhysRevLett.102.237601.

[70] Erik Bauch et al. “Ultralong Dephasing Times in Solid-State Spin Ensembles via Quantum Control”. In: *Phys. Rev. X* 8 (3 July 2018), p. 031025. DOI: 10.1103/PhysRevX.8.031025.

[71] L. Childress et al. “Coherent Dynamics of Coupled Electron and Nuclear Spin Qubits in Diamond”. In: *Science* 314.5797 (2006), pp. 281–285. DOI: 10.1126/science.1131871.

[72] L Rondin et al. “Magnetometry with nitrogen-vacancy defects in diamond”. In: *Reports on Progress in Physics* 77.5 (May 2014), p. 056503. ISSN: 1361-6633. DOI: 10.1088/0034-4885/77/5/056503.

[73] H. Hanzawa et al. “Zeeman effect on the zero-phonon line of the NV center in synthetic diamond”. In: *Physica B: Condensed Matter* 184.1 (1993), pp. 137–140. ISSN: 0921-4526. DOI: https://doi.org/10.1016/0921-4526(93)90337-6.

[74] S. Felton et al. “Hyperfine interaction in the ground state of the negatively charged nitrogen vacancy center in diamond”. In: *Phys. Rev. B* 79 (7 Feb. 2009), p. 075203. DOI: 10.1103/PhysRevB.79.075203.

[75] Benjamin Smeltzer, Lilian Childress, and Adam Gali. “13C hyperfine interactions in the nitrogen-vacancy centre in diamond”. In: *New Journal of Physics* 13.2 (Feb. 2011), p. 025021. DOI: 10.1088/1367-2630/13/2/025021.

[76] Takuya Isogawa, Yuichiro Matsuzaki, and Junko Ishi-Hayase. "Vector dc magnetic-field sensing with a reference microwave field using perfectly aligned nitrogen-vacancy centers in diamond". In: *Phys. Rev. A* 107 (6 June 2023), p. 062423. DOI: 10.1103/PhysRevA.107.062423.

[77] Maxime Perdriat et al. "Spin-Mechanics with Nitrogen-Vacancy Centers and Trapped Particles". In: *Micromachines* 12.6 (2021). ISSN: 2072-666X. DOI: 10.3390/mi12060651.

[78] ZhangQi Yin, Nan Zhao, and TongCang Li. "Hybrid opto-mechanical systems with nitrogen-vacancy centers". In: *Science China Physics, Mechanics & Astronomy* 58.5 (Feb. 2015), pp. 1–12. ISSN: 1869-1927. DOI: 10.1007/s11433-015-5651-1.

[79] Gerg ő Thiering and Adam Gali. "Theory of the optical spin-polarization loop of the nitrogen-vacancy center in diamond". In: *Phys. Rev. B* 98 (8 Aug. 2018), p. 085207. DOI: 10.1103/PhysRevB.98.085207.

[80] M. L. Goldman et al. "Phonon-Induced Population Dynamics and Intersystem Crossing in Nitrogen-Vacancy Centers". In: *Phys. Rev. Lett.* 114 (14 Apr. 2015), p. 145502. DOI: 10.1103/PhysRevLett.114.145502.

[81] M. L. Goldman et al. "State-selective intersystem crossing in nitrogen-vacancy centers". In: *Phys. Rev. B* 91 (16 Apr. 2015), p. 165201. DOI: 10.1103/PhysRevB.91.165201.

[82] U. Wahl et al. "Direct Structural Identification and Quantification of the Split-Vacancy Configuration for Implanted Sn in Diamond". In: *Phys. Rev. Lett.* 125 (4 July 2020), p. 045301. DOI: 10.1103/PhysRevLett.125.045301.

[83] Tobias Lühmann et al. "Charge-State Tuning of Single SnV Centers in Diamond". In: *ACS Photonics* 7.12 (2020). doi: 10.1021/acsphotonics.0c01123, pp. 3376–3385. DOI: 10.1021/acsphotonics.0c01123.

[84] Michael Tinkham. *Group theory and quantum mechanics*. Courier Corporation, 2003. URL: https://books.google.gr/books/about/Group_Theory_and_Quantum_Mechanics.html?id=xdwoAwAAQBAJ&redir_esc=y.

[85] Xinghan Guo et al. "Microwave-Based Quantum Control and Coherence Protection of Tin-Vacancy Spin Qubits in a Strain-Tuned Diamond-Membrane Heterostructure". In: *Phys. Rev. X* 13 (4 Nov. 2023), p. 041037. DOI: 10.1103/PhysRevX.13.041037.

[86] Romain Debroux et al. "Quantum Control of the Tin-Vacancy Spin Qubit in Diamond". In: *Phys. Rev. X* 11 (4 Nov. 2021), p. 041041. DOI: 10.1103/PhysRevX.11.041041.

[87] Eric I. Rosenthal et al. "Microwave Spin Control of a Tin-Vacancy Qubit in Diamond". In: *Phys. Rev. X* 13 (3 Aug. 2023), p. 031022. DOI: 10.1103/PhysRevX.13.031022.

[88] Ioannis Karapatzakis et al. *Microwave Control of the Tin-Vacancy Spin Qubit in Diamond with a Superconducting Waveguide*. 2024. arXiv: 2403.00521 [quant-ph].

[89] Johannes Görlitz et al. “Coherence of a charge stabilised tin-vacancy spin in diamond”. In: *npj Quantum Information* 8.1 (Apr. 2022). ISSN: 2056-6387. DOI: 10.1038/s41534-022-00552-0.

[90] Alison E. Rugar et al. “Quantum Photonic Interface for Tin-Vacancy Centers in Diamond”. In: *Phys. Rev. X* 11 (3 July 2021), p. 031021. DOI: 10.1103/PhysRevX.11.031021.

[91] Isaac B. W. Harris and Dirk Englund. “Coherence of group-IV color centers”. In: *Phys. Rev. B* 109 (8 Feb. 2024), p. 085414. DOI: 10.1103/PhysRevB.109.085414.

[92] Johannes Görlitz et al. “Spectroscopic investigations of negatively charged tin-vacancy centres in diamond”. In: *New Journal of Physics* 22.1 (2020), p. 013048. DOI: 10.1088/1367-2630/ab6631.

[93] N.B. Manson and J.P. Harrison. “Photo-ionization of the nitrogen-vacancy center in diamond”. In: *Diamond and Related Materials* 14.10 (2005), pp. 1705–1710. ISSN: 0925-9635. DOI: https://doi.org/10.1016/j.diamond.2005.06.027.

[94] G. Waldherr et al. “Dark States of Single Nitrogen-Vacancy Centers in Diamond Unraveled by Single Shot NMR”. In: *Phys. Rev. Lett.* 106 (15 Apr. 2011), p. 157601. DOI: 10.1103/PhysRevLett.106.157601.

[95] A. Dréau et al. “Avoiding power broadening in optically detected magnetic resonance of single NV defects for enhanced dc magnetic field sensitivity”. In: *Physical Review B* 84.19 (Nov. 2011). ISSN: 1550-235X. DOI: 10.1103/physrevb.84.195204.

[96] Y Matsuzaki et al. “Optically detected magnetic resonance of high-density ensemble of NV- centers in diamond”. In: *Journal of Physics: Condensed Matter* 28.27 (May 2016), p. 275302. DOI: 10.1088/0953-8984/28/27/275302.

[97] Zichuan Zhang et al. “Design of NV Centers Integrated Magnetometer and High-Resolution Output Module Based on the ODMR System”. In: *IEEE Sensors Journal* 23.6 (2023), pp. 6150–6155. DOI: 10.1109/JSEN.2023.3240885.

[98] Soya Saijo et al. “AC magnetic field sensing using continuous-wave optically detected magnetic resonance of nitrogen-vacancy centers in diamond”. In: *Applied Physics Letters* 113.8 (Aug. 2018), p. 082405. ISSN: 0003-6951. DOI: 10.1063/1.5024401.

[99] John F. Barry et al. “Sensitivity optimization for NV-diamond magnetometry”. In: *Rev. Mod. Phys.* 92 (1 Mar. 2020), p. 015004. DOI: 10.1103/RevModPhys.92.015004.

[100] Andreas F. L. Poulsen et al. *Investigation and comparison of measurement schemes in the low frequency biosensing regime using solid-state defect centers*. 2021. arXiv: 2109.13028 [quant-ph].

[101] Vitaly I. Konov, Taras V. Kononenko, and Vitali V. Kononenko. “Laser Micro- and Nanoprocessing of Diamond Materials”. In: *Optical Engineering of Diamond*. John Wiley & Sons, Ltd, 2013. Chap. 12, pp. 385–443. ISBN: 9783527648603. DOI: https://doi.org/10.1002/9783527648603.ch12.

[102] Newport Corporation. *Introduction to Waveplates*. URL: https://www.newport.com/n/introduction-to-waveplates.

[103] SPIE - The International Society for Optics and Photonics. *Malus's Law - Optipedia*. URL: https://spie-org.tudelft.idm.oclc.org/publications/spie-publication-resources/optipedia-free-optics-information/fg05_p03_maluss_law#_=_.

[104] Zhenxian Fan et al. "The Optimization of Microwave Field Characteristics for ODMR Measurement of Nitrogen-Vacancy Centers in Diamond". In: *Photonics* 11.5 (2024). ISSN: 2304-6732. DOI: 10.3390/photonics11050436.

[105] Oliver Roman Opaluch et al. "Optimized Planar Microwave Antenna for Nitrogen Vacancy Center Based Sensing Applications". In: *Nanomaterials* 11.8 (2021). ISSN: 2079-4991. DOI: 10.3390/nano11082108.

[106] Li Qin et al. "Near-field microwave radiation function on spin assembly of nitrogen vacancy centers in diamond with copper wire and ring microstrip antennas". In: *Japanese Journal of Applied Physics* 57.7 (June 2018), p. 072201. DOI: 10.7567/JJAP.57.072201.

[107] I. V. Zhukov, S. V. Anishchik, and Yu N. Molin. "ODMR Spectroscopy of NV^- Centers in Diamond Under High MW Power". In: *Applied Magnetic Resonance* 48.11 (2017), pp. 1461–1469. ISSN: 1613-7507. DOI: 10.1007/s00723-017-0933-6.

[108] G. Kucsko et al. "Nanometre-scale thermometry in a living cell". In: *Nature* 500.7460 (2013), pp. 54–58. ISSN: 1476-4687. DOI: 10.1038/nature12373.

[109] Maabur Sow et al. "High-throughput nitrogen-vacancy center imaging for nanodiamond photophysical characterization and pH nanosensing". In: *Nanoscale* 12 (42 2020), pp. 21821–21831. DOI: 10.1039/D0NR05931E.

[110] Anubhav Sinha. "Development of a platform for sensing cellular electrical activity using diamond nitrogen-vacancy centers". Ph.D. Thesis. Cambridge, MA: Massachusetts Institute of Technology, 2015. URL: https://dspace.mit.edu/handle/1721.1/106445.

[111] Metin Kayci et al. "Multiplexed sensing of biomolecules with optically detected magnetic resonance of nitrogen-vacancy centers in diamond". In: *Proceedings of the National Academy of Sciences of the United States of America* 118.51 (2021), pp. 1–8. ISSN: 00278424, 10916490. URL: https://www.jstor.org/stable/27117509.

[112] Martina Barbiero et al. "Nanoscale magnetic imaging enabled by nitrogen vacancy centres in nanodiamonds labelled by iron–oxide nanoparticles". In: *Nanoscale* 12 (16 2020), pp. 8847–8857. DOI: 10.1039/C9NR10701K.

[113] Nazanin Mosavian et al. "Super-Resolution Diamond Magnetic Microscopy of Superparamagnetic Nanoparticles". In: *ACS Nano* 18.8 (Feb. 2024), pp. 6523–6532. ISSN: 1936-086X. DOI: 10.1021/acsnano.3c12283.

[114] J. Yuan et al. "The Scattered Twelve Tribes of HEK293". In: *Biomedicine and Pharmacotherapy Journal* 11.2 (2018), pp. 621–625. DOI: 10.13005/bpj/1443.

[115] *BioNumbers*. URL: https://bionumbers.hms.harvard.edu/bionumber.aspx?id=108893.

[116] *HEK293 Cells: Background, Applications, Protocols, and More*. URL: https://www.synthego.com/hek293.

[117] Michael Barrow et al. "Tailoring the surface charge of dextran-based polymer coated SPIONs for modulated stem cell uptake and MRI contrast". In: *Biomater. Sci.* 3 (4 2015), pp. 608–616. DOI: 10.1039/C5BM00011D.

[118] Shelby Klomp et al. "Size-Dependent Crystalline and Magnetic Properties of 5–100 nm Fe_3O_4 Nanoparticles: Superparamagnetism, Verwey Transition, and FeO–Fe_3O_4 Core–Shell Formation". In: *IEEE Transactions on Magnetics* 56.11 (2020), pp. 1–9. DOI: 10.1109/TMAG.2020.3018154.

[119] Tobias Köhler et al. "Mechanism of magnetization reduction in iron oxide nanoparticles". In: *Nanoscale* 13 (14 2021), pp. 6965–6976. DOI: 10.1039/D0NR08615K.

[120] Hossein Asnaashari Eivari. "Getting saturation magnetization of superparamagnetic nanoparticles more accurately from room-temperature magnetization curve". In: *Journal of Nanoparticle Research* 25.7 (2023), p. 141. ISSN: 1572-896X. DOI: 10.1007/s11051-023-05756-9.

[121] L. Maldonado-Camargo, M. Unni, and C. Rinaldi. "Magnetic Characterization of Iron Oxide Nanoparticles for Biomedical Applications". In: *Methods Mol Biol* 1570 (2017), pp. 47–71. ISSN: 1064-3745 (Print). DOI: 10.1007/978-1-4939-6840-4_4.

[122] P. Maletinsky et al. "A robust scanning diamond sensor for nanoscale imaging with single nitrogen-vacancy centres". In: *Nature Nanotechnology* 7.5 (2012), pp. 320–324. ISSN: 1748-3395. DOI: 10.1038/nnano.2012.50.

[123] D. Le Sage et al. "Optical magnetic imaging of living cells". In: *Nature* 496.7446 (2013), pp. 486–489. ISSN: 1476-4687. DOI: 10.1038/nature12072.

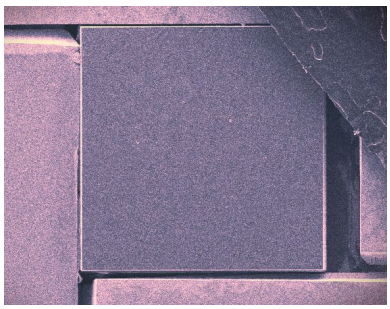
[124] H. Wei et al. "Superparamagnetic Iron Oxide Nanoparticles: Cytotoxicity, Metabolism, and Cellular Behavior in Biomedicine Applications". In: *International Journal of Nanomedicine* 16 (2021), pp. 6097–6113. DOI: 10.2147/IJN.S321984.

[125] E. Kwee et al. "Practical application of microsphere samples for benchmarking a quantitative phase imaging system". In: *Cytometry A* 99.10 (2021), pp. 1022–1032. ISSN: 1552-4922 (Print). DOI: 10.1002/cyto.a.24291.

3

FABRICATION & ION IMPLANTATION OF NV AND SNV CENTERS

This chapter presents the simulation, fabrication, and post-processing techniques used for the generation of nitrogen-vacancy (NV) and tin-vacancy (SnV) centers in diamond via ion implantation. Emphasis is placed on the preparation of high-purity (Type IIa) single-crystal diamond substrates, resist-based lithographic patterning, and the use of focused ion beam (FIB) and broad beam implantation methods for deterministic color center creation. Extensive simulations using SRIM/TRIM were performed to optimize implantation parameters, such as ion energy, depth profiles, and mask thickness, for both NV and SnV centers. These guided the fabrication of nanometer-scale implantation masks and defined dose windows for shallow and deep implantation. The cleanroom processes for resist spin coating, lithography, and sample preparation are detailed, with focus on achieving nanometer spatial resolution. Post-implantation overgrowth and annealing strategies, including both furnace and femtosecond laser techniques, are also investigated for vacancy activation and lattice recovery.



Parts of this chapter have been submitted for publication to TBD **TBD**, TBD (2025) https://doi.org/TBD [**X**].

3.1. INTRODUCTION TO COLOR CENTER FABRICATION

Fabrication of good quality color centers is pivotal for any quantum-based application, be it quantum computing or quantum sensing. Multiple steps need to be followed in order for nitrogen-vacancy (NV), tin-vacancy (SnV) or other types of color centers to be generated in a controlled and deterministic manner, both as ensembles or single emitters. First, the diamond itself needs to be fabricated, most often via chemical vapor deposition (CVD) or high-pressure high-temperature (HPHT) methods. The diamond is then cut into thin rectangular slabs, along the crystallographic axis that is suitable for a given experiment. afterward, it is processed inside a cleanroom facility, where it is cleaned, prepared, and potentially patterned for lithography, according to the design and type of emitters desired. Following this, it undergoes ion implantation. A number of ion implantation methods are investigated as part of this chapter. Then, depending on the type of color center implanted and the application, an overgrowth step may be included. Finally, annealing takes place, in order to mobilize the vacancies and result in color center generation.

3.1.1. A BRIEF RECAPITULATION OF DIAMOND TYPES

Numerous characteristics make up diamond's composition. These range from classification based on its impurity concentration, to its overall purity levels and the growth methods that are linked to that, as well as its crystallinity, all of which are briefly described below.

As mentioned earlier in subsection 2.1.1, diamonds can be categorized into four primary types. Type Ia diamonds have a high concentration of aggregated nitrogen (N) impurities, while Type Ib diamonds contain high amounts of N in mostly non-aggregated form. On the other hand, Type IIa diamonds contain very low amounts of nitrogen (<5 ppb) and are labeled as "electronic grade diamonds". Type IIb diamonds also have a low concentration of N, but significant boron (B) impurities instead.

Non-electronic grade diamonds are often used in ODMR experiments, most often in sensing, due to them having high NV center densities and not requiring extensive processing. The nitrogen concentration can range from few ppm up to hundreds of ppm, while natural conversion to NV centers is in the ppb range. However, quantum computing or quantum information applications need to utilize single color centers in order to create entanglement and have precise control of the qubit spin states. In these cases, electronic grade (IIa) diamonds are used, which are consequently processed in the cleanroom and implanted with ions, so that single emitters can be generated. Furthermore, single-crystal diamond is typically preferred in quantum applications, since their lack of grain boundaries (and absence of additional impurities) results in fewer decoherence factors, and, in turn, promotes enhanced coherence times and more precise control [1, 2, 3].

3.2. DIAMOND GROWTH METHODS

3.2.1. CHEMICAL VAPOR DEPOSITION (CVD)

The CVD diamond growth process is one of the most popular and typical diamond synthesis methods. It consists of several stages, which are hereby summarized. First, the substrate on which nucleation will take place is cleaned, chemically treated and prepared. This substrate can be a high-quality, high-purity, single-crystal diamond, on which epitaxial growth may be done, to achieve crystal structure similar to the substrate. It may also be a non-diamond substrate (such as silicon, ceramics, etc.), which is then treated to enhance nucleation density, often along with diamond powder, nanoparticles or a diamond seed layer deposited on top of it. This method is usually used to produce dense continuous films or polycrystalline diamond substrates [4].

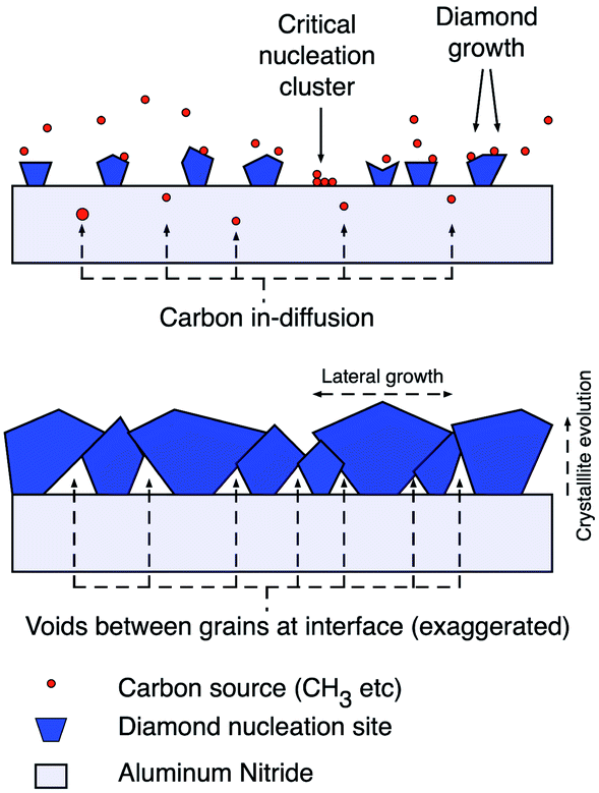


Figure 3.1: Schematic illustrating the diamond growth process at low seed density. In the early stages, diamond nucleates on the seeds while carbon also diffuses into the substrate. Image courtesy of Mandal *et al.* (2019) [5].

The substrate is then placed in a reaction chamber (see Figure 3.2), where a specific selection of gases provide the reactive species that are needed for diamond growth. Commonly used gases include a combination of hydrocarbon gases (usually methane - CH_4), which act as the carbon source, hydrogen (H_2) gas, which helps suppress and etch away graphite, argon (Ar) and helium (He) gases, which serve to stabilize and control the plasma energy during the reaction, and, less frequently, oxygen (O_2) gas, which also assists in removing excess carbon and controlling surface roughness. Finally, nitrogen (N_2) is often used, whenever higher impurity concentration is desired, instead of a high-purity substrate [2, 6, 7].

During the gas reaction phase, nucleation also takes place. The carbon source gas is

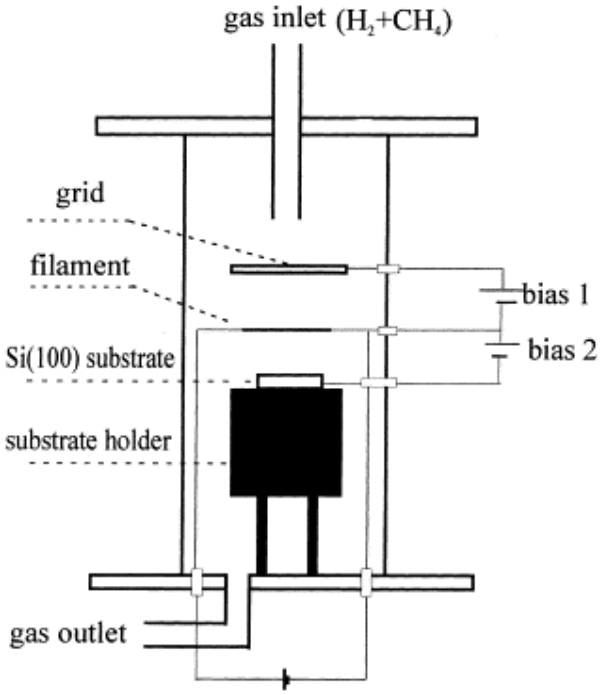


Figure 3.2: Schematic of the CVD reactor used by Zhou *et al.*, showing the double-biasing electrode configuration. Image courtesy of Zhou *et al.* (2000) [8].

responsible for deposition of carbon atoms on the substrate, while, in the meantime, hydrogen gas etches away any non-sp^3 carbon forms, promoting diamond growth. High - and controlled- nucleation density improves the quality and the uniformity of the grown film. After the nucleation sites have been well-established, diamond growth takes place (see Figure 3.1). During the growth process, careful and optimized manipulation of the gases and the pressure and temperature conditions within the reaction chamber is mandatory [2, 6, 7, 9].

3.2.2. HIGH-PRESSURE HIGH-TEMPERATURE (HPHT)

HPHT is another widely used diamond growth method (see Figure 3.3). It relies on the ability to turn carbon (most often pure graphite) into synthesized "man-made diamonds" [10]. HPHT diamonds are basically produced in a process that mimics the earth's natural diamond creation conditions.

First, a solvent metal, such as nickel (Ni), cobalt (Co), or iron (Fe) is added along with the carbon source into the reaction cell. Other elements may also be added, such as aluminum (Al), titanium (Ti), and others, in order to filter out the formation of unwanted compounds or remove excess nitrogen when high-purity diamonds are desired [11].

Next, extreme pressure is applied, in the order of GPa. Simultaneously, heating takes place, usually around ≈ 1300-1500 °C [12]. Lower or much higher (> 2300 °C) temperatures may also be used, depending on the target application and the desired type and concentration of impurities [11, 13]. The right balance between pressure and temperature needs to be determined for optimal diamond synthesis.

To aid the diamond growth process, diamond seeds are added to the reaction cell for homoepitaxial growth, acting as nucleation sites for the diamond to crystallize and build

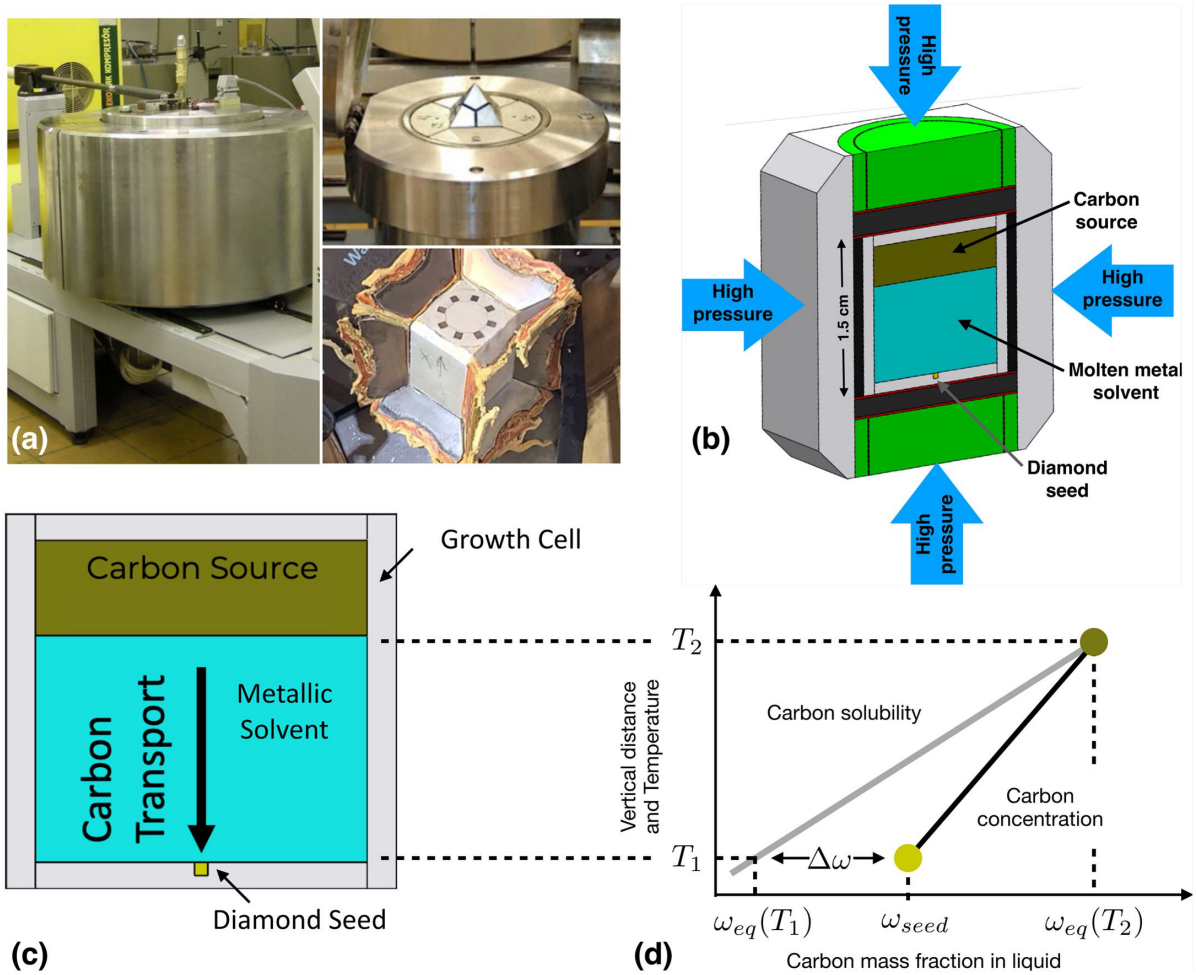


Figure 3.3: **(a)** Photo of a HPHT apparatus. **(b)** Cross-section of the growth cell, containing the carbon source, metallic solvent, and diamond seed. **(c)** Schematic of the growth cell illustrating carbon transport driven by a vertical temperature gradient. **(d)** The vertical temperature gradient lowers the equilibrium carbon solubility from top to bottom (gray line). Carbon dissolves at the source and diffuses downward (black line), increasing supersaturation and driving diamond growth on the seed. Image courtesy of Dossa *et al.* (2023) [12].

layers on [14]. Following growth, the system needs to be cooled down back to normal conditions, in a controlled manner [15].

While HPHT diamonds may be easier to fabricate and mass-produce, they often come with increased impurities, due to the metal solvents involved in the growth, or added strain, owing to the cooling process. In contrast, CVD-grown diamonds allow for better control over the impurities introduced and over the crystal orientation [3].

3.2.3. DIAMOND CUTTING & CRYSTALLOGRAPHIC PLANES

After the diamond has been synthesized, either by CVD or HPHT, it can then be cut into thinner substrates, along the desired crystallographic axis (see Figure 3.4). For HPHT-grown diamonds, cutting along the (111) plane is the easiest, since it has the lowest cleavage energy [16]. They are also often cut along the (100) plane, which is commonly used in quantum sensing applications with NV centers. CVD-grown diamonds may also be cut along the desired crystallographic plane, usually (100), (111) or (110) [17]. Using a diamond seed substrate with a specific crystallographic orientation facilitates the cut-

ting process, by making it easier to cut across the natural cleavage planes, in a safer and less destructive manner.

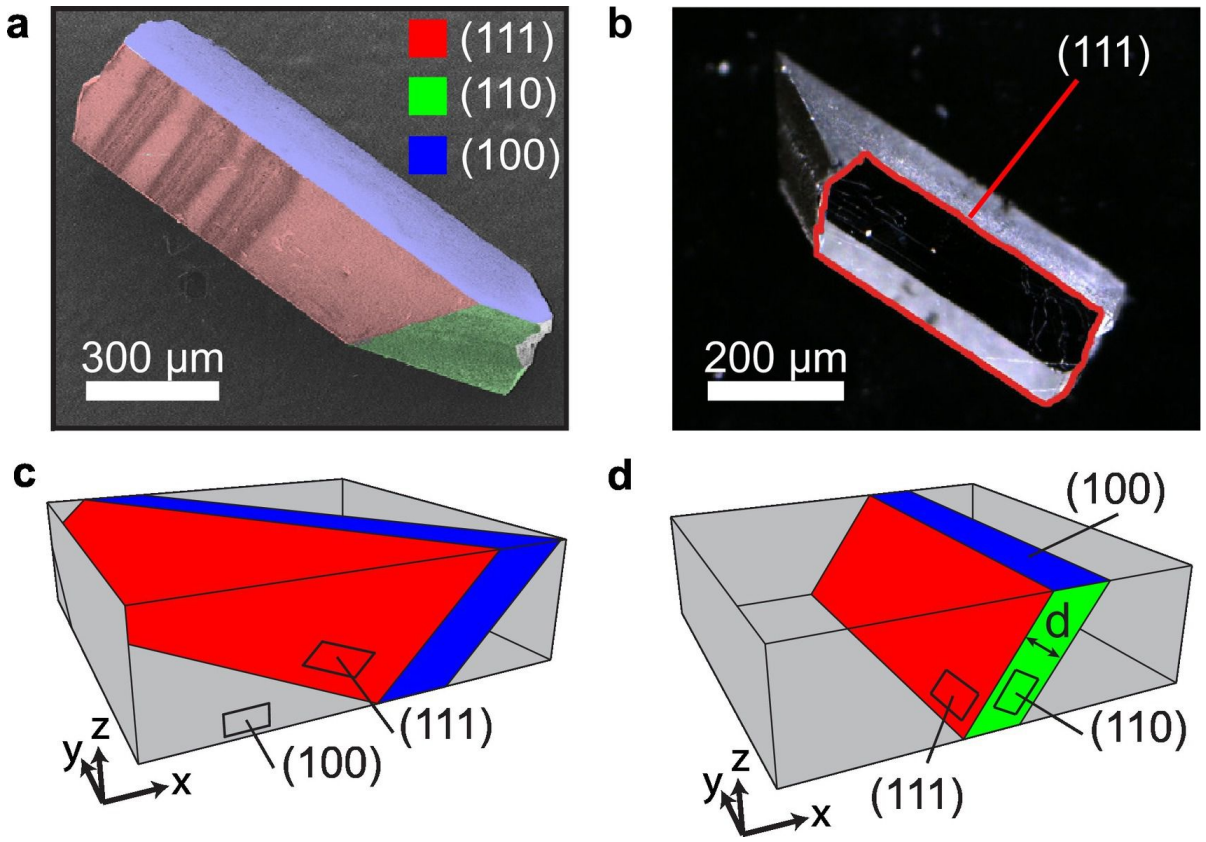


Figure 3.4: Laser-nucleated cleaving of single-crystal diamond. **(a)** SEM and **(b)** optical image of (111)-faced plates from a standard grade (100)-faced diamond. **(c)** and **(d)** illustrate the orientation of (111) plates from SG (100) and EG (110) substrates, respectively. Image courtesy of Parks *et al.* (2018) [18].

These crystallographic planes differ both in atomic arrangement and properties. Generally, (111) diamonds are harder to grow. Diamonds cut this way have the highest atomic density, making for a more compact arrangement. NV centers have four possible alignment orientations inside the diamond lattice, along each of the four [111] directions. However, (111) diamonds favor preferential alignment of the NV centers, uniformly along a singular direction, perpendicular to the (111) plane. This single-orientation NV alignment can be advantageous in cases where enhanced coherence properties and uniformity are desired [19]. On the contrary, (100) diamonds are much easier to fabricate, especially when aiming for ultra-pure, electronic grade substrates. They are less densely packed, while NV centers in them are randomly aligned along the [111] directions [20, 21]. Their fabrication consistency and stability make (100) substrates the most broadly available diamonds, with noteworthy applications in quantum technologies.

3.3. ION IMPLANTATION METHODS

The fabrication, cutting and polishing of the diamond itself is usually done by companies, which later supply the prepared substrates to universities and research facilities. The user obtains a few diamond substrates and, via multiple cleanroom processes, prepares them for ion implantation (outsourced as well most of the times). In this section, some of the most prominent ion implantation methods shall be discussed. Starting with broad beam implantation (see Figure 3.5), either for blanket implantation or mask ion implantation, and continuing with single ion implantation, which makes use of the focused ion beam (FIB) technique.

3.3.1. BROAD BEAM IMPLANTATION

Broad beam implantation, as the name suggests, is a method used to create a wide ion beam, in order to quickly and homogeneously implant ions over a large area of the target substrate. It consists of a few steps and typically takes place in a controlled, vacuum environment. First, an ion source is selected, depending on the type of dopant atoms desired. This is in the form of a gas, the atoms of which are ionized by high-energy electrons. The generated ions are then extracted and accelerated through an electric field that creates adjustable kinetic energy (usually in the keV to MeV range). These ions are shaped into a broad and uniform beam and filtered by a magnetic mass analyzer, which is able to separate the source ions from unwanted contaminants or other charged particles. The created ion beam has a certain current density, which controls the amount of ions that travel towards the target. By adjusting the current density, the implantation dose can be determined, which is measured in ions/cm^2 [22, 23, 24].

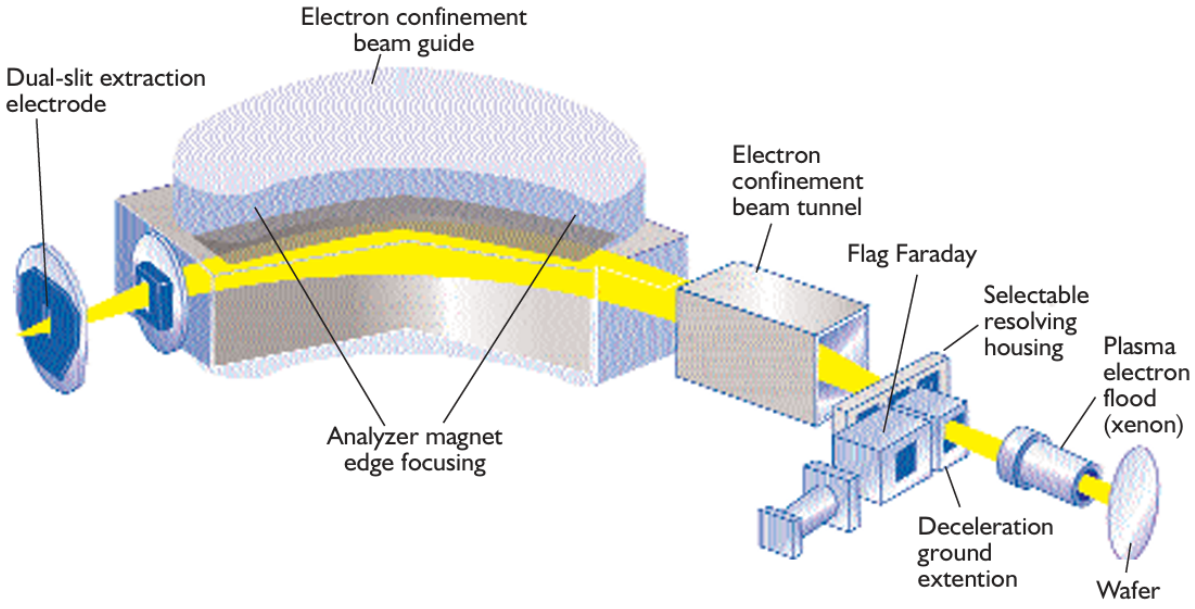


Figure 3.5: Schematic of an ion beam implantation tool. The electron confinement technology enables transport of multi-milliampere beams below 10 keV in modern high-current beamlines. Image courtesy of Rubin *et al.* (2003) [25].

The ion beam bombards the target substrate with energized ions, which penetrate the target substrate until they are stopped by inelastic collisions (see Figure 3.6). These

may involve interactions with the nuclei of substrate atoms (nuclear stopping) or collisions with electrons (electronic stopping). Therefore, it may be inferred that lattice damage is unavoidable and displacement of the target atoms can result in the generation of defects in the diamond. These defects can be substitutional, such as a nitrogen atom replacing a carbon atom (known as a P1 center), interstitial, such as a tin atom ending up between carbon bonds, or vacancies, which are empty sites in the lattice [24, 26].

Selecting the appropriate implantation dose and energy is crucial to a successful ion implantation process. The implantation energy determines the depth that these ions can reach, with higher energy resulting in deeper penetration. Another contributing factor is the atomic size of the ions. For a given energy, lighter ions can penetrate much deeper than heavier ions. An example case is that of the nitrogen and tin atoms. Assuming a beam with an energy of 100 keV and a diamond target, the N ions reach a depth of ≈ 115.1 nm, while the Sn ions reach a depth of ≈ 30.1 nm. Indicative charts and simulations can be found in the "Stopping and Range of Ions in Matter" (SRIM) website.

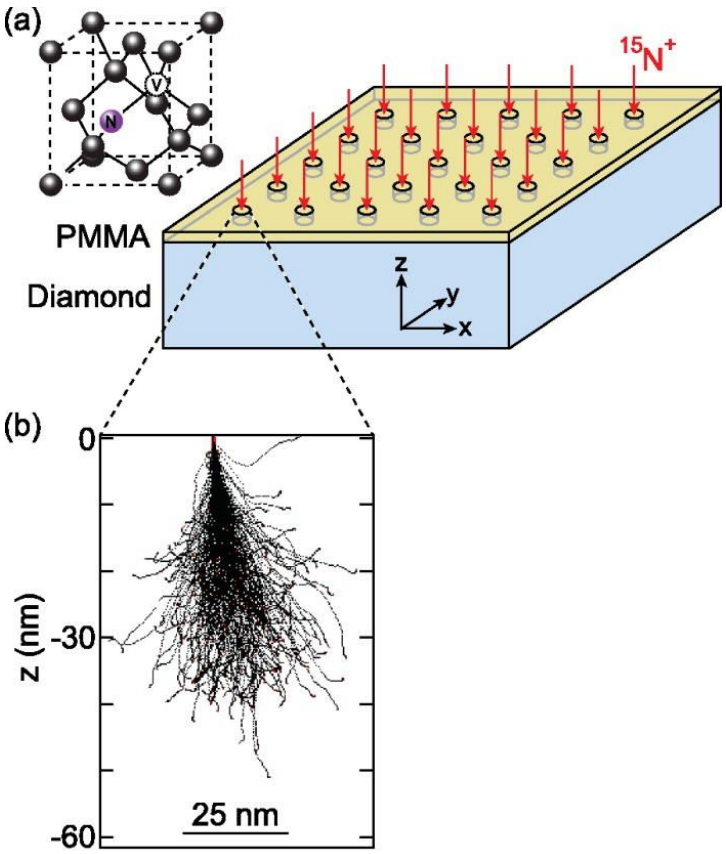


Figure 3.6: **(a)** Ion implantation through a 230 nm PMMA mask patterned with aperture arrays via electron beam lithography. **(b)** SRIM simulation of 20 keV ion implantation. Image courtesy of Sangtawesin *et al.* (2014) [27].

BLANKET IMPLANTATION

Blanket implantation refers to uniform implantation across the entire surface of the diamond using a broad ion beam. While this method lacks spatial selectivity, it still has its own advantages. Using blanket implantation, it is possible to generate a doped layer at specific depths beneath the diamond surface. This is usually performed using a high-purity diamond (Type IIa, N concentration < 5 ppb), containing very few impurities. Such a precisely located doped layer is particularly desirable when employing an ensemble of NV centers in diamond for quantum sensing, often with the target being sensed located in close proximity to the diamond surface.

MASK IMPLANTATION

By using lithographic techniques, small apertures can be created which act as screening masks, effectively filtering out any ions non-incident towards it. These masks are usually made out of resists which are suitable for electron beam lithography (EBL). After the diamond substrate has been thoroughly cleaned and prepared in the cleanroom, a liquid resist is deposited on its surface and spin coated to achieve a certain thickness. The final thickness depends on the ion energy during implantation later on. Nevertheless, it also affects the exposure dose during EBL. Thus, a fine balance between implantation energy, resist thickness and exposure parameters needs to be maintained.

During ion implantation, the ions have sufficient energy to penetrate the diamond up to the desired depth, only at the points where the mask contains apertures. Instead, ions that hit the mask are stopped before they reach the diamond. The size of these apertures varies in the order of tens of nanometers, however a smaller aperture typically results in more deterministic single color center generation [27, 28, 29, 30].

3.3.2. SINGLE ION IMPLANTATION: FOCUSED ION BEAM (FIB)

There exist a number of ways to achieve single emitters in diamond. One of the most common, and also the one employed in this research, makes use of the Focused Ion Beam (FIB) technique (see Figure 3.7). The ion generation and operating principle is quite similar to that of broad beam implantation, seen in subsection 3.3.1. FIB takes place in a vacuum chamber and consists of an ion source, dependent on which element is going to be implanted. Usually, this source is a Liquid Metal Ion Source (LMIS) with metals such as gallium (Ga) [31]. However, implantation of nitrogen needs to be done with a different source, using either nitrogen gas or nitrogen plasma.

The generated beam is accelerated through an electric field and then steered and focused onto the substrate by electrostatic lenses, with the resulting FIB having a diameter of a few nanometers. Using other techniques such as secondary electron detection in combination with the FIB system allows for precise monitoring and control of the amount of ions that penetrate the diamond at each site. Nonetheless, all things considered, successful generation of single emitters remains a statistical effect, that also relies on yield after annealing [32, 33].

FIB VS. MASK IMPLANTATION

Both FIB and mask implantation are well-investigated and widely used techniques. When it comes down to generation of single emitters, there are a few things to be taken into consideration. Most notably, the efficiency of each implantation method in creating the desired color centers, the total processing time, the spatial resolution, but also the lattice damage.

While mask implantation may lack in terms of complexity and required preprocessing time in the cleanroom, FIB excels in ease of implementation and patterning flexibility. Moreover, FIB offers unparalleled nanoscale spatial resolution, whereas mask implantation is hindered by the difficulties and limitations that the mask fabrication process entails. On the downside, the FIB process is linked to increased localized lattice damage, due to the nature of the high energy density of the focused beam. Regardless, annealing steps are used in both implantation techniques, to ensure color center generation and repair some of the lattice damage.

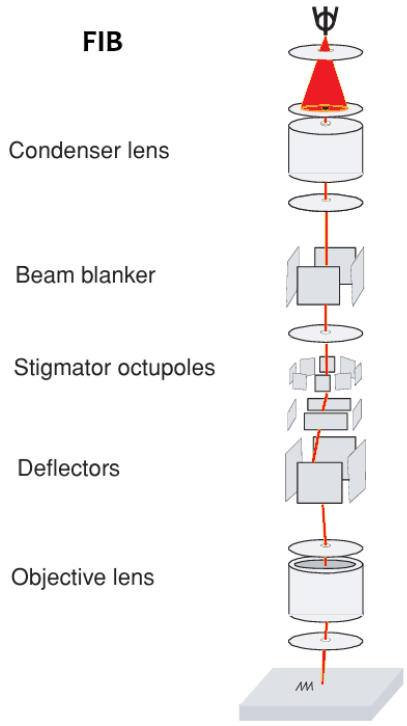


Figure 3.7: Illustration of the FIB optics. Image adapted based on the work of J. Gierak (2009) [34].

3.4. DIAMOND OVERGROWTH

Quantum sensing typically requires NV centers located very close to the surface of the diamond, in the 10-20 nm range, as seen in numerous studies. This depth is chosen as a compromise, so that the NV centers are still in close proximity to the sensing target, but also do not get affected as intensely by surface effects. Such effects arise from defects or impurities at the surface, which can trap electrons or holes, or contribute negatively to magnetic noise and. As a result, they may cause instabilities in charge states and dephasing, which drastically impacts spin coherence times [35, 36, 37, 38, 39, 40, 41].

However, in the context of quantum computing using SnV centers in diamond, a different color center depth is often chosen. Here, the aim is to generate color centers at a depth of roughly 100 nm from the surface. Unlike sensing applications, which require near-surface emitters for external coupling, quantum computing benefits from deeper placement to mitigate surface-related decoherence mechanisms. At this depth, the SnV centers experience fewer surface electric and magnetic field fluctuations, as well as reduced charge instability. Additionally, it places the centers outside regions typically affected by strain inhomogeneities, resulting in a more uniform and coherent optical environment.

Instead of implanting tin ions directly at the final depth, which would result in increased lattice damage and straggle, Sn ions are implanted shallowly, close to the surface. Subsequently, a high-purity diamond layer is grown on top, embedding the color centers at the desired depth with improved crystal quality [42].

The process of growing a (usually thin) diamond layer on top of an existing diamond substrate is called overgrowth. It is typically done using the CVD method, described earlier in subsection 3.2.1. It takes advantage of epitaxial growth, in order to develop a diamond layer on top of a diamond substrate with a certain crystallographic orientation, continuing its crystal structure. As with any CVD process, it takes place under heightened temperature conditions (around 1000 °C or below), thus, causing a certain amount of annealing [43, 44, 45]. However, most of the time, further annealing steps are performed thereafter.

3.5. ANNEALING TECHNIQUES

Annealing refers to a heat treatment process that typically takes place after ion implantation. It is vastly beneficial in improving the quality of the diamond and the color centers inside it. To begin with, annealing mobilizes vacancies, allowing them to pair with impurities, such as nitrogen or tin, to form stable color centers. This results in a higher yield of color centers and enhances activation efficiency. Additionally, the recombination of displaced atoms and vacancies aids in repairing lattice damage and minimizing the residual strain introduced during earlier processing steps, like ion implantation [46, 47]. Below, two popular annealing techniques are discussed, furnace annealing and laser annealing.

3.5.1. FURNACE ANNEALING

Furnace annealing is the most common version of thermal annealing. It is a process that typically takes place inside a cleanroom facility and makes use of large furnaces, inside which the diamond substrate is placed after it has undergone the necessary cleaning steps. The sample is then gradually heated to a high temperature of multiple hundreds up to a couple thousand degrees Celsius [48], depending on the type of implanted ions and the sample characteristics. Once a stable target temperature is reached, it is maintained for a set period of time. Following that, the substrate is cooled down to room temperature at a controlled rate. Note that the annealing process may involve multiple heating and cooling steps to achieve an optimized effect [47, 48, 49].



Figure 3.8: Photo of the Tempress Furnace used for annealing, located inside the cleanroom of Kavli Nanolab Delft.

3.5.2. LASER ANNEALING

Annealing using laser pulses is an emerging post-implantation activation technique. As opposed to conventional furnace annealing, which induces uniform, large-area heating, laser annealing relies on high-energy, focused pulses that can locally heat regions of interest with high spatial precision (see Figure 3.9). If the location of the implanted ions is known or can be estimated, this method enables targeted activation of color centers, while avoiding unnecessary thermal exposure of surrounding areas. The type of laser used varies based on the target substrate. For diamond, which is transparent in the ultraviolet (UV) to near-infrared (NIR) region, lasers that emit in these regions are usually preferred [50, 51].

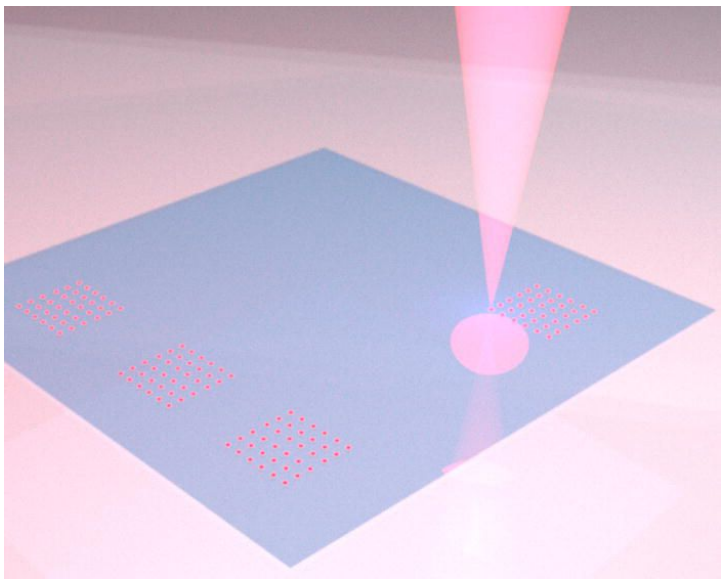


Figure 3.9: Artistic representation of the femtosecond annealing process. A pulsed fs laser writes arrays of color centers (red) in an ion-implanted region (blue). Fluorine or chlorine ions, shaped by a square aperture, enable color center formation near the surface. Image courtesy of Engel *et al.* (2023) [51].

The beam created by the laser is typically scanned over the sample using a piezo stage, following a predefined pattern. The laser produces ultrashort pulses in the femtosecond range, which locally increase the lattice temperature at the focal spot, due to the high energy that is carried by each laser pulse [52, 53]. This enables thermal activation of implanted vacancies. After each pulse, the irradiated region cools rapidly, as the heating is confined both spatially and temporally. However, the rapid cooling can sometimes result in undesirable stress or lattice distortion, depending on the pulse energy and repetition rate [51, 54].

The heat generated by these pulses facilitates selective, localized annealing by mobilizing vacancies to form stable color center configurations, such as NV or SnV centers. This type of annealing minimizes collateral damage to the surrounding lattice, which is essential for preserving coherence properties. However, when the local energy density exceeds a critical threshold, the irradiated area itself may undergo irreversible damage, including amorphization or graphitization of the diamond surface [50, 51, 53, 55]. As a result, laser parameters such as wavelength, pulse duration, repetition rate, and energy must be finely tuned to ensure high activation yield for any given color center, without

compromising lattice integrity [51].

Among these key parameters, pulse duration plays a central role in defining the spatial precision and thermal footprint of the annealing process [56]. A key advantage of femtosecond lasers lies in their ability to suppress the formation of a heat-affected zone (HAZ). This is a direct consequence of their ultrashort pulse duration, which is significantly shorter than the electron-phonon coupling time $\tau_{\mathrm{e-p}}$ [57, 58]. As a result, most of the deposited energy forms a hot electron gas rather than diffusing thermally. The characteristic thermal diffusion length l_d is defined as [59]:

$$l_d = \sqrt{D_{\mathrm{th}}\tau} \tag{3.1}$$

where D_{th} is the thermal diffusivity of the material and τ the pulse duration. Minimizing τ reduces l_d, which in turn enhances the spatial resolution and mitigates unintended lattice modifications.

Beyond thermal effects, femtosecond laser pulses can also drive nonlinear photoexcitation processes, particularly at high peak intensities [54]. In wide-bandgap materials such as diamond, the bandgap E_g typically exceeds the energy of individual photons, therefore rendering linear absorption ineffective [60]. However, under sufficient intensity, non-linear mechanisms such as multi-photon absorption and tunneling ionization become dominant pathways for carrier excitation [61, 50].

For even higher intensities, tunneling ionization may dominate. If the laser intensity is tuned close to the breakdown threshold of the material, the formation of single lattice defects becomes feasible. The probability of an electron overcoming the binding energy ε_b required for defect formation can be described by the Maxwell-Boltzmann distribution [62]:

$$P(E \geq \varepsilon_b) = \frac{2}{\sqrt{\pi}}\sqrt{\frac{\varepsilon_b}{k_B T}}\, e^{-\varepsilon_b / k_B T} \tag{3.2}$$

This statistical dependence implies that even slight fluctuations in local temperature or pulse energy may influence the probability of successful defect formation. Nevertheless, recent studies on femtosecond laser annealing techniques have demonstrated the feasibility of sub-10 nm precision, albeit with considerable experimental challenges [54].

3.6. SIMULATION & FABRICATION OF COLOR CENTERS

In this section, two different methods are explored for the fabrication of single color centers and ensembles. One of these uses broad beam implantation to fabricate ensembles of SnV centers (using blanket implantation) and single SnV centers (through a patterned mask). The other method involves preparation of diamonds for creation of ensembles, and also single color centers. This includes both NV and SnV centers, using a FIB implantation system.

3.6.1. INTRODUCTION TO MASK IMPLANTATION PREPARATION, SIMULATION & FABRICATION PROCESSES

This part of the project deals with simulations of stopping ranges of ions in diamond for determination of the sufficient thickness of the masking resist, for different resists. Extensive cleanroom processing and tests take place, before the sample is outsourced for ion implantation. The goal is shallow implantation of tin ions at ~ 8 nm from the surface (nitrogen ions are also similarly simulated) and subsequent overgrowth, in order to position them at a depth of about 80-100 nm; a depth suitable for quantum computing applications. For NV centers, a depth between 10-20 nm is desired.

For this purpose, two electronic grade (IIa, N concentration <5 ppb) diamonds are chosen. These are {100} diamonds from Element Six Technologies[1], with length and width of $2 \times 2\,\text{mm}^2$ and thickness of 300 µm.

Simulations were done for a diamond target and multiple different masks and implantation energies. First with nitrogen ions and later on with Sn ions. The diamond was simulated as a carbon target with a density of $3.52\,\text{g/cm}^3$, instead of carbon's standard density of $\sim 2.2\,\text{g/cm}^3$ at RT. For the simulations, the Transport of Ions in Matter (TRIM) program was used, which is part of the SRIM program package that uses Monte Carlo simulations of ion trajectories.

3.6.2. SIMULATIONS OF MASKS FOR NV CENTERS

To achieve shallow implantation of nitrogen atoms, energies of just a few keV are sufficient. The ion parameters, in this case, are set to nitrogen, N, with atomic number $Z = 7$ and mass of $m_N = 14.003\,\text{amu}$. For energies starting from 3 keV and up to 11 keV, numerous masks with varying thickness are simulated. A summary of the simulations performed for nitrogen implantation is given in Table 3.1.

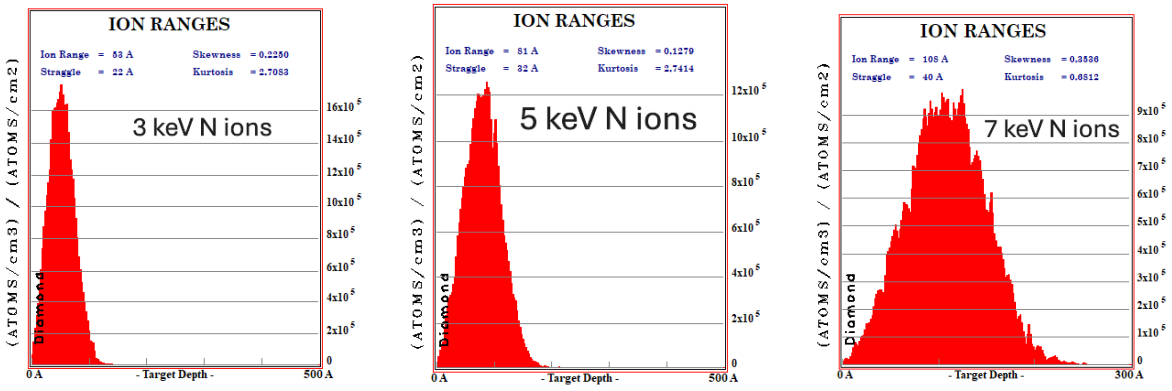
Energies of 3 keV and 5 keV would result in an implantation depth of $5.0 \pm 2.2\,\text{nm}$ and $7.7 \pm 3.1\,\text{nm}$ respectively. These depths fall a bit short of the requirement set earlier for shallow nitrogen implantation, which was in the 10-20 nm range. Furthermore, the mask thickness required to effectively mask the diamond might be too thin to spin coat using the available equipment in the cleanroom.

Increasing the ion energy to 7 keV gives a projected range of $10.3 \pm 4.0\,\text{nm}$, which just barely meets the criteria (as seen in the simulations in Figure 3.10). Finally, an energy of 11 keV results in a more flexible implantation depth of $15.5 \pm 5.5\,\text{nm}$, as calculated also by SRIM simulations.

[1] More detailed specifications can be found here: https://e6cvd.com/us/application/all/el-sc-plate-2-0x2-0x0-5mm.html

Table 3.1: List of the mask materials used for simulations at different nitrogen implantation energies.

Energy (keV)	No Mask	PMMA	Si_3N_4	SiO_2
3	✓	-	-	-
5	✓	-	-	-
7	✓	✓	✓	✓
11	-	✓	-	-



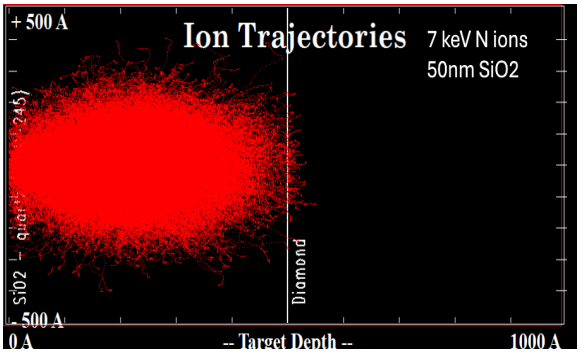
(a) (b) (c)

Figure 3.10: TRIM simulations of the penetration depth of nitrogen ions in a diamond substrate. (**a**) 3 keV, (**b**) 5 keV, and (**c**) 7 keV implantation energies. Simulations were run at 0° ion angle with 10,000 ions each.

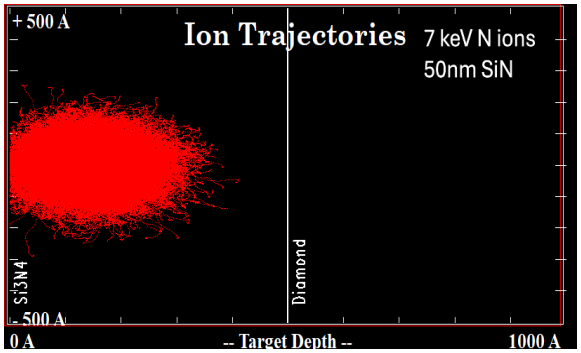
For simulations of stopping ranges on diamonds coated with different masks, attention is paid to eliminate the probability of any ions penetrating deeper than the mask thickness. Therefore, instead of looking at the mean stopping range, graphs of ion trajectories are used (see Figure 3.11).

The SiO_2 layer was used as an approximation of the hydrogen silsesquioxane (HSQ) mask. There, a mask thickness of 50 nm was chosen. TRIM simulations with these parameters (see Figure 3.11a) show that the mask thickness is not enough to shield the diamond against all nitrogen ions. Thus, either the thickness has to be increased, or a mask with different composition has to be used. On the other hand, simulations with a silicon nitride (Si_3N_4) mask (see Figure 3.11b), demonstrate what the desired implantation conditions would be, albeit in an exaggerated way, since there is too much distance between the stopping of the ions and the diamond layer. Unfortunately, achieving such thickness with a Si_3N_4 mask can be quite challenging.

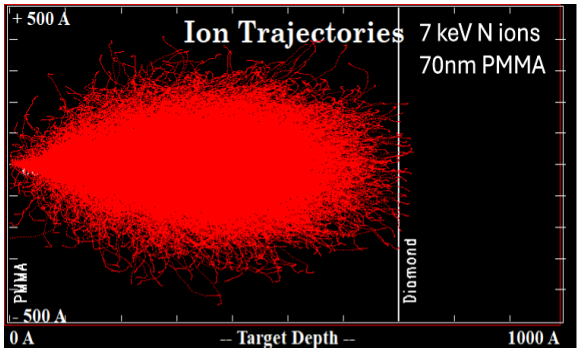
Polymethyl methacrylate (PMMA) is a very commonly used lithography resist. It exists in many variations, depending on its molecular weight and viscosity. Hence, by spin coating PMMA on top of a diamond substrate, it is possible to achieve a thickness of a few tenths of nanometers. Multiple simulations were run, starting from 10 nm of PMMA up to 70 nm, in order to determine the most suitable and realistic spin coating (and subsequently EBL) conditions. Increasing the thickness of the PMMA resist results in gradually more effective masking of the diamond substrate underneath. However, given that no nitrogen ions are allowed to penetrate the diamond at all, only a thickness of 70



(a) SiO_2, 50 nm, 20,000 ions



(b) Si_3N_4, 50 nm, 20,000 ions



(c) PMMA, 70 nm, 10,000 ions

Figure 3.11: TRIM simulations of 7 keV nitrogen ion trajectories in various masking layers on diamond, at normal incidence (0°).

nm or above could prove useful in masking the diamond under these energy conditions (Figure 3.11c).

For a nitrogen ion implantation energy of 11 keV, only a PMMA resist was simulated for its effectiveness in shielding the diamond. It is apparent that higher energy ions require increased thickness so that they are stopped before reaching the diamond. From Figure 3.12, it is evident that a PMMA resist thickness of ~ 120 nm and above would be able to protect the diamond substrate underneath from incoming nitrogen ions of 11 keV energy.

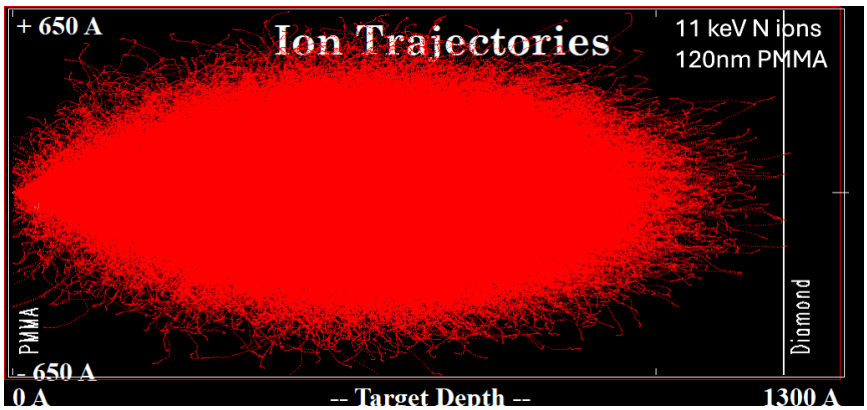


Figure 3.12: TRIM simulations of the penetration depth of 11 keV nitrogen ions in 120 nm of PMMA, on top of a diamond substrate, for an ion angle of 0° and 99,999 ions.

However, achieving a PMMA thickness of 120 nm is unrealistic, based on the combination of PMMA resist variant and "slow" spin coating speed required. The relevant spin curves can be found below, in Figure 3.13. There, it is indicated that to end up a thickness of ~ 120 nm, a 950K A2 PMMA resist has to be spin coated at a speed of 1000 rpm, which is not feasible in the Kavli Nanolab Delft cleanroom due to inconsistencies and uncertainties when using slow speeds.

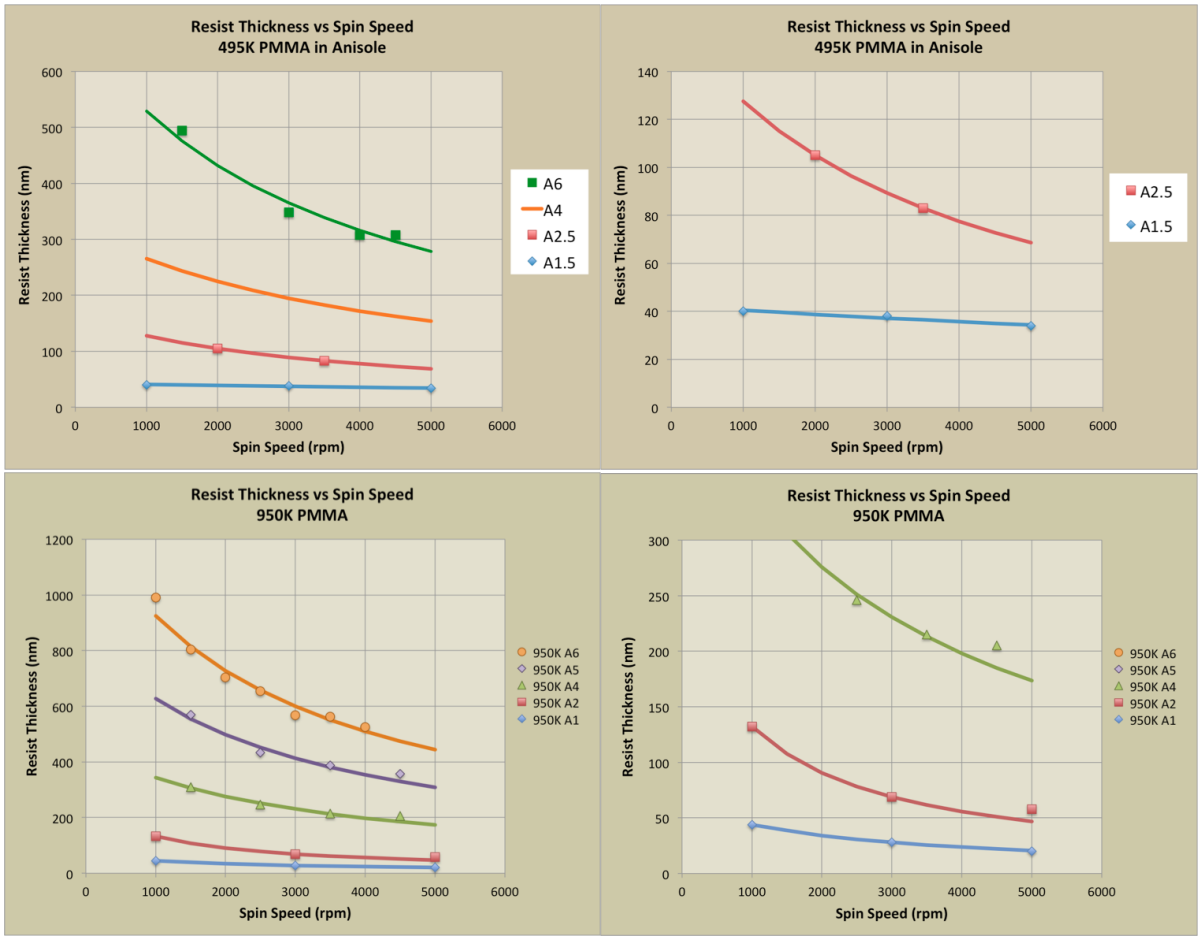


Figure 3.13: Spin curves for various PMMA concentrations. The color-enhanced images above were taken from the Washington Nanofabrication Facility[1]. Relevant data is provided by the supplier's (MicroChem) website, listed as "PMMA Data Sheet"[2].

[1]Washington Nanofabrication Facility PMMA spin curves: https://ebeam.mff.uw.edu/ebeamweb/process/process/pmma.html

[2]MicroChem PMMA Data Sheet: https://kayakuam.com/wp-content/uploads/2021/07/KAM-PMMA-Datasheet-4.12.21-final.pdf

Table 3.2 below summarizes the simulated masks and their effectiveness in shielding the diamond from 7 keV and 11 keV nitrogen ion energies.

Table 3.2: Mask effectiveness for N implantation

Ion Energy	Projected Range	Mask Material	Thickness	Effectiveness
7 keV	10.3±4.0 nm	PMMA	10 nm	X
		PMMA	30 nm	X
		PMMA	50 nm	X
		PMMA	60 nm	X
		PMMA	70 nm	✓
		Si_3N_4	50 nm	✓
		SiO_2	50 nm	X
11 keV	15.5±5.5 nm	PMMA	50 nm	X
		PMMA	55 nm	X
		PMMA	60 nm	X
		PMMA	65 nm	X
		PMMA	70 nm	X
		PMMA	75 nm	X
		PMMA	80 nm	X
		PMMA	85 nm	X
		PMMA	100 nm	X
		PMMA	120 nm	✓

3.6.3. SIMULATIONS OF MASKS FOR SNV CENTERS

For tin atoms, deep implantation (directly at a depth of ~ 80-100 nm) would mean extensive straggle, which limits the spatial resolution, as well as lattice damage caused by the high-energy ion beam. Therefore, shallow implantation and subsequent overgrowth is performed, based on the paper from Rugar *et al.* [42]. To achieve depths similar to those of nitrogen ions, tin ions require significantly more energy. This has to do with their atomic size and weight, which gives rise to increased interaction probability with the material it is directed towards. Some indicative TRIM values for deep-implantation penetration depths were obtained. Figure 3.14 shows that a deep implantation of tin would require energies above 300 keV. There, however, the longitudinal straggling would be in the order of tens of nanometers, thus introducing significant uncertainties.

For TRIM simulations, Sn ions were selected, with atomic number $Z = 50$ and mass of $m_{Sn} = 119.902$ amu. For low implantation energies, between 7 keV and 60 keV, the implantation depth varies from 5.5 ± 1.2 nm to 20.6 ± 3.5 nm. This is the energy range that was simulated with various mask thicknesses and combinations. A fine balance between implantation energy and mask thickness is of utmost importance. As was the case with N ion TRIM simulations, attention is once again paid to eliminate the probability of any ions penetrating deeper than the mask thickness. Hence, graphs of ion trajectories are used to determine the appropriate parameters. A full list of the simulations performed for Sn ions with different energy and mask combinations can be found in Table 3.3.

Table 3.3: List of simulations performed for different Sn implantation energies & masks. A green tick (✓) indicates which masks were simulated.

Energy (keV)	No Mask	PMMA	SiO2 #1	SiO2 #2	Si3N4	Al on Si3N4	Al2O3 on Si3N4	Cr on Si3N4
7	-	✓	-	-	-	-	-	-
10	-	✓	-	-	-	-	-	-
15	-	✓	-	-	-	-	-	-
20	-	✓	-	-	✓	-	-	-
40	-	✓	-	-	✓	-	-	-
60	-	✓	✓	-	✓	-	-	-
295	✓	✓	✓	✓	✓	✓	✓	✓
296	✓	-	-	-	-	-	-	-
298	✓	-	-	-	-	-	-	-
300	✓	-	-	-	-	-	-	-
310	✓	-	-	-	-	-	-	-
320	✓	-	-	-	-	-	-	-
350	✓	-	-	-	-	-	-	-
500	✓	-	-	-	-	-	-	-

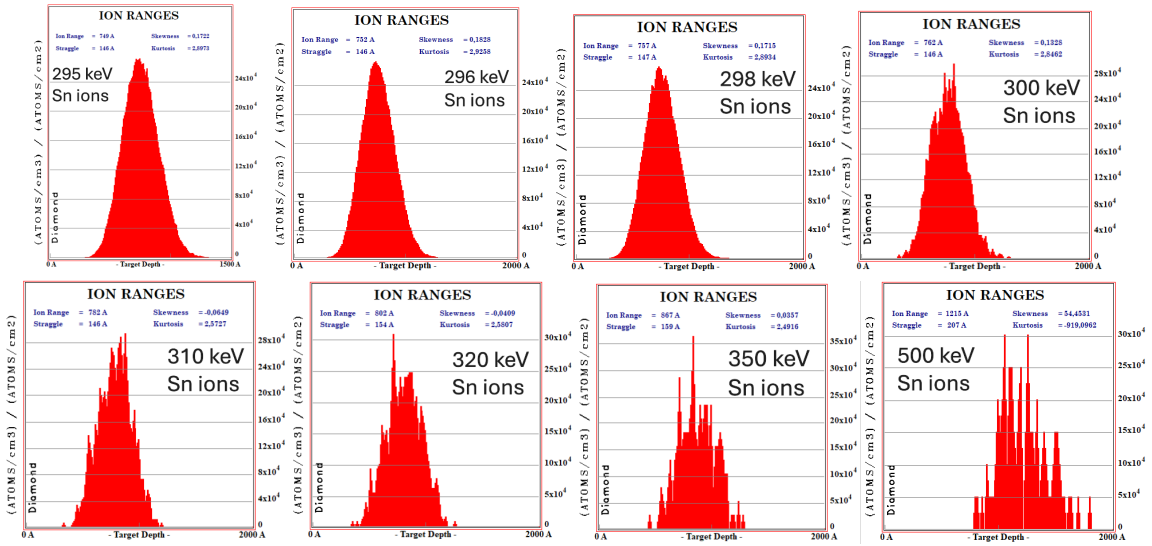


Figure 3.14: TRIM simulations of the penetration depth of tin ions in a diamond substrate for various ion energies. All simulations were run for an ion angle of 0° and for varying number of total ions: 50,000 ions (295 keV, 296 keV, 298 keV, 300 keV), and 30,000 ions (310 keV, 320 keV, 350 keV, 500 keV). However, simulations for energies between 300 keV and 500 keV were stopped early, before the full amount of ions was simulated.

SHALLOW SNV IMPLANTATION SIMULATIONS

To begin with, Sn ions with 7 keV energy were simulated for a PMMA resist thickness of 52 nm. This thickness was initially chosen as a test/validation of the findings of the paper cited above [42]). Energy of 7 keV results in a projected range of 5.5 ± 1.2 nm. In this case, overgrowth would be required afterward (as with any "low" implantation energy simulation in this section). TRIM simulations using PMMA reveal that a thickness of 52 nm is more than adequate in masking the diamond from 7 keV Sn ions. Likewise, an implantation energy of 10 keV would result in a projected range of 6.6 ± 1.4 nm. Simulation with a 52 nm thick PMMA resist shows that such thickness can indeed protect the diamond from incoming tin ions. Similarly, 15 keV Sn ions were simulated incident on a PMMA resist with a thickness of 52 nm, at an angle of 0° and 7°. The results can be seen below, in Figure 3.15. Such energy corresponds to an implantation depth of 8.4 ± 1.7 nm.

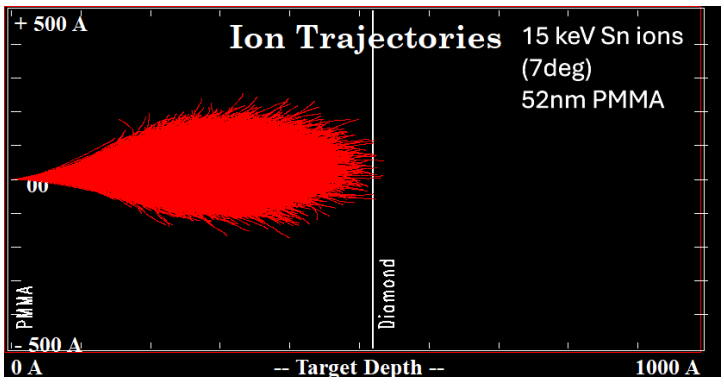


Figure 3.15: TRIM simulations of tin ion trajectories, with an energy of 15 keV. The target is a 52 nm thick layer of PMMA on top of a diamond. Obtained for an ion angle of 7° and for 65,900 total ions.

Before choosing the ideal mask thickness and ion energy combination, further ion energies were simulated. The results can be seen in Table 3.4.

Table 3.4: Mask effectiveness for Sn implantation

Ion Energy	Projected Range	Mask Material	Thickness	Effectiveness
7 keV	5.5±1.2 nm	PMMA	52 nm	✓
10 keV	6.6±1.4 nm	PMMA	52 nm	✓
15 keV	8.4±1.7 nm	PMMA	52 nm, 7°	✓
20 keV	10.0±1.9 nm	PMMA	50 nm	X
		PMMA	52 nm	X
		PMMA	65 nm	✓
		PMMA	80 nm	✓
		Si_3N_4	25 nm	✓
		Si_3N_4	30 nm	✓
		Si_3N_4	35 nm	✓
40 keV	15.6±2.8 nm	PMMA	80 nm	X
		PMMA	100 nm	✓
		Si_3N_4	30 nm	X
		Si_3N_4	35 nm	X
		Si_3N_4	40 nm	✓
		Si_3N_4	45 nm	✓
		Si_3N_4	50 nm	✓
60 keV	20.6±3.5 nm	PMMA	100 nm	X
		PMMA	120 nm	✓
		PMMA	140 nm	✓
		Si_3N_4	40 nm	X
		Si_3N_4	45 nm	X
		Si_3N_4	50 nm	✓
		SiO_2	45–75 nm	X
		SiO_2	80 nm	✓

For an energy of 20 keV (and an implantation depth of 10.0 ± 1.9 nm), simulations were performed for PMMA and Si_3N_4 masks with variable thickness. Starting with PMMA, the thickness was increased from 50 nm to 80 nm. In addition, a Si_3N_4 mask was simulated, for a thickness of 25 nm, 30 nm, and 35 nm. All three simulated thicknesses seem to be able to shield the diamond, when bombarded with 20 keV Sn ions. For 40 keV Sn ions, various PMMA and Si_3N_4 mask thickness were simulated once again. This energy corresponds to an implantation depth of 15.6 ± 2.8 nm.

From the above simulations, it is evident that a PMMA resist thickness exceeding 80 nm is required for sufficient masking during 40 keV Sn ion implantation. For the Si_3N_4 mask, thicknesses of 40 nm or greater are acceptable. While the fabrication of such thin layers on diamond is feasible, it often involves additional processing steps that cost increased fabrication time and may introduce more sources of error.

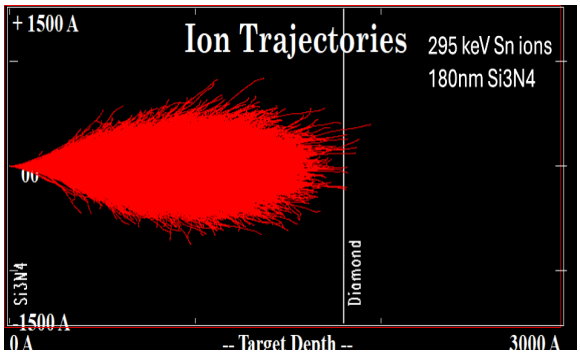
A projected range of 20.6 ± 3.5 nm is expected from a tin ion implantation with 60 keV energy. Such depth starts to bring increased uncertainties in spatial resolution, both in longitudinal and lateral straggling, and is not quite efficient when taking into account the mask thickness required, additional fabrication and preparation steps, and EBL exposure dose. Nonetheless, simulations were performed for three different masks, namely PMMA, Si_3N_4 and SiO_2. These simulations make it apparent how masks with different material compositions and densities result in very different ion stopping profiles.

CHOICE OF 15 KEV AS SN ION IMPLANTATION ENERGY

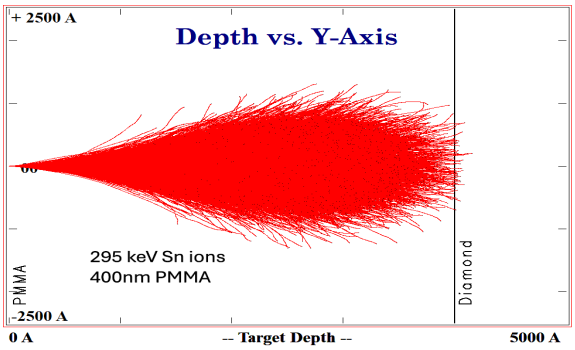
A tin ion energy of 15 keV in combination with a 52 nm PMMA resist has the potential to bring about a good balance of shallow implantation and effective masking of the diamond substrate. Therefore, this Sn ion energy of 15 keV was selected as the implantation parameter that dictated how the subsequent cleanroom processing should be performed. The fabrication process is described in subsection 3.6.4.

DEEP SNV IMPLANTATION SIMULATIONS

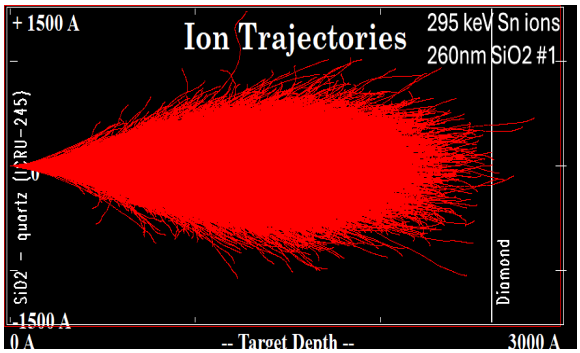
Finally, simulations were done with a tin ion energy of 295 keV, which would cause deep implantation, at a depth of ~ 74 nm from the surface. This, however, comes with increased straggle that would essentially cause increased lattice damage and deteriorate the spatial resolution. For an energy of 295 keV the following masks were simulated with TRIM: SiO_2 #1 (referring to standard density SiO_2), SiO_2 #2 (referring to SiO_2 with less density), Si_3N_4, 10 nm of Al on Si_3N_4, 10 nm of Al_2O_3 on Si_3N_4, 10 nm of Cr on Si_3N_4, and PMMA. Some of the simulation results can be seen below, in Figure 3.16.



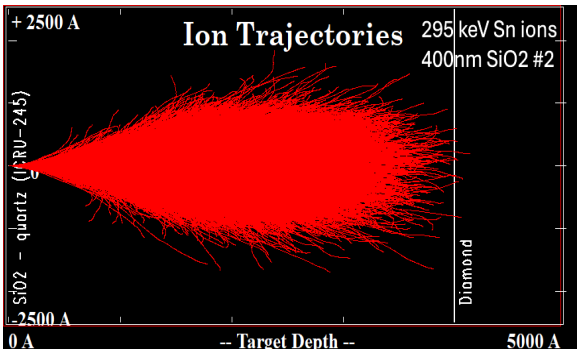
(a) Si_3N_4, 180 nm, 50,000 ions



(b) PMMA, 400 nm, 10,000 ions



(c) SiO_2#1, 260 nm, 30,000 ions



(d) SiO_2#2, 400 nm, 30,000 ions

Figure 3.16: TRIM simulations of 295 keV tin ion trajectories in various masking layers on top of diamond. All simulations were performed at 0° ion angle.

At this energy, the fabrication of masks with reasonable thickness (feasible without introducing too many additional processing steps) remains a challenge in the cleanroom. Moreover, the aforementioned issue with ion straggling is increasingly pronounced at higher implantation energies. As shown in Table 3.5, the effectiveness of shielding the diamond substrate against 295 keV Sn ions is inconclusive, given the challenges involved in fabricating these mask layers.

Table 3.5: Effectiveness of the masks simulated for 295 keV Sn ions. An orange box indicates partial masking, while green indicates effective masking.

Resist / Thickness	PMMA	Si_3N_4	Al on Si_3N_4	Al_2O_3 on Si_3N_4	Cr on Si_3N_4	SiO_2 #1	SiO_2 #2
50 nm	-	-	X	X	-	-	-
100 nm	-	X	X	X	X	X	-
110 nm	-	X	-	-	-	-	-
120 nm	-	X	-	X	-	-	-
130 nm	-	X	-	-	-	-	-
140 nm	-	X	-	-	-	-	-
150 nm	-	X	-	X	X	-	-
160 nm	-	X	-	-	-	-	-
170 nm	-	X	-	-	-	-	-
180 nm	-	X	-	-	-	X	-
190 nm	-	✓	-	-	-	-	-
200 nm	X	✓	-	-	-	-	-
210 nm	X	-	-	-	-	-	-
215 nm	X	-	-	-	-	-	-
220 nm	X	-	-	-	-	X	X
240 nm	-	-	-	-	-	X	-
250 nm	X	-	-	-	-	-	X
260 nm	-	-	-	-	-	X	-
300 nm	X	-	-	-	-	-	X
350 nm	X	-	-	-	-	-	X
375 nm	-	-	-	-	-	-	X
400 nm	X	-	-	-	-	-	X
420 nm	X	-	-	-	-	-	-
450 nm	✓	-	-	-	-	-	-

Figure 3.17 below displays a summary of both shallow and deep tin ion implantation energies versus masks of various thicknesses.

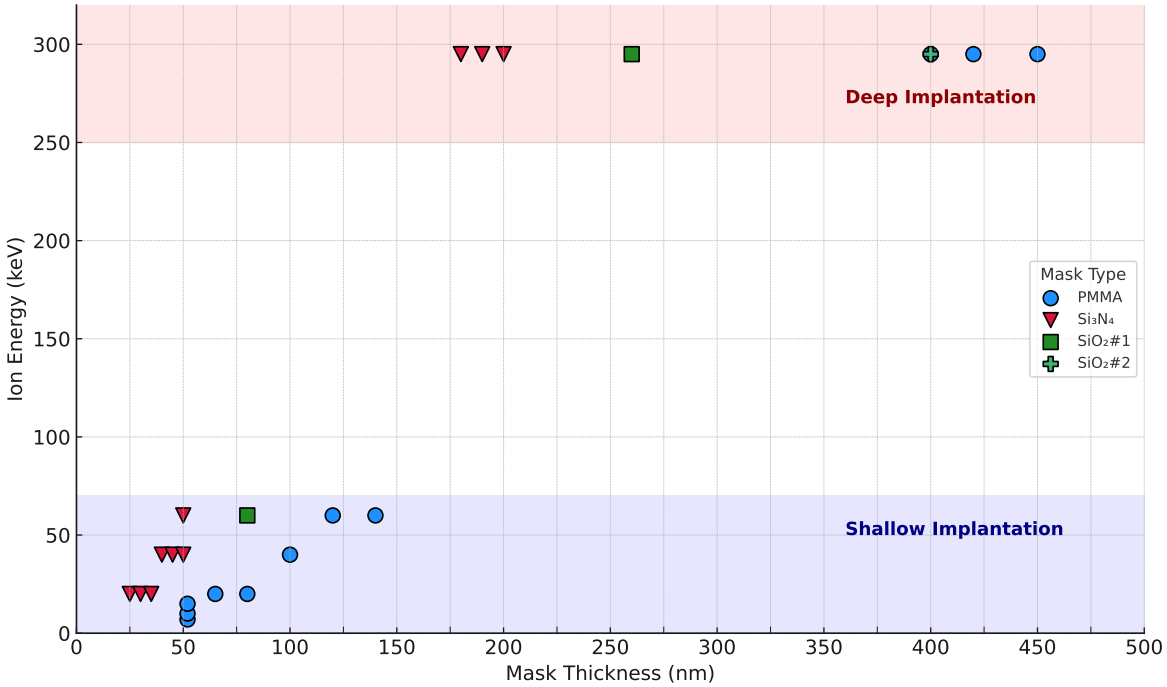


Figure 3.17: Tin ion energy vs. mask thickness for various mask materials. Successful and partial masking conditions are plotted, with shallow and deep implantation regions highlighted.

3.6.4. CLEANROOM FABRICATION OF SNV CENTERS

Having performed the necessary simulations, a suitable tin ion implantation energy was selected, along with the corresponding resist to serve as mask and the appropriate thickness. For this purpose, an energy of 15 keV was chosen, along with a PMMA resist with a thickness of 52 nm, as determined earlier in subsection 3.6.3.

The samples that were processed were two electronic grade diamonds with length and width of $2 \times 2\,\text{mm}^2$ and thickness of 300 µm (see subsection 3.6.1). However, before sending these samples for ion implantation, the process workflow and feasibility was first tested with silicon substrates as substitutes. The cleanroom processing steps can be seen in Figure 3.18. In addition, Appendix C contains manually-written step-by-step guides to some of the cleanroom processes mentioned in this section. Below, the diamond preparation process is described, which started with optimization tests on silicon chips.

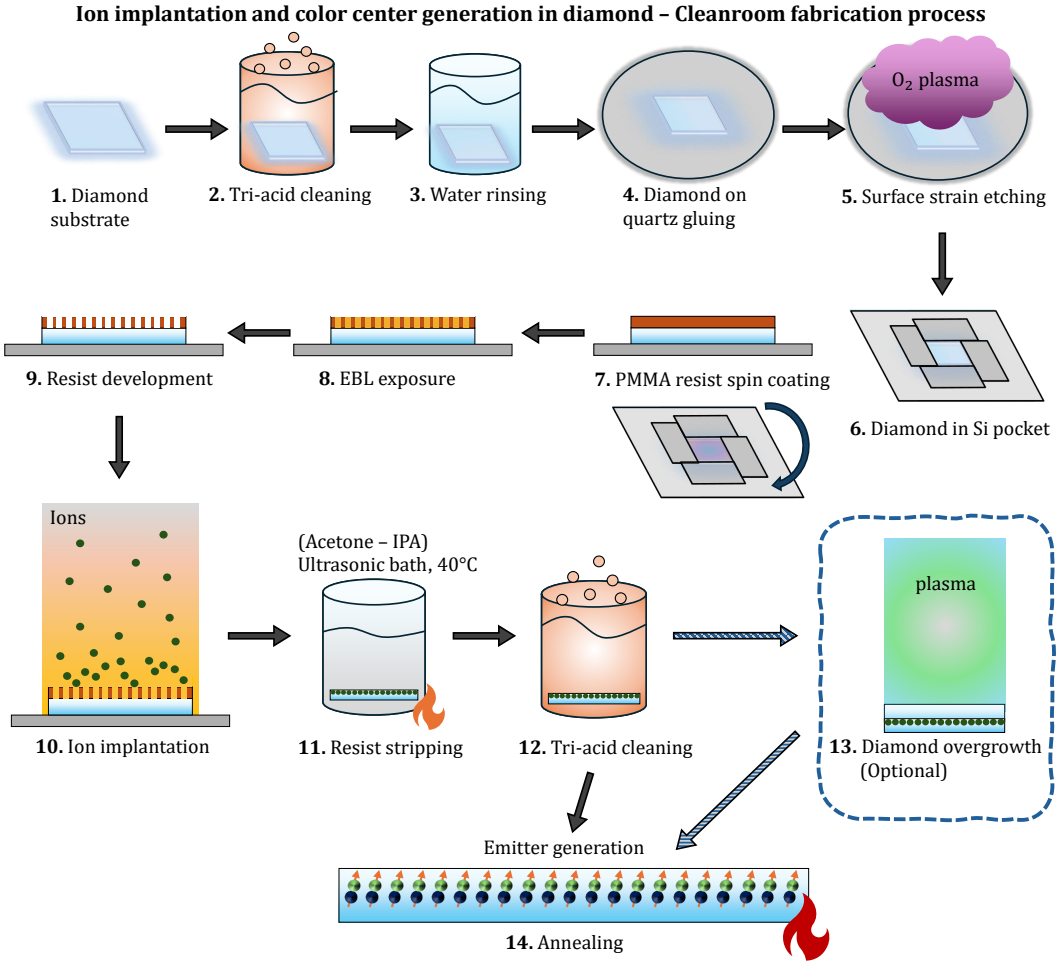
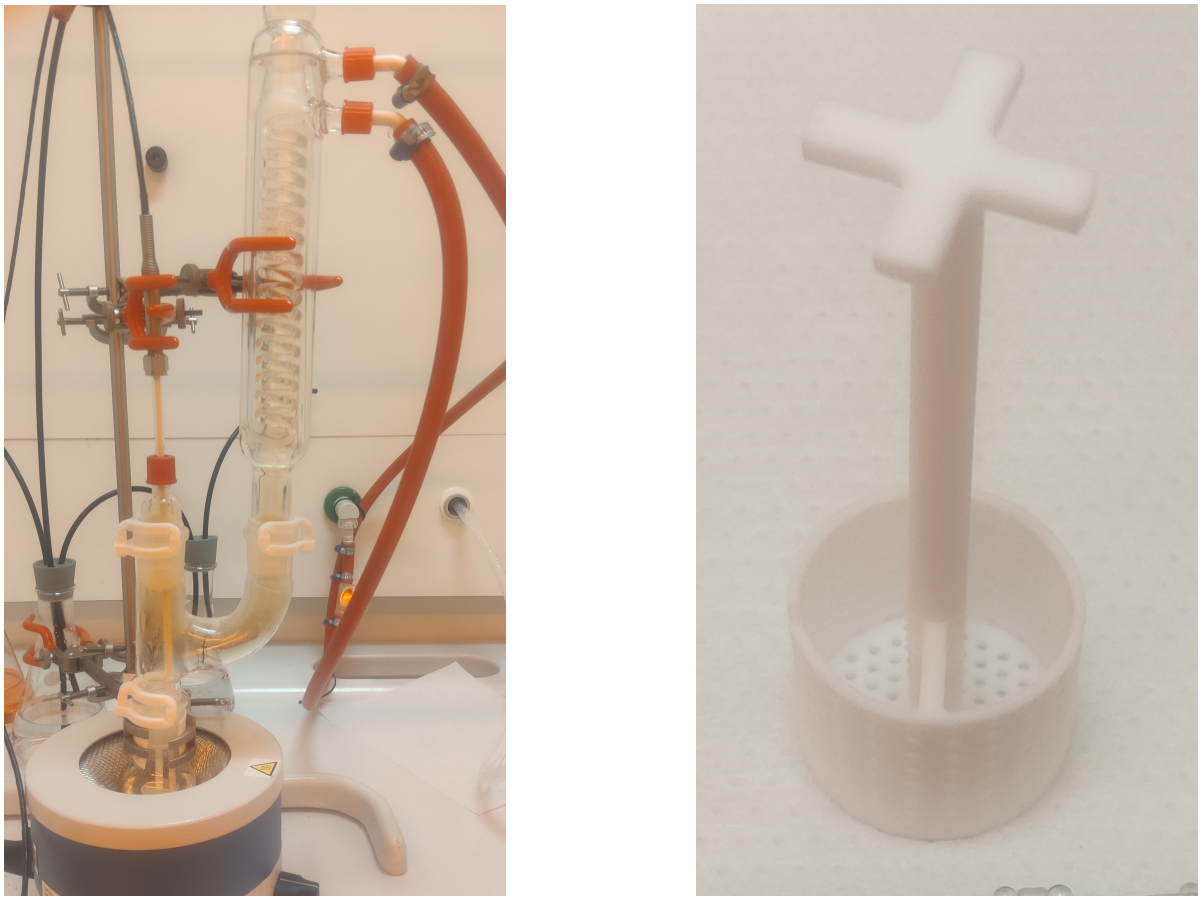


Figure 3.18: Cleanroom process steps toward masked ion implantation and color center generation. The diamond overgrowth step may be omitted when deep placement of the color centers is not required.

CLEANING OF THE SAMPLE

The first step to any successful cleanroom process is cleaning of the samples, in order to remove any potential contaminants or, sometimes, provide the necessary chemical treatment of the surface. Based on the type of contaminants, various cleaning liquids are used. The most common (and least complicated to carry out) is cleaning with fuming nitric acid (HNO_3, 99% concentration). Nitric acid is particularly useful for removing organic contaminants, such as lithography masks, and certain metallic impurities that can be easily oxidized, while not affecting the diamond itself.



(a) (b)

Figure 3.19: (**a**) Photo of the tri-acid cleaning setup inside the Kavli Nanolab Delft cleanroom. (**b**) Teflon sample holder used for tri-acid cleaning.

Another potent chemical solution is the one referred to as Piranha. It is a mixture of sulfuric acid (H_2SO_4) and hydrogen peroxide (H_2O_2), typically in a 3:1 ratio. It is also very efficient in removing heavy organic contaminants and also creates a hydrophilic diamond surface, which facilitates adhesion (useful later on in chapter 4).

One of the most corrosive solutions is the tri-acid mixture. A tri-acid mixture consists of hydrochloric acid (HCl), nitric acid (HNO_3, 65%), and sulfuric acid (H_2SO_4), usually in a 1:1:1 ratio. It can remove organic contaminants, but it is mostly used pre- or post-processing in order to get rid of metallic impurities. It is a rather complicated, dangerous and tedious process, but quite effective in its use.

SPIN COATING OF THE SAMPLE

Following tri-acid cleaning, the sample has to be spin coated with a lithography mask. However, small samples, such as the $2 \times 2\,\text{mm}^2$ diamond prove difficult to spin coat efficiently. This is largely due to having very little area for the resist to spread uniformly, resulting in uneven coated surfaces. To deal with this problem, a spin coating technique was developed by the Ronald Hanson lab in QuTech. This technique makes use of small silicon chips surrounding the diamond sample, in order to create a pocket in which the diamond is placed, effectively increasing its surface area and potentially eliminating non-uniform resist spin coating.

First, a silicon carrier wafer (or chip) is required. On top of it, a small droplet of 950K PMMA A4 resist is deposited. The diamond is carefully placed with tweezers on top of the droplet, at the center of the silicon carrier chip. The chip with the diamond is then placed inside a hotplate and heated to ~ 120°C, for two to three minutes. Afterward, it is taken out, and another PMMA droplet is deposited next to the diamond, so that a small silicon chip can be fixed right next to the diamond, leaving as little distance between them as possible. Quickly after placing the small chip next to the diamond, the whole chip is once again placed inside the hotplate for two to three minutes at ~ 120°C. This process is repeated three more times, so that a total of four silicon chips are fixed in a pocket configuration around the diamond. In between each process round, optical inspection checks can be performed to ensure proper attachment of the chips. A silicon pocket example is shown below in Figure 3.20.

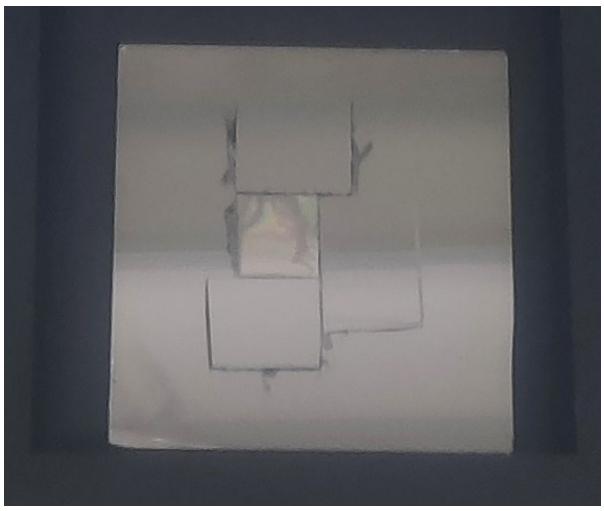


Figure 3.20: An incomplete configuration of a silicon pocket, on top of a silicon carrier chip, before spin coating.

These silicon chips have dimensions comparable to those of the diamond, but at least two to three times bigger, so that they can provide a larger effective spin coating surface. Attention needs to be paid to the dicing of the silicon chips, so that their edges are straight and smooth.

Following the successful fabrication of a silicon pocket, spin coating takes place. A droplet of 950K PMMA A2 is deposited on top of the diamond substrate, which is then spun at 6000 rpm, in order to achieve a resist thickness of 52 nm.

DESIGN OF THE LITHOGRAPHY MASK

Prior to exposure, the mask has to be designed and uploaded onto the software of the electron beam lithography tool. The mask design was done using KLayout. First, a dose test mask was created, containing lines and discs of varying size (see Figure 3.21), in order to determine the most suitable exposure dose during EBL.

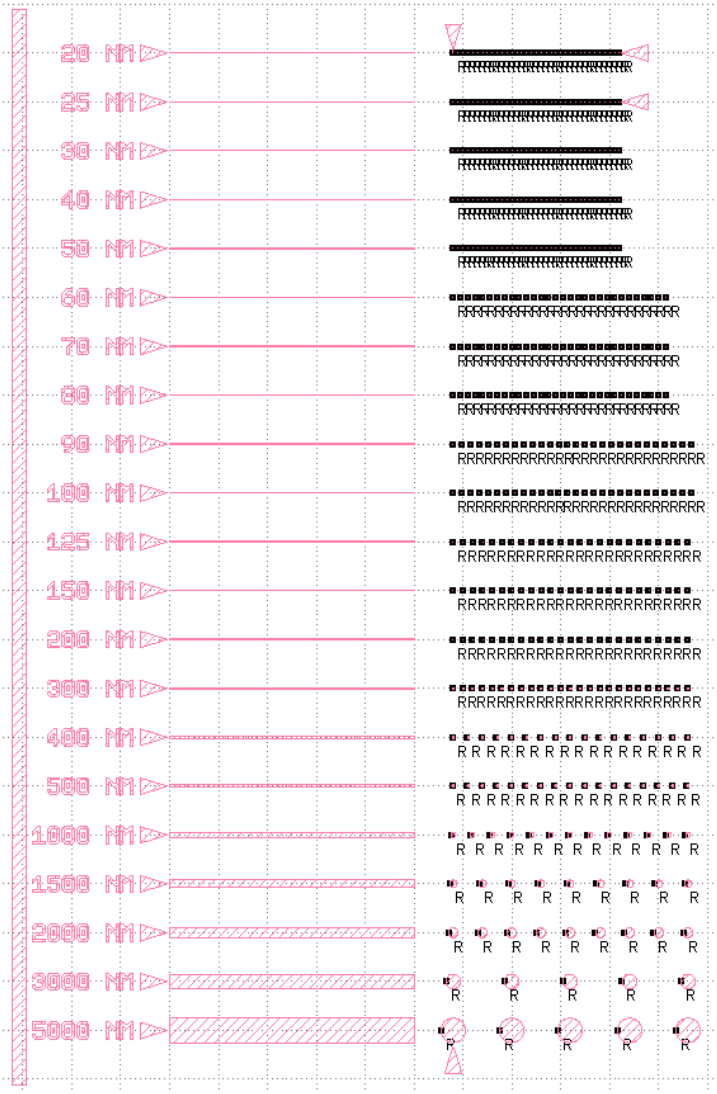


Figure 3.21: Mask used during EBL for dose test with a silicon chip.

After the dose tests were concluded, another mask was developed. This mask consisted of an array of apertures, ranging from 20 nm to 150 nm with a pitch of 20 µm, and was meant to be used as the final mask for tin ion implantation.

ELECTRON BEAM LITHOGRAPHY OF THE DIAMOND SAMPLE

When spin coating is complete, the carrier chip containing the diamond in the silicon pocket is mounted and inserted in the EBL tool. There, the electron beam scans the diamond on the patterned areas and interacts with the resist coating, allowing subsequent removal of the exposed areas. For EBL, the Raith EBPG 5000+ tool in Kavli Nanolab Delft was used. Given that the minimum feature size of the mask is $f_d = 20$ nm in diameter,

and that four spots should fit within that 20 nm linewidth, then the distance between them is:

$$d_{spot} = \frac{f_d}{N_{spots}} = \frac{20\,\text{nm}}{4} = 5\,\text{nm} \tag{3.3}$$

Assuming a safety factor of $S = 1.5$, the beam step size (d_{BSS}) is then chosen to be:

$$d_{BSS} = \frac{d_{spot}}{S} = \frac{f_d}{N_{spots}S} = \frac{5\,\text{nm}}{1.5} \simeq 3\,\text{nm} \tag{3.4}$$

This $d_{BSS} = 3\,\text{nm}$ number is entered as a parameter during editing of the mask file, called "job", using the BEAMER software. This job file is further edited to define the appropriate parameters for accurate and efficient exposure. In this case, the `1nA6_200um.beam_100` beam was chosen for exposure. The EBL tool can be seen in Figure 3.22.



Figure 3.22: The electron beam lithography tool (Raith EBPG 5000+) used in Kavli Nanolab Delft, in order to expose the designed mask on the diamond substrate.

Based on the tests performed using the dose test mask and performing inspection of the substrate (described later on), an optimal exposure dose of 820 $\mu C/cm^2$ was determined and used for the final lithography process.

DEVELOPMENT OF THE RESIST

During the development process, the exposed mask regions, where molecular bonds were broken during EBL, are selectively dissolved by the developer, creating the desired mask.

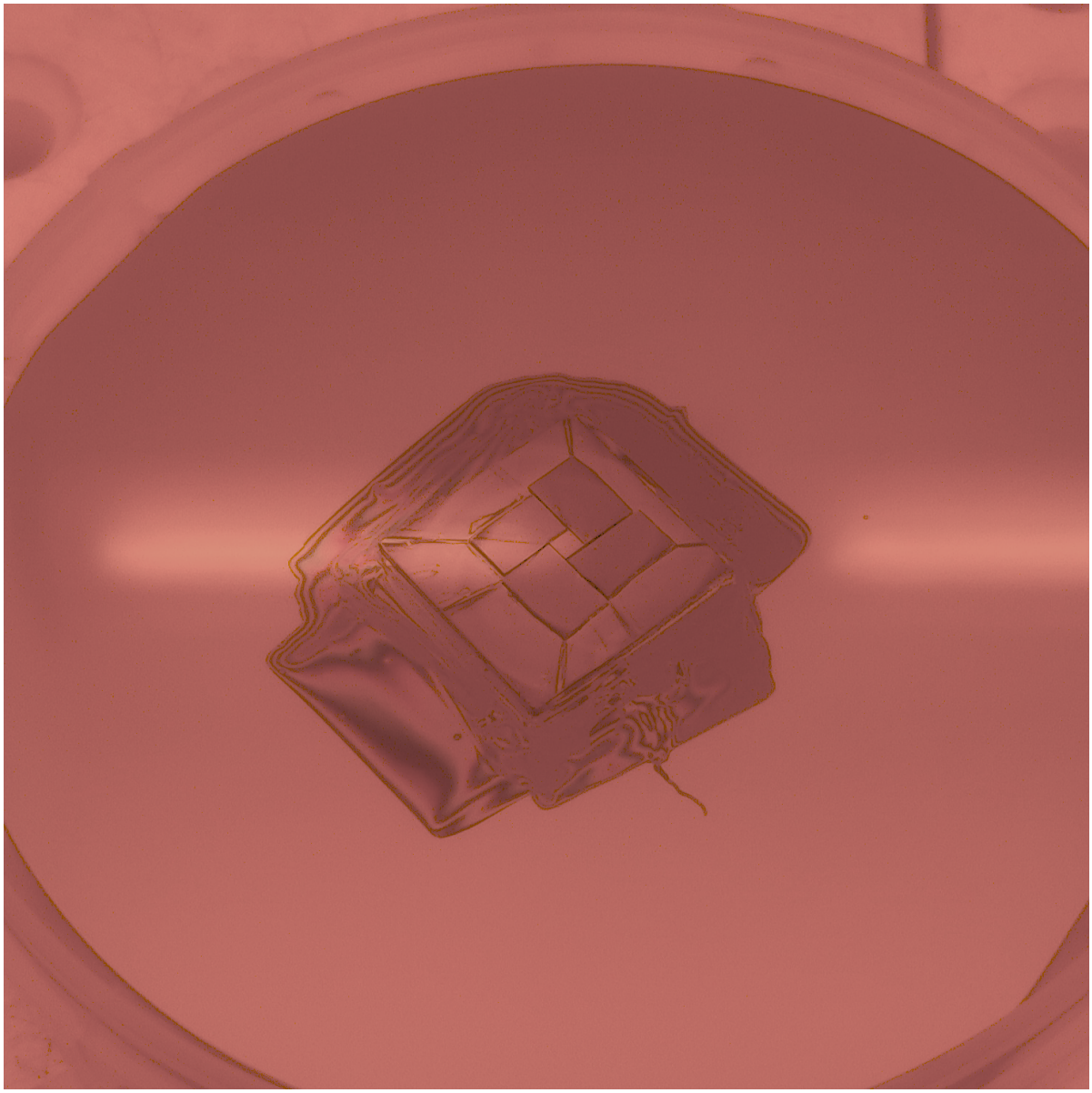
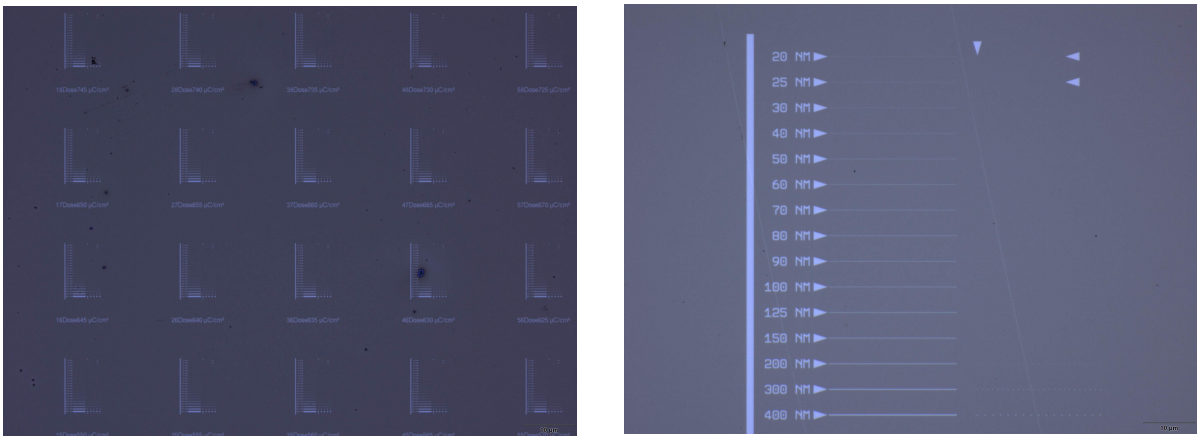


Figure 3.23: Photo of a diamond inside a Si pocket, after exposure and development.

The chemicals used for development depend on the type of lithography resist used. For PMMA, a solution of MIBK (methyl isobutyl ketone) and IPA (isopropyl alcohol) mixed in a 1:3 ratio is used as the developer. The carrier chip with the diamond substrate is immersed in this mixture for 60 seconds. Immediately afterward, the chip is rinsed in pure IPA for 30 seconds, which acts as a stopper, halting the development process. Care must be taken to avoid over-developing the resist, as this could compromise the integrity of the exposed structure.

INSPECTION OF THE FABRICATED MASK AND SUBSTRATE

At this stage, the diamond substrate on the silicon carrier chip was packaged and sent for ion implantation. Prior to that, however, the test silicon substrate -fabricated in the same manner and also made use of a silicon carrier chip and a silicon pocket- underwent several iterations and rounds of inspection with both a standard optical microscope and a scanning electron microscope (SEM).



(a) Array of patterned dose test masks on the test silicon chip. (b) 50x zoom on a mask exposed with 820 $\mu C/cm^2$.

Figure 3.24: Optical microscope images of dose test masks patterned on a silicon test chip inside Kavli Nanolab Delft. (a) Overview of array; (b) Close-up of mask exposed at 820 $\mu C/cm^2$.

In Figure 3.24b, features as small as 20 nm can be observed. Therefore, such an exposure dose of 820 $\mu C/cm^2$ has the potential to create the desired pattern and its nanometer-sized features. Nevertheless, further validation is needed, so the SEM was used to view the patterned region more precisely and at a smaller scale. Before inserting the silicon test chip into the SEM, a piece of sticky copper tape was placed on one of its corners, in order to reduce charging effects, as seen in Figure 3.25.

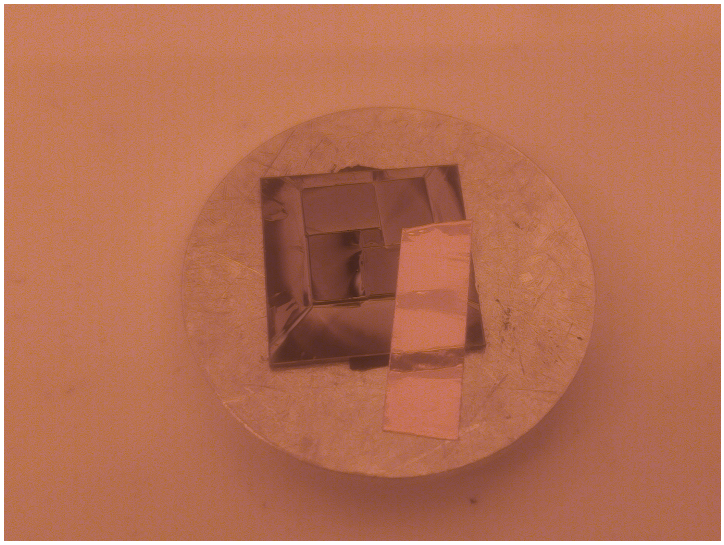
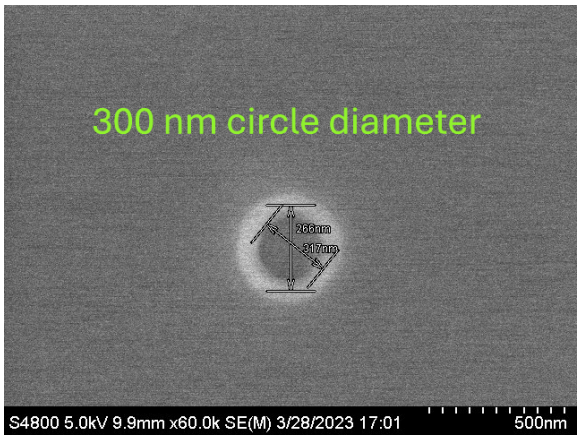
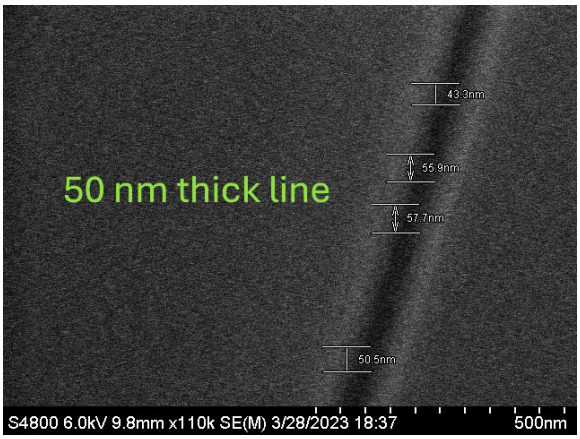


Figure 3.25: Photo of a sample inside a silicon pocket with a piece of copper tape attached to it, in preparation for SEM inspection.

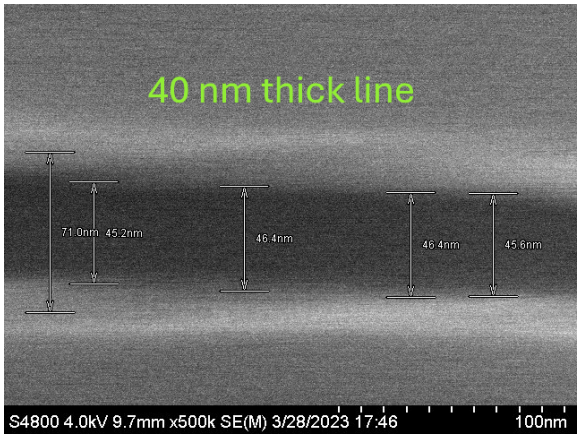
Below are some SEM images from the dose tests on the silicon test chip. From these SEM images (see Figure 3.26), it can be confidently stated that using an exposure dose of approximately 820 μC/cm^2 during EBL can result in well-patterned features down to 30 nm. Ideally, mask apertures should be fabricated as small as possible, down to even 10 nm in diameter. This way, there are fewer ions entering the diamond substrate, thereby increasing the chances of generating single color centers. Additionally, smaller apertures result in significantly improved spatial resolution and help mitigate excessive ion straggling [63, 64]. Nevertheless, larger apertures in the range of 80-100 nm can still prove sufficient in single emitter fabrication.



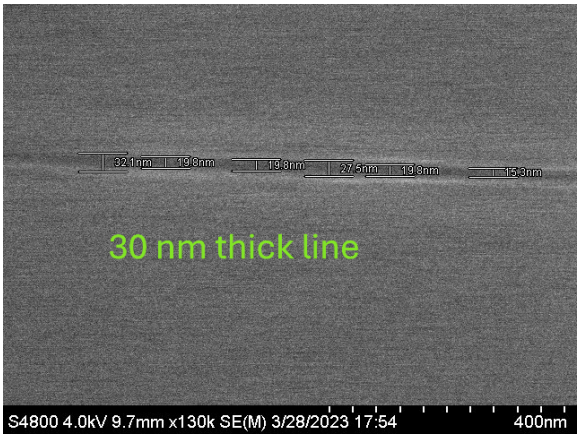
(a) 300 nm diameter circle.



(b) 50 nm thick line.



(c) 40 nm thick line.



(d) 30 nm thick line.

Figure 3.26: SEM images of dose test structures patterned on a silicon test chip. Structures include a 300 nm circle (a), and lines with thicknesses of 50 nm (b), 40 nm (c), and 30 nm (d). All images were acquired after EBL exposure and development in Kavli Nanolab Delft.

MASK IMPLANTATION OF SN IONS

After fabricating the mask, the diamond -along with the silicon carrier chip it was attached on- was sent to Ion Beam Services (IBS) in France for the implantation of tin ions into the diamond substrate. Specifically, two diamond samples were sent for implantation: one was the cleanroom-processed diamond substrate that underwent the aforementioned fabrication, and the other was a non-processed, maskless diamond substrate for blanket implantation.

A tin ($^{120}Sn^{+}$) ion energy of 15 keV was selected for the implantation, along with a dose of $2 \cdot 10^{13}$ atoms/cm^2 and an angle of 7°. Such an implantation angle works in favor of preventing channeling effects, i.e. ions penetrating deeper into the substrate than intended, due to alignment with the diamond's crystalline lattice. The lattice's regular structure can create open paths between atomic planes, allowing ions to travel farther. However, using an implantation angle of just 7° can sufficiently mitigate this problem.

OVERGROWTH ON SN-IMPLANTED DIAMOND SUBSTRATE

This ion implantation process resulted in shallow placement of Sn ions at 8.4 ± 1.7 nm, according to SRIM simulations. In order to achieve the desired depth of 80-100 nm, there needs to be a subsequent overgrowth step. This way, a diamond layer will be epitaxially grown on top of the existing diamond substrate, continuing its crystal structure (as described in section 3.4).

Before overgrowth, however, the diamonds needs to have the PMMA resist/mask stripped off of it. This is done with either a solvent stripper called remover PG or acetone. Here, the samples were immersed in acetone, heated to 50°C inside an ultrasonic bath for 5 minutes (see Figure 3.27). Immediately afterward, they were rinsed with pure IPA to get rid of any residues. Next, tri-acid cleaning was performed on these samples to make sure that there are no remaining impurities on the surface.



Figure 3.27: Photo of a beaker with a sample holder containing a processed diamond substrate, dipped inside an acetone solution. This solution is heated to 50°C inside an ultrasonic bath for 5 minutes. Photo taken inside the Kavli Nanolab Delft cleanroom.

Overgrowth was performed by Takashi Yamamoto from QuTech, TU Delft. The growth time lasted 83 minutes, which, given a growth rate of 48 nm/h, results in roughly 65-70 nm of added film thickness, pushing the Sn ions to a depth of ≈ 75 nm. The final film thickness was calculated to be 80 nm, although such a number is too small to accurately measure using white light interferometry. For a more precise measurement of the final substrate thickness, secondary-ion mass spectrometry (SIMS) may be employed. During overgrowth, the temperature was set to 800°C. This temperature might not be fully capable of activating the SnV color centers, but could potentially produce a few. Hence, optical characterization measurements took place (see section 3.7) using a spectrometer and the ODMR setup described in the previous chapter. To ensure proper color center generation, an additional annealing process needs to take place after overgrowth.

IBS Samples	Implantation details	Measurement	Overgrowth	Measurement	Furnace annealing	Laser annealing	Measurement
Blanket	Ions: ^{120}Sn, Angle: 7°, Energy: 15 keV, Dose: $2 \times 10^{13} \frac{\text{atoms}}{\text{cm}^2}$	Raman	Done	PL, Raman	Planned	Planned	Planned
Mask	Ions: ^{120}Sn, Angle: 7°, Energy: 15 keV, Dose: $2 \times 10^{13} \frac{\text{atoms}}{\text{cm}^2}$	PL, Raman	Done	PL, Raman	Planned	Planned	Planned

Figure 3.28: Table summarizing the blanket and mask ion implantation, characterization and activation (annealing) processes.

3.6.5. SUBSTRATE PREPARATION FOR SINGLE ION IMPLANTATION USING FIB

Single ion implantation using FIB (see subsection 3.3.2) was investigated, as a separate implantation method. This was performed as a comparison between this and the aforementioned mask implantation method, and was part of a collaboration between TU Delft and the University of Surrey, in the UK. It made use of the pump-priming program, within the scope of RAISIN (Roadmap for Applications of Implanted Single Impurities Network).

The diamonds that were scheduled for this round of single ion implantation were electronic grade (IIa) substrates, of {100} orientation. A number of them have an area of $2 \times 2\,\text{mm}^2$ and a thickness of either 300 µm or 500 µm, while others have an area of $4.5 \times 4.5\,\text{mm}^2$ and a thickness of 50 µm. Before any diamonds were sent to the University of Surrey for single ion implantation, they were thoroughly cleaned with a tri-acid solution and had a few microns etched away from their surface using O_2 plasma to remove unwanted strain effects (see Figure 3.29). Subsequent annealing is going to be required for all the ion implanted samples above, in order to efficiently activate the color centers and repair damage done during implantation.

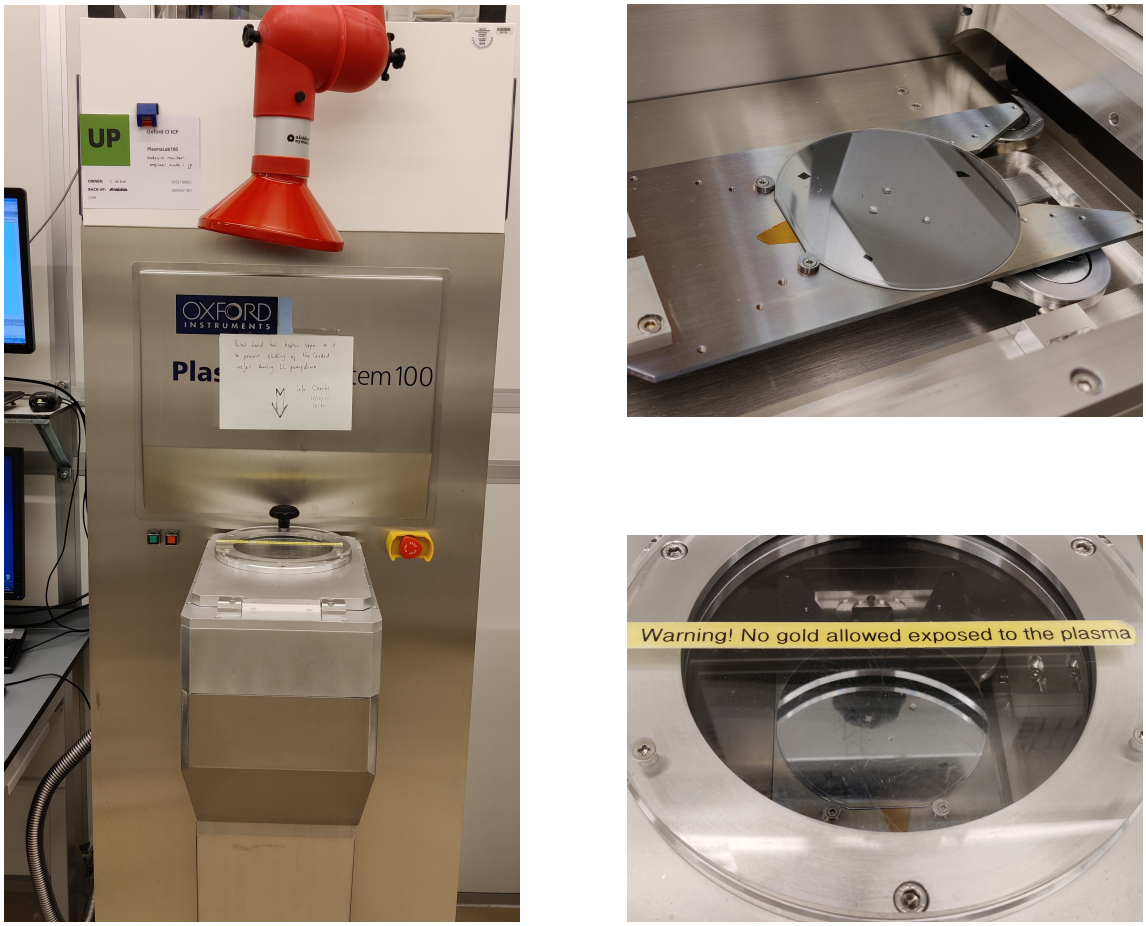


Figure 3.29: Photos of the Oxford ICP Cl equipment tool inside Kavli Nanolab Delft, used for surface etching with O_2 plasma. The samples can be seen mounted on a wafer, which is inserted inside the machine.

IMPLANTATION PATTERN DESIGNS FOR N ION IMPLANTATION

Three different implantation patterns were designed for nitrogen implantation, based on the desired outcome and the diamond size. The first of these was a 16×16 array with regards to the center of the diamond sample, as seen in Figure 3.30. This design was meant to be used as part of the final CMOS-integrated NV-based diamond sensor described in section 1.6. The implantation parameters here were set to 20 ^{14}N ions per point, at an energy of 11 keV, which would result in 15.5 ± 5.5 nm deep placement of nitrogen ions, and an angle of 7°. The pitch (distance between each implanted ion) was chosen to be 42.34 µm horizontally and 43.02 µm vertically, in order to match the pitch of the designed SPAD array chip, for potential emission coupling later on.

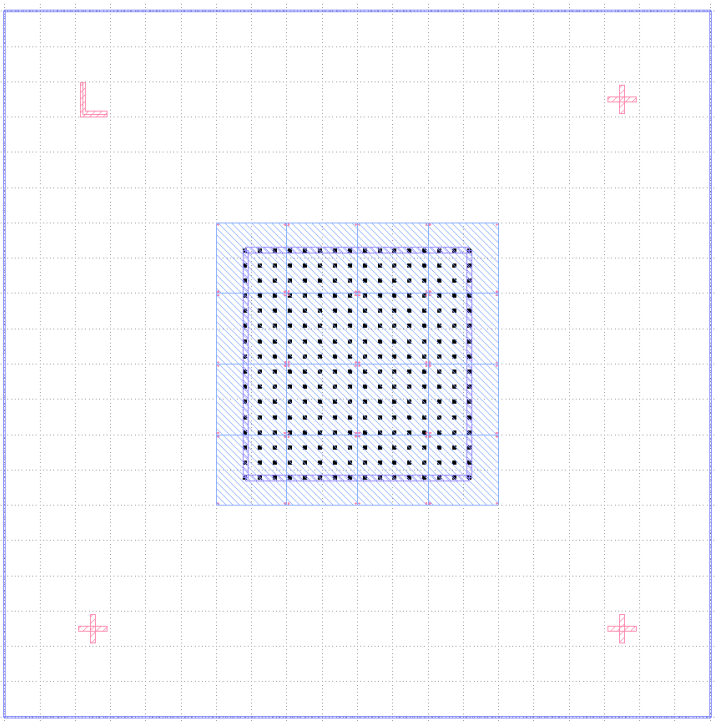


Figure 3.30: KLayout image depicting the pattern designed for a 16×16 nitrogen ion implantation.

The second pattern consists of an array of ^{14}N ions, with a pitch of 1 µm between them. It is designed for the samples with an area of $2 \times 2\,\text{mm}^2$, with the goal of performing an ion "dose test". For this purpose, the sample's area was split into 10 sites, with each site corresponding to a different number of nitrogen ions per point, ranging from 10 ions/point to 50 ions/point, as seen in Figure 3.32. The implantation energy was set to 11 keV, at an angle of 7°. The KLayout design can be found in Figure 3.31.

The third and final nitrogen implantation pattern was designed for the $4.5 \times 4.5\,\text{mm}^2$ diamond substrates. It contains the design seen in Figure 3.32 in a 2×2 matrix and uses the same implantation parameters.

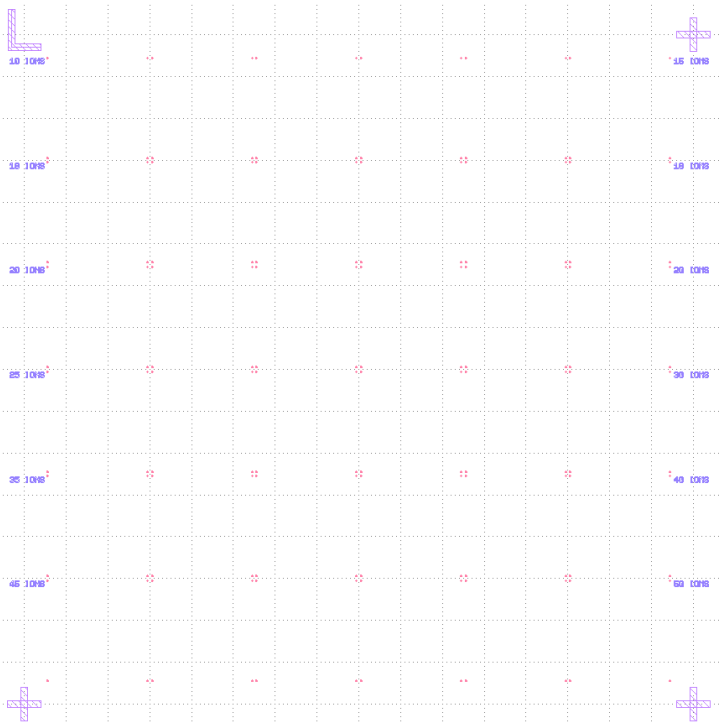


Figure 3.31: KLayout image depicting the pattern designed for nitrogen single-ion implantation on $2 \times 2\,\mathrm{mm}^2$ diamond substrates.

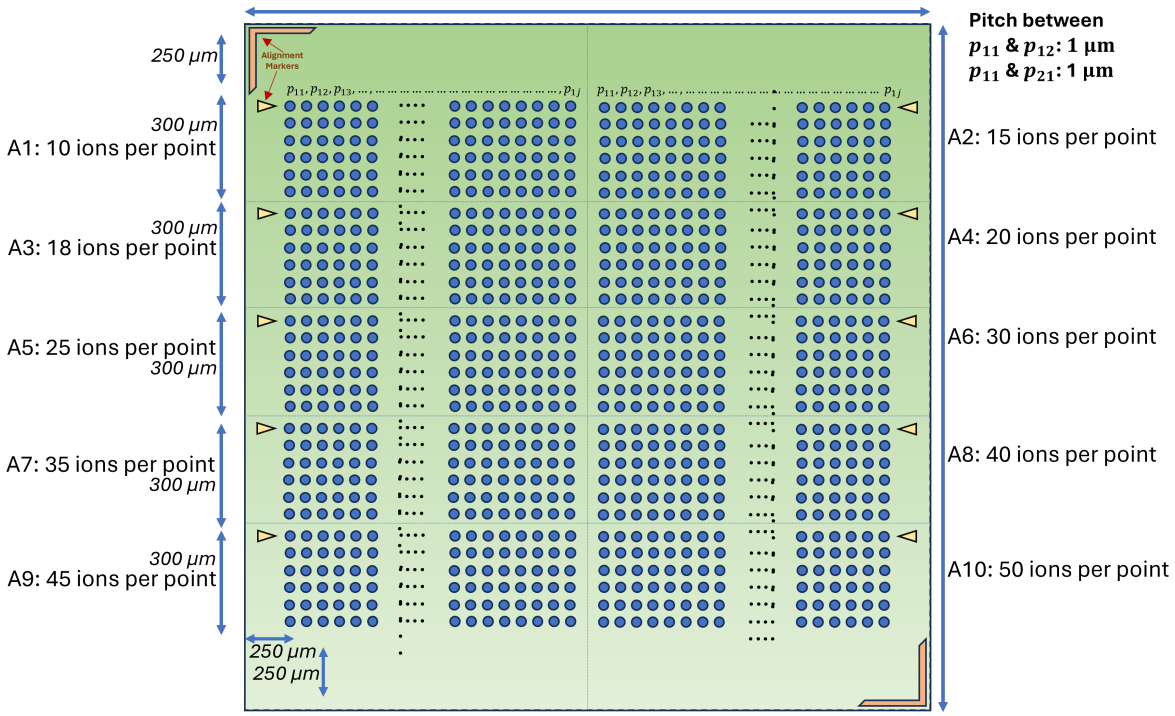
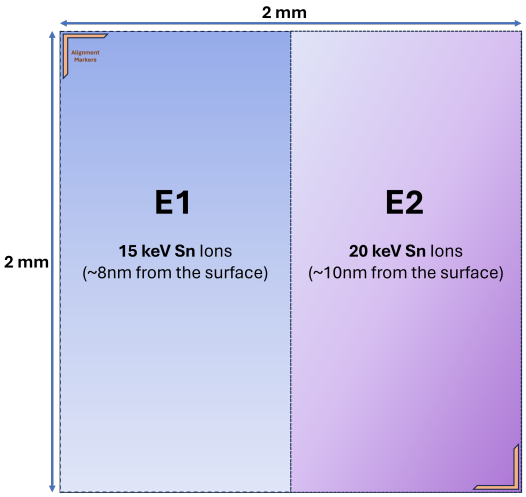


Figure 3.32: Pattern designed for nitrogen single ion implantation on $2 \times 2\,\mathrm{mm}^2$ diamond substrates.

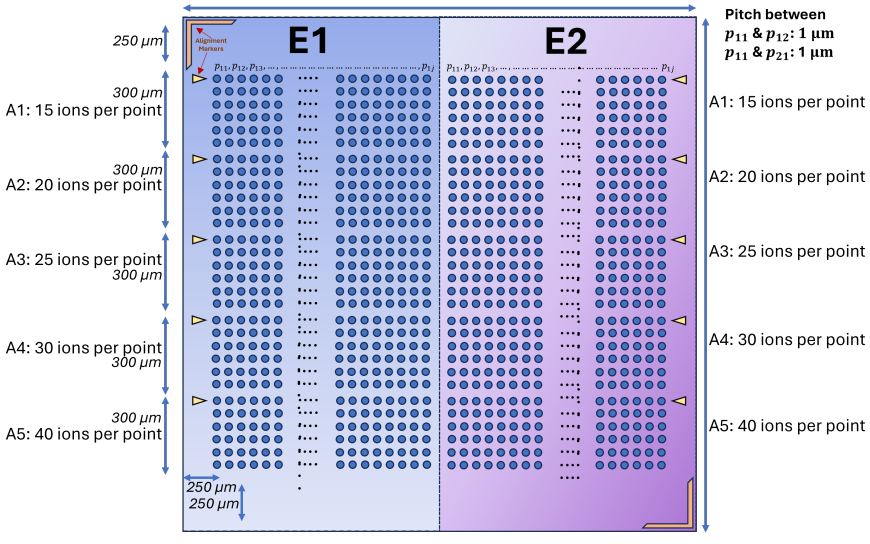
IMPLANTATION PATTERN DESIGN FOR SN ION IMPLANTATION

Following the same concept as the nitrogen ion implantation described above, a tin ion "dose test" implantation pattern was designed for the $2 \times 2\,\mathrm{mm}^2$ diamond substrates. This time, the diamond's surface was "split" in two, in order to implant each area with a different ion energy, for subsequent testing and comparison. One area was chosen to be implanted with 15 keV $^{120}Sn^{+}$ ions, while the other was to be subjected to implantation with 20 keV ions, resulting in implantation depths of $8.4 \pm 1.7\,\mathrm{nm}$ and $10.0 \pm 1.9\,\mathrm{nm}$, respectively (see Figure 3.33a).

Each implantation energy area was then subdivided into five sites. There, each site was designed to be implanted with a different amount of tin ions per point, ranging from 15 ions/point to 40 ions/point (see Figure 3.33b). These diamond substrates are going to require subsequent overgrowth and annealing, in order to efficiently activate the SnV color centers.



(a)



(b)

Figure 3.33: Patterns designed for tin single-ion implantation on $2 \times 2\,\mathrm{mm}^2$ diamond substrates. **(a)** Overview showing two distinct implantation-energy areas. **(b)** Detailed view of the five implantation sites per energy (15–40 ions/point).

3.7. OPTICAL CHARACTERIZATION OF SN-IMPLANTED DIAMOND SUBSTRATES

3.7.1. CHARACTERIZATION FOLLOWING OVERGROWTH

To verify the presence of SnV color centers in diamond, the broad beam implanted diamonds (both blanket- and mask-implanted substrates) underwent a series of optical characterization measurements. First, Raman spectroscopy was employed immediately following the overgrowth process on the implanted samples. The mask-implanted substrate did not exhibit any obvious signatures of SnV center presence at first glance. This can be partly attributed to the large pitch of the implanted ions (20 µm), the lack of orientation markers facilitating the precise localization of emitters, and also the inadequate annealing, which is crucial for defect activation and lattice restoration. Additionally, the Raman spectroscopy sensitivity might have been insufficient to detect sparse emitters that are distributed over such large areas, as the laser spot size was significantly smaller than the implantation pitch, severely limiting the statistical probability of directly measuring an implanted site. In contrast, the blanket Sn-implanted sample showed clear indications of SnV center formation after overgrowth, as demonstrated in Figure 3.34.

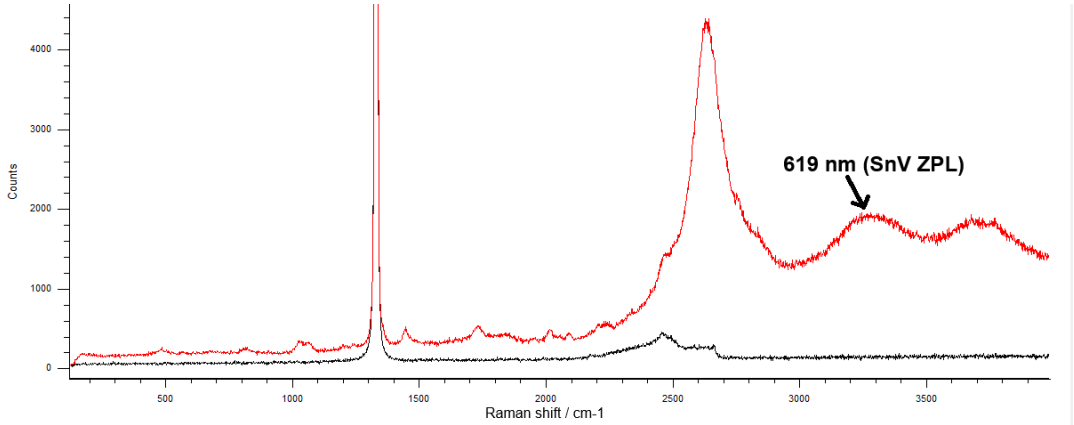


Figure 3.34: Raman spectroscopy image of the blanket Sn-implanted diamond substrate. The red spectrum corresponds to the experimentally measured data, taken close to the front side of the sample, where the Sn implantation took place. The black spectrum corresponds to the back side, where no SnV centers are expected. Excitation was done using a 514 nm green laser. The peak corresponding to 619 nm can be labeled as SnV ZPL emission, thus confirming the presence of activated SnV centers.

While the Raman measurements provided initial evidence of SnV center formation, particularly for the blanket-implanted sample, further confirmation was sought through photoluminescence spectroscopy using a fiber-coupled spectrometer setup. Both the blanket and mask-implanted samples were examined to identify clear SnV emissions upon excitation with a 532 nm green laser. The spectrometer utilized components of the ODMR setup described in chapter 2. However, in this configuration, emitted photons were coupled into a fiber guiding them into the spectrometer, rather than a photodetector. Additionally, the longpass filter with a 633 nm cutoff was replaced with a 600 nm filter due to the expected ZPL of SnV centers around 620 nm.

Nonetheless, the spectra recorded appeared inconclusive, lacking clear emission peaks around 619–621 nm (see Figure 3.36). Several factors could account for these unclear outcomes. Firstly, insufficient defect activation was likely due to the absence of ap-



Figure 3.35: Photos of the fabricated blanket and mask Sn-implanted diamond substrates.

propriate high-temperature annealing, necessary for mobilizing implanted ions and vacancies to form stable SnV centers. Secondly, the collection efficiency may have been severely compromised by suboptimal fiber coupling, misalignment between the sample and fiber, or improper focusing of excitation and collection optics. Moreover, the presence of background fluorescence or scattering from defects and impurities introduced during implantation or diamond overgrowth may have obscured the weak SnV emission peaks. Lastly, potential inaccuracies in the spectrometer's calibration could have further contributed to the ambiguity of the obtained data.

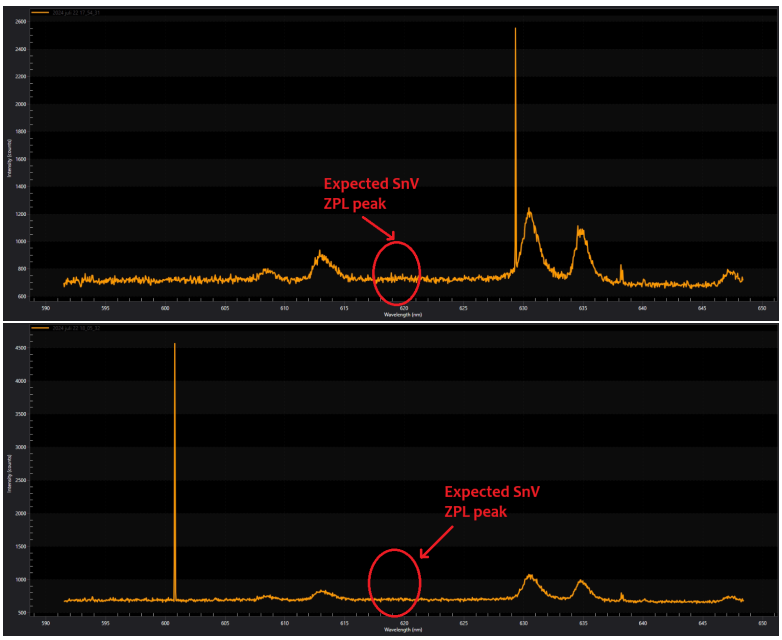


Figure 3.36: PL spectra of the mask-implanted diamond substrate, acquired with a spectrometer with a grating set to 600 grooves/mm, and using a 532 nm excitation laser with a power of 1.08 mW. Although, some peaks are visible around 631 nm and 635 nm, there is no definitive evidence of SnV center presence in these spectra.

Given the limited clarity of the spectrometer results, spatially resolved PL scans were subsequently performed using the previously assembled confocal ODMR setup equipped with a 600 nm cutoff longpass filter. These measurements were conducted to spatially map potential emission sites and evaluate SnV center activation across the samples' surfaces. As previously mentioned, the lack of adequate annealing significantly impacted the results, limiting observable activated SnV centers. Adding to these challenges, tech-

nical limitations such as drift in the piezo scanning stage, instability of laser power, or variations in the confocal microscope's focal plane could also negatively affect the spatial accuracy and sensitivity of these scans, further complicating the clear identification and localization of the expected SnV emission sites. The PL maps for both blanket and mask Sn-implanted diamond substrates are presented in Figure 3.37.

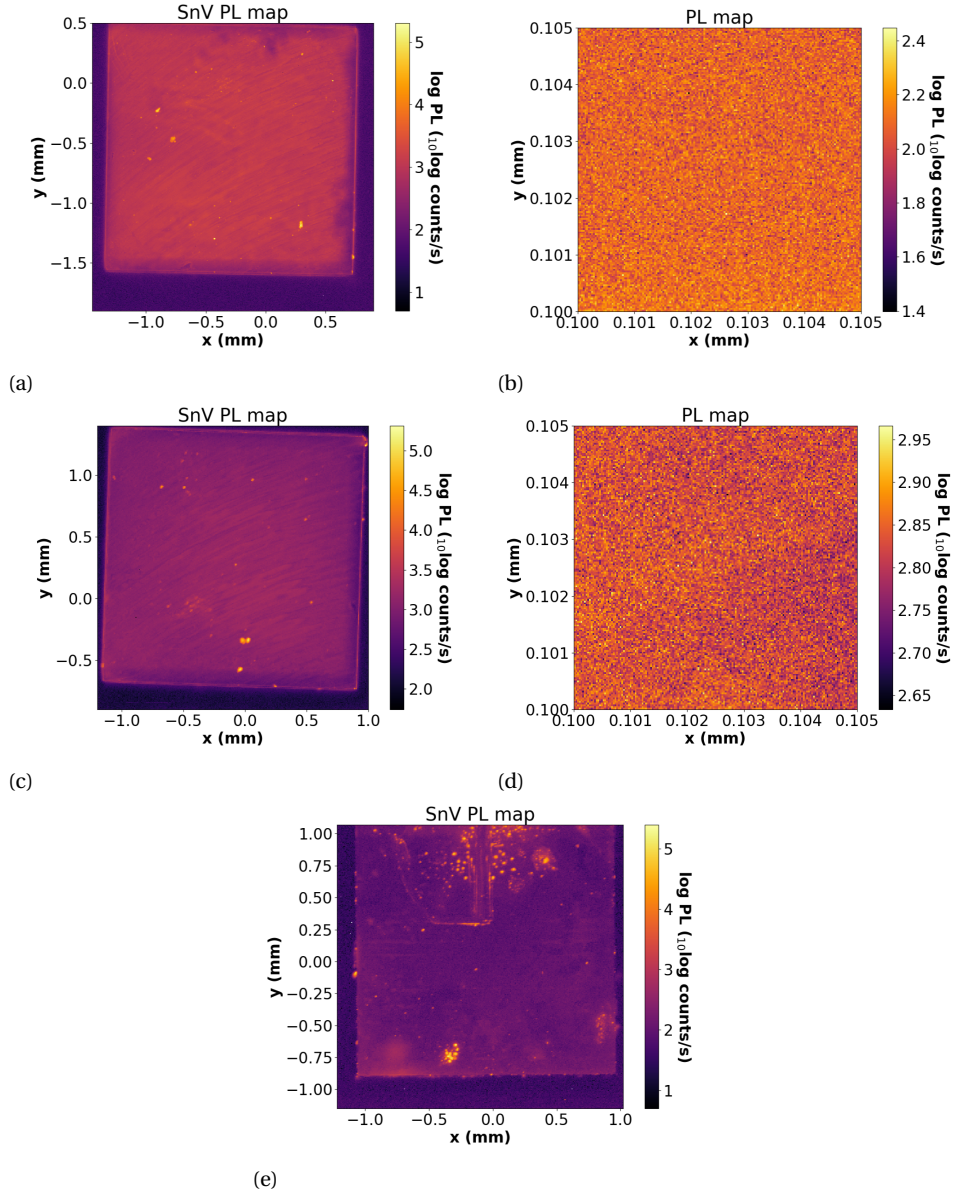


Figure 3.37: PL maps of tin-implanted diamond substrates under 532 nm excitation. **(a)** Blanket implantation, front side whole-sample map at ≃ 0.95 mW. **(b)** Blanket implantation, front side $5 \times 5\ \mu m^2$ zoom at ≃ 0.99 mW. **(c)** Blanket implantation, back side whole-sample map at ≃ 4.22 mW. **(d)** Blanket implantation, back side $5 \times 5\ \mu m^2$ zoom at ≃ 0.99 mW. **(e)** Masked single-ion implantation, front side whole-sample map at ≃ 0.95 mW.

Despite the efforts to detect photoluminescence from activated centers, the absence of a post-implantation annealing step significantly limited the formation of optically active SnV centers in the overgrown substrates. This underscores the crucial role of thermal or laser-based annealing in enabling vacancy diffusion and subsequent complex formation with implanted Sn atoms.

3.7.2. CHARACTERIZATION FOLLOWING ANNEALING

To investigate the impact of annealing on SnV center activation, a set of post-processing experiments was conducted, in a research carried out by E. Görk (2025). These were performed on a separate batch of identically blanket tin-implanted diamond substrates that had not undergone overgrowth, in order to isolate and evaluate the role of annealing alone in defect activation. These substrates -which had tin ions implanted at a depth of roughly 75 nm- exhibited clear and distinct emitter generation following femtosecond-laser and high-temperature furnace annealing.

FEMTOSECOND-LASER ANNEALING

The first of the two selected samples was subjected to a sequence of fs-laser scans aimed at activating the implanted tin atoms. Specifically, the sample underwent four sequential fs-laser annealing sessions. The three first made use of a 800 nm wavelength laser, with a beam radius of 4 mm at the diamond surface and increasing fluences of $0.1\,\mathrm{J\,cm^{-2}}$, $10\,\mathrm{J\,cm^{-2}}$ and $20\,\mathrm{J\,cm^{-2}}$, followed by a final session with a 400 nm wavelength fs-laser with a beam radius that is estimated to be < 4 mm. The pulse duration was 60 fs, with a repetition rate of 1.4 kHz. The fs-laser annealing parameters are summarized in Table 3.6 below:

Table 3.6: Femtosecond-laser annealing parameters.

Parameter	Session 1	Session 2	Session 3	Session 4
Wavelength (nm)	800	800	800	400
Beam radius (mm)	4	4	4	<4
Laser power (mW)	15.8	15.7	155	15.2
Fluence $\left(\mathrm{J\,cm^{-2}}\right)$	0.1	10.0	20.0	5.5e-5
Pulse duration (fs)	60	60	60	60
Repetition rate (kHz)	1.4	1.4	1.4	1.4
Dwell time	4 s	5 min 20 s	1 min 4 s	14 min 24 s

Subsequently, the optical response was characterized using Raman spectroscopy with a 514 nm excitation laser, through a 50× objective lens with an NA of 0.75. Measurements were taken both before and after fs-laser annealing (see Figure 3.38), in order to estimate the activation yield, and to confirm the formation of SnV centers.

After the fourth fs-laser annealing session, emission at the 619 nm wavelength was detected, corresponding to the SnV^-'s ZPL. Additionally, a weak shoulder also became visible near 595 nm, associated with type-II SnV centers. However, the ZPL intensity remained weak, at less than 1.5× the background level, while the type-II peak was barely resolved. The limited optical activation can be attributed to several physical constraints. First, the limited optical activation can be partly attributed to the shallow thermal penetration depth of fs-laser pulses, especially at shorter wavelengths, where nonlinear absorption limits energy deposition to a sub-micrometer region near the surface [56]. Furthermore, the high thermal conductivity of diamond leads to rapid heat dissipation on

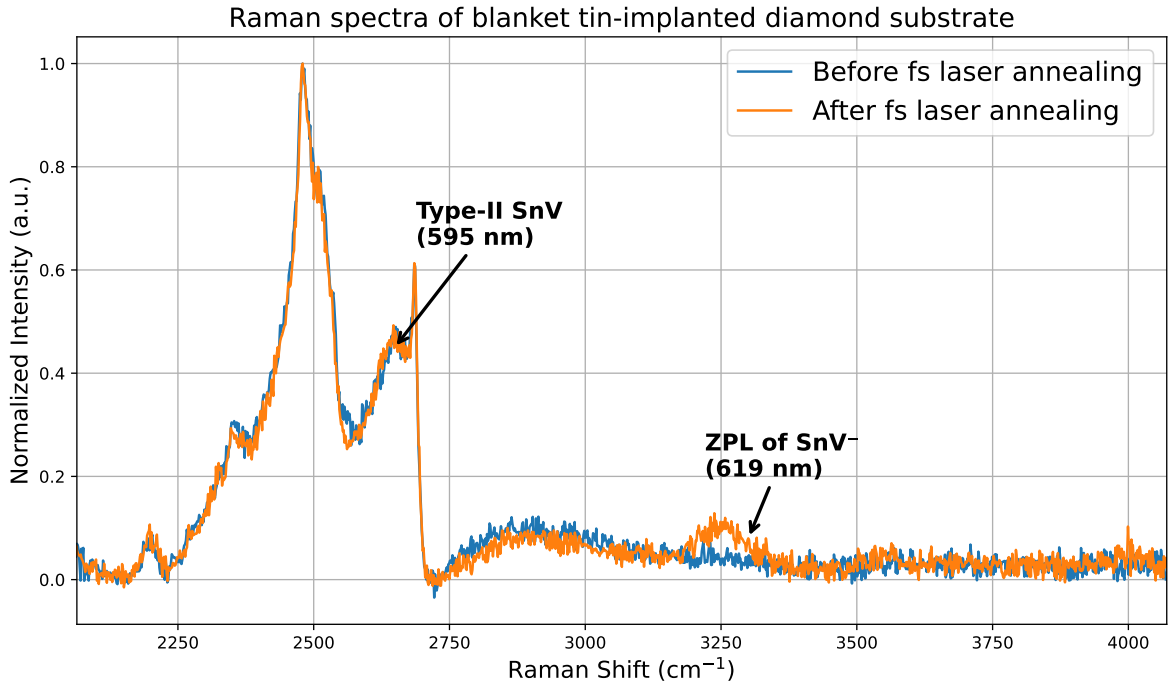


Figure 3.38: Raman spectra of a blanket tin-implanted diamond substrate, measured before and after fs-laser annealing, with a laser power of 2.5 mW. After annealing, weak peaks appear at 595 nm and 619 nm, corresponding to type-II SnV centers and the ZPL of SnV^- centers, respectively.

the picosecond timescale, resulting in ultrafast quenching. This effect could prevent sufficient atomic mobility for lattice recovery or stable SnV center formation [56].

HIGH-TEMPERATURE FURNACE ANNEALING

The second sample was annealed in a high-vacuum furnace. The temperature was ramped up to a peak of 1100°C and held constant for 10 h, for a total of 54 h of furnace dwell time, including ramp-up and cool-down stages. Table 3.7 below summarizes the furnace annealing process parameters.

Table 3.7: Temperature profile of the high-vacuum furnace annealing process.

Stage	Temperature Range (°C)	Duration
Ramp 1	20 → 400	4 h
Hold 1	400	8 h
Ramp 2	400 → 800	12 h
Hold 2	800	8 h
Ramp 3	800 → 1100	12 h
Hold 3	1100	10 h

As shown in Fig. 3.39, this treatment resulted in a dramatic enhancement of the optical signal. The clearly resolved peak of the SnV^- centers' ZPL at 619 nm exceeded the

background by over an order of magnitude, necessitating a fivefold reduction in excitation laser power to avoid detector saturation. Moreover, a weak peak appeared at 595 nm, confirming the formation of type-II SnV centers. This significant improvement is attributed to more efficient diffusion of vacancies over hundreds of micrometers, sufficient to overlap with the implanted tin profile (implantation depth ~ 75 nm) and enable effective color center formation.

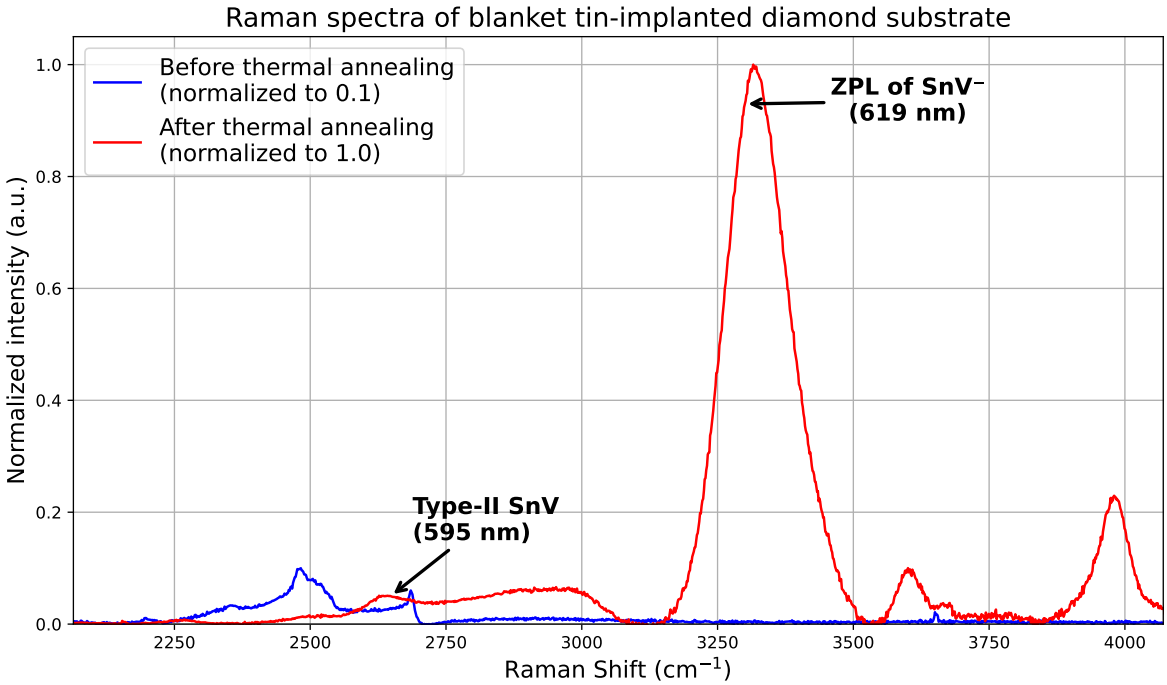


Figure 3.39: Raman spectra of a blanket tin-implanted diamond substrate, measured before (with a laser power of 2.5 mW) and after thermal annealing (with a laser power of 0.5 mW). Following annealing, a weak peak emerges at 595 nm, attributed to type-II SnV centers, while a distinct peak at 619 nm corresponds to the ZPL of SnV^- centers.

In closing, a direct experimental comparison of the two annealing approaches and their impact on SnV optical signatures is presented in Table 3.8 below.

Table 3.8: Summary of annealing conditions and resulting optical signatures for each sample.

Sample	Annealing protocol	SnV^- ZPL (619 nm)	Type-II SnV^- (595 nm)
Diamond #1	4× fs-laser annealing (800 nm) + 1× fs-laser (400 nm)	< 1.5× background	weak
Diamond #2	Furnace annealing at 1100 °C	> 10× background	weak

BIBLIOGRAPHY

[1] Matthias Schreck et al. “Large-area high-quality single crystal diamond”. In: *MRS Bulletin* 39.6 (2014), pp. 504–510. ISSN: 1938-1425. DOI: 10.1557/mrs.2014.96.

[2] Robert J. Nemanich et al. “CVD diamond—Research, applications, and challenges”. In: *MRS Bulletin* 39.6 (2014), pp. 490–494. DOI: 10.1557/mrs.2014.97.

[3] Ying Ren et al. “Recent progress in homoepitaxial single-crystal diamond growth via MPCVD”. In: *Journal of Materials Science: Materials in Electronics* 35.7 (2024), p. 525. ISSN: 1573-482X. DOI: 10.1007/s10854-024-12267-3.

[4] Soumen Mandal. “Nucleation of diamond films on heterogeneous substrates: a review”. In: *RSC Adv.* 11 (17 2021), pp. 10159–10182. DOI: 10.1039/D1RA00397F.

[5] Soumen Mandal et al. “Thick, Adherent Diamond Films on AlN with Low Thermal Barrier Resistance”. In: *ACS Applied Materials & Interfaces* 11.43 (2019). PMID: 31603642, pp. 40826–40834. DOI: 10.1021/acsami.9b13869.

[6] S.-Tong Lee, Zhangda Lin, and Xin Jiang. “CVD diamond films: nucleation and growth”. In: *Materials Science and Engineering: R: Reports* 25.4 (1999), pp. 123–154. ISSN: 0927-796X. DOI: https://doi.org/10.1016/S0927-796X(99)00003-0.

[7] Alix Gicquel et al. “CVD diamond films: from growth to applications”. In: *Current Applied Physics* 1.6 (2001), pp. 479–496. ISSN: 1567-1739. DOI: https://doi.org/10.1016/S1567-1739(01)00061-X.

[8] X.T Zhou et al. “Heteroepitaxial nucleation of diamond on Si(100) via double bias-assisted hot filament chemical vapor deposition”. In: *Diamond and Related Materials* 9.2 (2000), pp. 134–139. ISSN: 0925-9635. DOI: https://doi.org/10.1016/S0925-9635(99)00264-2.

[9] Huimin Liu and David S. Dandy. “Studies on nucleation process in diamond CVD: an overview of recent developments”. In: *Diamond and Related Materials* 4.10 (1995), pp. 1173–1188. ISSN: 0925-9635. DOI: https://doi.org/10.1016/0925-9635(96)00297-2.

[10] F. P. Bundy et al. “Man-Made Diamonds”. In: *Nature* 176.4471 (1955), pp. 51–55. ISSN: 1476-4687. DOI: 10.1038/176051a0.

[11] H. Sumiya and S. Satoh. “High-pressure synthesis of high-purity diamond crystal”. In: *Diamond and Related Materials* 5.11 (1996), pp. 1359–1365. ISSN: 0925-9635. DOI: https://doi.org/10.1016/0925-9635(96)00559-6.

[12] Scott S. Dossa et al. “Analysis of the High-Pressure High-Temperature (HPHT) growth of single crystal diamond”. In: *Journal of Crystal Growth* 609 (2023), p. 127150. ISSN: 0022-0248. DOI: https://doi.org/10.1016/j.jcrysgro.2023.127150.

[13] Inga A. Dobrinets, Victor G. Vins, and Alexander M. Zaitsev. "Parameters of HPHT Treatment". In: *HPHT-Treated Diamonds: Diamonds Forever*. Berlin, Heidelberg: Springer Berlin Heidelberg, 2013, pp. 27–37. ISBN: 978-3-642-37490-6. DOI: 10.1007/978-3-642-37490-6_3.

[14] A. Tallaire et al. "Thick CVD diamond films grown on high-quality type IIa HPHT diamond substrates from New Diamond Technology". In: *Diamond and Related Materials* 77 (2017), pp. 146–152. ISSN: 0925-9635. DOI: https://doi.org/10.1016/j.diamond.2017.07.002.

[15] Nikolay I. Alekseyev et al. "Temperature- and Pressure-Reducing Regimes in the Growth Cell of HPHT Diamonds, Optimal for Preserving Crystal Integrity after Growth Completion". In: *C* 9.2 (2023). ISSN: 2311-5629. DOI: 10.3390/c9020052.

[16] R. H. Telling et al. "Theoretical Strength and Cleavage of Diamond". In: *Phys. Rev. Lett.* 84 (22 May 2000), pp. 5160–5163. DOI: 10.1103/PhysRevLett.84.5160.

[17] A. Tallaire et al. "High quality thick CVD diamond films homoepitaxially grown on (111)-oriented substrates". In: *Diamond and Related Materials* 41 (2014), pp. 34–40. ISSN: 0925-9635. DOI: https://doi.org/10.1016/j.diamond.2013.11.002.

[18] Samuel M. Parks et al. "Fabrication of (111)-faced single-crystal diamond plates by laser nucleated cleaving". In: *Diamond and Related Materials* 84 (2018), pp. 20–25. ISSN: 0925-9635. DOI: https://doi.org/10.1016/j.diamond.2018.02.013.

[19] Julia Michl et al. "Perfect alignment and preferential orientation of nitrogen-vacancy centers during chemical vapor deposition diamond growth on (111) surfaces". In: *Applied Physics Letters* 104.10 (Mar. 2014). ISSN: 1077-3118. DOI: 10.1063/1.4868128.

[20] Th. Frauenheim et al. "Stability, reconstruction, and electronic properties of diamond (100) and (111) surfaces". In: *Phys. Rev. B* 48 (24 Dec. 1993), pp. 18189–18202. DOI: 10.1103/PhysRevB.48.18189.

[21] R. Graupner et al. "Dispersions of surface states on diamond (100) and (111)". In: *Phys. Rev. B* 55 (16 Apr. 1997), pp. 10841–10847. DOI: 10.1103/PhysRevB.55.10841.

[22] Feng Yucai and Tian Feng. "Broad beam ion source for ion implantation". In: *Review of Scientific Instruments* 61.1 (Jan. 1990), pp. 318–320. ISSN: 0034-6748. DOI: 10.1063/1.1141281.

[23] Yusheng Rao et al. "A versatile broad-beam ion source". In: *Review of Scientific Instruments* 61.1 (Jan. 1990), pp. 321–323. ISSN: 0034-6748. DOI: 10.1063/1.1141282.

[24] Emanuele Rimini. *Ion Implantation: Basics to Device Fabrication*. 1st ed. The Springer International Series in Engineering and Computer Science. Springer New York, NY, 1995, pp. XIII, 393. ISBN: 978-0-7923-9520-1. DOI: 10.1007/978-1-4615-2259-1.

[25] Leonard Rubin and John Poate. “Ion implantation in silicon technology”. In: *Industrial Physicist* 9.3 (2003), pp. 12–15. URL: https://www.researchgate.net/publication/279705780_Ion_implantation_in_silicon_technology.

[26] Roman A. Khmelnitsky et al. “Damage accumulation in diamond during ion implantation”. In: *Journal of Materials Research* 30.9 (2015), pp. 1583–1592. ISSN: 2044-5326. DOI: 10.1557/jmr.2015.21.

[27] S. Sangtawesin et al. “Highly tunable formation of nitrogen-vacancy centers via ion implantation”. In: *Applied Physics Letters* 105.6 (Aug. 2014), p. 063107. ISSN: 0003-6951. DOI: 10.1063/1.4892971.

[28] Birgit J M Hausmann et al. “Single-color centers implanted in diamond nanostructures”. In: *New Journal of Physics* 13.4 (Apr. 2011), p. 045004. DOI: 10.1088/1367-2630/13/4/045004.

[29] Igal Bayn et al. “Generation of Ensembles of Individually Resolvable Nitrogen Vacancies Using Nanometer-Scale Apertures in Ultrahigh-Aspect Ratio Planar Implantation Masks”. In: *Nano Letters* 15.3 (2015). PMID: 25621759, pp. 1751–1758. DOI: 10.1021/nl504441m.

[30] Shuntaro Ishizu et al. “Spin coherence and depths of single nitrogen-vacancy centers created by ion implantation into diamond via screening masks”. In: *Journal of Applied Physics* 127.24 (June 2020), p. 244502. ISSN: 0021-8979. DOI: 10.1063/5.0012187.

[31] Y.J. Xiao et al. “The study of Ga+ FIB implanting crystal silicon and subsequent annealing”. In: *Nuclear Instruments and Methods in Physics Research Section B: Beam Interactions with Materials and Atoms* 307 (2013). The 18th International Conference on Ion Beam Modifications of Materials (IBMM2012), pp. 253–256. ISSN: 0168-583X. DOI: https://doi.org/10.1016/j.nimb.2012.12.112.

[32] Syuto Tamura et al. “Array of bright silicon-vacancy centers in diamond fabricated by low-energy focused ion beam implantation”. In: *Applied Physics Express* 7.11 (Oct. 2014), p. 115201. DOI: 10.7567/APEX.7.115201.

[33] Midrel Wilfried Ngandeu Ngambou et al. “Hot ion implantation to create dense NV center ensembles in diamond”. In: *Applied Physics Letters* 124.13 (Mar. 2024), p. 134002. ISSN: 0003-6951. DOI: 10.1063/5.0196719.

[34] Jacques Gierak. “Focused ion beam technology and ultimate applications”. In: *Semiconductor Science and Technology* 24.4 (Mar. 2009), p. 043001. DOI: 10.1088/0268-1242/24/4/043001.

[35] F. Jelezko and J. Wrachtrup. “Single defect centres in diamond: A review”. In: *physica status solidi (a)* 203.13 (2006), pp. 3207–3225. DOI: https://doi.org/10.1002/pssa.200671403.

[36] P. Maletinsky et al. “A robust scanning diamond sensor for nanoscale imaging with single nitrogen-vacancy centres”. In: *Nature Nanotechnology* 7.5 (2012), pp. 320–324. ISSN: 1748-3395. DOI: 10.1038/nnano.2012.50.

[37] D. Le Sage et al. “Optical magnetic imaging of living cells”. In: *Nature* 496.7446 (2013), pp. 486–489. ISSN: 1476-4687. DOI: 10.1038/nature12072.

[38] David R. Glenn et al. “Single-cell magnetic imaging using a quantum diamond microscope”. In: *Nature Methods* 12.8 (2015), pp. 736–738. ISSN: 1548-7105. DOI: 10.1038/nmeth.3449.

[39] Albert Boretti and Stefania Castelletto. “Nanometric resolution magnetic resonance imaging methods for mapping functional activity in neuronal networks”. In: *MethodsX* 3 (2016), pp. 297–306. ISSN: 2215-0161. DOI: https://doi.org/10.1016/j.mex.2016.04.003.

[40] Valentin Radu et al. “Dynamic Quantum Sensing of Paramagnetic Species Using Nitrogen-Vacancy Centers in Diamond”. In: *ACS Sensors* 5.3 (2020). PMID: 31867948, pp. 703–710. DOI: 10.1021/acssensors.9b01903.

[41] Federico Gorrini et al. “Long-Lived Ensembles of Shallow NV– Centers in Flat and Nanostructured Diamonds by Photoconversion”. In: *ACS Applied Materials & Interfaces* 13.36 (2021). PMID: 34468122, pp. 43221–43232. DOI: 10.1021/acsami.1c09825.

[42] Alison E. Rugar et al. “Generation of Tin-Vacancy Centers in Diamond via Shallow Ion Implantation and Subsequent Diamond Overgrowth”. In: *Nano Letters* 20.3 (2020). doi: 10.1021/acs.nanolett.9b04495, pp. 1614–1619. ISSN: 1530-6984. DOI: 10.1021/acs.nanolett.9b04495.

[43] Y. H. Tang, B. Bi, and B. Golding. “Diamond Heteroepitaxial Lateral Overgrowth”. In: *MRS Online Proceedings Library* 1734.1 (2014), pp. 20–25. ISSN: 1946-4274. DOI: 10.1557/opl.2015.175.

[44] Shi Tang et al. “A Thick Overgrowth of CVD Synthetic Diamond on a Natural Diamond”. In: *The Journal of Gemmology* 36 (Jan. 2018), pp. 134–141. DOI: 10.15506/JoG.2018.36.2.134.

[45] Christoph Findler et al. “Indirect overgrowth as a synthesis route for superior diamond nano sensors”. In: *Scientific Reports* 10.1 (2020), p. 22404. ISSN: 2045-2322. DOI: 10.1038/s41598-020-79943-2.

[46] S. B. van Dam et al. “Optical coherence of diamond nitrogen-vacancy centers formed by ion implantation and annealing”. In: *Phys. Rev. B* 99 (16 Apr. 2019), p. 161203. DOI: 10.1103/PhysRevB.99.161203.

[47] Srivatsa Chakravarthi et al. “Window into NV center kinetics via repeated annealing and spatial tracking of thousands of individual NV centers”. In: *Phys. Rev. Mater.* 4 (2 Feb. 2020), p. 023402. DOI: 10.1103/PhysRevMaterials.4.023402.

[48] Alan T. Collins et al. “High-temperature annealing of optical centers in type-I diamond”. In: *Journal of Applied Physics* 97.8 (Apr. 2005), p. 083517. ISSN: 0021-8979. DOI: 10.1063/1.1866501.

[49] T. Yamamoto et al. “Extending spin coherence times of diamond qubits by high-temperature annealing”. In: *Phys. Rev. B* 88 (7 Aug. 2013), p. 075206. DOI: 10.1103/PhysRevB.88.075206.

[50] Tzveta Apostolova, Vasyl Kurylo, and Iaroslav Gnilitskyi. “Ultrafast Laser Processing of Diamond Materials: A Review”. In: *Frontiers in Physics* 9 (Dec. 2021). DOI: 10.3389/fphy.2021.650280.

[51] Johannes Engel et al. “Combining femtosecond laser annealing and shallow ion implantation for local color center creation in diamond”. In: *Applied Physics Letters* 122.23 (June 2023), p. 234002. ISSN: 0003-6951. DOI: 10.1063/5.0143922.

[52] F. Stock et al. “UV laser annealing of Diamond-Like Carbon layers obtained by Pulsed Laser Deposition for optical and photovoltaic applications”. In: *Applied Surface Science* 464 (2019), pp. 562–566. ISSN: 0169-4332. DOI: https://doi.org/10.1016/j.apsusc.2018.09.085.

[53] Aaron M. Day et al. “Laser writing of spin defects in nanophotonic cavities”. In: *Nature Materials* 22.6 (2023), pp. 696–702. ISSN: 1476-4660. DOI: 10.1038/s41563-023-01544-x.

[54] Xiao-Jie Wang et al. “Laser Writing of Color Centers”. In: *Laser & Photonics Reviews* 16.1 (2022), p. 2100029. DOI: https://doi.org/10.1002/lpor.202100029.

[55] Toshiyuki Nakamiya, Shin-ichi Aoqui, and Kenji Ebihara. “Experimental and numerical study on pulsed-laser annealing process of diamond-like carbon thin films”. In: *Diamond and Related Materials* 10.3 (2001). 11th European Conference on Diamond, Diamond-like Materials, Carbon Nanotubes, Nitrides and Silicon Carbide, pp. 905–909. ISSN: 0925-9635. DOI: https://doi.org/10.1016/S0925-9635(00)00536-7.

[56] Rafael R. Gattass and Eric Mazur. “Femtosecond laser micromachining in transparent materials”. In: *Nature Photonics* 2.4 (2008), pp. 219–225. ISSN: 1749-4893. DOI: 10.1038/nphoton.2008.47.

[57] Sivanandan S. Harilal et al. “Femtosecond Laser Ablation: Fundamentals and Applications”. In: *Laser-Induced Breakdown Spectroscopy: Theory and Applications*. Ed. by Sergio Musazzi and Umberto Perini. Berlin, Heidelberg: Springer Berlin Heidelberg, 2014, pp. 143–166. ISBN: 978-3-642-45085-3. DOI: 10.1007/978-3-642-45085-3_6.

[58] Lan Jiang et al. “Electrons dynamics control by shaping femtosecond laser pulses in micro/nanofabrication: modeling, method, measurement and application”. In: *Light: Science & Applications* 7.2 (2018), pp. 17134–17134. ISSN: 2047-7538. DOI: 10.1038/lsa.2017.134.

[59] Koji Sugioka and Ya Cheng. “Femtosecond laser three-dimensional micro- and nanofabrication”. In: *Applied Physics Reviews* 1.4 (Dec. 2014), p. 041303. ISSN: 1931-9401. DOI: 10.1063/1.4904320.

[60] Juliana M. P. Almeida et al. “Nonlinear optical spectrum of diamond at femtosecond regime”. In: *Scientific Reports* 7.1 (2017), p. 14320. ISSN: 2045-2322. DOI: 10.1038/s41598-017-14748-4.

[61] Cong Wang et al. “Nonlinear ionization mechanism dependence of energy absorption in diamond under femtosecond laser irradiation”. In: *Journal of Applied Physics* 113.14 (Apr. 2013), p. 143106. ISSN: 0021-8979. DOI: 10.1063/1.4801802.

[62] Guillaume Savriama. *TUTORIAL: TWO TEMPERATURE MODEL FOR ULTRASHORT PULSE LASER WITH COMSOL MULTIPHYSICS*. July 2021. DOI: 10.13140/RG.2.2.24211.81449.

[63] M. Schukraft et al. “Invited Article: Precision nanoimplantation of nitrogen vacancy centers into diamond photonic crystal cavities and waveguides”. In: *APL Photonics* 1.2 (May 2016), p. 020801. ISSN: 2378-0967. DOI: 10.1063/1.4948746.

[64] Tae-Yeon Hwang et al. “Sub-10 nm Precision Engineering of Solid-State Defects via Nanoscale Aperture Array Mask”. In: *Nano Letters* 22.4 (Feb. 2022), pp. 1672–1679. ISSN: 1530-6992. DOI: 10.1021/acs.nanolett.1c04699.

4

STRAIN EFFECTS IN A DIRECTLY BONDED DIAMOND-ON-INSULATOR SUBSTRATE

The direct bonding process of a diamond-on-insulator (DOI) substrate enables monolithic integration of diamond photonic structures for quantum computing by improving photon collection efficiency and entanglement generation rate between emitters. It also addresses key fabrication challenges, such as robustness, bonding strength, and scalability. In this study, we investigate strain effects in DOI substrates following direct bonding. Strain generation is expected near the diamond-SiO_2/Si interface due to thermal expansion coefficient mismatch between the bonded materials. Strain-induced lattice distortions are characterized using nitrogen-vacancy (NV) centers in diamond via optically detected magnetic resonance (ODMR) and photoluminescence (PL) mapping. PL mapping reveals interference fringes in unbonded regions, indicating bonding irregularities. Depth-resolved ODMR measurements show a volumetric strain component increase of ~0.45 MHz and a shear component increase of ~0.71 MHz between the top surface and the DOI interface. However, ODMR signal contrast and peak linewidth remain largely unaffected, suggesting no visible deterioration in the optical properties of the emitters. By combining ODMR and PL mapping, this work establishes a robust methodology for assessing bonding quality and strain impact on NV centers, an essential step toward advancing scalable quantum technologies and integrated photonic circuits.

Parts of this chapter have been published in Physica Status Solidi (a), (22-07-2025) https://doi.org/10.1002/pssa.202500277 [1].

4.1. INTRODUCTION TO INTEGRATION TECHNOLOGY

One of the challenges in achieving robust quantum communication and high-fidelity quantum computing has long been the entanglement generation rate between NV centers, which is limited by the relatively low fraction of emitted coherent photons that can be detected. A solution to address this problem is to integrate NV centers into optical cavities with a high ratio of quality factor to mode volume. This is done to increase the zero-phonon line (ZPL) emission and improve collection efficiency [2].

However, current applications are limited by the challenges of growing large single crystal diamond (SCD) via chemical vapor deposition (CVD), which restricts its use in integrated photonics [3]. To overcome this, researchers are developing thin film diamond integrated with color centers in photonic crystal (PhC) cavities [4]. Two prominent approaches are hybrid and monolithic all-diamond systems [5]. Hybrid systems use non-diamond materials like silicon nitride or gallium phosphide coupled with diamond color centers for easier manufacturing and integration [6, 7, 8]. Nevertheless, they face issues with limited coupling efficiency. Monolithic all-diamond systems, which entail fabricating optical cavities directly on single crystal diamond substrates, have shown success with not only NV [9], but also SiV [10, 11], and GeV centers [9].

Such a monolithic fabrication technique is the direct bonding of diamond on insulator substrates. Hydrophilic (water-attracting) direct bonding, in particular, is preferred over indirect methods using adhesives, due to its high bonding strength, temperature stability, and industrial scalability [12]. Similar to Silicon-On-Insulator (SOI) substrate bonding [13], Diamond-On-Insulator (DOI) bonding adheres to the same operating principles. After the surface of the diamond and the insulator (in this case SiO_2) have been activated, they are then brought into contact, in order for them to create a bond, as a result of van der Waals forces, and form covalent bonds [13]. The material is subsequently annealed in order to enhance the quality of the interface [14].

However, despite the effectiveness of direct bonding and subsequent annealing in enhancing interface quality, this fabrication process can introduce unintended strain effects within the diamond structure. It is probable that the diamond, having undergone the aforementioned chemical processing, will exhibit further stress effects on the surface which is bonded to the insulator substrate. Furthermore, part of the direct bonding process takes place under a temperature of 200°C. During the cooling period, each of the bonded materials contracts at different rates, according to their unique thermal expansion coefficients. This mismatch between the thermal expansion rates between the diamond and the SiO_2/Si can lead to the generation of strain at their interface [15, 16], and potentially further deep into the diamond lattice.

These strain effects can cause deformations to the crystal lattice, which result in inhomogeneous broadening and degradation of the spin dephasing time of the NV centers. Therefore, it is deemed critical to be able to understand and visually map the effects of strain, providing meaningful insight into the quality of the bonded samples.

4.2. DIRECT BONDING PROCESS OVERVIEW

The fabrication of the diamond-on-insulator (DOI) substrate utilized in this work follows a hydrophilic direct bonding process, outlined in Figure 4.1. No adhesives were used in the bonding, which relied entirely on surface chemical activation and low-temperature annealing to achieve interfacial adhesion.

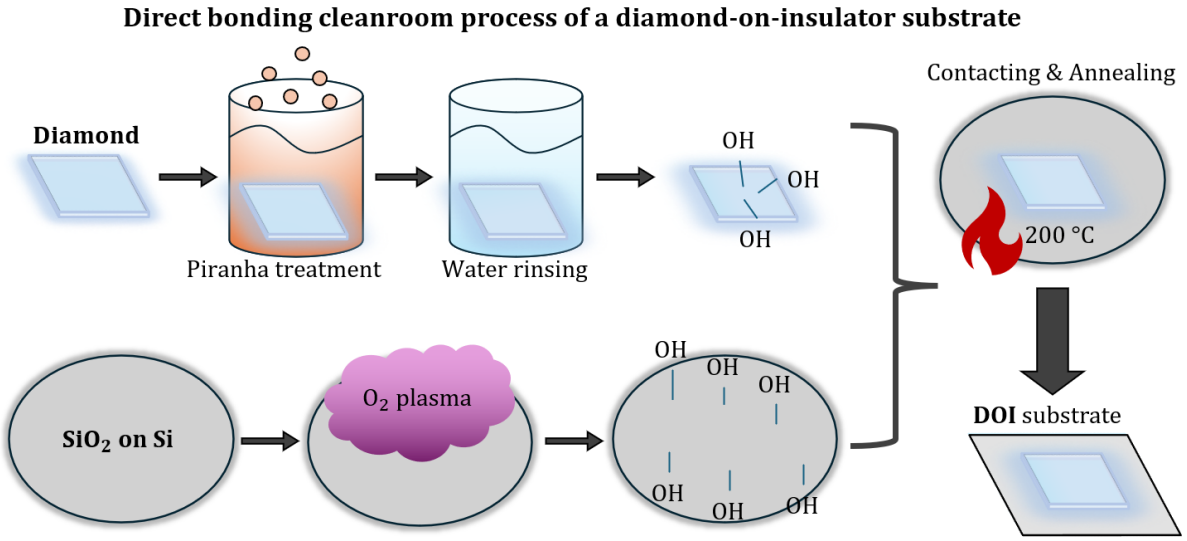


Figure 4.1: Schematic overview of the hydrophilic direct bonding process used to fabricate the diamond-on-insulator (DOI) substrate. The process begins with a type Ib, single-crystal, double-side polished, (100)-oriented diamond substrate, and a Si substrate, coated with a 300 nm PECVD SiO_2 layer, and diced into 25×25 mm^2 chips. Both substrates undergo chemical activation. The diamond is cleaned using Piranha solution (3:1 H_2SO_4:H_2O_2) at 75°C for 30 min and rinsed in deionized (DI) water for 5–10 min. Meanwhile, the SiO_2/Si substrate is rinsed with DI water for 5 min, and is then subjected to O_2 plasma treatment (1000 W, 5 min, with 400 sccm O_2 flow) using a PVA Tepla system. These steps remove surface contaminants and enrich the surface with silanol (Si–OH) groups, promoting hydrophilicity. After cleaning, the substrates are brought into contact at room temperature (20°C) and ambient humidity (~40%), allowing van der Waals and hydrogen bonding to form across a thin interfacial water layer. This pre-bonding interaction is stabilized through a low-temperature anneal at 200°C for 24 h, under N_2 flow. The annealing induces interfacial dehydration, resulting in covalent bond formation, thus completing the DOI heterostructure. The bonded stack typically exhibits high mechanical integrity with no visible voids or delamination.

Hydrophilic direct bonding is a process that involves creating a bond between surfaces treated to exhibit hydrophilic properties. The first step is surface activation, which prepares the surfaces for subsequent bonding by introducing reactive hydroxyl groups (–OH). For the diamond substrate, this involves thorough cleaning using a Piranha solution, a highly oxidative mixture of sulfuric acid (H_2SO_4) and hydrogen peroxide (H_2O_2) in a 3:1 ratio. The Piranha solution does not etch the diamond, but removes organic contamination and promotes surface hydrophilicity. This process results in the termination of the diamond surface with hydroxyl groups (C–OH), enhancing its reactivity, by providing essential reactive sites for bonding with other molecules and facilitating further chemical reactions [17, 14].

The insulator substrate is composed of a 300 nm, PECVD-grown layer of SiO_2 on Si. Hydrophilic bonding relies on the formation of silanol (Si–OH) groups on the SiO_2 surface. Therefore, following rinsing of the SiO_2/Si substrate with DI water, it undergoes O_2 plasma treatment, a common method for cleaning and oxidizing silicon surfaces [17].

This treatment both removes surface contamination and increases silanol group density by oxidizing siloxane (Si–O–Si) bridges in the presence of water vapor. These hydroxyl-terminated surfaces are hydrophilic and attract adsorbed water molecules from the environment.

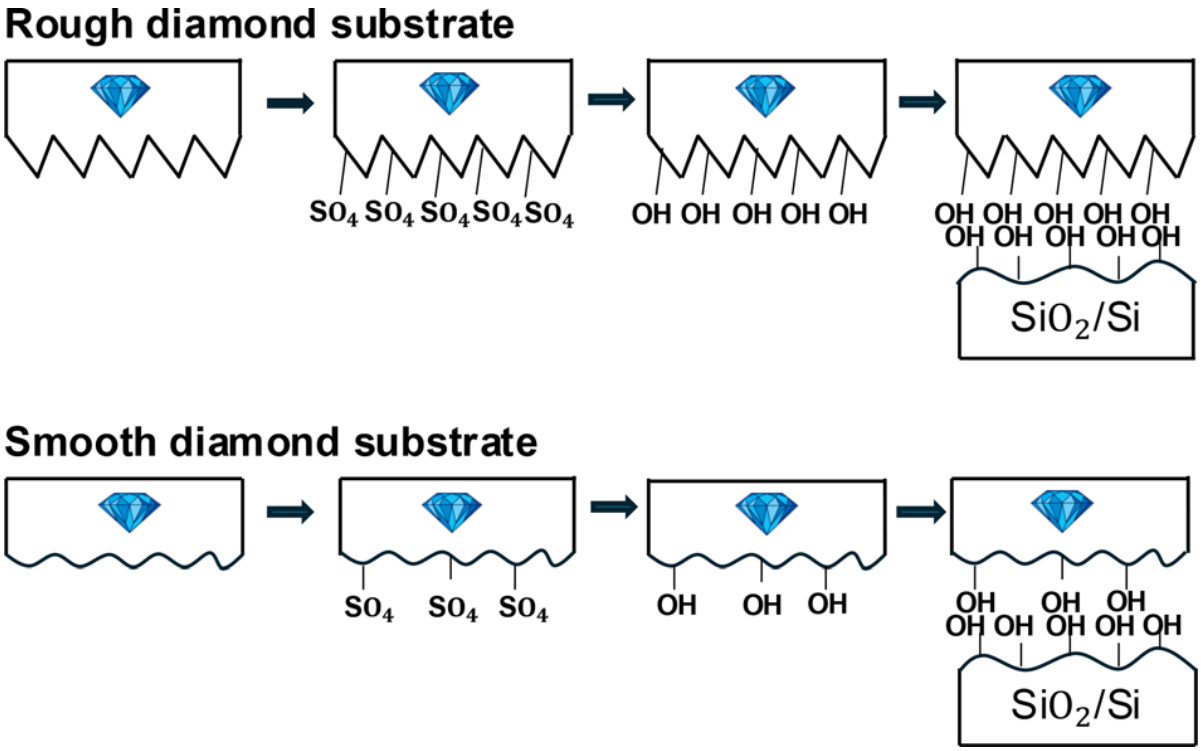


Figure 4.2: Illustration of the interfacial bonding mechanism between diamond and SiO_2. Increased surface roughness enhances the density of hydroxyl (–OH) terminations, facilitating more effective hydrogen bonding and improving the overall bonding success. Reproduced with permission from Chen *et al.*[12]. © 2025 AIP Publishing.

Once activated, both the diamond and SiO_2 surfaces become highly hydrophilic due to the formation of surface hydroxyl (–OH) groups. This promotes the adsorption of ambient water molecules, leading to the formation of a thin hydration layer on each surface. When the substrates are brought into contact under ambient conditions, hydrogen bonding and van der Waals interactions across this interfacial water layer enable initial adhesion and stabilize the alignment of the surfaces (see Figure 4.2). Specifically, hydroxyl groups such as C–OH and Si–OH participate in hydrogen bonding, which, although individually weak, collectively contribute significantly to the mechanical integrity of the interface [18].

Following initial contact, the DOI stack undergoes annealing, with temperature and duration serving as critical parameters for achieving robust interfacial bonding. Utilizing low-temperature annealing at 200°C, the bond strength is enhanced through dehydration reactions between adjacent silanol groups, producing strong Si–O–C covalent bridges across the interface [18]. This irreversible covalent bonding process completes the formation of the DOI heterostructure, as expressed by the reaction seen below:

$$\mathrm{C-OH + HO-Si \longrightarrow C-O-Si + H_2O}$$

Throughout this process, care was taken to maintain surface roughness within an optimal range. The surface roughness values of the diamond and the SiO_2/Si substrate fall within the 2–5 nm range typically reported as suitable for reliable hydrophilic bonding [12]. Notably, no high-temperature processing or aggressive etching was applied that could significantly modify surface topography prior to bonding.

The bonded interface remains intact through post-processing steps, and no delamination or void formation is typically observed. This is consistent with the formation of strong interfacial bonds and the maintenance of a mechanically coherent interface. The process flow has been replicated multiple times, further validating its general applicability and reproducibility.

4.3. STRAIN EFFECTS IN THE DOI SYSTEM

4.3.1. ORIGIN AND MECHANISMS OF STRAIN IN DIRECTLY BONDED DOI STRUCTURES

The direct bonding process of a diamond-on-insulator (DOI) substrate inevitably induces strain at the interface, with the most significant contribution arising from thermal expansion mismatch between the bonded materials [16], since prior to bonding, the residual stress in both the diamond and SiO_2/Si substrates is minimal [19]. The diamond used did not undergo post-growth annealing or epitaxy, which would otherwise introduce non-uniform stress [20]. Additionally, optical inspection revealed no bowing, indicating negligible macroscopic stress. Similarly, the underlying substrate remains mechanically relaxed [19]. Any pre-existing uniform residual stress is accounted for as a constant offset in the ODMR measurements, as the observed strain is induced post-bonding.

The annealing process at 200°C, necessary for bond stabilization, introduces thermal strain in the DOI heterostructure upon cooling to room temperature. This strain arises due to the mismatch in thermal expansion coefficients between the constituent materials. Diamond exhibits a low thermal expansion coefficient, with $\alpha_D \approx 1.1 \times 10^{-6}$ K^{-1} at room temperature and $\alpha_D \approx 2.3 \times 10^{-6}$ K^{-1} at 200°C [21]. In contrast, amorphous silica (SiO_2) has an expansion coefficient of $\alpha_{SiO_2} \approx 2.5 \times 10^{-6}$ K^{-1} at room temperature [22] and $\alpha_{SiO_2} \approx 3.0 \times 10^{-6}$ K^{-1} at 200°C [22, 23]. Silicon, on the other hand, expands significantly more than the diamond, with $\alpha_{Si} \sim 2.6 \times 10^{-6}$ K^{-1} at room temperature and $\alpha_{Si} \sim 3.3 \times 10^{-6}$ K^{-1} at 200°C [24, 25]. Table 4.1 summarizes the relevant thermal expansion coefficients. Since the SiO_2 layer is only 300 nm thick, while the underlying Si substrate is several hundred microns thick, the thermal and mechanical behavior of the bonded insulator stack is dominated by the silicon. The diamond layer, in turn, is constrained by this underlying Si substrate across the interfacial SiO_2 layer, which behaves elastically under these conditions. Upon cooling, the Si substrate contracts more than the diamond, imposing compressive in-plane strain on the diamond layer [26]. For a temperature drop of $\Delta T \sim 180$ K, the resulting in-plane thermal mismatch strain is estimated as $\varepsilon \approx (\alpha_{Si}^{200^\circ C} - \alpha_D^{200^\circ C})\Delta T \approx -1.8 \times 10^{-4}$.

Table 4.1: Linear thermal expansion coefficients (α) of materials in the DOI stack.

Material	α (RT) ($\times 10^{-6}$ K^{-1})	α (200°C) ($\times 10^{-6}$ K^{-1})
Diamond	~ 1.1	~ 2.3
PECVD SiO_2	~ 2.5	~ 3.0
Silicon	~ 2.6	~ 3.3

While the SiO_2 layer serves as the direct interface between diamond and Si, it is important to consider whether it could act as a strain-relieving buffer. In particular, viscous relaxation or interfacial slippage could potentially mitigate strain transfer. However, previous studies report that viscous flow in SiO_2 requires temperatures above 900–950°C [27], well beyond the 200°C annealing conditions used here. At these lower temperatures, the oxide behaves elastically. Moreover, the formation of covalent interfacial

bonds effectively suppresses slippage at the diamond–SiO_2 interface [12]. As a result, the bonded stack behaves as a mechanically coherent system, with strain transmitted directly from the silicon substrate to the diamond through the thin, elastically deforming oxide layer.

Surface roughness is another potential contributor to strain. However, in our study, the bonded diamond surface had an initial roughness of $R_a < 2$ nm, preserved through the Piranha and DI water cleaning steps. O_2 plasma etching was applied to the unbonded top diamond surface, with no measurable change in surface roughness. The SiO_2 layer had a measured RMS roughness of $S_q = 4.44$ nm prior to bonding. Both these values fall within the 2–5 nm range considered suitable for uniform bonding [12].

Finally, localized surface defects, such as scratches or implantation damage, are known to produce sharp strain gradients and localized ODMR shifts [28]. In contrast, the strain fields observed in our bonded samples are spatially extended and homogeneous over tens of microns, without any localized stress anomalies. Delamination is also not typically observed, following this direct bonding process. These features are inconsistent with surface-defect-induced strain, and instead match the expected thermomechanical strain distribution in a bonded multilayer stack. Therefore, the strain analyzed in this work originates predominantly from thermal expansion mismatch, transmitted through the SiO_2 layer without significant relaxation.

4.3.2. STRAIN PHYSICS IN NV CENTERS

The Hamiltonian $\hat{H}$ of the ground-state spin triplet state of the NV center in diamond, in the absence of imperfections (no strain) and external fields, can be described by the electron spin-spin interaction, which arises from second-order perturbation theory applied to the spin-orbit interaction [29]. Defining the z-axis along the NV-axis results in the following expression for the Hamiltonian:

$$\frac{\hat{H}}{h} = DS_z^2 \tag{4.1}$$

where h is Planck's constant, $\mathbf{S}$ is the spin operator of the NV center, and $D = 2.87$ GHz is the zero-field splitting (ZFS) tensor.

SPIN-STRAIN INTERACTION

In reality, numerous imperfections exist inside the diamond lattice, making the spin-strain interaction non-negligible. According to Udvarhelyi *et al.* (2018) [30], the spin-strain interaction for the ground-state spin triplet can be described as a deformation in the diamond crystal, causing the strain tensor ε_{ij} to couple to the NV spin through the symmetry-allowed Hamiltonian:

$$\hat{H}_\varepsilon = \hat{H}_\varepsilon^0 + \hat{H}_\varepsilon^1 + \hat{H}_\varepsilon^2 \tag{4.2}$$

where each term couples to different spin transitions. $\hat{H}_\varepsilon^0$ concerns the $|m_S = 0\rangle$ to $|m_S = 0\rangle$ transition (shifting or splitting the $|m_S = 0\rangle$ level), $\hat{H}_\varepsilon^1$ the $|m_S = 0\rangle$ to the $|m_S = \pm 1\rangle$ transition, and $\hat{H}_\varepsilon^2$ the $|m_S = +1\rangle$ to the $|m_S = -1\rangle$ transition.

In the NV reference frame (x, y, z), aligned so that z is the NV-axis and (x, y) spans the perpendicular plane, the general spin-strain Hamiltonian allowed by the C_{3v} symmetry is written as [30]:

$$\begin{aligned}\hat{H}_\varepsilon/h = \; & \Big\{[h_{41}(\varepsilon_{xx}+\varepsilon_{yy})+h_{43}\,\varepsilon_{zz}]S_z^2 \\ & +\tfrac{1}{2}[h_{26}\,\varepsilon_{zx}-\tfrac{1}{2}h_{25}(\varepsilon_{xx}-\varepsilon_{yy})]\{S_x,S_z\} \\ & +\tfrac{1}{2}[h_{26}\,\varepsilon_{yz}+h_{25}\,\varepsilon_{xy}]\{S_y,S_z\} \\ & +\tfrac{1}{2}[h_{16}\varepsilon_{zx}-\tfrac{1}{2}h_{15}(\varepsilon_{xx}-\varepsilon_{yy})](S_y^2-S_x^2) \\ & +\tfrac{1}{2}[h_{16}\,\varepsilon_{yz}+h_{15}\,\varepsilon_{xy}]\{S_x,S_y\}\Big\} \\ & \equiv M_z S_z^2 + N_x\{S_x,S_z\} + N_y\{S_y,S_z\} + M_x(S_y^2-S_x^2) + M_y\{S_x,S_y\}.\end{aligned} \tag{4.3}$$

where h_{ij} are coupling parameters (in units of GHz/strain) that depend on the microscopic electronic structure of the NV center (see Table 4.2), M_x, M_y, and M_z are the strain tensor amplitudes (in MHz) and N_x, N_y are non-diagonal strain terms that induce coupling between $|m_S = 0\rangle$ and the $|m_S = \pm 1\rangle$ states, and ε_{ij} is the strain tensor, with $\mathbf{u}(\mathbf{r})$ being the displacement field:

$$\varepsilon_{ij} = \frac{1}{2}\left(\frac{\partial u_i}{\partial x_j} + \frac{\partial u_j}{\partial x_i}\right) \tag{4.4}$$

If the resulting strain-induced mixing between $m_S = 0$ and $m_S = \pm 1$ states is small compared to the zero-field splitting D, the off-diagonal components N_x, N_y may then be treated as a small perturbation and be neglected.

Table 4.2: Spin-strain (h) coupling-strength parameters calculated from density functional theory by Udvarhelyi *et al.* (2018) [30].

Parameter	Value (MHz/strain)
h_{43}	2300 ± 200
h_{41}	-6420 ± 90
h_{25}	-2600 ± 80
h_{26}	-2830 ± 70
h_{15}	5700 ± 200
h_{16}	19660 ± 90

EIGENFREQUENCIES INCLUDING THE ZEEMAN TERM

In the presence of a homogeneous magnetic field $\mathbf{B}$, the NV Hamiltonian acquires an extra term:

$$\frac{\hat{H}_B}{h} = \gamma \mathbf{B}\cdot\mathbf{S}, \tag{4.5}$$

where γ is the electron gyromagnetic ratio, 2.8 MHz/G. After diagonalizing this matrix and including the spin-strain interaction Hamiltonian, the following equation is obtained:

$$f_{\pm} = D + M_z \pm \sqrt{(\gamma B_z)^2 + M_x^2 + M_y^2} \tag{4.6}$$

where $f_{\pm}$ is the frequency of each spin transition. From Equation 4.6, the following relations can be derived:

$$\Delta f_{\text{shift}} = \frac{1}{2}(f_+ + f_-) - D = M_z \tag{4.7}$$

where M_z is the volumetric (axial) strain amplitude, quantifying lattice compression or expansion along the NV center axis, directly affecting the resonance frequency shift observed in ODMR measurements, and:

$$\Delta f_{\text{split}} = f_+ - f_- = 2\sqrt{(\gamma B_z)^2 + M_x^2 + M_y^2} \tag{4.8}$$

where M_x and M_y represent the shear (transverse) strain components, corresponding to lattice distortions perpendicular to the NV axis. These transverse components primarily influence the magnitude of peak splitting in the ODMR spectra. Therefore, the effects of strain can be directly characterized by ODMR [31], as lattice distortions lead to measurable frequency shifts and splittings of the spin resonance transitions.

4.4. METHOD

The primary objective of this study is to measure the effects of strain in diamonds that have undergone direct bonding with an insulator (SiO_2/Si) substrate. To achieve this, NV centers are used due to their excellent properties that make them highly sensitive to external magnetic fields and strain fields. As already described above, strain can cause splitting and shifts in the energy levels of NV centers.

To enable these measurements, a confocal Optically Detected Magnetic Resonance (ODMR) setup is used, as seen in Figure 4.3. With ODMR, these changes in the energy states and spins can be quantified in the form of the presence of a magnetic, electric, or strain field, or temperature variations. The frequency shift Δf_{shift} and frequency splitting Δf_{split} are related to the strain tensor components ϵ_{ij}, through Equation 4.3.

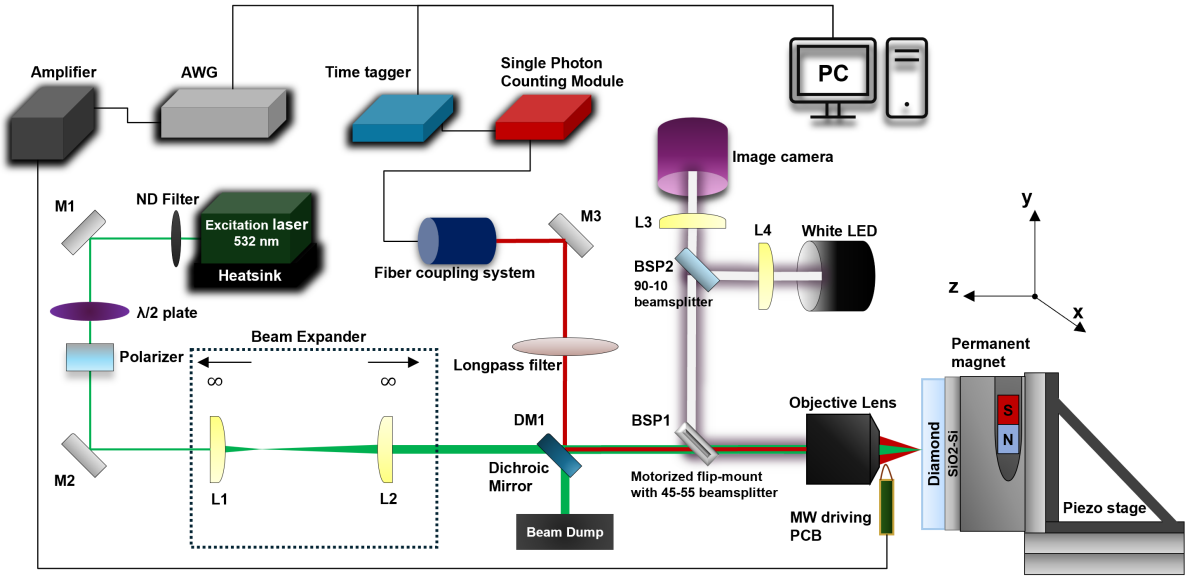


Figure 4.3: Schematic illustration of the confocal Optically Detected Magnetic Resonance (ODMR) setup used in this work. A 532 nm CW-laser provides optical excitation of the NV centers, with fluorescence collected via a high-NA objective and directed through a dichroic mirror and filters to a single-photon counting module (SPCM). Microwave excitation is delivered via a wire loop placed near the diamond surface. A bias magnetic field (B_z) is applied along the NV axis to lift spin degeneracy, enabling detection of frequency shifts and splittings associated with strain.

Solving Equation 4.7 for for M_z gives:

$$M_z = \Delta f_{\text{shift}} \tag{4.9}$$

while solving Equation 4.8 for $M_{xy} = \sqrt{M_x^2 + M_y^2}$ results in:

$$M_{xy} = \sqrt{\frac{\Delta f_{\text{split}}^2}{4} - (\gamma B_z)^2} \tag{4.10}$$

Therefore, by measuring the strain amplitudes (M_x, M_y, M_z) through ODMR measurements, one can partially reconstruct the strain tensor. Specifically, the volumetric strain component, M_z, provides a linear combination of the axial strain terms (ϵ_{xx}, ϵ_{yy}, and ϵ_{zz}), weighted according to their orientation with respect to the NV center's crystallographic axis. In this research, the difference in values for M_{xy}, and M_z is acquired,

after comparing ODMR-obtained spectra at different depths of the diamond's volume, as illustrated in Figure 4.4.

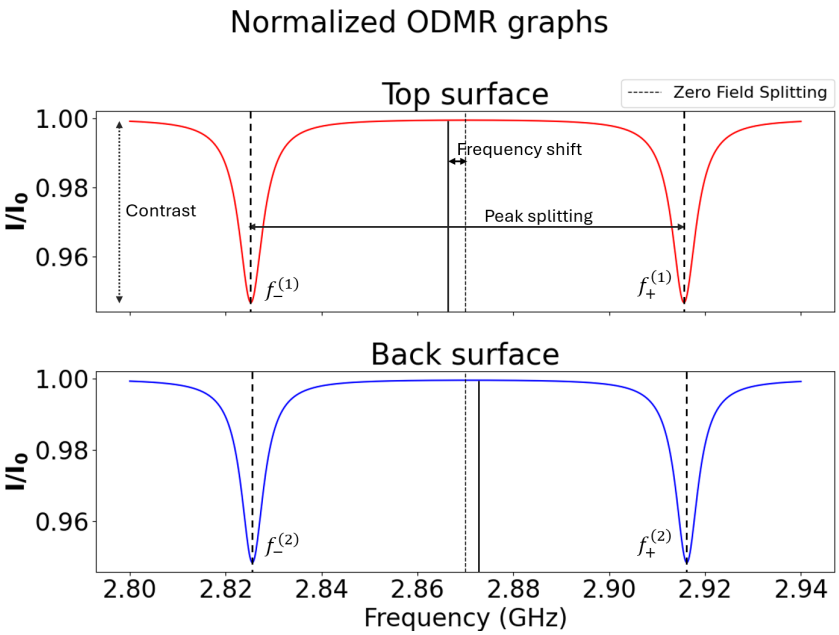
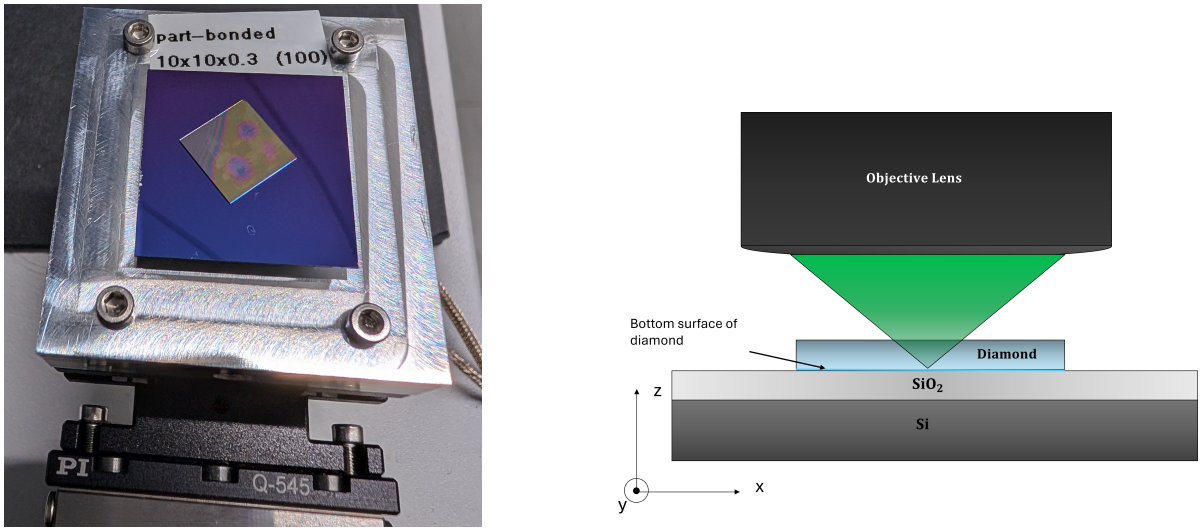


Figure 4.4: Indicative ODMR spectra obtained at the top and at the back surface.

For the experiment, a $10 \times 10\,\text{mm}^2$ bulk diamond substrate (supplied by EDP), with a thickness of ~ 300 µm is investigated, hereafter referred to as DS_{PB} (see Figure 4.5a). It is a CVD-grown substrate, cut along the {100} crystallographic plane, that contains randomly distributed ensembles of NV centers with a concentration of roughly 15 ppb. The diamond substrate was double-side polished, exhibiting an initial surface roughness of $R_a < 2$ nm, as specified by the supplier. The SiO_2 surface on the Si wafer, prior to bonding, exhibited a root mean square (RMS) roughness of $S_q = 4.44$ nm, as measured by AFM.

The top (unbonded) surface of the diamond was later etched by approximately 50 µm, using O_2 plasma, with no considerable change to surface roughness, in order to allow focusing on the back surface (diamond-SiO_2/Si interface). This challenge arose due to the objective lens' small working distance of 400 µm and the 100 µm diameter of the microwave delivery wire, which is placed between the objective and the piezo stage. Although the refractive index of diamond, $n = 2.4$, provides some leniency by modifying the effective distance of the objective-to-diamond, further etching of the surface ensures that proper focus on the back surface can be achieved and eliminates any worries of collision of the diamond with the objective during 2D scanning.

This diamond sample underwent the direct bonding process, but, due to its large surface area, the result was partial bonding of the DOI substrate, meaning that two regions of interest are present—both bonded and unbonded—on the same sample. Different strain fields may exist in these regions, since only part of its surface formed a strong bond with the insulator substrate underneath it. This bonded region has potentially experienced increased strain effects compared to the unbonded one. By comparing the ODMR peak splitting and frequency shift values at the top surface and at the bottom surface (diamond-SiO_2/Si interface), an overall increase in strain is observed in the in-



(a) (b)

Figure 4.5: **(a)** Mounted diamond sample DS_{PB}, used in the partially-bonded configuration. **(b)** Schematic of the objective lens focusing the green excitation laser onto the bottom diamond surface at the diamond-SiO_2/Si interface.

terface.

It should be noted that the following measurements are performed in the presence of an external bias magnetic field $B_z = 15.7$ G (or 43.9 MHz splitting) along the z-axis. A 532 nm green laser is used for optical excitation, at a power of 0.25 mW, and the emitted fluorescence is collected via a single-photon counting module (COUNT-10C-FC), coupled to a fiber.

4.5. RESULTS AND DISCUSSION

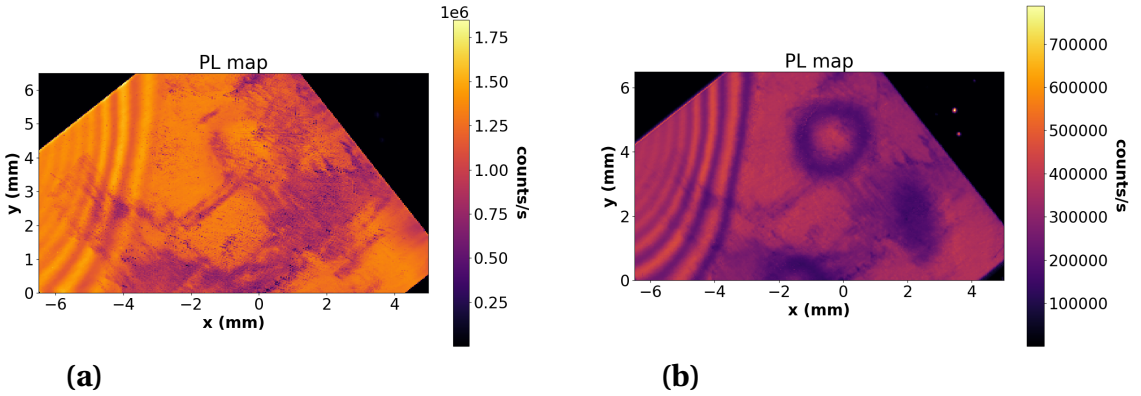


Figure 4.6: Coarse PL maps of the partially-bonded diamond substrate. a) Top surface, b) Back surface.

In Figure 4.6, differences in the acquired photoluminescence (PL) maps of the top and back surfaces are visible. During the direct bonding process, even with thorough cleaning of the substrates in a cleanroom environment, trapped particles or residues at the diamond-SiO_2/Si interface may still remain, hindering proper bonding and inducing localized strain regions. This effect is particularly pronounced in the sample investigated here, owing to its large size of $10 \times 10\,\mathrm{mm}^2$.

The bonded and unbonded regions can be clearly distinguished, providing a useful tool for evaluating the success and quality of the direct bonding process. Specifically, interference fringes are more apparent in the PL map closer to the bottom surface. This may indicate the presence of particles or impurities that were either not thoroughly rinsed or introduced during one of the direct bonding steps, and subsequently became trapped at the interface.

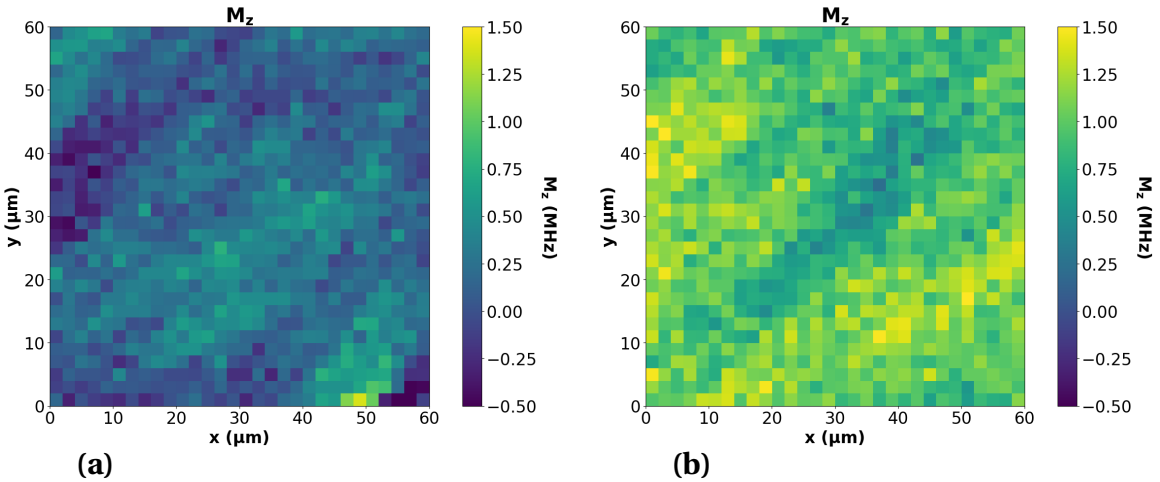


Figure 4.7: ODMR 2D scans performed in a $60 \times 60\ \mu\mathrm{m}^2$ area, depicting the effects of the volumetric strain amplitude M_z. a) Top surface, b) Back surface.

Such particles could hinder proper adhesion and potentially lead to localized unbonded regions. These regions are linked to non-uniform bonding or strain effects that can alter the observed layer thickness and local refractive index. The direct bonding

quality has to be improved, especially regarding substrates with larger surfaces. This would enable high-quality, reproducible bonding and more precise strain mapping.

Afterward, 2D ODMR maps were obtained, starting with a $60 \times 60\ \mu m^2$ area at the top surface, and then focusing on the diamond plane close to the diamond-SiO_2/Si interface. Figure 4.7 represents volumetric strain variation, obtained by calculating the frequency shift Δf_{shift} of every point in the map, relative to the zero field splitting (ZFS) value of $D = 2.87$ GHz, and solving for M_z, as seen in Equation 4.9.

The milder volumetric strain effects at the top surface are attributed to intrinsic strain in the diamond. However, moving closer towards the back surface shows increased strain effects, which are assumed to have been caused by the thermal expansion mismatch that occurs during the direct bonding process.

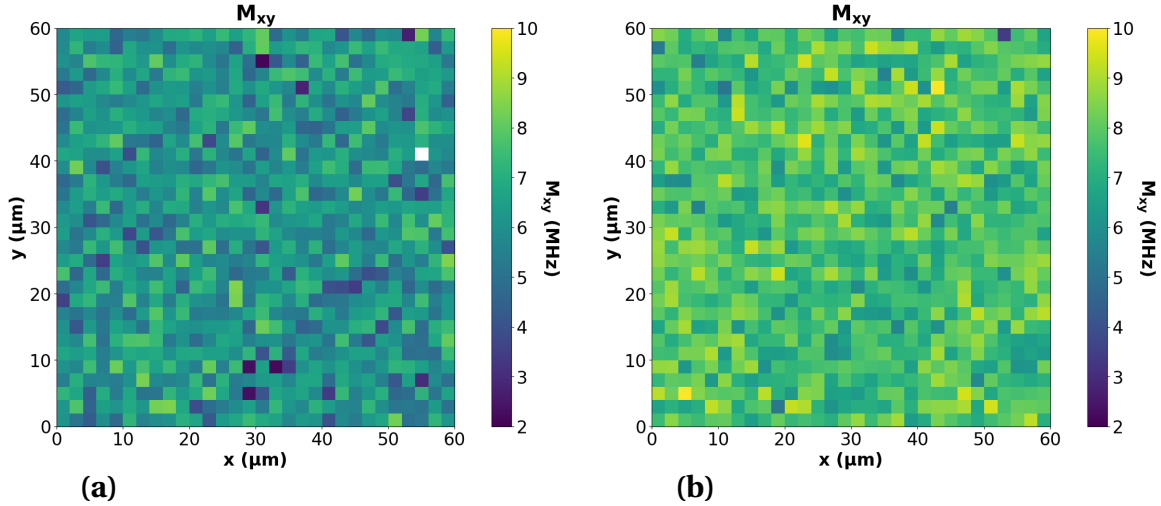


Figure 4.8: ODMR 2D scans performed in a $60 \times 60\ \mu m^2$ area, depicting the effects of the transverse strain amplitude M_{xy}. a) Top surface, b) Back surface.

Similarly, Figure 4.8 demonstrates the spatial variation of shear (transverse) strain, obtained via 2D ODMR mapping by analyzing the peak splitting at each measurement point according to Equation 4.10. Calculating the transverse strain amplitude (M_{xy}) reveals the magnitude of lattice distortions in planes perpendicular to the NV axis (i.e., the xy, yz, and xz planes). An increase in shear strain is observed near the diamond–SiO_2/Si interface, consistent with expectations based on the thermal expansion coefficient mismatch between the bonded materials.

Next, ODMR measurements were performed at various depths (z-axis scans), starting from the top surface of the DS_{PB} sample and finishing close to the bottom surface (diamond-SiO_2/Si interface). These ODMR measurements provide information on multiple quantities, such as the frequency shift, which is related to volumetric strain, the frequency splitting, related to shear strain, ODMR peak contrast, which provides insight into the signal-to-noise ratio (SNR) and peak broadening. These measurements include data from both bonded and seemingly-unbonded regions.

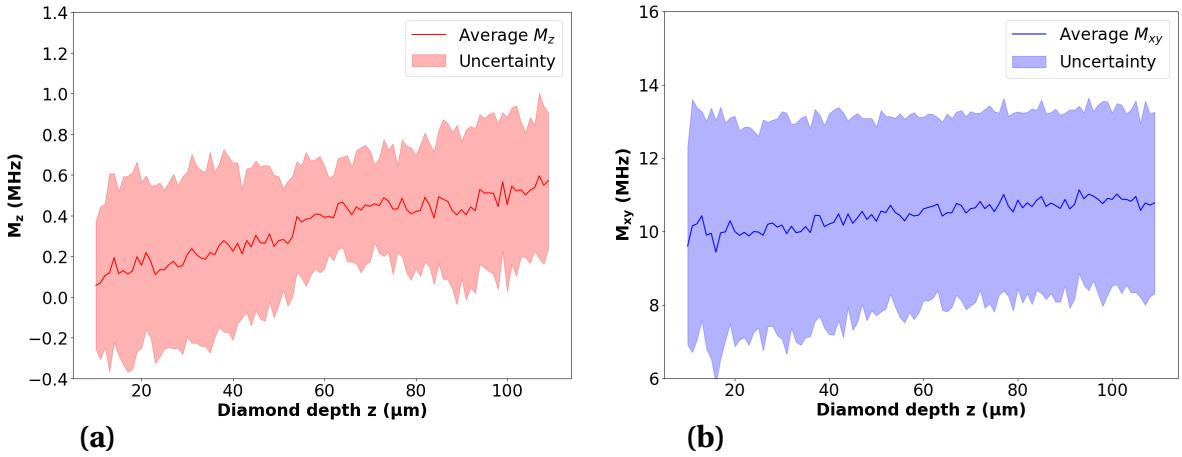


Figure 4.9: Data from different ODMR graphs, obtained at varying planes of the diamond substrate. The data is averaged out of nine different ODMR scans, each starting from a different region of the surface of the diamond. a) Shows the increase of the M_z parameter, acquired via frequency shift compared to the default ZFS value in ODMR measurements, and corresponding to volumetric strain, and b) shows the increase of the M_{xy} parameter, acquired via peak splitting in ODMR measurements, and corresponding to shear strain components.

In Figure 4.9, a gradual increase in both volumetric and shear strain can be seen. Contrary to the 2D ODMR maps discussed earlier, such a measurement allows a direct observation of how the strain effects are increasingly more intense close to the interface. Values of M_z range from 0.11 MHz up to 0.56 MHz, whereas values of M_{xy} range from 10.05 MHz to 10.76 MHz.

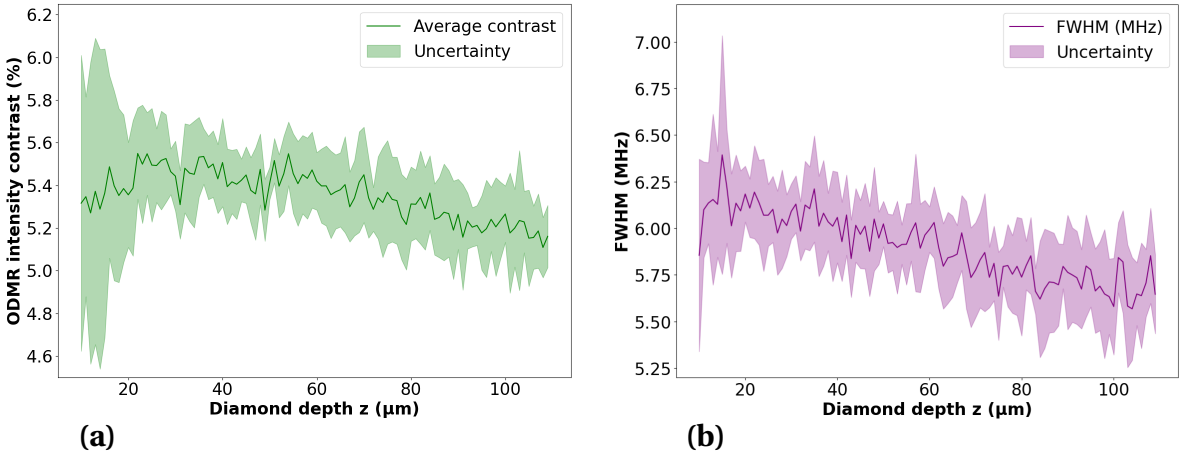


Figure 4.10: Data from different ODMR graphs, obtained at varying planes of the diamond substrate. The data is averaged out of nine different ODMR scans, each starting from a different region of the surface of the diamond. **a)** Shows the decline in average ODMR intensity contrast. **b)** Shows the decline in the FWHM of the ODMR peaks.

The contrast of the peaks in an ODMR graph can provide important information on the quality of the color centers. It not only regards the signal-to-noise ratio (SNR), but is also affected by effects of decoherence and inhomogeneous broadening, which significantly impact the optical properties of the emitters. These phenomena can be caused by many factors, including the presence of strain fields which are investigated here. Figure 4.10 demonstrates how contrast deteriorates close to the diamond-SiO_2/Si interface. The initial ODMR intensity contrast at the top surface is approximately 5.32%, increas-

ing to an average of 5.51% in the region where the NV centers exhibit the best signal, and finally decreasing to approximately 5.15% close to the interface.

The average Full Width Half Maximum (FWHM) of the peaks in the ODMR spectra follows a similar trend, as it seems to diminish close to the interface. It drops from an average of 6.08 MHz close to the top surface, down to an average of 5.70 MHz close to the interface. This is an unexpected result, as one would anticipate that the observed linewidth worsens under increased strain conditions, similar to how contrast decreases.

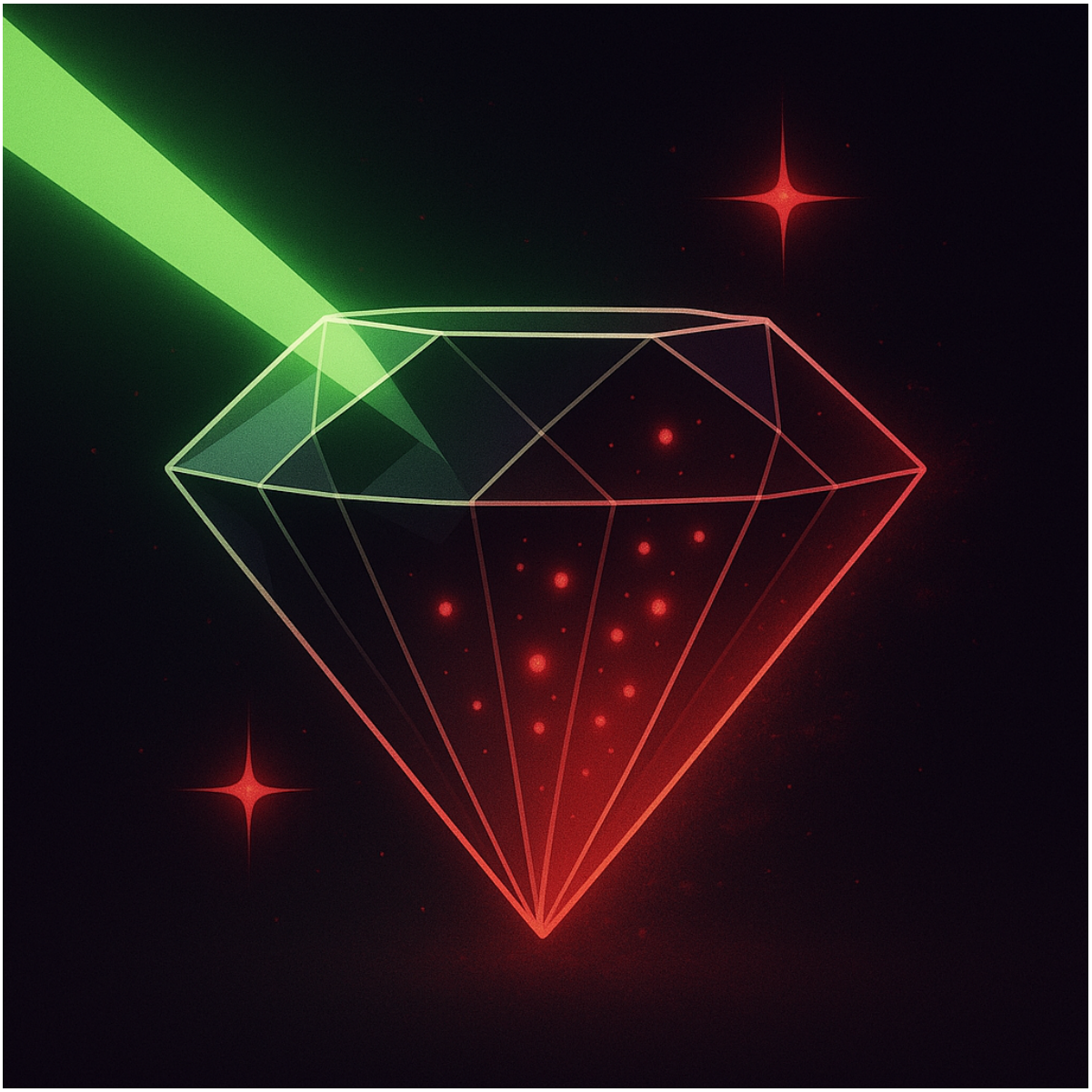
Regarding the experimental setup, problems occasionally arise when focusing on the back surface of a thick substrate, due to limits set by the working distance of the objective lens, as well as obstruction by the microwave delivery wire. This necessitates thinning of the diamond layer by O_2 plasma etching; a rather time-consuming process. Lastly, the ODMR measurement process itself is another factor to take into consideration concerning the quality of the measurements. Long scanning durations make the samples more prone to thermal drifts and can introduce experimental parameter fluctuations. The time inefficiency is further exacerbated by the long direct bonding processing time of approximately a week. It is worth noting that future DOI substrates may be comprised of diamonds with a thickness of a few micrometers or even in the nanometer range. In such cases, the aforementioned strain effects and the quality of the emitters are bound to differ and be more localized.

4.6. CONCLUSION

Strain characterization was performed on a diamond directly bonded to an insulator substrate (SiO_2/Si). The mismatch in thermal expansion coefficients between diamond and SiO_2/Si during the direct bonding process induces strain effects, particularly pronounced near the interface. In this study, strain properties were evaluated across regions exhibiting different bonding conditions by conducting depth-resolved measurements using optically detected magnetic resonance (ODMR). The ODMR technique allowed for the correlation of resonance frequency shifts and splittings to volumetric and shear strain amplitudes, respectively. Results revealed increased lattice deformations when approaching the diamond–SiO_2/Si interface, with the volumetric strain parameter exhibiting an increase of 0.45 MHz and the shear strain parameter rising by 0.71 MHz. Additionally, photoluminescence (PL) mapping of partially bonded diamond areas identified interference fringes that likely indicate localized strain or imperfect bonding at the interface. In this investigation, only minor changes in ODMR contrast and linewidth were observed, suggesting negligible deterioration in emitter quality. Specifically, contrast deteriorated by approximately 0.36%, while unexpectedly, the linewidth (FWHM) also decreased by 0.38 MHz. In conclusion, we have determined that PL mapping serves as an effective preliminary method for assessing bonding quality, while ODMR provides detailed insights into the magnitude and nature of strain and its impact on NV centers. Nevertheless, further detailed measurements are required to fully understand how strain influences the optical and electronic properties of color centers in directly bonded diamond substrates.

ACKNOWLEDGEMENTS

We gratefully acknowledge support from the joint research program “Modular quantum computers” by Fujitsu Limited and Delft University of Technology, co-funded by the Netherlands Enterprise Agency under project number PPS2007.



BIBLIOGRAPHY

[1] Ioannis Varveris et al. “Strain Effects in a Directly Bonded Diamond-on-Insulator Substrate”. In: *physica status solidi (a)* n/a.n/a (), p. 2500277. DOI: https://doi.org/10.1002/pssa.202500277.

[2] Andrei Faraon et al. “Coupling of Nitrogen-Vacancy Centers to Photonic Crystal Cavities in Monocrystalline Diamond”. In: *Phys. Rev. Lett.* 109 (3 July 2012), p. 033604. DOI: 10.1103/PhysRevLett.109.033604.

[3] Jean-Charles Arnault, Samuel Saada, and Victor Ralchenko. “Chemical Vapor Deposition Single-Crystal Diamond: A Review”. In: *physica status solidi (RRL) – Rapid Research Letters* 16.1 (2022), p. 2100354. DOI: https://doi.org/10.1002/pssr.202100354.

[4] Sophie W. Ding et al. *"High-Q Cavity Interface for Color Centers in Thin Film Diamond"*. 2024. arXiv: 2402.05811 [quant-ph].

[5] R. Ishihara et al. “3D Integration Technology for Quantum Computer based on Diamond Spin Qubits”. In: *2021 IEEE International Electron Devices Meeting (IEDM)*. 2021, pp. 14.5.1–14.5.4. DOI: 10.1109/IEDM19574.2021.9720552.

[6] Paul E. Barclay et al. “Hybrid Nanocavity Resonant Enhancement of Color Center Emission in Diamond”. In: *Phys. Rev. X* 1 (1 Sept. 2011), p. 011007. DOI: 10.1103/PhysRevX.1.011007.

[7] Maximilian Ruf et al. “Quantum networks based on color centers in diamond”. In: *Journal of Applied Physics* 130.7 (Aug. 2021), p. 070901. ISSN: 0021-8979. DOI: 10.1063/5.0056534.

[8] Kinfung Ngan et al. “Quantum Photonic Circuits Integrated with Color Centers in Designer Nanodiamonds”. In: *Nano Letters* 23.20 (2023). PMID: 37782048, pp. 9360–9366. DOI: 10.1021/acs.nanolett.3c02645.

[9] Sichen Mi et al. “Integrated photonic devices in single crystal diamond”. In: *Journal of Physics: Photonics* 2.4 (Aug. 2020), p. 042001. DOI: 10.1088/2515-7647/aba171.

[10] Francesco Lenzini et al. “Diamond as a Platform for Integrated Quantum Photonics”. In: *Advanced Quantum Technologies* 1.3 (2018), p. 1800061. DOI: https://doi.org/10.1002/qute.201800061.

[11] Shuo Sun et al. “Cavity-Enhanced Raman Emission from a Single Color Center in a Solid”. In: *Phys. Rev. Lett.* 121 (8 Aug. 2018), p. 083601. DOI: 10.1103/PhysRevLett.121.083601.

[12] Tianyin Chen et al. *Hydrophilic direct bonding of (100) diamond and deposited SiO_2 substrates*. 2025. DOI: https://arxiv.org/abs/2501.12831. arXiv: 2501.12831 [cond-mat.mtrl-sci].

[13] V. Masteika et al. “A Review of Hydrophilic Silicon Wafer Bonding”. In: *ECS Journal of Solid State Science and Technology* 3.4 (Feb. 2014), Q42. DOI: 10.1149/2.007403jss.

[14] Takashi Matsumae et al. “Hydrophilic direct bonding of diamond (111) substrate using treatment with H2SO4/H2O2”. In: *Japanese Journal of Applied Physics* 59.SB (Nov. 2019), SBBA01. DOI: 10.7567/1347-4065/ab4c87.

[15] Taras Plakhotnik et al. “All-Optical Thermometry and Thermal Properties of the Optically Detected Spin Resonances of the NV– Center in Nanodiamond”. In: *Nano Letters* 14.9 (2014). doi: 10.1021/nl501841d, pp. 4989–4996. ISSN: 1530-6984. DOI: 10.1021/nl501841d.

[16] Andris Berzins et al. “NV microscopy of thermally controlled stresses caused by thin Cr2O3 films”. In: *Opt. Express* 31.11 (May 2023), pp. 17950–17963. DOI: 10.1364/OE.489901.

[17] T. Matsumae et al. “Hydrophilic direct bonding of monocrystalline (111) diamond substrate onto Si wafer”. In: *2019 6th International Workshop on Low Temperature Bonding for 3D Integration (LTB-3D)*. 2019, pp. 70–70. DOI: 10.23919/LTB-3D.2019.8735180.

[18] Takashi Matsumae et al. “Low-temperature direct bonding of diamond (100) substrate on Si wafer under atmospheric conditions”. In: *Scripta Materialia* 191 (2021), pp. 52–55. ISSN: 1359-6462. DOI: https://doi.org/10.1016/j.scriptamat.2020.09.006.

[19] C. Malhaire et al. “Determination of stress in thin films using micro-machined buckled membranes”. In: *Journal of Vacuum Science & Technology A* 41.4 (May 2023), p. 043401. ISSN: 0734-2101. DOI: 10.1116/6.0002590.

[20] I. Vlasov et al. “Intrinsic Stress Origin in High Quality CVD Diamond Films”. In: *physica status solidi (a)* 174.1 (1999), pp. 11–18. DOI: https://doi.org/10.1002/(SICI)1521-396X(199907)174:1<11::AID-PSSA11>3.0.CO;2-T.

[21] Stanislav Stoupin and Yuri V. Shvyd’ko. “Ultraprecise studies of the thermal expansion coefficient of diamond using backscattering x-ray diffraction”. In: *Phys. Rev. B* 83 (10 Mar. 2011), p. 104102. DOI: 10.1103/PhysRevB.83.104102.

[22] F. Jansen et al. “Thermal expansion and elastic properties of plasma-deposited amorphous silicon and silicon oxide films”. In: *Applied Physics Letters* 50.16 (Apr. 1987), pp. 1059–1061. ISSN: 0003-6951. DOI: 10.1063/1.97969.

[23] Haruna Tada et al. “Thermal expansion coefficient of polycrystalline silicon and silicon dioxide thin films at high temperatures”. In: *Journal of Applied Physics* 87.9 (May 2000), pp. 4189–4193. ISSN: 0021-8979. DOI: 10.1063/1.373050.

[24] K. G. Lyon et al. “Linear thermal expansion measurements on silicon from 6 to 340 K”. In: *Journal of Applied Physics* 48.3 (Mar. 1977), pp. 865–868. ISSN: 0021-8979. DOI: 10.1063/1.323747.

[25] C. A. Swenson. “Recommended Values for the Thermal Expansivity of Silicon from 0 to 1000 K”. In: *Journal of Physical and Chemical Reference Data* 12.2 (Apr. 1983), pp. 179–182. ISSN: 0047-2689. DOI: 10.1063/1.555681.

[26] Jocelyn T. L. Gamler et al. “Effect of lattice mismatch and shell thickness on strain in core@shell nanocrystals”. In: *Nanoscale Adv.* 2 (3 2020), pp. 1105–1114. DOI: 10.1039/D0NA00061B.

[27] Robert H. Doremus. “Oxidation of Silicon: Stress Relaxation in Silica”. In: *Journal of The Electrochemical Society* 134.8 (Aug. 1987), p. 2001. DOI: 10.1149/1.2100806.

[28] D. A. Broadway et al. “Microscopic Imaging of the Stress Tensor in Diamond Using in Situ Quantum Sensors”. In: *Nano Letters* 19.7 (2019). PMID: 31150580, pp. 4543–4550. DOI: 10.1021/acs.nanolett.9b01402.

[29] J. H. N. Loubser and J. A. van Wyk. “Electron spin resonance in the study of diamond”. In: *Reports on Progress in Physics* 41.8 (Aug. 1978), p. 1201. DOI: 10.1088/0034-4885/41/8/002.

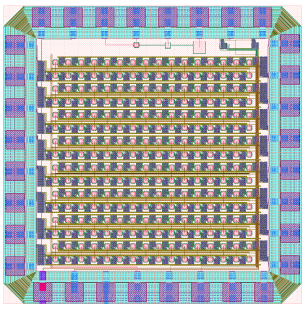
[30] Péter Udvarhelyi et al. “Spin-strain interaction in nitrogen-vacancy centers in diamond”. In: *Physical Review B* 98.7 (Aug. 2018). ISSN: 2469-9969. DOI: 10.1103/physrevb.98.075201.

[31] M. Sahnawaz Alam et al. “Determining strain components in a diamond waveguide from zero-field optically detected magnetic resonance spectra of negatively charged nitrogen-vacancy-center ensembles”. In: *Phys. Rev. Appl.* 22 (2 Aug. 2024), p. 024055. DOI: 10.1103/PhysRevApplied.22.024055.

5

CHARACTERIZATION AND INTEGRATION OF SPAD ARRAYS WITH NV CENTERS IN DIAMOND

Single-photon detection plays a crucial role when it comes down to quantum applications. It enables the precise measurement of extremely weak light signals, essential for quantum communication and advanced imaging protocols. Single-photon avalanche diodes (SPADs) are able to resolve individual photons with high sensitivity and timing accuracy at room temperature, rendering them highly suitable for performing imaging of biological tissues. They can be fabricated with CMOS technology, which enables their integration into a compact sensing platform, such as the one investigated in this project, which utilizes NV centers in diamond. In this chapter, chips with 16×16 *SPAD arrays are fabricated in 40 nm technology, and are subsequently characterized with I-V and C-V measurements. Finally, the fabricated chip is integrated with diamond into a compact widefield setup, which, by employing ODMR techniques, can provide proof-of-concept of the realization of a high-sensitivity, high-speed compact imaging sensor.*



Parts of this chapter have been submitted for publication to IEEE Transactions on Quantum Engineering (2026).

5.1. INTRODUCTION

5.1.1. BACKGROUND

Single-Photon Avalanche Diodes (SPADs) are a sub-category of Avalanche Photodiodes (APDs), that function in reverse bias, above the breakdown voltage. They feature shot-noise limited single-photon sensitivity and very precise timing resolution. This opens up the potential for numerous applications like fluorescence lifetime imaging microscopy (FLIM), time-of-flight (ToF) imaging, light detection and range (LiDAR), and quantum cryptography, among others [1].

As the years pass, there has been an increased interest in the integration of SPADs with CMOS technology, while also making use of progressively smaller nodes. This has multiple advantages, including high cell density and fill factor, cost efficiency, scalability, and smaller transistor sizes, which in turn results in lower power consumption [1, 2, 3].

Taking this one step further, the goal is to integrate a CMOS chip, containing a 16×16 array of SPADs with on-chip quenching and readout circuits, with a diamond containing a doped layer of nitrogen-vacancy (NV) centers, as described in section 1.6. NV centers in diamond function as a system with well-documented (bio)sensing capabilities [4], due to their sensitivity to small electromagnetic fields and temperature gradients. They also exhibit unique properties, such as room-temperature operation, photostability, long coherence times [5] and biocompatibility [6]. By creating such a compact sensor, the opportunity to accurately perform rapid imaging of the magnetic footprint of biological systems arises.

The first part of this chapter focuses on the electrical characterization of basic SPAD properties, including I-V curves and experimental C-V measurements. Before this, a brief rundown of the SPADs' operating principles and properties is provided. In the second part, the integration of the aforementioned CMOS-fabricated SPAD array with a diamond containing NV centers is investigated, as well as the challenges that come with it.

5.1.2. STATE-OF-THE-ART SPAD ARRAYS IN 40 NM TECHNOLOGY

In recent years, the fabrication of SPAD arrays has seen significant progress, towards more and more advanced CMOS technologies. The cutting edge research that is being performed is rapidly transitioning into increasingly smaller fabrication nodes, in order to fully utilize high density arrays with enhanced fill factor. In 2017, Pellegrini *et al.* [7] demonstrated the first mature SPAD array in 40nm technology, featuring 64 SPADs divided into four macropixels of 16 SPADs each, with dedicated electronics for each macropixel. In parallel, a research group from the University of Edinburgh introduced a 96×40 integrated SPAD array, implemented on a $1 \times 1\,\mathrm{mm}^2$ chip [8], and two years later published their work on a 192×128 SPAD array using STMicroelectronics 40nm CMOS technology [3]. This was a significant step forward in the resolution and integration density of SPAD arrays. So far, the largest SPAD array published is a 3.2 Megapixel array by Morimoto *et al.* [9], albeit using different technology node, and 3D-stacking techniques. Although few, there have also been some works on the implementation and optimization of SPADs in 28nm CMOS technology [10, 11, 12]. The state-of-the-art of NV-based compact biosensors has already been discussed in section 1.3.

5.2. SPAD BASICS

5.2.1. OPERATING PRINCIPLES

SPADs are based on p-n junctions that operate in Geiger mode, meaning that they are reverse-biased above their breakdown voltage and generate a high electric field (see Figure 5.1). A photon incident on the active area of the SPAD generates an electron-hole pair, which is then accelerated by this electric field, leading to a chain reaction of charge carrier generation. This self-sustaining avalanche effect results in a measurable current, which provides information on the detection of a photon [13].

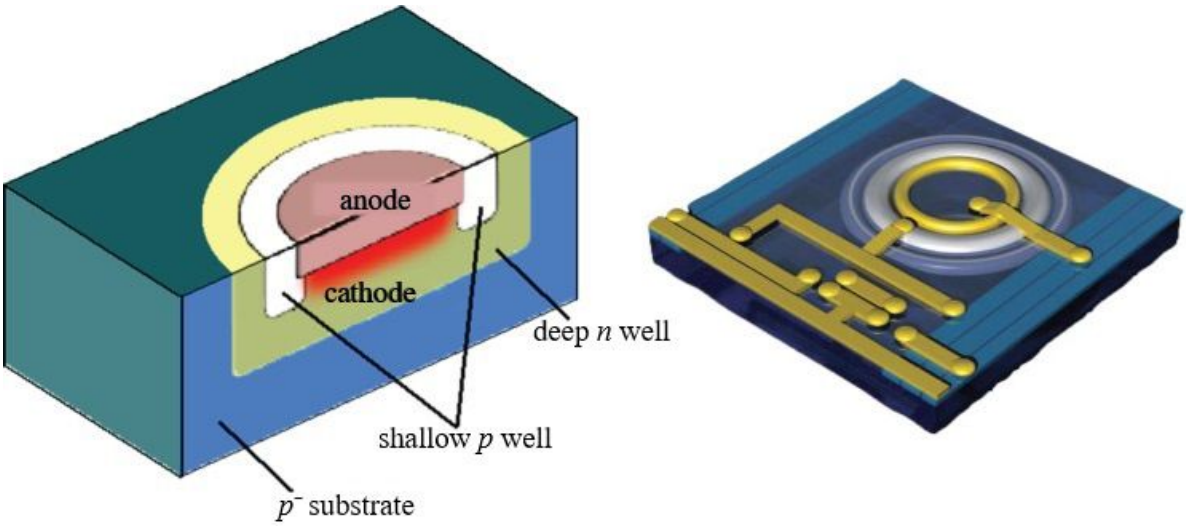


Figure 5.1: Indicative cross-sectional schematic of a SPAD implemented in a standard CMOS process. The structure includes a p^+ anode implant formed using the same layout and doping step as the p^+ regions in standard PMOS transistors. This region is surrounded by a guard ring (e.g., from a shallow p-well) and encapsulated within a deep n-well to ensure electrical isolation. Adapted image, courtesy of E. Charbon (2014) [14].

After an avalanche event has occurred, the SPAD needs to be "reset", so that it can be ready to detect the next photon. For this reason, the avalanche has to be quenched. There are two main quenching mechanisms: passive and active quenching. The simplest way is passive quenching, which is typically done by placing a ballast resistor in series with the SPAD. This resistor limits the current through the SPAD, which in turn reduces the voltage to below the breakdown value, decreasing the electric field and quenching the avalanche. The voltage across the SPAD then gradually recovers, resetting the SPAD. Although simpler and cost-effective, passive quenching is less efficient than active quenching and can result in higher afterpulsing [15].

On the other hand, active quenching utilizes an electronic circuit that detects the avalanche current and immediately reduces the bias voltage to below the breakdown value. The decrease of the electric field stops the avalanche, but this circuit helps to quickly restore the voltage and reset the SPAD. A great benefit of active quenching is the ability to control the dead time, which can be essential in certain applications [16]. A typical I-V diagram can be seen in Figure 5.2 [17].

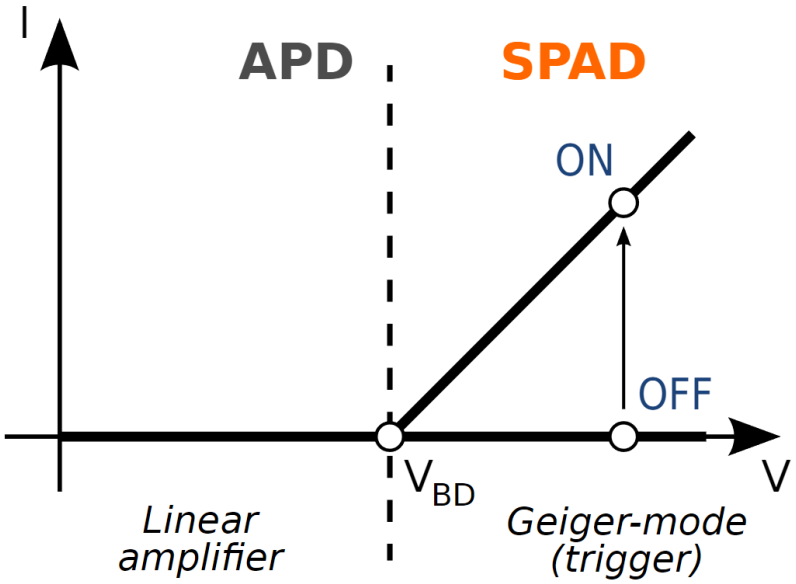


Figure 5.2: I-V diagram showing the difference in operation between standard APDs and SPADs when SPADs are biased beyond their breakdown voltage [17].

5.2.2. OVERVIEW OF SPAD PARAMETERS

SPADs are usually characterized by the following properties:

- Photon detection efficiency (PDE) refers to the probability that an incident photon causes a detectable avalanche [1, 13]. For the SPAD array design investigated in this project, a peak detection efficiency between 600-800 nm is desirable.
- SPADs offer excellent timing resolution, which is critical for applications that require precise time measurements. Timing jitter, i.e. uncertainty in timing measurement, can be as low as a few tens of picoseconds, enabling extremely accurate time-of-flight (ToF) measurements and time-correlated single-photon counting (TCSPC) [18].
- There are two main effects of internal noise in this detector, the first of which is the dark count rate (DCR). DCR indicates the amount of false avalanche events, which are caused by thermal excitations or other noise sources [1, 19]. When obtaining fluorescence emission signal from an ensemble of NV centers, a DCR of few kHz or less is needed.
- The second effect is called afterpulsing. Afterpulsing is the occurrence of unwanted avalanches, due to trapped residual charges in the multiplication region of the SPAD. However, advanced quenching circuits and optimized doping profiles can help mitigate afterpulsing [19, 18]. To mitigate afterpulsing, the design in this project incorporates controllable dead time, during which the SPAD is turned off and is insensitive to new detection events. Without this, the SPAD could be re-triggered during the recharge phase, making it susceptible to correlated noise from previous avalanches.

5.3. DESIGNING THE SPADS

The 40 nm technology node by TSMC is selected for the fabrication of the 16 × 16 SPAD arrays. This choice was shaped based on a few factors. Not only does it offer much higher integration density, with smaller pixel pitches, but also entails significantly lower power consumption. Another important reason for this node choice was the collectively planned tape-out of the Quantum & Computer Engineering (QCE) department of TU Delft.

5.3.1. DESIGN CONSIDERATIONS

Each SPAD in the array is being designed to detect photons emitted from an ensemble of NV centers. Therefore, the detection electronics need to be fast enough to detect successive photon emissions without bottlenecking the measurement resolution. To ensure a low probability of missing events, the aim is a photon detection rate above 3 Mcounts/s, or a cycle time of 333 ns.

Fabricating SPAD arrays in 40 nm fabrication technology comes with decreased pixel pitch. This, however, raises concerns about increased crosstalk between pixels. A crosstalk probability of a few percent is estimated for a pixel pitch of ≈ 20 µm.

To meet the high detection rate requirement, the quenching and recharge circuits must complete a full cycle in less than 333 ns. Given that both afterpulsing and crosstalk are affected by the accumulated charge in the breakdown region, it is crucial to limit the avalanche pulse time. For this purpose, a quenching time of less than 20 ns is set as the goal [20].

To comply with this tape-out's standard packaging parameters, the designed chips have 32 I/O (input/output) pins. However, the total number of SPADs in the 16 × 16 array far exceeds the number of available I/O pins. Therefore, the data from the SPADs must be serialized. To achieve this, an interface controller is designed in order to efficiently communicate the status of the connected SPADs without missing any events.

Finally, the 40 nm TSMC process imposes an additional constraint on the on-chip circuitry design, specifying that the transistors must operate at a supply voltage of 1.1 V.

5.3.2. CHIP SPECIFICATIONS

As seen in Figure Figure 5.3, the designed chip consists of four distinct 16 × 16 SPAD array chips, each with three extra "stray" testing SPADs on the top. The difference in design parameters of each chip were implemented in order to be able to characterize and compare between SPADs with different types of active areas, varying size of active areas, and also, potentially, observe the effects of added shielding of the SPAD against parasitic electric fields and crosstalk reduction.

Regarding the fourth SC_4 design, specifically, three additional metal layers were implemented to form a grating structure designed to filter out undesired green excitation light (532 nm), while allowing red light in our range of interest (600-800 nm) to pass. By optimizing the metal grating dimensions and periodicity, green light is blocked through destructive interference, while red light is transmitted through constructive interference. Due to constraints of the TSMC 40 nm process node, the metal layers M_1, M_3, and M_6 were selected to form the grating structure.

The layout design of the chips was performed using Cadence Virtuoso, a widely used

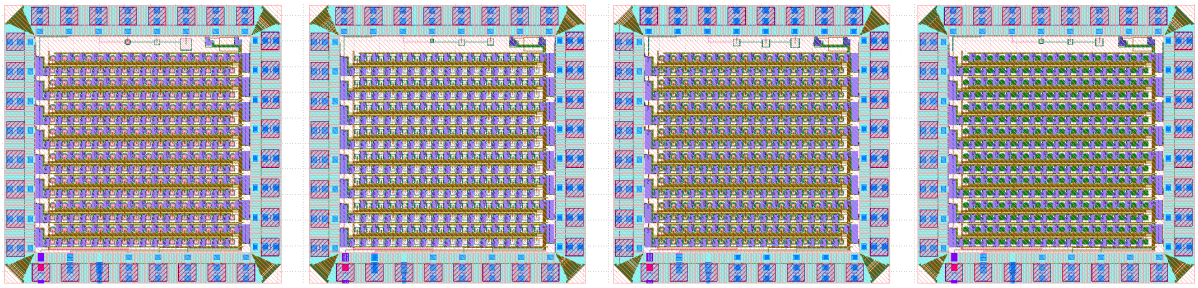


Figure 5.3: The layout of the four chips containing 16 × 16 SPAD arrays, each with different design parameters. These chips are labeled from left to right: SC_1, SC_2, SC_3, SC_4. The SPADs in the array of chip SC_1 have a 12 µm diameter active area in a round configuration, with three extra testing SPADs on the top: i) 12 µm diameter round (active area), ii) 12 × 12 µm^2 square, iii) 36 × 36 µm^2 square. In SC_2, the SPADs in the array have a square 10 × 10 µm^2 active area, with three extra testing SPADs: i) 4 µm diameter round (active area), ii) 14 × 14 µm^2 square, iii) 16 × 16 µm^2 square. SC_3 features SPADs in the array with a 12 µm diameter active area, but also includes a metal border for additional shielding. It also has three stray SPADs: i) 16 × 16 µm^2 square, ii) 20 × 20 µm^2 square, and iii) 26 × 26 µm^2 square. Finally, chip SC_4 contains SPADs with 12 µm diameter active area, with an added metal grating. This grating is specifically designed to block green excitation light from reaching the detector. The three extra testing SPADs have active areas of: i) 8 × 8 µm^2 square, ii) 10 × 10 µm^2 square #1, and iii) 10 × 10 µm^2 square #2.

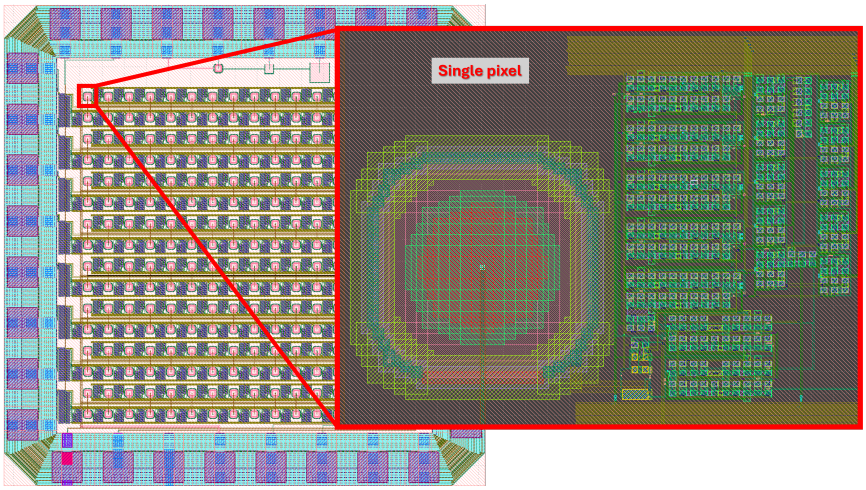


Figure 5.4: Layout of the first out of the four SPAD chips containing 16 × 16 SPAD arrays and on-chip active quenching and readout electronics.

software for integrated circuit (IC) design. Each of the four different chips with SPAD arrays originally occupied a total area of 1085 × 1085 µm^2. However, the fabrication process introduces a shrink factor of 0.9, reducing the final chip dimensions to 976.5 × 976.5 µm^2 after tape-out. This shrink factor is uniformly applied to all features of the chips designed in Cadence. The pitch between each chip was set to 100 µm (after shrink), in order to accommodate individual chip dicing in subsequent processing steps. Lastly, the internal ESD diodes in the I/O ring were detached to address biasing issues identified during characterization of the SPADs fabricated in a previous round, enabling proper SPAD operation above 3 V. The layout of the first SPAD chip can be seen in Figure 5.4.

5.3.3. INDIVIDUAL CHIP DESIGN OVERVIEW

In this subsection, a design overview of the chip's top-level structure is provided. This is followed by an outline of the control electronics, responsible for quenching, recharge and readout.

TOP-LEVEL OVERVIEW

The top-level structure of the chip, as illustrated in Figure 5.5, features a grid layout with 16 rows, each containing 16 SPAD units. Each SPAD unit is connected to its neighbors via a bus and incorporates a 16-bit Parallel-In-Serial-Out (PISO) circuit to facilitate data transfer. At the top right corner of the chip, two 5-bit Serial-In-Parallel-Out (SIPO) modules are included to configure the width and delay of the hold-off circuit's recharge pulse. On the left of the SIPO modules, the three stray SPADs for characterization can be seen.

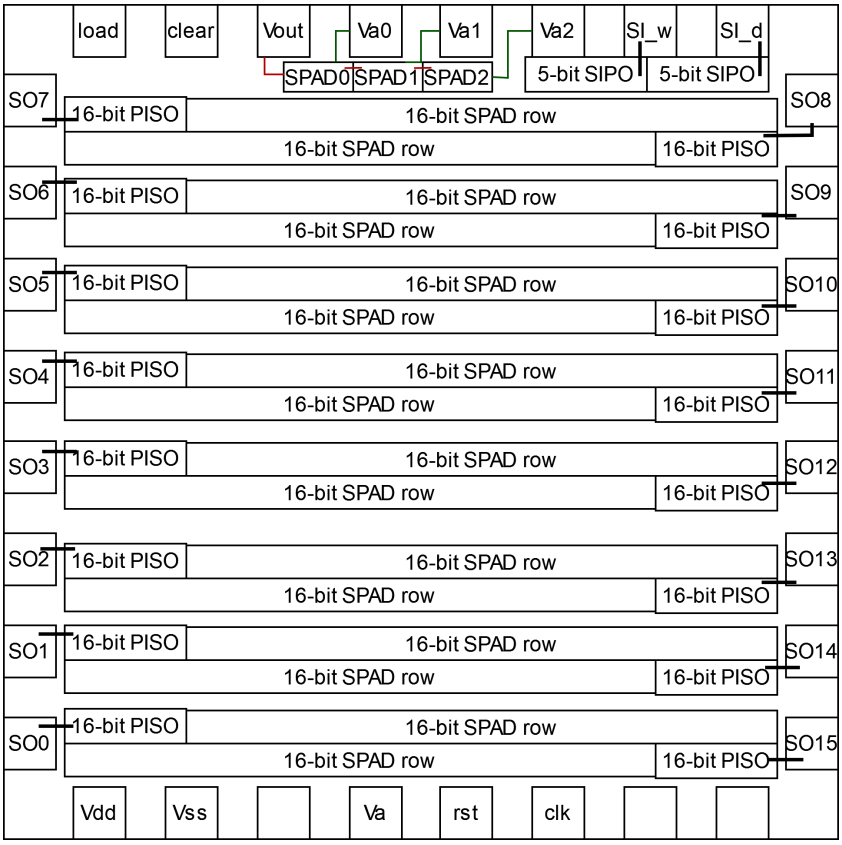


Figure 5.5: The top-level structure of each SPAD chip. This includes the three additional characterization SPADs, the 16-bit SPAD pixel row, the sixteen 16-bit PISO circuits, the two 5-bit SIPO circuits, and the chip's pin-out.

SPAD ARRAY-LEVEL OVERVIEW

The core of the SPAD chip is the 16 × 16 SPAD array. Each SPAD in this array is equipped with its own control electronics, including a quenching and recharge circuit, as well as a readout circuit. The data from each row of SPADs is serialized and sent off-chip through a PISO circuit. Given the limited maximum number of 32 available I/O pins, the 16 serial lines from each row are used, instead, to notify a Field Programmable Gate Array (FPGA) if an avalanche event has occurred within a specific time frame.

In Figure 5.6, the interconnection of the SPAD rows and their respective PISO circuits can be observed. Each SPAD unit's output (labeled "aqc_out") is connected in parallel to the PISO circuit. A global bus is used to propagate the applied voltage V_a, the clock signal, the width and delay bits, and the reset signal to the SPAD units in each row, ensuring that they are all synchronized and can efficiently transmit their status to the FPGA.

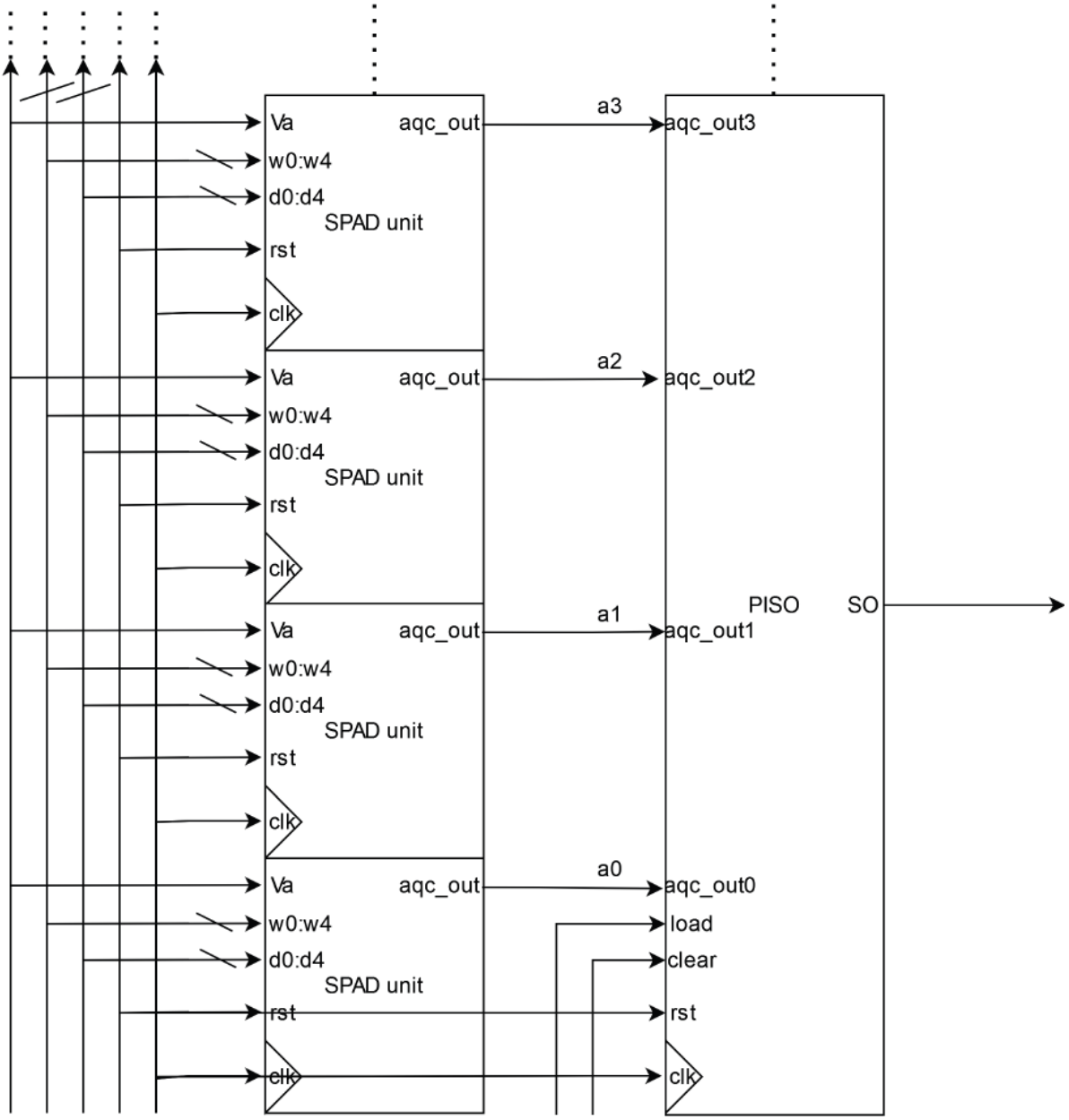


Figure 5.6: Example schematic of the first four SPAD units connected to form a row.

SPAD UNIT-LEVEL OVERVIEW

Every SPAD unit within the chip features an active quenching circuit (AQC) and a hold-off circuit. Both of these components are crucial for the quenching and recharging processes necessary for detecting single photons. Figure 5.7 depicts how each SPAD unit is interconnected with the necessary circuits. There, the V_a signal biases the SPAD, while

the "pwm_out" signal generates the recharge pulse. The output from the AQC ("out") is inverted and connected to the hold-off module, which in turn produces the SPAD's output, "aqc_out". This output indicates whether an avalanche event has occurred.

CADENCE VIRTUOSO LAYOUT DESIGN

As previously mentioned, design of the SPAD chips took place in Cadence Virtuoso, making use of 40 nm TSMC technology.

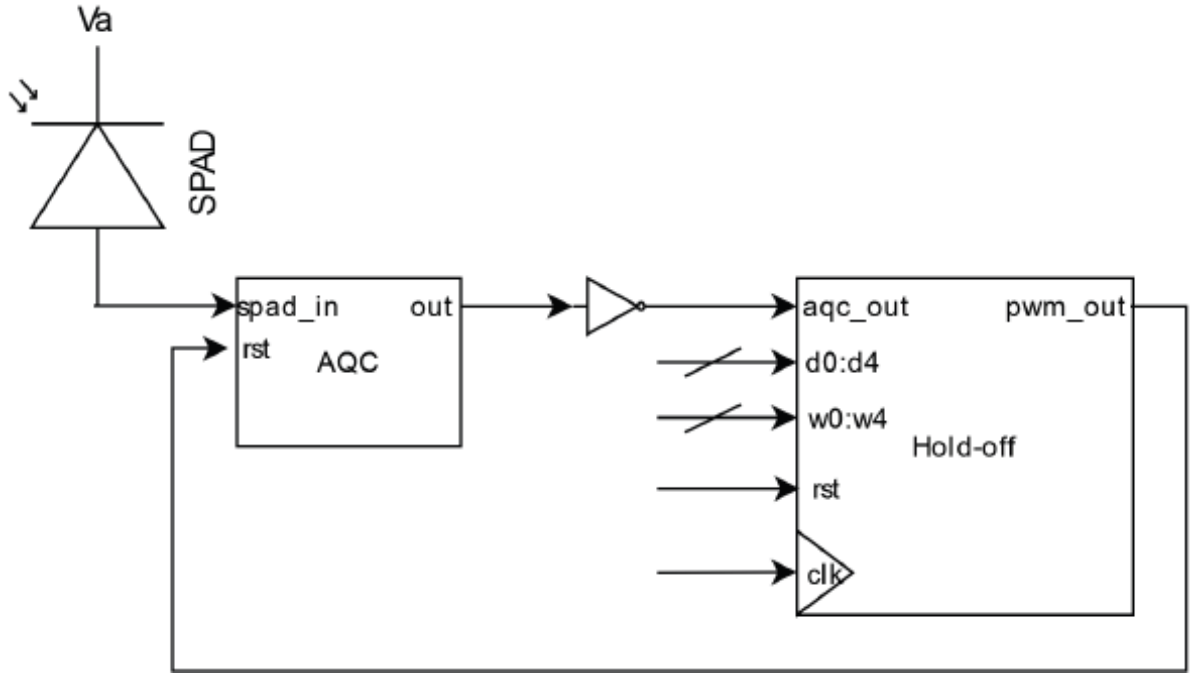


Figure 5.7: Schematic of an individual SPAD unit and the interconnections between it, the quenching circuit (AQC) and the hold-off circuit.

5.3.4. SPAD CHIP MODELING

The SPAD model used in this work is based on the behavioral model developed by Mita *et al.* (2012) [21]. This model describes the SPAD behavior using Verilog-A and aligns with the I-V curve and breakdown characteristics of the fabricated device. Since in the previous fabrication round the SPADs had an unexpected I/O ring issue, direct experimental I-V characterization of the fabricated SPADs was not possible, therefore the ESD diode characteristics were used as reference instead. Based on this, a breakdown voltage of 7.42 V and a series resistance of 5650 Ω were determined experimentally. The parasitic capacitance contributions were estimated at 1–2 pF, as proposed by Zappa *et al.* (2009) [22].

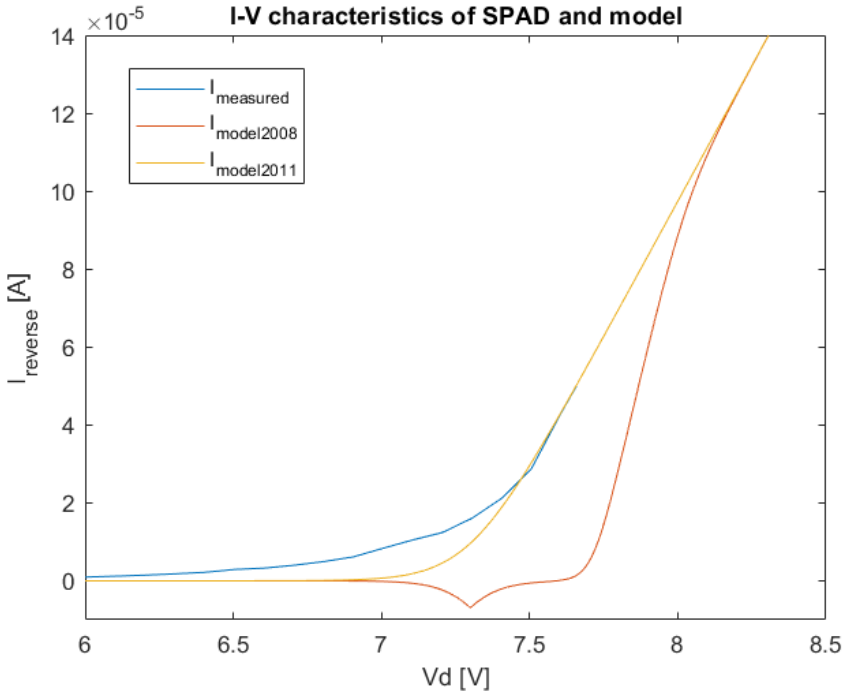


Figure 5.8: I-V curve showing the models of Mita *et al.* [23, 21], and a reference measurement of the previous SPAD chips.

In this model, the SPAD is represented as a voltage-controlled current source with a quiescent inverse saturation current and an avalanche current dependent on the breakdown resistance R_{BD}, the excess voltage $V_D - V_B$ (V_D being the voltage across the SPAD, and V_B being the breakdown voltage), and the normalization voltage V_n, as seen in Equation 5.1. Moreover, a dynamic current model accounts for parasitic capacitances and depletion region charges, which influence the quenching and recharge behavior. Photon detection is simplified in the model, by assuming every photon triggers an avalanche. Avalanche quenching occurs when the current falls below the latching current threshold, set to 100 µA [22].

$$I_{\text{SPAD}} = \begin{cases} I_s, & \text{no avalanche} \\ I_s + \frac{V_n}{R_{BD}} \ln\left(1 + e^{\frac{V_D - V_n}{V_n}}\right), & \text{avalanche} \end{cases} \tag{5.1}$$

5.3.5. ON-CHIP CIRCUITRY

ACTIVE QUENCHING CIRCUIT

Active quenching utilizes a circuit to detect the onset of an avalanche, quench it, and recharge the SPAD back to its operating voltage. This approach eliminates the dependency on large ballast resistors, enabling faster recharge and higher photon detection rates exceeding several hundred Mcounts/s [24]. The process involves three stages: sensing the avalanche, quenching the current via a feedback loop, and resetting the SPAD after a user-defined dead time. The dead time balances afterpulsing effects and the maximum achievable count rate [15]. The controllable hold-off circuit allows for optimization of these trade-offs.

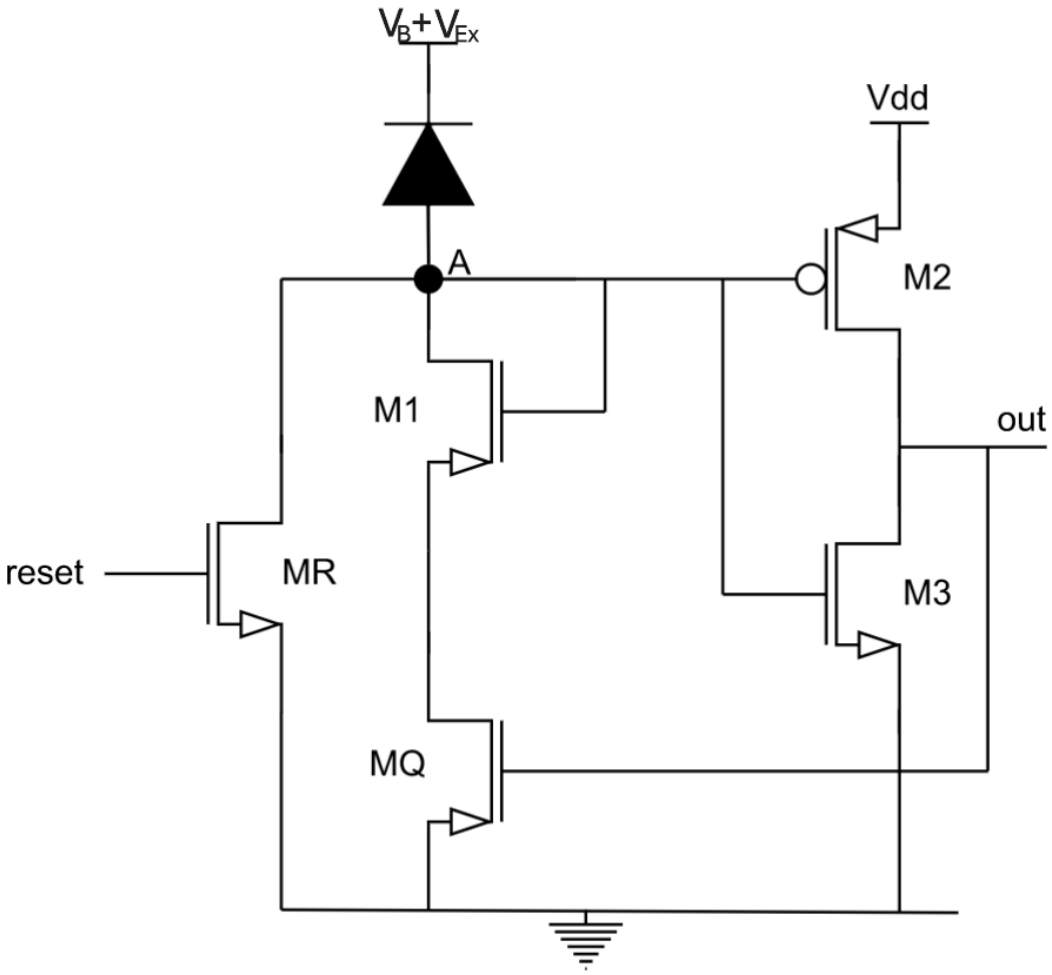


Figure 5.9: The active quenching circuit employed in the design of the SPAD arrays.

The selected active quenching circuit (AQC) is again based on Mita *et al.* [21] (see Figure 5.9). It incorporates five transistors and operates through a positive feedback loop to rapidly quench the avalanche current and reset the SPAD. The transistor design prioritizes minimal parasitic capacitances for M1, M2, and MQ, while MR is optimized with a larger aspect ratio (width to length) to accelerate the reset phase. Simulations confirm this AQC's ability to quench avalanches in 20 ns and reset the SPAD within 1 ns, achieving a maximum count rate of 40 Mcounts/s.

HOLD-OFF CIRCUIT

The hold-off circuit depicted in Figure 5.10 is an integral component of the AQC design, implemented to control the dead time between successive avalanche events. This dead time minimizes afterpulsing effects, by allowing sufficient time for traps to depopulate before the SPAD is recharged. The digital implementation of the hold-off circuit includes a 5-bit counter, two comparators, and two JK flip-flops. All of these components work in conjunction to provide precise control over delay and pulse width, which can be configured using 5-bit SIPO modules.

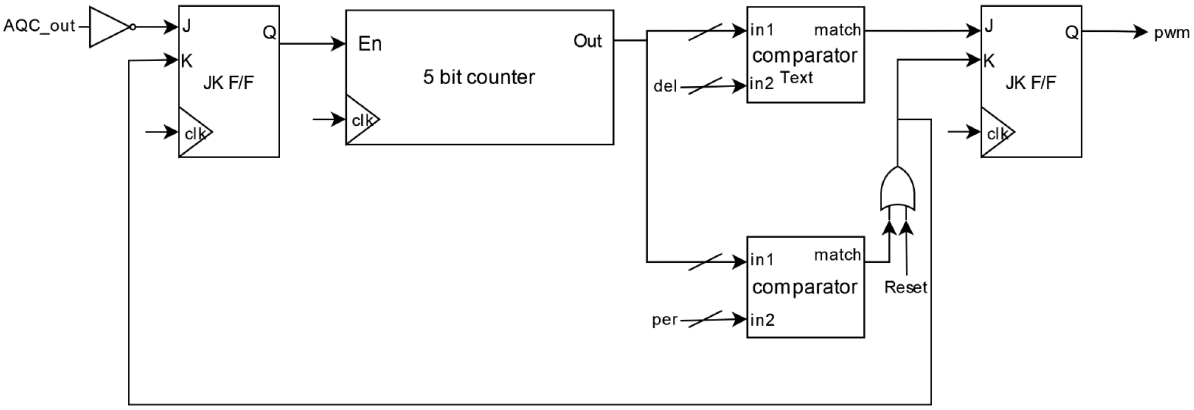


Figure 5.10: Schematic of the digital hold-off circuit.

Specifically, the JK flip-flop functions as a buffer to maintain sequential operation. It is configured in a master-slave arrangement and ensures stable timing signals, essential for high-speed photon detection. The 5-bit counter operates asynchronously, and is driven by the SPAD detection signal. It measures the clock cycles required to set the hold-off delay and reset pulse width. The comparator plays a key role by matching the counter's output with preset delay and width values. This matching triggers the circuit to recharge the SPAD precisely when needed, minimizing afterpulsing while maximizing detection rates. Since the hold-off circuit and its components are integral to the SPAD design, they are fully implemented on-chip as part of the final layout. This on-chip integration enhances performance and eliminates the need for external timing and control hardware.

DIGITAL COMMUNICATION AND CONTROL MODULES

To manage data efficiently, 16-bit PISO modules are implemented to communicate the SPAD status to an FPGA, while 5-bit SIPO modules configure the hold-off circuit. Each PISO module includes a shift register and buffer to serialize SPAD avalanche events, supporting a 16×16 SPAD array. The SIPO module enables precise control of the hold-off circuit's delay and width via bitstreams, thereby enhancing flexibility in adjusting timing parameters. Simulations demonstrated that both PISO and SIPO modules operate successfully. The PISO module enables reliable serialization of SPAD events for FPGA readout, ensuring no photon events are missed even at high rates. Similarly, the SIPO module accurately receives and locks configuration bitstreams for the hold-off circuit. Together, these modules enable the chip to meet the communication and I/O requirements, while maintaining speed and accuracy.

DESIGN VALIDATION

Finally, the top-level layout of each chip, including all aforementioned components, was simulated to ensure proper functioning, as seen in Figure 5.11. Each layout underwent Design Rule Check (DRC) and Layout Versus Schematic (LVS) validation, with resistances, capacitances, and coupling capacitances extracted via parasitic extraction (PEX) for post-layout simulations. The SPAD unit, including its quenching and hold-off circuit, achieved a validated cycle of 20 ns with negligible signal degradation. Similarly, the 16-bit SPAD row, connected via a bus and PISO, achieved a 30 ns readout cycle, comfortably meeting the photon detection speed requirements.

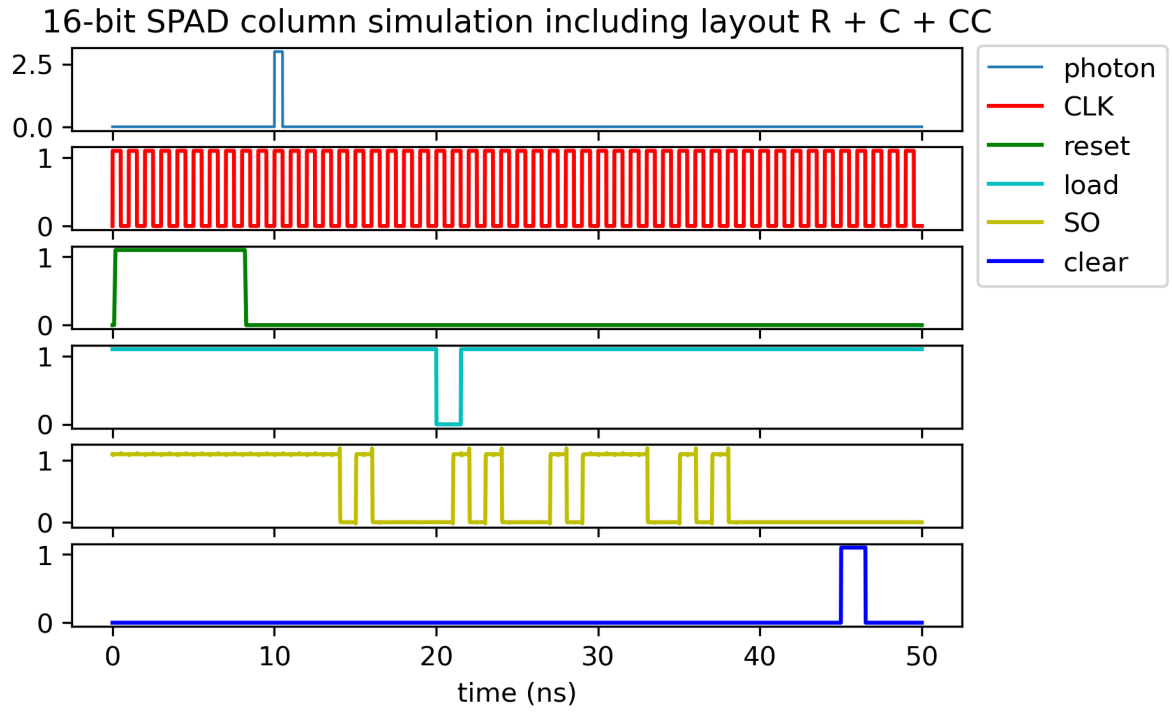


Figure 5.11: Post-layout 16-bit SPAD simulation, including the SPAD components and the on-chip circuitry.

5.4. ELECTRICAL CHARACTERIZATION

In this section, the electrical characterization setup is described, along with the custom PCB that was designed for this. Afterward, electrical characterization measurements are performed on the added, stray SPAD chips located on the top of each chip containing SPAD arrays. The breakdown voltage V_B is determined and the behavioral difference of the SPADs is observed. The SPAD arrays are digitally controlled, and their operation is investigated further later on in this chapter (see subsection 5.5.2). A link to the SPAD control software can be found in Appendix B.

5.4.1. PCB DESIGN

For characterization of the fabricated CMOS chips containing SPAD arrays, a custom printed circuit board (PCB) was designed, as seen in Figure 5.12. This PCB contains the necessary components for passive quenching of the SPADs, as well as analog-based characterization of the SPADs. The characterization circuit employs a ballast resistor for passive quenching and a sensing resistor to calculate current based on voltage measurements (see Figure 5.13). A comparator converts photon count signals into digital pulses for FPGA processing. The digital connections on the PCB are straightforward, with all signals, except the clock, routed to a 2×20 GPIO connector. The clock signal is connected through an SMA connector. Grounding of the chip is done via one of the cables.

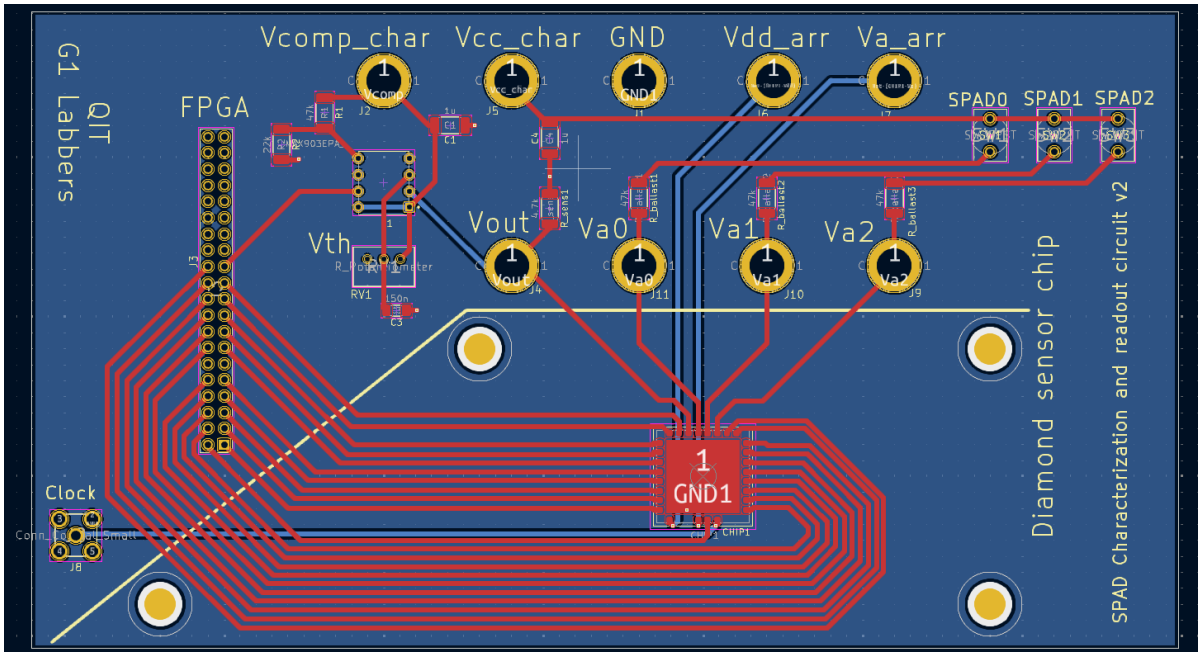


Figure 5.12: The custom PCB for electrical characterization of the stray SPADs of each full chip with SPAD arrays, designed by Dylan Aliberti.

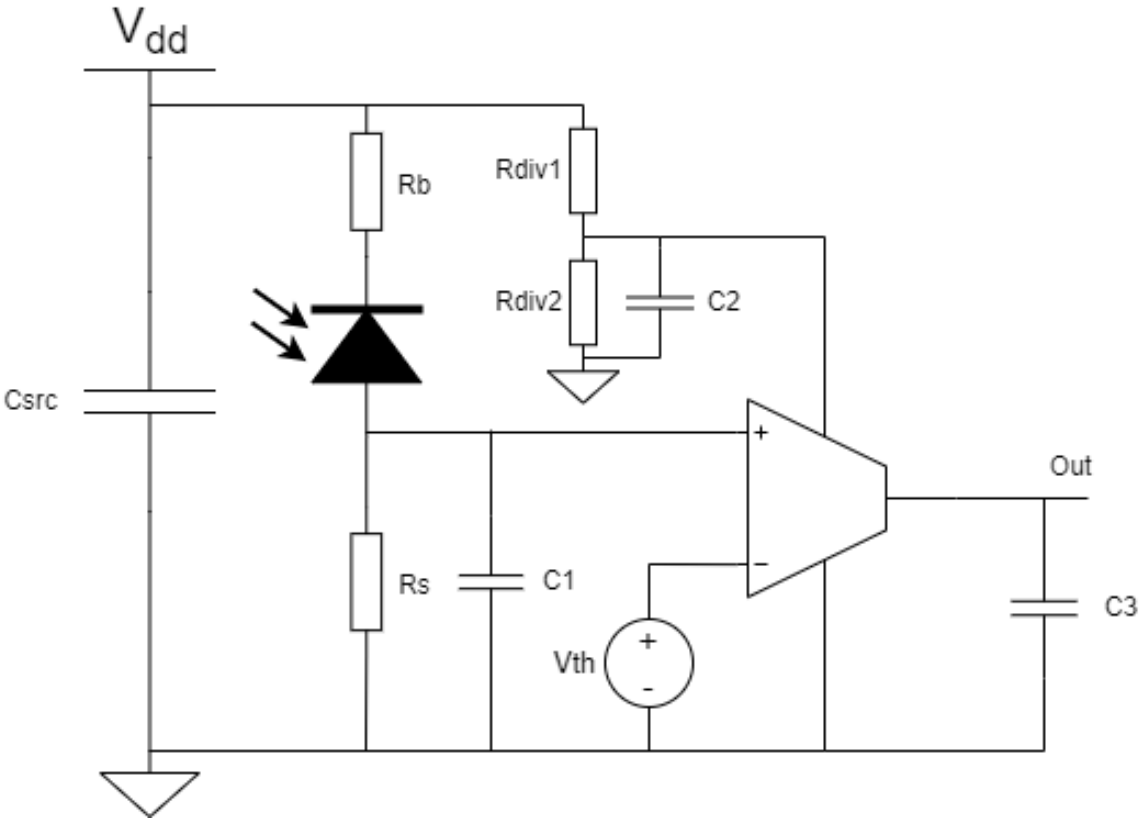
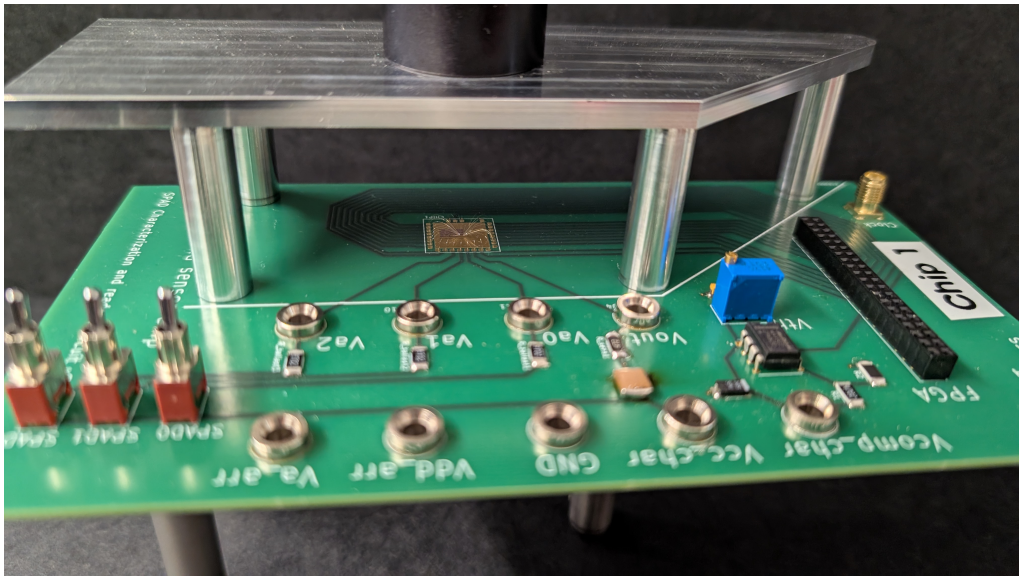
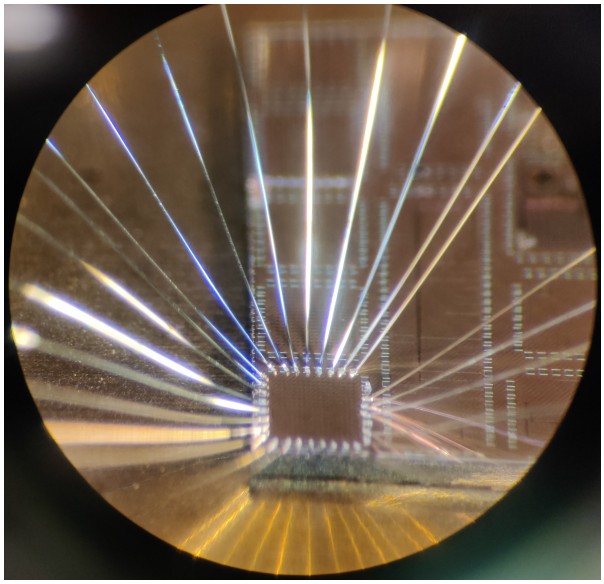


Figure 5.13: The custom PCB for electrical characterization of the stray SPADs of each full chip with SPAD arrays, designed by Dylan Aliberti.

In Figure 5.14a, the PCB can be seen mounted on a custom-designed stage, which is later integrated into the widefield ODMR setup configuration. For attachment onto the PCB, the chip's bonding pads need to be wire-bonded (see Figure 5.14b). For this purpose, 25 µm diameter wires were used. The wire bonding process took place in QuTech, TU Delft.



(a)



(b)

Figure 5.14: **(a)** Photo of the custom PCB mounted on a custom stage for use later in the widefield ODMR setup. **(b)** The wirebonded CMOS chip on the custom PCB. Here, the first chip out of the four designed chips is bonded.

5.4.2. ELECTRICAL CHARACTERIZATION RESULTS

The breakdown voltages of the stray SPADs were determined by manually varying the reverse bias voltage of the power supply. Most SPADs exhibited breakdown voltages between −15 V and −16 V, values that are consistent with the findings of Pellegrini *et al.* [7], who also characterized SPADs fabricated using 40 nm CMOS technology. Full I-V and C-V curves were subsequently measured using a probe station, with a small hysteresis observed between forward and backward sweeps. The I-V curves are shown in Figure 5.15.

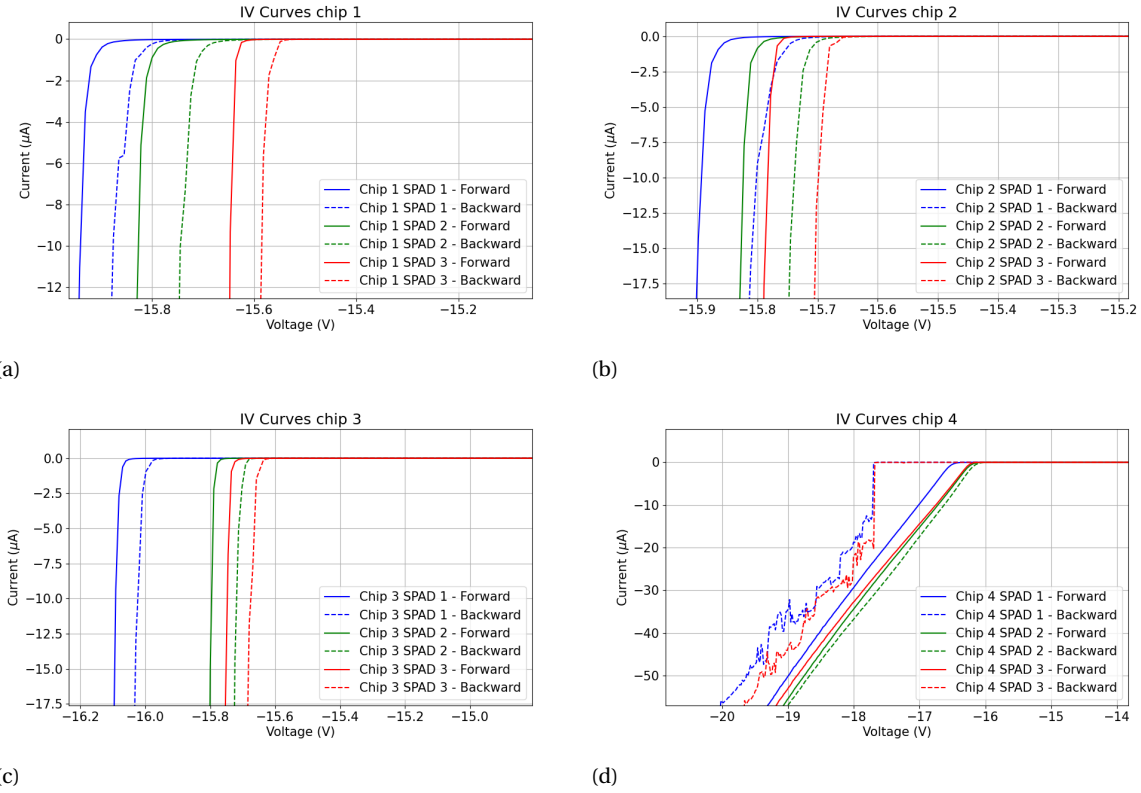
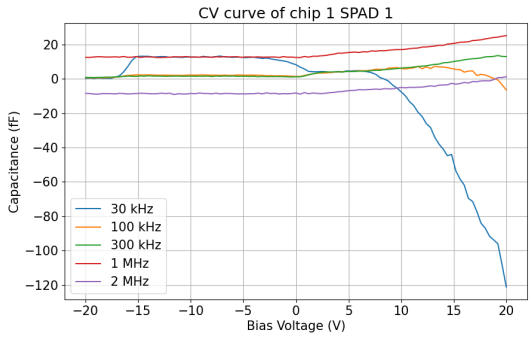


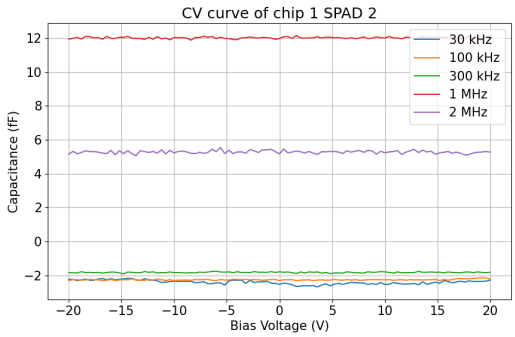
Figure 5.15: I-V curves of the three additional stray SPADs of each individual chip containing SPAD arrays. During forward and backward sweeps, a small hysteresis can be seen. For the first three chips, the breakdown voltage V_B is calculated to be between −15.5 V and −16.1 V. The fourth one exhibits somewhat different behavior and a slightly increased V_B between −16.1 V and −17.7 V. **(a)** Corresponds to the SPADs of SC_1, **(b)** corresponds to the SPADs of SC_2, **(c)** corresponds to the SPADs of SC_3, and **(d)** corresponds to the SPADs of SC_4.

The C-V curves, which generally aligned with typical diode characteristics, did show frequency dependency but no voltage dependency. Three of the most representative measured C-V curves are presented in Figure 5.16, with the full data being available in Appendix E.

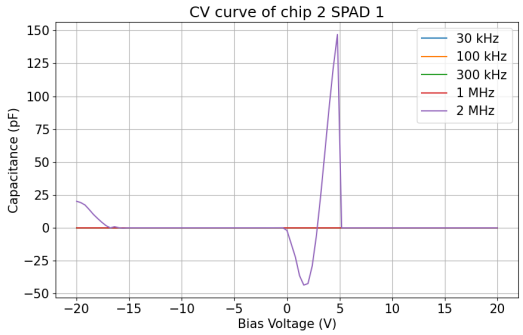
Efforts to observe avalanche pulses were conducted by connecting the SPADs to an oscilloscope through the PCB and powering them above their breakdown voltage, reaching up to 28 V. However, instead of producing pulses, the SPADs remained in a continuous avalanche state, indicating a failure to properly quench. To address this, various resistors, ranging from 10^5 to 10^6 Ω, were incorporated into the passive quenching circuit to test whether slower quenching could resolve the issue, but no improvement was



(a)



(b)



(c)

Figure 5.16: C-V curves of the three specific stray SPADs belonging to different chips, representative of the rest of the C-V measurements. The current limit was set to 100 µA. **(a)** Corresponds to SPAD #1 of SC_1. Its C-V curve exhibits an upward trend as it approaches forward bias from lower voltages across most frequencies. However, beyond the forward voltage, the curve becomes unreliable due to the 100 µA current limit. At a frequency of 30 kHz, a distinct plateau appears in the C-V curve, corresponding to the bias region where the SPAD operates as a blocking diode. **(b)** Corresponds to SPAD #2 of SC_1. Here, the capacitance remains largely stable across all voltage ranges but demonstrates a noticeable dependence on frequency, with the highest capacitance observed at 1 MHz. **(b)** Corresponds to SPAD #1 of SC_2. This SPAD exhibits erratic behavior both below the breakdown voltage and beyond the forward bias region. The spike near the forward bias voltage aligns with typical diode behavior [25]. However, the dip showing negative capacitance is likely a result of measurement inaccuracies or calibration artifacts.

observed.

To verify the oscilloscope's functionality, a separate, unrelated SPAD[1] equipped with its own passive quenching circuit was tested under similar conditions. Pulses were successfully detected, ruling out any issues with the oscilloscope setup. Given that the passive quenching circuit relies solely on a resistor and multiple resistor values were tested without success, it is unlikely that the circuit itself is the source of the problem. This strongly suggests a design flaw in the fabricated SPADs, preventing them from quenching effectively. Further analysis will be necessary to pinpoint and resolve the underlying issue.

[1] This SPAD chip was provided by Robert van Veldhoven, from NXP Semiconductors.

5.5. INTEGRATION OF DIAMOND WITH CMOS CHIP

5.5.1. SPAD ARRAY READOUT

The chip containing the SPAD arrays is wire-bonded onto a custom PCB connected to an FPGA. The FPGA manages high-speed signal processing, aggregates the data, and sends a slower signal to an Arduino, which, in turn, relays the data to a computer, using its built-in digital communication modules. From there, the data is processed with Python scripts, turning it into an image. The chip-to-computer communication process is depicted in Figure 5.17.

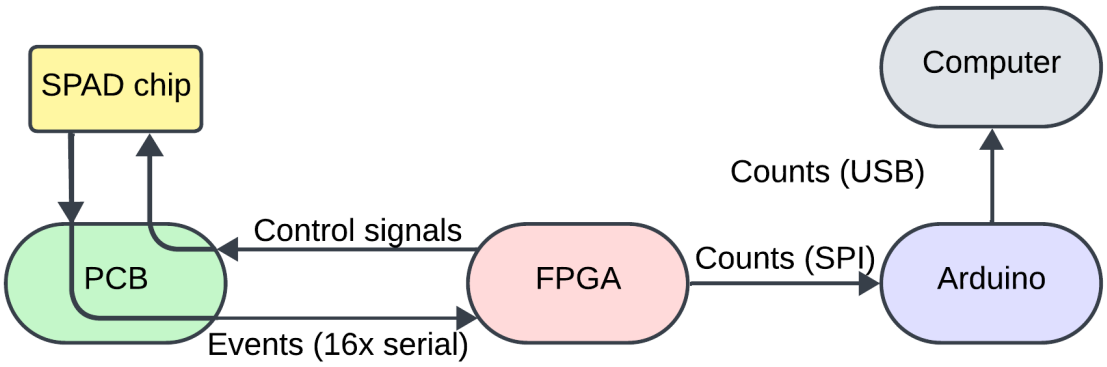


Figure 5.17: Schematic of the communication process between SPAD chip, PCB, FPGA, Arduino and computer.

The chip's logic voltage of 1.1 V introduced a mismatch with the FPGA's minimum logic level of 1.5 V. To address this, simple voltage dividers were implemented, lowering the FPGA output voltage to 1.085 V. This addition caused distortions to the high-frequency signals, requiring a reduction in the FPGA clock frequency to 1 MHz. For chip output, the FPGA interprets voltages above 975 mV as logical highs, allowing the chip's 1.1 V output to be correctly recognized. This narrow voltage margin, however, increases susceptibility to noise and voltage drops.

In order for the chips with the SPAD arrays to communicate their signal to the FPGA, and for it to subsequently reach the Arduino and the lab computer, software[2] had to be developed to coordinate these signals. The FPGA serves as a high-speed parallel counter that decodes the 16 channels of serial data from the SPAD chip and aggregates photon counts. It operates in a repetitive readout cycle, polling the SPAD chip to retrieve and clear photon event data before updating its internal 32-bit counters. Once the readout cycles are complete, the aggregated data is transferred to the Arduino via Serial Peripheral Interface (SPI), with the FPGA acting as the SPI master. This streamlined process enables data acquisition to proceed simultaneously with the transmission of previous measurements.

The Arduino facilitates communication between the FPGA and the computer, transmitting raw data received via SPI without any processing. The USB connection between the Arduino and computer ensures continuous data flow, enabling real-time visualization and analysis. On the lab computer, the incoming data is interpreted and assem-

[2] Software was developed by Dylan Aliberti.

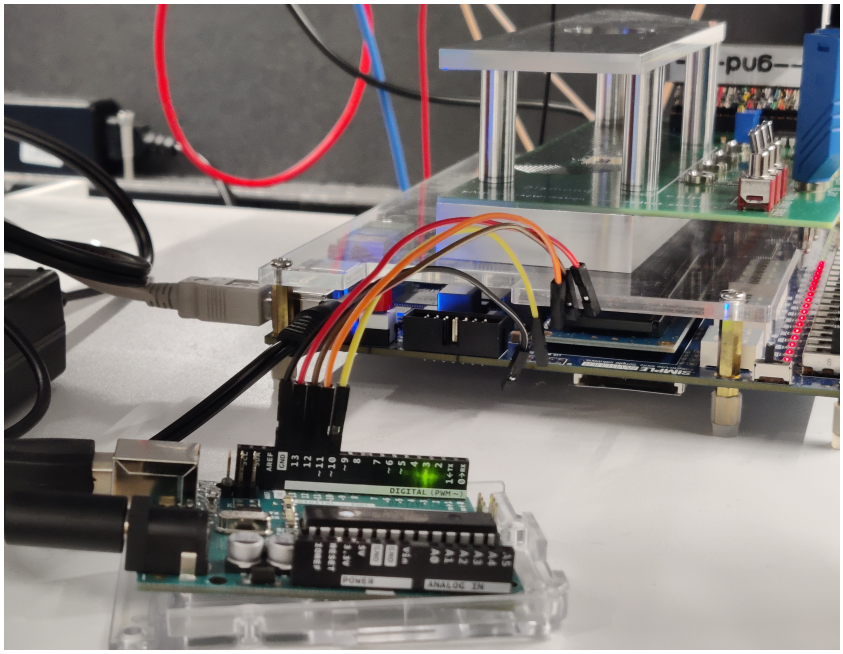


Figure 5.18: Photo showing how the PCB is connected to FPGA, which is, in turn, connected to the Arduino.

bled into a 2D array, reconstructing the SPAD array's photon count image. The image can be displayed live or used for further analysis, including ODMR processing. Below, a schematic can be found, depicting the overall communication process between the different electronic modules (Figure 5.19).

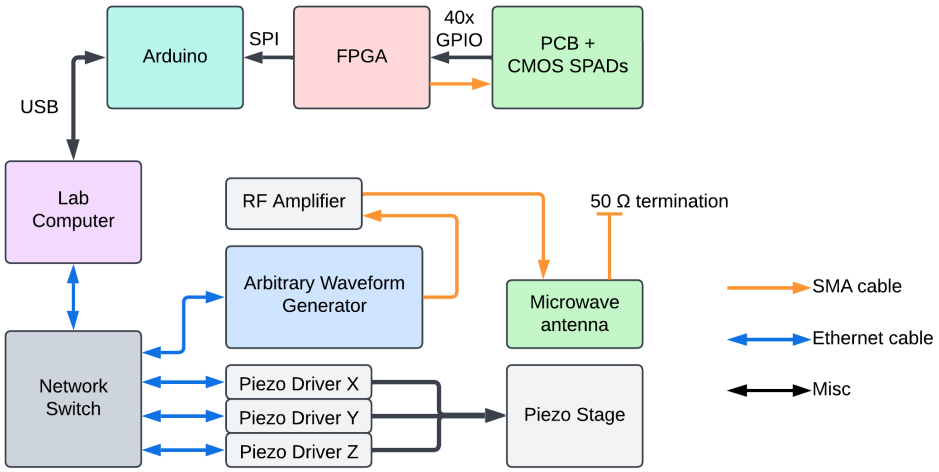
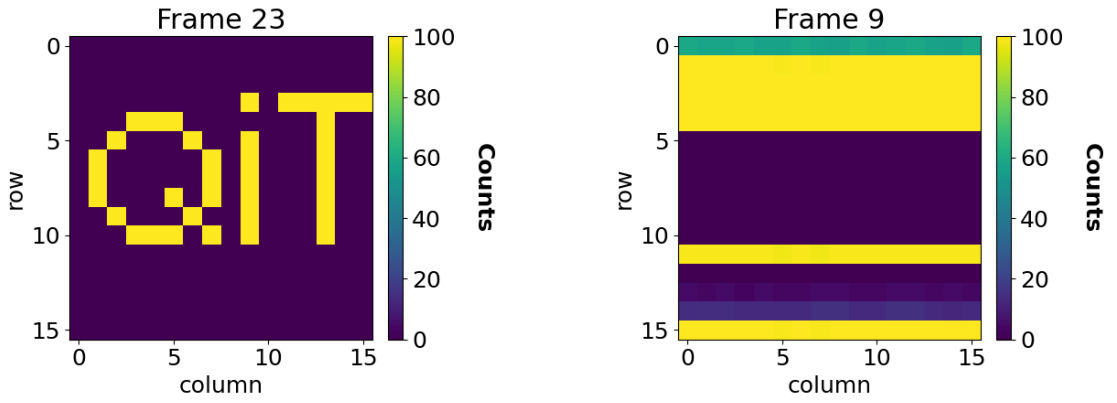


Figure 5.19: Schematic showing the overall communication process between each electronic module in the widefield ODMR setup.

5.5.2. SPAD ARRAY OPERATION TESTS

Before integrating the SPAD chip into the widefield testing setup, multiple tests were performed, but no signal was detected from the chip. Initially, an FPGA design generating a predefined test signal mimicking SPAD behavior confirmed the proper functioning of the FPGA-Arduino-computer communication chain (Figure 5.20a). When the SPAD chip was connected to the FPGA and powered, but the SPADs remained unpowered, the output showed undefined signals with rows randomly alternating between saturated and zero counts, favoring saturation in the top and bottom rows (Figure 5.20b). However, even powering the SPADs did not resolve this issue.



(a) (b)

Figure 5.20: **(a)** FPGA output, mimicking the behavior of the SPAD chip. **(b)** Snapshot of the FPGA output with the actual SPAD array chip connected to it.

Another attempt was made to acquire and analyze the SPAD's signals, this time using an oscilloscope. The test involved connecting only the LOAD and CLOCK wires between the FPGA and the SPAD chip, with the chip powered. While the CLOCK and LOAD signals were confirmed to reach the chip, no output was observed on the serial wires. The expected flag bit and photon event data were absent, and the serial wires remained at approximately 420 mV, indicating no driving signal from the chip.

Additional tests involved pulling the FPGA's input pins to ground and 1.1 V using resistors, yielding expected results, with measured voltages at 1.07 V and 50 mV, respectively. This verified that the FPGA input pins were functioning as intended, but the SPAD chip failed to drive the serial wires as required. The results suggest a malfunction in the SPAD chip, preventing it from sending the expected signals.

5.5.3. IMPLEMENTATION OF THE WIDEFIELD ODMR SETUP

In order to perform ODMR measurements using the fabricated chips with SPAD arrays, modifications were done to the confocal ODMR configuration (previously described in section 2.5), turning it into a more compact, widefield setup. The schematic of this altered version can be seen below in Figure 5.21, while Figure 5.22 and Figure 5.23 show photos of it.

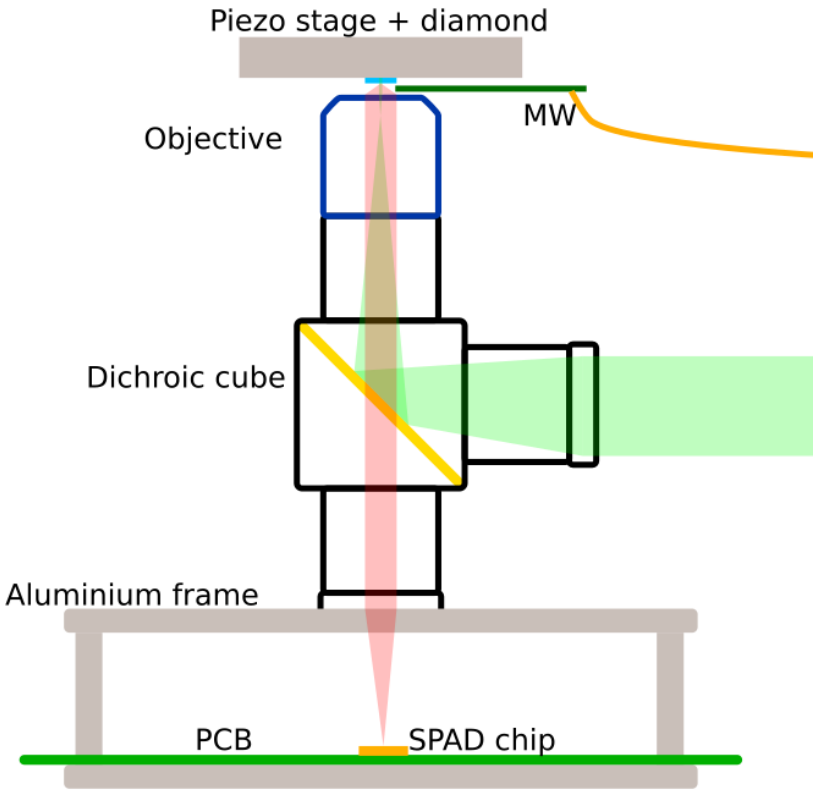


Figure 5.21: Schematic of the SPAD chip integrated with the diamond substrate, in a widefield setup configuration. In this image, the excitation path is not shown, as it has already been described in other chapters.

This setup follows the same operating principles as the confocal ODMR version described earlier, but, this time, the SPCM and the time tagger unit are replaced by the CMOS-fabricated SPAD chip. A dichroic mirror is used once again, this time reflecting the green excitation light towards the sample, while allowing the red emission light to propagate towards the SPADs underneath the diamond. The diamond itself is now mounted on a differently designed custom mounting plate, seen in Figure 5.23c. The green light is collimated by a lens, right before the objective lens, and comes out as a collimated beam incident on the diamond. Although the excitation path is the same as before, such a configuration makes the setup significantly more compact, occupying drastically less area than before. Furthermore, by scaling up the number of SPADs in the array and using further integration techniques, it has the potential for high-sensitivity high-speed quantum sensing and imaging.

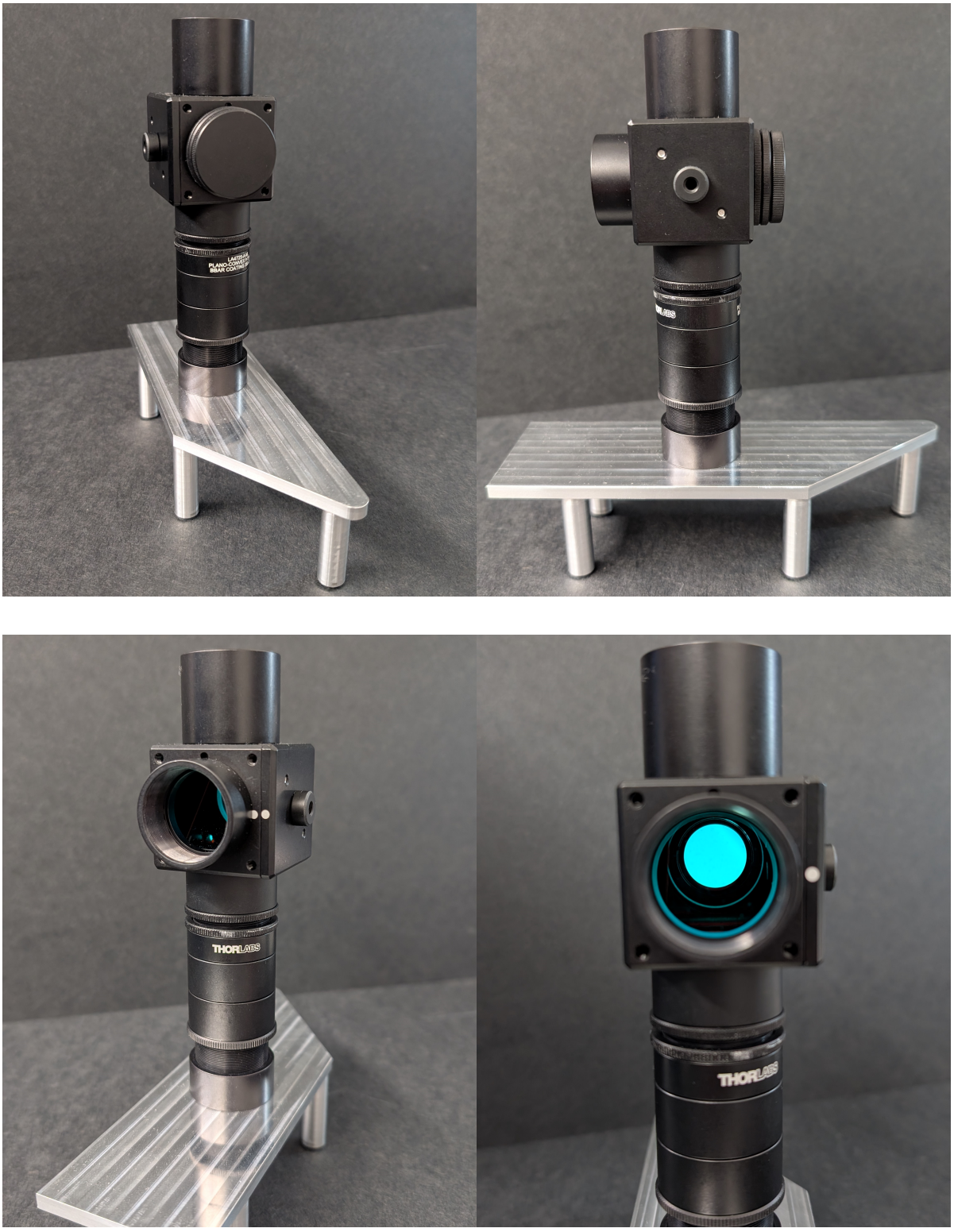
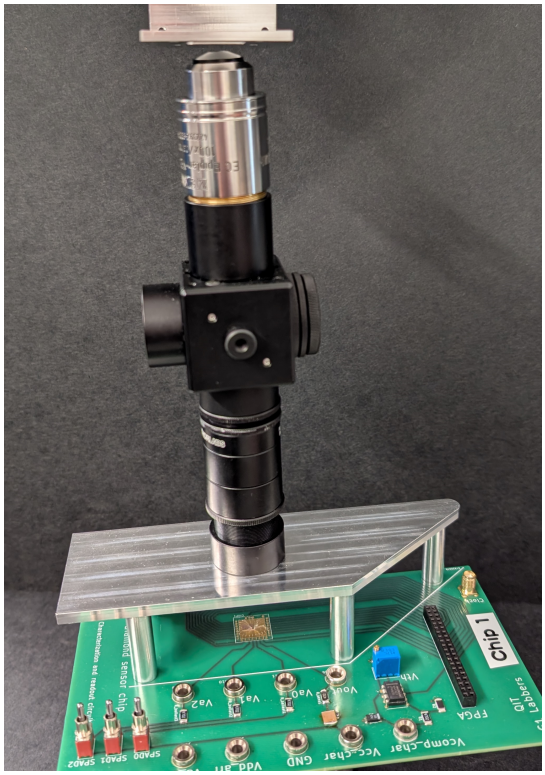
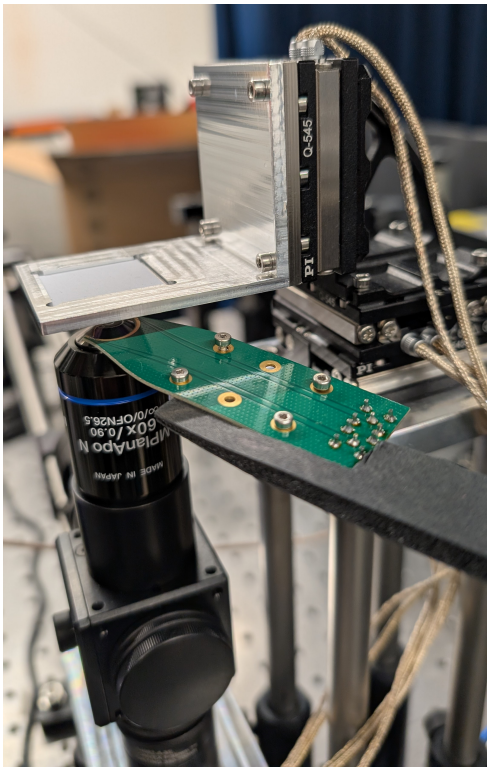


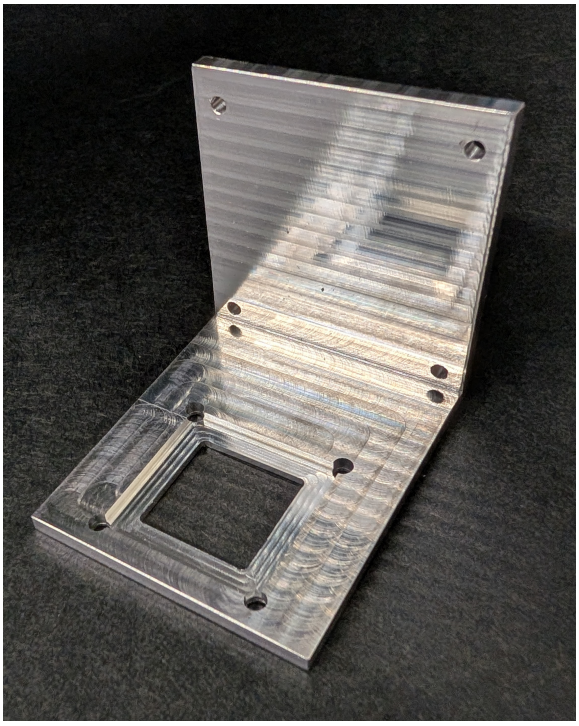
Figure 5.22: Photos of the custom-designed integrated widefield ODMR system, showing the configuration of the excitation and collection optics, mounted on top of a stage that houses the PCB and the SPAD chips.



(a)



(b)



(c)

Figure 5.23: Photos of the custom-designed integrated widefield ODMR system. **(a)** Shows a full image of the configuration of the excitation and collection optics, which are mounted on top of a stage that houses the PCB and the SPAD chips. **(b)** Shows a photo of the complete integrated widefield ODMR setup incorporated on the optical table. **(c)** Shows a photo of the custom-designed diamond substrate mounting plate, made for use in the integrated widefield ODMR setup.

5.5.4. EXPERIMENTAL RESULTS

As mentioned in subsection 5.5.2, the SPADs did not seem to exhibit proper SPAD behavior and could not drive the signal as expected. Therefore, alternatives were sought out, so that at least the operation of the designed widefield setup could be validated, and some proof-of-concept measurements could be performed.

ALTERNATIVE SPAD TESTS

An alternative SPAD was connected to the testing setup using an SMA cable adapted to the main PCB's banana inputs, allowing the FPGA to process photon events. To minimize noise, a custom adapter was soldered to reduce the unshielded cable length. While oscilloscope measurements showed clean SPAD pulses when using SMA-BNC cables (see Figure 5.25a), connecting through the PCB introduced significant noise. The SPAD pulses (20 mV) were overwhelmed by external noise (50 mV), making reliable signal amplification unfeasible, as seen in Figure 5.25c and Figure 5.25d. Furthermore, attempts to use an external RF amplifier yielded inconsistent results. Although amplified pulses were observed, they were accompanied by oscillations of variable magnitude and duration, rendering the signal unsuitable for FPGA processing (see Figure 5.25b). With more time and better electronics and cable connections, proper signal driving and readout would be possible. The connections of the PCB to this SPAD can be seen in Figure 5.24.

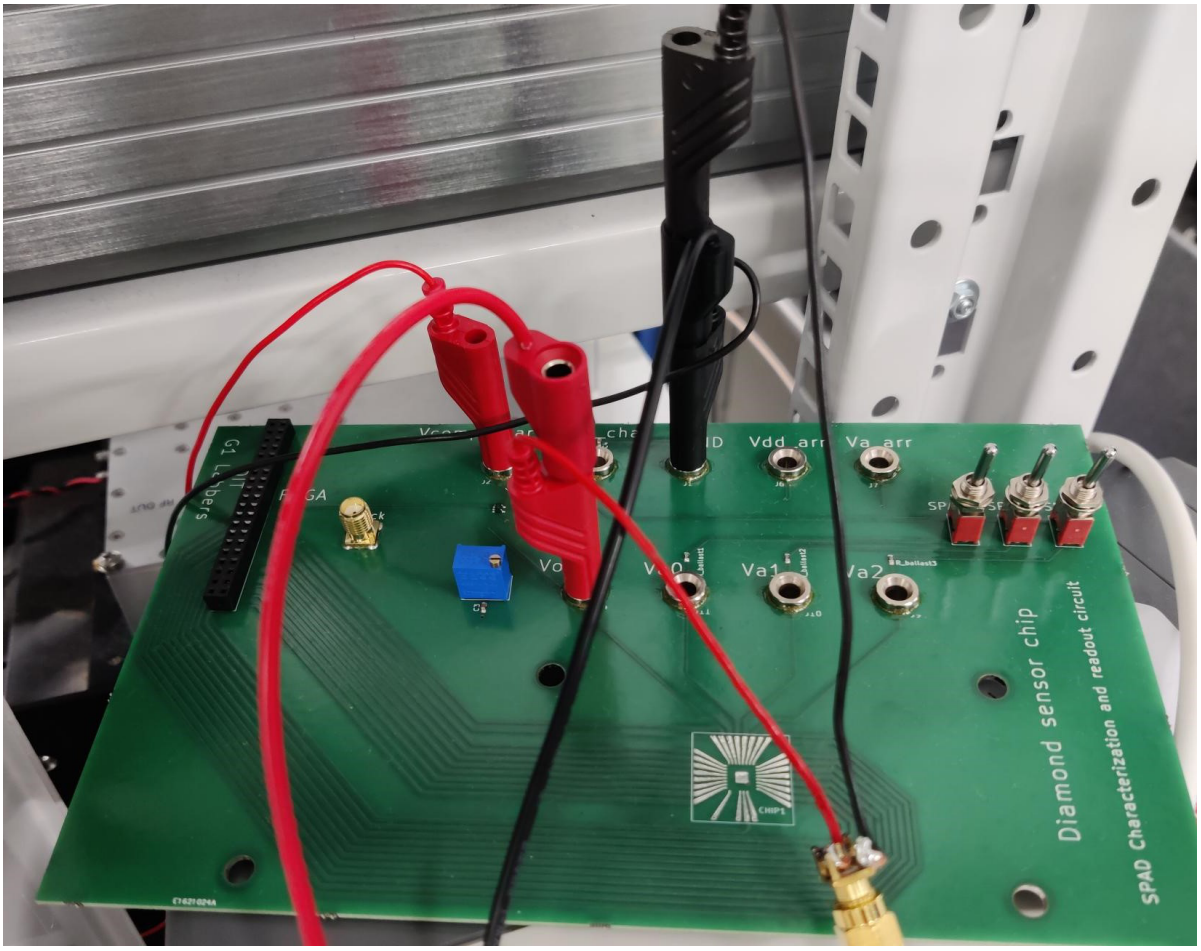
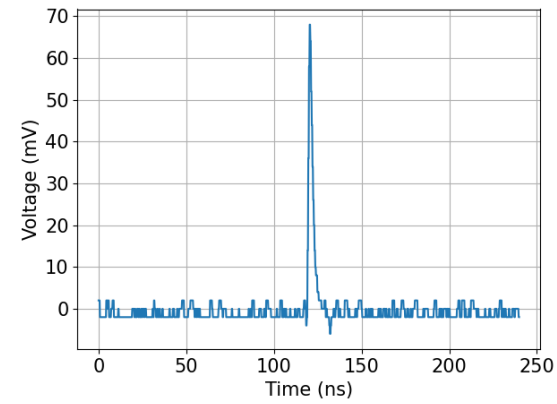
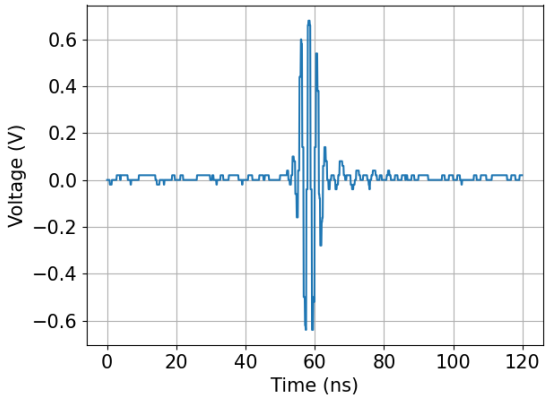


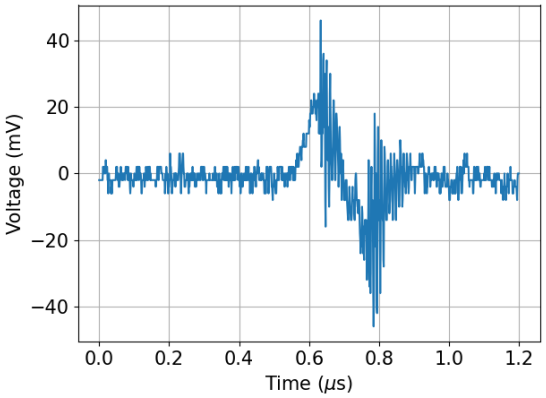
Figure 5.24: PCB connected with an SMA connector to the alternative SPAD that was tested.



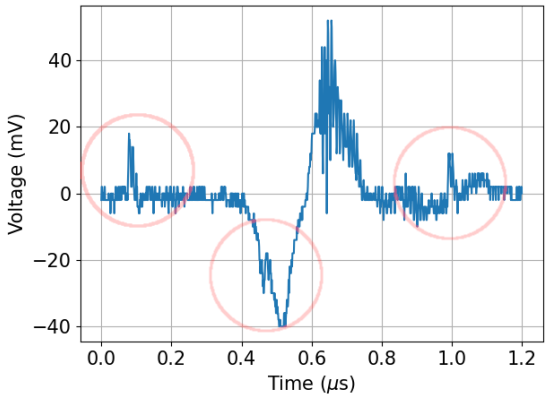
(a)



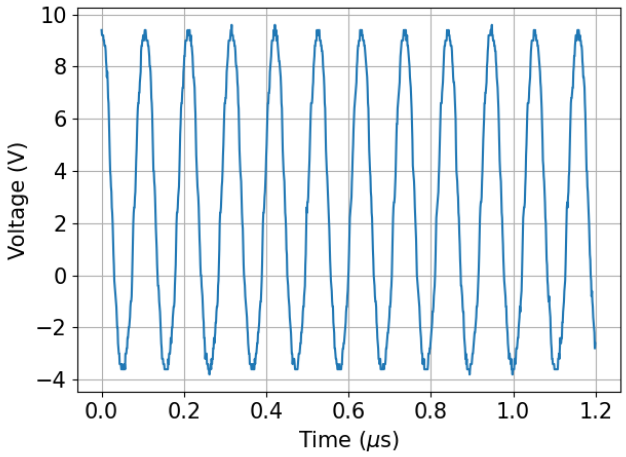
(b)



(c)



(d)

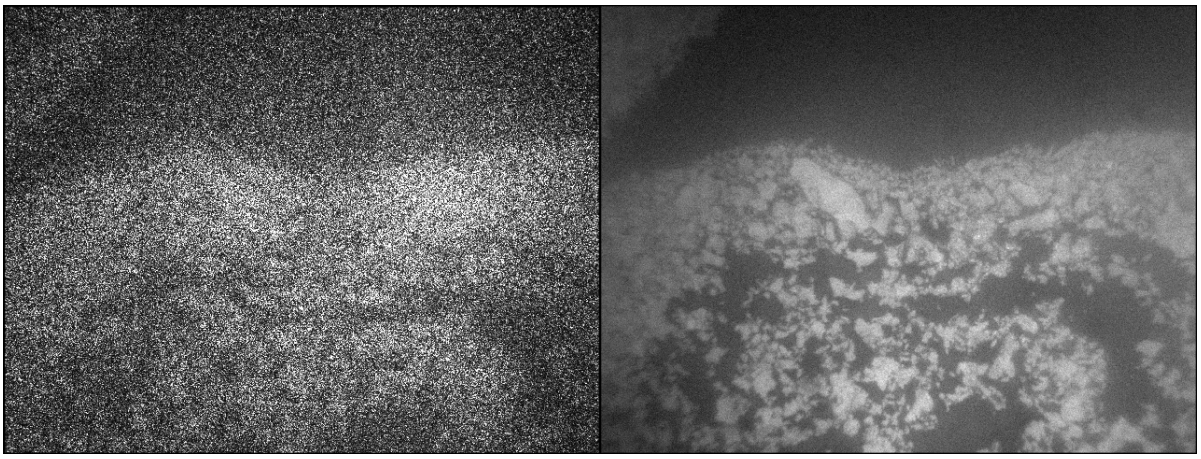


(e)

Figure 5.25: Oscilloscope captures showing various SPAD signal conditions and challenges during testing. **(a)** Oscilloscope signal of the alternative SPAD that was tested. **(b)** SPAD signal on the oscilloscope, amplified by an external RF amplifier. The inconsistent oscillations in the pulses make this amplifier not suitable for connection with the FPGA, which expects certain voltage and square pulses. **(c)** Noise signal measured at the entry point to the PCB, while the SPAD is off. **(d)** SPAD signal measured at the entry point to the PCB. SPAD pulses are still visible, but significantly affected by the noise of the electronics. **(e)** Oscilloscope signal of the PCB-integrated comparator, which has a non-zero output when the SPAD is powered. These oscillations, however, indicate that it is not functioning as expected.

IMAGING CAMERA TESTS

Finally, the imaging camera, previously used in the confocal ODMR setup for viewing of the sample for alignment before the measurements, was mounted underneath the diamond, where the SPAD chip was located earlier. First, the diamond was illuminated by a 30 mW 532 nm laser, although, due to the laser's high power and insufficient filtering of the stray green light by the dichroic mirror, the resulting image was obscured. Using a white LED produced a clear image of the diamond, verifying correct alignment and placement of the optics, in a way that would allow the setup to perform the type of imaging it was designed for. The corresponding images can be found in Figure 5.26.



(a) (b)

Figure 5.26: Images acquired by the imaging camera. **(a)** Acquired after illumination with a 532 nm excitation laser. **(a)** Acquired after illumination with a white LED.

BIBLIOGRAPHY

[1] Franco Zappa et al. “Principles and features of single-photon avalanche diode arrays”. In: *Sensors and Actuators A: Physical* 140.1 (2007), pp. 103–112. DOI: 10.1016/j.sna.2007.06.021.

[2] Myung-Jae Lee et al. “High-Performance Back-Illuminated Three-Dimensional Stacked Single-Photon Avalanche Diode Implemented in 45-nm CMOS Technology”. In: *IEEE Journal of Selected Topics in Quantum Electronics* 24.6 (2018), pp. 1–9. DOI: 10.1109/jstqe.2018.2827669.

[3] Robert K. Henderson et al. “A 192 X 128 time correlated SPAD image sensor in 40nm CMOS technology”. English. In: *IEEE Journal of Solid-State Circuits* 54.7 (July 2019), pp. 1907–1916. ISSN: 0018-9200. DOI: 10.1109/JSSC.2019.2905163.

[4] Romana Schirhagl et al. “Nitrogen-Vacancy Centers in Diamond: Nanoscale Sensors for Physics and Biology”. In: *Annual Review of Physical Chemistry* 65.Volume 65, 2014 (2014), pp. 83–105. ISSN: 1545-1593. DOI: https://doi.org/10.1146/annurev-physchem-040513-103659.

[5] Gopalakrishnan Balasubramanian et al. “Ultralong spin coherence time in isotopically engineered diamond”. In: *Nature Materials* 8.5 (2009), pp. 383–387. ISSN: 1476-4660. DOI: 10.1038/nmat2420.

[6] Vadym N Mochalin et al. “The properties and applications of nanodiamonds”. In: *Nature Nanotechnology* 7.1 (2012), pp. 11–23. DOI: 10.1038/nnano.2011.209.

[7] S. Pellegrini et al. “Industrialised SPAD in 40 nm technology”. In: *2017 IEEE International Electron Devices Meeting (IEDM)*. San Francisco, CA, USA, 2017, pp. 16.5.1–16.5.4. DOI: 10.1109/IEDM.2017.8268404.

[8] Tarek Al Abbas et al. “8.25µm Pitch 66% Fill Factor Global Shared Well SPAD Image Sensor in 40nm CMOS FSI Technology”. In: International Image Sensor Workshop 2017, IISW 2017 ; Conference date: 30-05-2017 Through 02-06-2017. June 2017. URL: https://www.research.ed.ac.uk/en/publications/825%CE%BCm-pitch-66-fill-factor-global-shared-well-spad-image-sensor-i.

[9] K. Morimoto et al. “3.2 Megapixel 3D-Stacked Charge Focusing SPAD for Low-Light Imaging and Depth Sensing”. In: *2021 IEEE International Electron Devices Meeting (IEDM)*. 2021, pp. 20.2.1–20.2.4. DOI: 10.1109/IEDM19574.2021.9720605.

[10] T. Chaves de Albuquerque et al. “Integration of SPAD in 28nm FDSOI CMOS technology”. In: *2018 48th European Solid-State Device Research Conference (ESSDERC)*. 2018, pp. 82–85. DOI: 10.1109/ESSDERC.2018.8486852.

[11] D. Issartel et al. “Architecture optimization of SPAD integrated in 28 nm FD-SOI CMOS technology to reduce the DCR”. In: *Solid-State Electronics* 191 (2022), p. 108297. ISSN: 0038-1101. DOI: https://doi.org/10.1016/j.sse.2022.108297.

[12] Shaochen Gao et al. *Correlations between DCR and PDP of SPAD integrated in a 28 nm FD-SOI CMOS Technology*. 2023, International Image Sensor Workshop (IISW), Crieff, United Kingdom, 21-25 May, 2023. Poster. May 2023. URL: https://hal.science/hal-03977945.

[13] S. Cova et al. “Evolution and prospects for single-photon avalanche diodes and quenching circuits”. In: *Journal of Modern Optics* 51.9–10 (2004), pp. 1267–1288. DOI: 10.1080/09500340408235272.

[14] Edoardo Charbon. “Single-photon imaging in complementary metal oxide semiconductor processes”. In: *Philosophical Transactions of the Royal Society A: Mathematical, Physical and Engineering Sciences* 372.2012 (Feb. 2014), p. 20130100. DOI: 10.1098/rsta.2013.0100.

[15] S. Cova et al. “Avalanche photodiodes and quenching circuits for single-photon detection”. In: *Appl. Opt.* 35.12 (Apr. 1996), pp. 1956–1976. DOI: 10.1364/AO.35.001956.

[16] Henri Dautet et al. “Photon counting techniques with silicon avalanche photodiodes”. In: *Appl. Opt.* 32.21 (July 1993), pp. 3894–3900. DOI: 10.1364/AO.32.003894.

[17] UlrikeKlein. *SPAD-APD characteristic comparison*. https://commons.wikimedia.org/wiki/File:Spad-apd-characteristic-comparison.svg. Accessed: 2025-04-22. 2010.

[18] M. Stipčević, H. Skenderović, and D. Gracin. “Characterization of a novel avalanche photodiode for single photon detection in VIS-NIR range”. In: *Optics Express* 18.16 (July 2010), p. 17448. ISSN: 1094-4087. DOI: 10.1364/oe.18.017448.

[19] Mathieu Sicre et al. “Dark Count Rate in Single-Photon Avalanche Diodes: Characterization and Modeling study”. In: *ESSDERC 2021 - IEEE 51st European Solid-State Device Research Conference (ESSDERC)*. 2021, pp. 143–146. DOI: 10.1109/ESSDERC53440.2021.9631797.

[20] M. Ghioni et al. “Compact active quenching circuit for fast photon counting with avalanche photodiodes”. In: *Review of Scientific Instruments* 67.10 (Oct. 1996), pp. 3440–3448. ISSN: 0034-6748. DOI: 10.1063/1.1147156.

[21] G. Giustolisi, R. Mita, and G. Palumbo. “Behavioral modeling of statistical phenomena of single-photon avalanche diodes”. In: *International Journal of Circuit Theory and Applications* 40.7 (2012), pp. 661–679. DOI: https://doi.org/10.1002/cta.748.

[22] F. Zappa et al. “SPICE modeling of single photon avalanche diodes”. In: *Sensors and Actuators A: Physical* 153.2 (2009), pp. 197–204. ISSN: 0924-4247. DOI: https://doi.org/10.1016/j.sna.2009.05.007.

[23] R. Mita, G. Palumbo, and P.G. Fallica. “Accurate model for single-photon avalanche diodes”. In: *IET Circuits, Devices & Systems* 2 (2 2008), pp. 207–212. DOI: 10.1049/iet-cds:20070180.

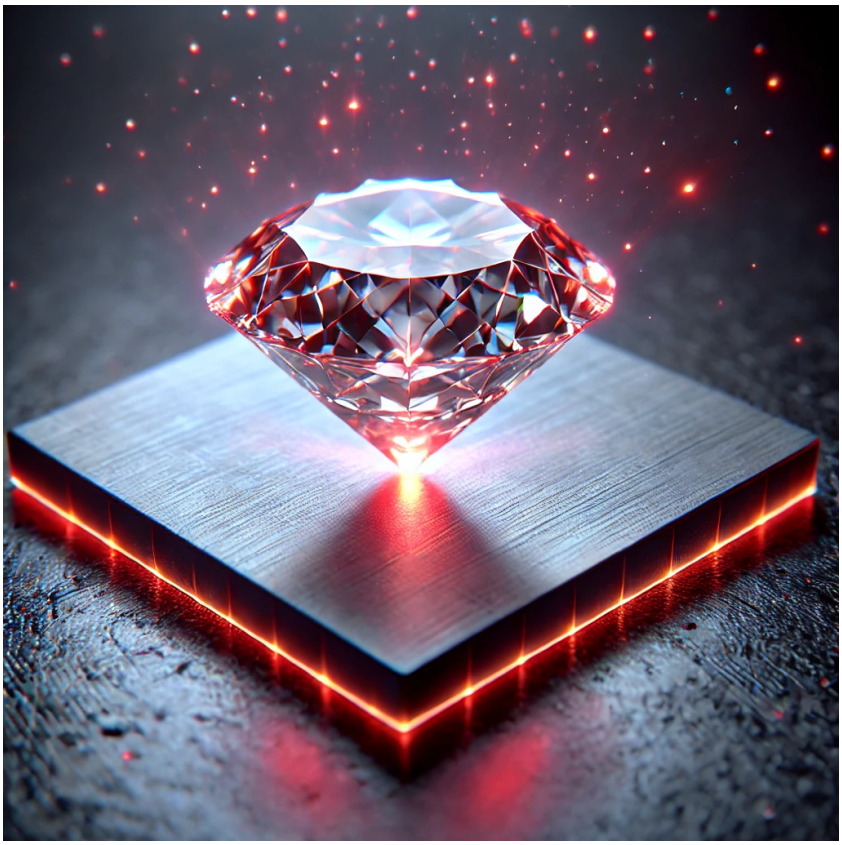
[24] Mohammadreza Dolatpoor Lakeh et al. “An Ultrafast Active Quenching Active Reset Circuit with 50% SPAD Afterpulsing Reduction in a 28 nm FD-SOI CMOS Technology Using Body Biasing Technique”. In: *Sensors* 21.12 (2021). ISSN: 1424-8220. DOI: 10.3390/s21124014.

[25] El-Mostafa Bourim and Jeong In Han. “Electrical characterization and thermal admittance spectroscopy analysis of InGaN/GaN MQW blue LED structure”. In: *Electronic Materials Letters* 11.6 (2015), pp. 982–992. ISSN: 2093-6788. DOI: 10.1007/s13391-015-5180-0.

6

Conclusion

If you made it this far, congratulations! Now is the time to summarize the key points and findings of each chapter, as well as provide an overview of the challenges that were posed, and recommendations for future improvement of the techniques, processes and methodologies used in this dissertation.



6.1. SUMMARY

This dissertation explored aspects of various scientific fields. With color centers in diamond as the protagonist and the ultimate goal of working towards a compact quantum biosensor with integrated on-chip arrays of SPADs and electronics, many different research topics were explored along the way.

Before anything else, chapter 2 has provided all the necessary knowledge needed to understand the basic physics behind the function of both NV centers and SnV centers in diamond. First, diamonds were introduced, along with their properties and crystal structure that enables the creation of color centers within them. Then, the atomic structure of the NV centers was described, as well as their electronic, optical properties, and magnetic properties that allow them to shine as quantum sensors. Additionally, the NV center Hamiltonian was provided, and the terms that contribute to the NV center's unique properties. Similarly, the SnV center was described, with its own structure, and electrical and optical properties. The reason behind the SnV center's popularity as a quantum computing qubit was given, together with a brief explanation of its Hamiltonian.

After a robust theoretical background was established, an in-house custom confocal ODMR setup was designed (as described in section 2.5). In parallel, research was conducted on the preparation of HEK293T biological cells and their culturing on a diamond substrate. These cells had superparamagnetic nanoparticles (SPIONs) injected during growth, acting as magnetic tags. The biosamples were later measured employing the designed ODMR setup. Photoluminescence (PL) maps as well as 2D ODMR scans were performed to evaluate SPION uptake and the resulting magnetic fields. Due to the low magnetization of the SPIONs under our relatively weak bias field, clear magnetic signatures were not observed. Optical artifacts, such as surface scattering, NV density inhomogeneities, and background luminescence, were also identified as limiting factors. However, the NV ensemble's sub-microtesla sensitivity was confirmed, and subtle peak-splitting features hinted at localized field variations.

Performing imaging with the conceptualized integrated biosensor requires sufficiently NV center-doped diamonds. Meanwhile, quantum computing applications have migrated towards other color centers as qubits, such as the tin-vacancy (SnV) center in diamond. Therefore, chapter 3 investigated the fabrication and generation of NV and SnV color centers in diamond. This entails cleanroom processing, various ion implantation techniques, and subsequent annealing of the diamonds. First, simulations were performed on both nitrogen and tin ions incident on diamond. A suitable ion energy was determined, so that implantation could take place through a lithography mask containing precisely fabricated apertures, enabling high spatial resolution. The tin ions were implanted at a specific depth, close to the surface, and overgrowth took place afterward, so that the color centers would be protected from surface charge effects. Subsequently, femtosecond-laser annealing and thermal annealing were employed for emitter activation. The resulting samples were characterized using photoluminescence spectroscopy, confocal ODMR, and Raman measurements. While color center formation was not evident in the mask-implanted substrate, the blanket-implanted sample exhibited a clear post-annealing SnV signature. An initial direct comparison between fs-laser and high-temperature furnace annealing demonstrated the efficiency of thermal treatments in

significantly enhancing the optical activation of SnV centers. These early findings may provide critical insights for the future integration of SnV centers in quantum photonic platforms.

Moving on to chapter 4, strain characterization took place on a diamond that was directly bonded to an insulator substrate (SiO_2/Si). According to the literature, thermal expansion coefficient mismatch can induce strain effects in the materials involved, particularly at their interface. Hence, the strain properties of diamond substrates were characterized in unbonded, bonded and partially bonded conditions. The strain-induced splitting of the NV center's energy levels before bonding provided a measure of the intrinsic strain present in the diamond. By measuring the strain at different depths, plots of strain versus depth were generated from ODMR peak splitting, where it became clear that measurements closer to the diamond-SiO_2/Si interface exhibit increased lattice deformations, with volumetric and shear strain components rising by approximately 0.45 MHz and 0.71 MHz, respectively. Furthermore, PL maps of a partially bonded diamond revealed interference fringes at various depths, indicative of strain or non-uniform bonding in the examined areas. This makes PL mapping a powerful initial tool for assessing the quality of the bonding process. Combined with thorough strain measurements using ODMR, a characterization methodology has been created that can quantify the degree to which the electronic and optical properties of the bonded sample have deteriorated.

Finally, in chapter 5, four different CMOS chips were fabricated in TSMC's 40 nm technology, each containing a 16×16 Single-Photon Avalanche Diode (SPAD) array and additional testing SPADs at the top. These chips were characterized electrically with I-V and C-V measurements, and their breakdown voltages were determined. Their values were found to be between -15.5 V and -17.7 V, typical for such SPADs. Nevertheless, tests did not demonstrate clear SPAD pulse behavior. Therefore, integration with the diamond into a compact widefield sensor was performed using an alternate, properly functioning SPAD chip from NXP. Using this chip, the designs of the widefield ODMR setup and the accompanying SPAD driving electronics were validated, ensuring that a functional SPAD array would be able to be integrated and perform as intended. This serves as proof-of-concept of the envisioned quantum biosensor using CMOS-integrated NV centers in diamond.

6.2. CHALLENGES & DISCUSSION

Several challenges emerged during the course of this research, starting with the problems that emerged in the biosensing experiments described in chapter 2. First, SPION uptake by HEK293T cells proved insufficient. This highlights the need to optimize cell-culture protocols and to functionalize and coat the magnetic nanoparticles for targeted internalization. Furthermore, the low saturation magnetization of the SPIONs under the modest bias fields achievable with small permanent magnets limited the potentially detectable ODMR effects, indicating that a dedicated electromagnet might be required to reach the tens-to-hundreds-millitesla regime with high spatial uniformity. Finally, excitation through the biological layer and the confocal collection geometry introduced significant optical losses and background scattering, reducing ODMR contrast and sensitivity to sub-microtesla fields.

Next, chapter 3 dealt with simulations of ions of different energies incident on materials deposited on top of a diamond substrate, in order to determine the best type of resist and resist thickness for ion implantation through a lithographic mask. It also concerned cleanroom tests, processing and fabrication of the simulated masks on diamond substrates, and subsequent overgrowth and measurement of the implanted samples. Nonetheless, a few challenges arise that complicate this whole process. Firstly, working in the cleanroom is quite a tedious process. Keeping in mind that most of the cleanroom work took place during the pandemic, additional restrictions were imposed on the cleanroom working regime that significantly impacted the scheduling and the timeline of the fabrication. Coupled with the lack of trained mentors within our research group, this part of the project experienced serious delays. Nevertheless, due to complications, further annealing and characterization steps need to take place.

As described in chapter 4, a few issues persist on the road to precise and efficient determination of strain effects, despite the promising results achieved in measuring and mapping strain effects in DOI substrates using ODMR. Regarding the experimental setup, problems occasionally arise when focusing on the back surface of a thick substrate, due to limits set by the working distance of the objective lens, as well as obstruction by the microwave wire, which adds to this problem. This creates the need for thinning of the diamond layer by O_2 plasma; a rather time-consuming process. In terms of the direct bonding process, even with thorough cleaning of the substrates in the cleanroom, trapped particles or residues at the diamond-SiO_2/Si interface may still remain, hindering proper bonding and inducing localized strain regions. This effect is particularly pronounced in the samples investigated in this chapter, owing to their large size of $10 \times 10\,\mathrm{mm}^2$. Last but not least, the ODMR measurement process itself is another factor to take into consideration concerning the quality of the measurements. Long scanning durations make the samples more prone to thermal drifts and can introduce experimental parameter fluctuations. The time inefficiency is further exacerbated by the long direct bonding processing time of approximately a week.

Finally, chapter 5 introduced a number of challenges. Although the confocal ODMR setup proved highly effective, transitioning to the widefield configuration came with additional complexities regarding integration of the chips with the SPAD arrays with the PCB and the setup itself, but also in the excitation and collection scheme. Moreover, the SPAD arrays failed to operate as intended, owing to design flaws in their layout and in the

quenching circuits, rendering the completion of the visualized integrated sensor not feasible. Finally, signal degradation in the SPAD-PCB-FPGA communication chain and the noise susceptibility of the system underscored the need for better electronic design and shielding. These issues limited the operational capability of the envisioned widefield ODMR setup and the CMOS-integrated NV-based sensor, and will need to be addressed in future iterations.

6.3. FUTURE WORK & OUTLOOK

Although significant progress has been made on the aforementioned topics, there is plenty of room for future work and improvement of the methods, designs and techniques employed.

To begin with, in chapter 2, adaptation of the ODMR setup to include an electromagnet is a crucial step forward to efficient magnetic labeling and mapping of the magnetic fields generated by the SPIONs within the HEK293T cells. This upgrade should be accompanied by rigorous calibration of the electromagnet's strength and spatial uniformity, ensuring that measured ODMR peak splittings can be converted into absolute magnetic flux densities. Next, a closed-loop current controller may be implemented to stabilize, or even modulate, the bias field in real time, thus enabling time-resolved, in situ studies of nanoparticle dynamics. Lastly, HEK293T cells may be replaced with more application-relevant tissues or cell types, helping assess the sensor's performance across varied biological environments.

In chapter 3 several issues in the diamond preparation and ion implantation workflow became apparent, as well as clear paths for improvement. First, the lithographic aperture fabrication and implantation parameters should be iteratively optimized to achieve precise depth control and minimal surface damage. Second, post-implantation annealing protocols must be expanded beyond conventional thermal treatments, to include localized femtosecond-laser annealing, which offers ultrafast, spatially confined heating that can enhance vacancy diffusion and lattice repair with reduced graphitization. Once samples have been annealed, a combination of photoluminescence intensity mapping, ODMR contrast and linewidth measurements, and high-resolution spectroscopy will provide quantitative metrics on color center yield, charge-state activation efficiency, and residual strain. By correlating these metrics with both thermal and laser annealing conditions, the optimal processes for near-deterministic NV and SnV center generation can be established.

Concerning chapter 4, the direct bonding quality has to be improved, especially regarding substrates with larger surfaces. This will allow more high-quality, reproducible bonding that will enable more precise mapping of the strain effects caused that come with it, as well as other characterization measurements. Furthermore, the experimental setup itself needs to be adjusted in order to better accommodate such strain measurements, that primarily investigate the back plane of the substrate. The first step to achieve this is modification of the microwave wire placement, so that it does not obstruct or interfere with the scanning measurements. To get a more clear understanding of how strain affects the quality and the properties of the color centers in diamond after direct bonding, additional, thorough measurements need to take place. Given the large amounts of time required to fully complete all these measurements, a configuration like the one described in section 1.6, utilizing large arrays of compact, diamond-integrated, highly-sensitive single-photon detectors has the potential to drastically improve measurement efficiency.

Finally, since the SPADs that were designed in chapter 5 did not function as expected, the design layout has to be re-examined to determine what went wrong during the tape-out process, and LVS (Layout Versus Schematic) tests have to be performed again. Additionally, the electronics and connections between the components have to be refined,

so that noise does not exceed the discernible signal levels. Assuming the photodetectors are operating as expected, the integrated sensor itself can be enhanced. The excitation light can be directed to the layer containing the NV centers using an optical fiber, at an angle that corresponds to total internal reflection, while avoiding illumination -and potential damage- to the biological tissue above the diamond substrate. Moreover, using a combination of waveguides and/or microlenses, the emitted light can be focused and delivered more efficiently to the SPADs underneath the diamond, drastically improving the photon collection efficiency of the quantum biosensor.



ACKNOWLEDGEMENTS

The completion of this dissertation would not have been possible without the assistance, guidance, and support of multiple individuals and organizations. I would like to express my gratitude to everyone that contributed to this long journey.

QIT RESEARCH GROUP

I want to start by thanking my promotor and PI of our research group, **Ryoichi Ishihara**, for giving me the opportunity to work in such an innovative, interesting, and multidisciplinary project. Through his continued guidance, motivation, and resources, I was able to see this project through to the end. I also want to thank **Salahuddin Nur** for providing invaluable guidance and taking the time to discuss both trivial everyday topics and research problems. Bonus thanks for (occasionally) allowing me to keep the light in the office off. I wish you success in your tenure as a professor.

A thanks to my fellow PhD candidates within QIT, **Alan**, **Erbing**, **Maurice**, and **Wagno**, with whom I have had plenty of meaningful/meaningless -but mostly interesting- discussions. A special shout-out goes to the multiple members of **The Frappers**, a music band which formed in 2023 as a joke, but ended up bringing us closer together, as well as countless enjoyable moments and *#nightstoremember*.

Next, I want to extend my gratitude to the many students I have supervised over the years, many of which I currently consider friends. First, to my one and only MSc student, **Gianni D.**, who provided critical assistance and with whom I have spent countless hours of troubleshooting and brainstorming. A big thanks to **Nikolaj**, whose work attitude enabled deep discussions and challenged me, and whose character helped create a nice atmosphere within our group. I am grateful to **Alfie** and **Filip**, for being great students, for introducing me to bouldering and for being fun people to be around and chat with. Last but not least, I thank **Floris**, **Diederik**, **Ruben**, and **Ecem** for being part of my projects and contributing to my research.

QCE DEPARTMENT

Moving on, I would like to thank **Fabio Sebastiano**, **Luc**, **Niels**, **Stein**, **Sadık**, and **Samantha**, for their collaboration and invaluable assistance in the SPAD chip design and characterization part of my project.

QUTECH

I am very grateful to **Tim Hiep** and **Nico Alberts** from the QuTech Workshop, for bringing to life numerous requests for lab part accessories and custom mounts.

In addition, I would like to thank **Nina** and **Julia** for always being available to discuss and enlighten me with their cleanroom fabrication expertise.

I also want to thank **Takashi Yamamoto** for promptly assisting us with our overgrowth processing needs.

MANAGEMENT & SUPPORT

I thank **Shannon**, **Francis**, and **Helen**, for always assisting me with the logistics of doing a PhD and providing significant support. I also need to thank **Ali**, for assisting with the organization of our lab.

KAVLI NANOLAB

I am thankful to multiple members of the Kavli cleanroom, starting with **Eugene Straver**, who helped train me on certain modules and tried to accommodate my urgent cleanroom requests. Next, I want to thank **Charles de Boer** for promptly fulfilling my silicon wafer and storage needs, as well as **Lodi Schriek** and **Anja van Langen-Suurling** for assisting me and training me on the optical inspection and lithography modules, respectively. An enormous thanks to **Carel Heerkens** (†), whose unparalleled cleanroom mentorship and fabrication knowledge were instrumental in launching my research.

ORGANIZATIONS

I gratefully acknowledge support from the joint research program "Modular quantum computers" by Fujitsu Limited and Delft University of Technology, co-funded by the Netherlands Enterprise Agency under project number PPS2007.

Further, I want to thank **René Vollmer** from TNO for his leadership in coordinating the collaboration between QIT and TNO, as well as for providing valuable technical insights and continuous support.

Additionally, I want to thank **Daan Brinks** and **Qiangrui Dong** from the ImPhys Department of TNW, TU Delft, for collaborating with us for the preparation and handling of biological tissues, which were used to demonstrate bio-imaging.

From DEMO, I extend my gratitude to **Yannick van der Linden** and **Lars Leenheer** for generously sharing their expertise in electronics characterization and for their assistance with numerous soldering tasks, which were critical to the success of this work.

I would also like to express my appreciation to **Ella Schneider**, **David Cox**, and **Steven Clowes** for including our project in their Pump Priming 2024 scheme, and for their collaboration on the ion implantation of diamond substrates.

Next, I must thank **Robert van Veldhoven** from NXP, for lending us some of their SPAD chips and being open to troubleshoot and help resolve potential issues with our own designs.

I am also grateful to **Emilio Depero** from Zurich Instruments, for his expert customer support and insights in setting up and performing measurements using their arbitrary waveform generator (AWG) module.

Lastly, I would like to acknowledge OpenAI's ChatGPT for the creation of some of the images that appear in this dissertation.

FRIENDS & FAMILY

A heartfelt thanks goes out to **Lupita** and to my **family** for their continuous support. And finally, a shout-out to my friends in the Netherlands and in Greece (**Tapout** and **Ioanna**, **Niki**, **Artemis**, and **Vaso**), for always being fun to hang out with.

A

THEORY

A.1. COULOMB INTERACTION AND THE SINGLET MANIFOLD

The energy hierarchy ${}^3A_2 <^1 E <^1 A_1$ in the NV centre is governed by the interplay between the *direct* Coulomb (Hartree) integral J_{ee} and the *exchange* integral K_{ee}. For two electrons occupying the degenerate e orbitals $\phi_e(\mathbf{r})$, these integrals are defined as:[1]

$$J_{ee} = \iint \left|\phi_e(\mathbf{r}_1)\right|^2 \frac{e^2}{4\pi\varepsilon_0 r_{12}} \left|\phi_e(\mathbf{r}_2)\right|^2 d\mathbf{r}_1\, d\mathbf{r}_2,$$

$$K_{ee} = \iint \phi_e^*(\mathbf{r}_1)\,\phi_e(\mathbf{r}_2) \frac{e^2}{4\pi\varepsilon_0 r_{12}} \phi_e^*(\mathbf{r}_2)\,\phi_e(\mathbf{r}_1)\, d\mathbf{r}_1\, d\mathbf{r}_2$$

While J_{ee} quantifies the classical repulsion between the electrons, K_{ee} lowers the energy in spin-symmetric (triplet) configurations and vanishes for spin-antisymmetric (singlet) states, therefore stabilizing the triplet ground state ${}^3A_2$. In this triplet ground state, the antisymmetric spatial wavefunction allows K_{ee} to partially cancel J_{ee}, yielding the lowest energy. However, the singlet states lack this exchange stabilization and are instead raised in energy. ${}^1A_1$ is penalized most because its paired electrons occupy the same orbital with maximal spatial overlap, while ${}^1E$ sits slightly lower, due to reduced overlap and a symmetry-lowering Jahn–Teller distortion.

This Coulomb-determined ordering is responsible for the efficiency of spin-selective intersystem crossing, the microsecond lifetime of the metastable singlet manifold, and the strong Stark tunability exploited in NV-based optical read-out.

A.2. QUANTIZATION OF ENERGY

The fundamental relationship between the energy E of a photon and its wavelength λ follows from the quantum hypothesis that electromagnetic radiation is emitted and absorbed in discrete quanta of energy $E = h\nu$. Using the dispersion relation $\nu = c/\lambda$ yields

[1] For a more detailed discussion, see A. Szabo and N. S. Ostlund, *Modern Quantum Chemistry: Introduction to Advanced Electronic Structure Theory* (Dover Publications, 1996).

the expression:

$$E = \frac{hc}{\lambda}$$

This equation arises directly from the quantization of electromagnetic radiation, a foundational result of quantum mechanics established by Planck in his work on blackbody radiation. It was later refined by Einstein's photoelectric effect explanation[2]. Here, $h \approx 6.626 \times 10^{-34}\,\mathrm{J\,s}$ is Planck's constant and $c \approx 3 \times 10^{8}\,\mathrm{m/s}$ is the speed of light in vacuum.

In many fields, it is more convenient to express photon energies in electronvolts (eV) instead of joules. By definition,

$$1\,\mathrm{eV} = 1.602 \times 10^{-19}\,\mathrm{J}$$

Thus, multiplying by $\frac{1\,\mathrm{eV}}{1.602\times10^{-19}\,\mathrm{J}}$, gives:

$$E\,[\mathrm{eV}] = \frac{hc}{\lambda} \times \frac{1\,\mathrm{eV}}{1.602 \times 10^{-19}\,\mathrm{J}} \approx \frac{1240\,\mathrm{eV\cdot nm}}{\lambda\,[\mathrm{nm}]}$$

For the NV center's zero-phonon line at $\lambda = 637\,\mathrm{nm}$, this gives

$$E = \frac{(6.626 \times 10^{-34}\,\mathrm{J\,s})(3 \times 10^{8}\,\mathrm{m/s})}{637 \times 10^{-9}\,\mathrm{m}} \approx 3.12 \times 10^{-19}\,\mathrm{J} \approx 1.95\,\mathrm{eV}$$

Since diamond's wide bandgap is $\approx 5.5\,\mathrm{eV}$, this 1.95 eV transition occurs well inside the gap, enabling a purely optical, phonon-free (ZPL) excitation from the ground state $^3A_2$ to the excited state ^3E at visible wavelengths.

A.3. DEBYE–WALLER FACTOR IN NV CENTER EMISSION

The Debye–Waller factor (DW) quantifies the fraction of optical emission that occurs in the zero–phonon line (ZPL) versus the total emission (ZPL plus phonon sidebands)[3]. It is defined as:

$$\mathrm{DW} = \frac{I_{\mathrm{ZPL}}}{I_{\mathrm{ZPL}} + I_{\mathrm{PS}}},$$

where I_{ZPL} is the integrated intensity of the purely electronic, phonon-free transition (e.g. the 637 nm line) and I_{PS} is the integrated intensity of all phonon-sideband emission.

In NV centers the majority of emission occurs into the broad phonon sideband extending from the ZPL up to $\sim 800\,\mathrm{nm}$, with only about 4% of photons emitted at the ZPL. Hence,

$$\mathrm{DW}_{\mathrm{NV}} \approx 0.04$$

This small DW reflects strong coupling between the NV electronic transition and lattice vibrations, particularly under non-resonant (532 nm) excitation, where excess energy $\Delta E = hc/\lambda_{\mathrm{pump}} - hc/\lambda_{\mathrm{ZPL}}$ is rapidly dissipated into phonons.

[2] A. Einstein, "On a Heuristic Point of View Concerning the Production and Transformation of Light," *Ann. Phys.* **17**, 132–148 (1905).

[3] G. Davies and M. F. Hamer, "Optical studies of the 1.945 eV vibronic band in diamond," *Proc. Roy. Soc. A* **348**, 285–298 (1976).

A low Debye–Waller factor has two major implications for NV-based sensing and photonics: first, most fluorescence is emitted at wavelengths red-shifted from the ZPL, reducing the fraction of indistinguishable photons useful for coherent quantum operations; second, techniques such as phonon-mode suppression or coupling to optical cavities are required to enhance the ZPL emission fraction and improve spin-photon interfaces.

A.4. INTERSYSTEM CROSSING IN NV CENTERS

Intersystem crossing (ISC) in the NV center is a non-radiative relaxation pathway that connects the spin-conserving triplet manifold (^3E, $^3A_2$) to the spin-forbidden singlet manifold (^1E, $^1A_1$)[4]. Although direct optical transitions between triplet and singlet states ($\Delta S \neq 0$) are forbidden, ISC is enabled by a combination of spin–orbit coupling (which mixes electronic spin states) and electron–phonon interactions (which supply the required energy and angular-momentum matching). The dominant ISC pathway is as follows:

1. Upon resonant excitation, the NV center is promoted to the ^3E excited triplet. Here, the spin–orbit interaction

$$\hat{H}_{\mathrm{SO}} = \lambda \mathbf{L}\cdot\mathbf{S}$$

   causes the wavefunction to include a small component of the nearby singlet $^1A_1$ state, providing a pathway for non-radiative decay.

2. Phonons provide (or remove) the precise energy difference $\Delta E = E(^3E) - E(^1A_1)$, allowing non-radiative transfer at a rate $\Gamma_{\mathrm{ISC}}^{(E\to A_1)}$.

3. The system rapidly relaxes within the singlet manifold via phonon cascade from $^1A_1$ down to the lower ^1E state.

4. Finally, spin–orbit coupling again mixes ^1E with $^3A_2$, and phonons carry away the remaining energy to complete the non-radiative decay back to the triplet ground state at rate $\Gamma_{\mathrm{ISC}}^{(E\to A_2)}$.

Because ISC selectively depletes the $m_s = \pm 1$ sublevels of ^3E more efficiently than $m_s = 0$, optical pumping through this pathway leads to spin polarization into the $m_s = 0$ ground state. This effect is vital to NV-based magnetometry and quantum information protocols.

The effective fluorescence lifetime τ_{fl} of the NV center is determined by competition between radiative decay ($^3E \to {}^3A_2$) and ISC. Using a radiative rate of

$$\Gamma_{\mathrm{rad}} \approx 8.3 \times 10^7 \ \mathrm{s}^{-1}$$

and a typical room temperature ISC rate of

$$\Gamma_{\mathrm{ISC}} \approx 5 \times 10^6 \ \mathrm{s}^{-1},$$

[4] N. B. Manson, J. P. Harrison, and M. J. Sellars, "Nitrogen-vacancy center in diamond: Model of the electronic structure and associated dynamics," *Phys. Rev. B* **74**, 104303 (2006).

the total decay rate becomes

$$\Gamma_{\text{tot}} = \Gamma_{\text{rad}} + \Gamma_{\text{ISC}} \approx 8.8 \times 10^7 \text{ s}^{-1},$$

which corresponds to a fluorescence lifetime

$$\tau_{\text{fl}} = \frac{1}{\Gamma_{\text{tot}}} \approx 11.4 \text{ ns}$$

This value lies well within the experimentally observed range of 10–30 ns for single NV centers in both nanodiamonds and bulk diamond.

A.5. DYNAMICAL DECOUPLING

Dynamical decoupling (DD) is a control-based technique that employs sequences of coherent π pulses to suppress environmental dephasing and extend the spin coherence time T_2[5]. In its simplest form, the Hahn echo, a single π pulse is applied at time τ, which inverts the NV's spin state, refocusing quasi-static magnetic noise and producing an echo at $t = 2\tau$. More sophisticated DD protocols, such as Carr–Purcell–Meiboom–Gill (CPMG) and XY-family sequences, apply N evenly spaced π pulses, effectively filtering out noise components with frequencies below a cutoff $\omega_c \approx N\pi/T$, where T is the total evolution time[6].

Experimentally, applying CPMG sequences to single NV centers at room temperature has yielded more than a 25-fold extension of T_2, and in isotopically purified diamond DD has enabled spin coherence times exceeding one second. Such dramatic enhancements are critical, especially when dealing with quantum information protocols.

A.6. RAMSEY INTERFEROMETRY

Ramsey interferometry is the standard pulse-sequence technique for measuring the inhomogeneous dephasing time T_2^*. The sequence consists of:

1. A first $\pi/2$ microwave pulse, which rotates the NV spin from $|0\rangle$ into an equal superposition
$$\frac{1}{\sqrt{2}}\left(|0\rangle + e^{i\phi_0}|1\rangle\right)$$
2. A free precession interval of duration τ, during which the spin picks up a relative phase $\Delta\omega\,\tau$, with
$$\Delta\omega = \omega_{\text{NV}} - \omega_{\text{MW}},$$
due to detuning between the NV's resonance (ω_{NV}) and the applied microwave frequency (ω_{MW}).
3. A second $\pi/2$ pulse, which converts the accumulated phase into a population difference between $|0\rangle$ and $|1\rangle$.

[5] T. de Lange *et al.*, "Universal dynamical decoupling of a single solid-state spin from a spin bath," *Science* **330**, 60–63 (2010).

[6] Ł. Cywiński, R. M. Lutchyn, C. P. Nave, and S. Das Sarma, "How to enhance dephasing time in solid-state spin qubits," *Phys. Rev. B* **77**, 174509 (2008).

4. Optical read-out of the spin state via spin-dependent fluorescence intensity $S(\tau)$.

The measured signal takes the form

$$S(\tau) = S_0\, e^{-(\tau/T_2^*)^2} \cos\!\big(\Delta\omega\,\tau + \varphi\big) + S_{\text{offset}},$$

where the Gaussian envelope $\exp[-(\tau/T_2^*)^2]$ arises from quasi-static variations in local fields, and φ is a fit phase[7]. Fitting this envelope to data collected over a series of τ values yields the inhomogeneous dephasing time T_2^*. Since T_2^* is limited by slow fluctuations, such as those from nearby ^{13}C nuclear spins, strain gradients, or magnetic field inhomogeneities, the Ramsey sequence provides a direct measure of ensemble or single-spin frequency stability under free evolution.

A.7. SPIN-BATH DRIVING

Spin-bath driving uses resonant radio-frequency fields to continuously flip the surrounding ^{13}C nuclear spins, averaging out their quasi-static magnetic noise and narrowing the NV ensemble's resonance. Bauch *et al.* demonstrated that driving the nuclear bath increases T_2^* from a few microseconds to tens of microseconds in dense NV ensembles[8].

In practice, the NV centers are first polarized into the $m_s = 0$ state. Afterward, a continuous-wave RF field, tuned to the ^{13}C Larmor frequency, is applied. Under these Hartmann–Hahn matching conditions, nuclear spin flips occur at a Rabi frequency much higher than the static dipolar coupling, which averages out quasi-static bath fields and suppresses inhomogeneous broadening. By optimizing the RF amplitude and detuning[9], one can minimize power-broadening while maximizing the spectral narrowing of the NV transition. This protocol enables order-of-magnitude improvements in T_2^* even in high-density samples[10].

A.8. DOUBLE QUANTUM COHERENCE MAGNETOMETRY

Double quantum coherence magnetometry (DQCM) exploits the pair of $|m_s = +1\rangle$ and $|m_s = -1\rangle$ ground state levels to suppress common-mode noise and enhance sensitivity. The typical pulse sequence is:

1. A first pair of $\pi/2$ pulses, one at each of the $|0\rangle \rightarrow |+1\rangle$ and $|0\rangle \rightarrow |-1\rangle$ transition frequencies, creates the superposition

$$\frac{1}{\sqrt{2}}\big(|+1\rangle + e^{i\varphi}|-1\rangle\big).$$

[7] G. Balasubramanian *et al.*, "Ultralong spin coherence time in isotopically engineered diamond," *Nat. Mater.* **8**, 383–387 (2009).

[8] J. Bauch *et al.*, "Ultralong dephasing times in ensembles of nitrogen-vacancy centres via spin bath driving," *Nat. Commun.* **9**, 2012 (2018).

[9] T. H. Taminiau *et al.*, "Detection and control of individual nuclear spins using a weakly coupled electron spin," *Phys. Rev. Lett.* **109**, 137602 (2012).

[10] S. London *et al.*, "Strong driving of a small nuclear spin ensemble with a single electron spin," *Phys. Rev. Lett.* **111**, 067601 (2013).

2. The spin precesses freely for a time τ, accumulating a relative phase

$$\Delta\omega_{\mathrm{DQ}}\,\tau = \big(\omega_{+1} - \omega_{-1}\big)\,\tau = 2\,\gamma\,B\,\tau,$$

where γ is the NV's gyromagnetic ratio and B the local magnetic field.

3. A second pair of $\pi/2$ pulses, applied at the same $|0\rangle \rightarrow |+1\rangle$ and $|0\rangle \rightarrow |-1\rangle$ transition frequencies, recombines the DQ coherence so that the accumulated phase is converted into a population imbalance. Optical excitation then reads out this imbalance via the difference in fluorescence intensity between the $|0\rangle$ and $|\pm1\rangle$ states, yielding a signal oscillating as $\cos(\Delta\omega_{\mathrm{DQ}}\tau + \varphi)$.

Because shifts in ZFS (e.g. from temperature drift or strain) enter with the same sign into both $m_s = +1$ and $m_s = -1$ levels, they cancel in the differential phase $\omega_{+1} - \omega_{-1}$. In contrast, magnetic shifts change sign and thus add, doubling the magnetic sensitivity. As a result, the inhomogeneous dephasing time in the DQ basis, $T^*_{2,\mathrm{DQ}}$, can exceed the single-quantum Ramsey T^*_2 by an order of magnitude, with reported values up to $\sim 100\ \mu$s in isotopically purified diamond[11]. This enhancement directly translates into improved DC magnetometric performance, since the magnetic field sensitivity scales as $1/\sqrt{T^*_2}$.

[11] M. ,W. Doherty *et al.*, "The nitrogen-vacancy colour centre in diamond," *Physics Reports* **528**, 1–45 (2013).

B

ODMR AND SPAD CONTROL SOFTWARE

This code has been developed within the Quantum Integration Technology (QIT) research group (Ishihara Lab) in TU Delft, as part of the MEP thesis of Dylan Aliberti (dylan.aliberti@gmail.com), titled *"Characterization of Single-Photon Avalanche Diodes and Integration with Diamond for Quantum Bio-sensing"*, and the PhD research project of Ioannis Varveris (ynsvrv@gmail.com), titled *"Quantum sensing and fabrication of color centers in diamond: Toward a quantum biosensor based on CMOS-integrated NV centers"*. This code is intended to be viewed and used by subsequent lab users/researchers and should not be distributed without prior permission by the authors.
The online version can be found on GitHub:
`https://github.com/ynsvrv/ODMR_and_SPAD_control_software`

B.1. OVERVIEW

The code consists of two main parts:

- **Confocal-scan control and processing**
  Python scripts for 2D scans and z–scans:
  - `ODMR_2D.py` [data acquisition for 2D scans]
  - `ODMR_2D_process.py` [processing and plotting of the acquired data]
  - `z_scan.py` [z–scan acquisition]

  When setting up a measurement, edit the parameter dictionary at the top of `ODMR_2D.py`, or supply a JSON file path. Outputs are saved as `.npy` and JSON metadata.

To view results, type in the terminal (example):

```
python3 ODMR_2D_process.py /home/user/measurements/scan1.npy
```

B

These scripts depend on the modules:

`point_in_triangle.py` and
`double_dip_fitter.py`

- **SPAD-array readout**
  The control code for the SPAD array includes FPGA, Arduino, and Python modules. Readout scripts provide both full-array and single-SPAD modes, and the Arduino package offers a frame-generation test program so the Python reader can be exercised without actual FPGA or chip hardware. Since this code is tailored to the current setup, parameters will need to be adjusted when testing new SPAD or FPGA revisions. If you are interested in using this code to test new SPAD hardware, feel free to contact the author at dylan.aliberti@gmail.com.

B.2. HOW TO USE THE CODE

This section covers only the confocal scan part; for SPAD-array details, please contact the author.

B.2.1. GENERAL PROCEDURE FOR A 2D SCAN AND DATA VIEWING

This procedure assumes the diamond is mounted on the piezo stage. Part of the workflow uses external TNO alignment code (commands prefixed `rtcs`). Valid for the setup as of December 2024; hardware or software changes may require adaptation.

LAUNCHING GUI AND SETTING UP

After mounting:

1. In a terminal, run: `rtcs gui`
2. Auto-zero all piezo axes.
3. Flip down the pellicle beamsplitter, turn on camera and LED (set LED to 12 mA).
4. Move the piezo stage slowly in $+z$ to find the LED double-square focus ($\pm$ surface).

DETERMINING TILT

Move by a few millimeters in x (and separately in y) and note the required Δz to refocus the LED. The tilt is $\Delta z/\Delta x$ (and $\Delta z/\Delta y$). Enter these values (in mm per mm) as `ax` and `ay` in `ODMR_2D.py`.

FINDING THE EXACT SURFACE FOCUS

1. Turn off LED, turn on laser.
2. Use the camera to focus the laser spot (fine z steps, $\sim 12\,\mu$m offset from LED focus).
3. (Optional) Do a z–scan: two count-rate maxima mark the top and back surfaces. Investigate any disagreement between camera focus and scan peaks.
4. Record the (x_0, y_0, z_0) of the laser focus point for the scan script.
5. Turn off camera and raise the pellicle beamsplitter.

B.2.2. CHECKING ODMR

In the terminal, type:

```
rtcs esr-scan --show --num-sweeps 1
```

Adjust parameters as needed. Use `-help` to list available options.

B.2.3. PREPARING AND RUNNING THE MEASUREMENT SCRIPT

1. Open `ODMR_2D.py`
2. Set `ax, ay, x0, y0, z0`
   and other parameters (steps, sweeps, `measurement_type`, etc.).
3. In the terminal, type: `cd/home/dl-lab-pc3/Dylan/`
4. Then, to run the measurement type: `python3 ODMR_2D.py`
5. Monitor the runtime estimate and PL readings after each sweep.

B.2.4. VIEWING ACQUIRED DATA

After completion, note the output file path (e.g. `data.npy`). Then type:

```
python3 ODMR_2D_process.py   path/to/data.npy
```

First, ten random pixels are shown for quick quality check; then the full 2D plots appear one by one. Close each window to advance. All figures are saved with the original filename as a prefix. Make sure the data is available locally (in the computer), in OneNote/OneDrive, and also synchronized with a data storage unit in the cloud (e.g. `U:\QIT Research Data\Username`).

B.2.5. CUSTOMIZING PLOTS

To change titles, fonts, units or clipping thresholds, edit the calls to `plot_map(...)` in `ODMR_2D_process.py`. Update units and conversion rates consistently.

C

CLEANROOM PROCESS MANUALS

C.1. KN WET BENCH PROCESSES

C.1.1. CLEANING WITH FUMING HNO_3

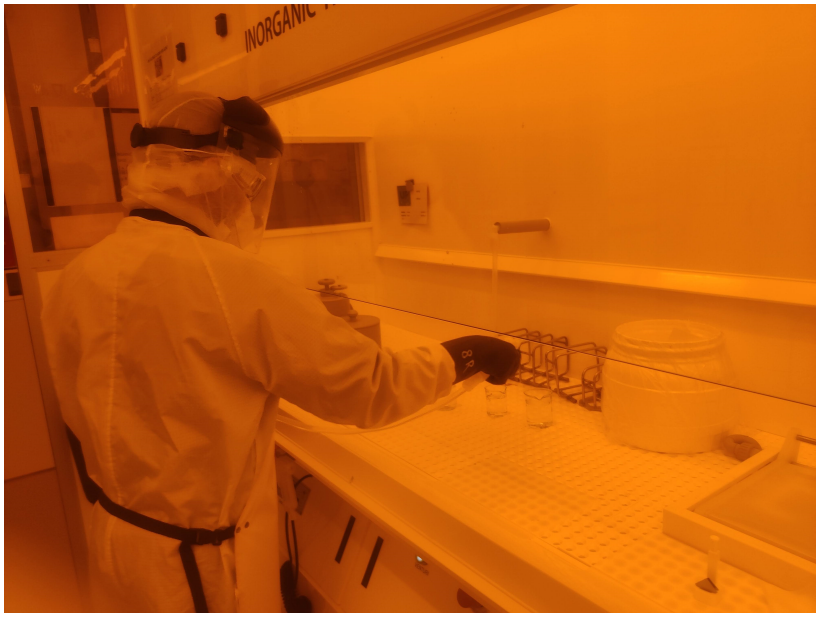
Buddy required **v3.1 (10-09-2021)**

1. Clean your faceguard with ethanol, put it on, and don an apron.
2. Press the `Window up` button at the wet bench for 2 seconds.
3. Place two tissues at the edge of the wet bench.
4. Label a 50 mL to 80 mL beaker for HNO_3 with your name and the corresponding chemical, and place it inside the bench.
5. Label two 100 mL beakers for H_2O and place them to the right of the HNO_3 beaker.
6. Lay out your sample holder and white tweezers on a clean tissue.
7. Retrieve your sample from its case and mount it in the holder.
8. Don **black gloves** and test them for leaks with the N_2 gas gun.

---

9. Arrange the beakers near the center of the draft chamber to leave room for safely handling HNO_3.
10. Fill the water beakers about half to three-quarters full using the water gun.
11. Open the chemical locker (black handle), lift out the HNO_3 bottle with both hands, bring it into the bench, then close the locker.
12. Carefully open the HNO_3 bottle, set the cap down facing down, and pour enough acid into its beaker to submerge your sample holder.

13. Reseal the acid bottle, set it aside, and rinse its neck downward (three gentle rotations) with the water gun.
14. Blow the rinsed bottle dry with the N_2 gun.
15. Place a tissue under the bottle, wipe away any droplets, return the bottle to the locker shelf, and discard the tissue.
16. Using tweezers, lower the sample holder into the HNO_3 beaker and have a colleague ("buddy") time 2 min.
17. Transfer the holder into the first water beaker for 2 min, then into the second water beaker for 2 min.
18. If the second rinse remains acidic (test using pH paper with the help of your buddy), rinse and refill it via the Venturi system until near neutral pH.
19. Remove the holder, place it on a tissue, extract the sample, and dry it with the N_2 gun.
20. Return the sample to its case via tweezers (ask your buddy to help you out).
21. Pour one quarter of the used HNO_3 into each water beaker in turn.
22. Refill the empty HNO_3 beaker with water.
23. Activate the Venturi system by using the button above the shelf (not with your fingertips) and drain each beaker.
24. Refill all beakers to three-quarters full and repeat the Venturi rinse three more times.
25. Invert each beaker, spray with water, then blow dry with the N_2 gun.



26. Repeat the rinse and dry steps for the sample holder and tweezers.
27. Place all cleaned glassware and tools (facing down) in the Used Glassware cabinet and close it.
28. Spray the work area inside the chamber with water, wipe with a tissue, and discard it.
29. Rinse your gloved hands with water, then remove and properly stow the black gloves, while avoiding contact with the exterior.
30. Remove and return your apron.
31. Clean the faceguard again with ethanol and return it.

C.1.2. SPIN-COATING WITH E-BEAM RESISTS

Buddy not required **v1.1 (29-07-2021)**

1. Press the `Window up` button for 2 seconds.
2. Place two tissues at the left edge of the bench.
3. Label a 30 mL to 50 mL beaker for your resist and set it on a tissue.
4. Lay out a syringe and its cap on a separate tissue.
5. Open the bottom drawer, select a spin chuck for your sample, and mount it on the spin-coater.



6. Using tweezers, center your sample on the chuck.
7. Press `VAC` to secure the sample.
8. Power on the hotplate at 50%–60% and set the temperature per your resist's spec.
9. Choose the spin recipe matching your resist and desired thickness (refer to bench notes for RPM codes).
10. Don **PE gloves**.

---

11. Retrieve the EBL resist bottle, place it on a tissue, and close the cabinet.
12. Open the resist bottle and pour a small amount into the beaker.

13. Draw resist into the syringe, expel air into a tissue, recap, and repeat until bubble-free.
14. Deposit a couple of drops around the chuck, then coat the sample surface evenly.
15. Close the spin-coater lid.
16. Press the recipe start button (`I` under `VAC`).
17. When the display reads “END” (3/3), open the lid.
18. Transfer the sample to the hotplate, close its cover, and start the bake timer.
19. After baking, return the sample to its case.
20. Power off the hotplate.
21. Bring the organic-waste bottle to the bench, discard any leftover resist from the syringe into the bottle, then discard the syringe.
22. Rinse the resist beaker with acetone into the waste bottle, then rinse again.
23. Store the used beaker in the Used Glassware cabinet.
24. Return the waste bottle to its cabinet.
25. Wipe any spilled resist from the bottle with a tissue and return it.
26. Soak a tissue in acetone and clean the chuck thoroughly.
27. Repeat the acetone wipe for all spin-coater components.
28. Remount the parts and stow the chuck in its drawer.
29. Discard tissues and PE gloves.



C.2. KN LITHOGRAPHY PROCESSES

C.2.1. ACCESSING TERMINAL, BEAMER & UPLOADING .gpf FILES TO EBPG TERMINAL

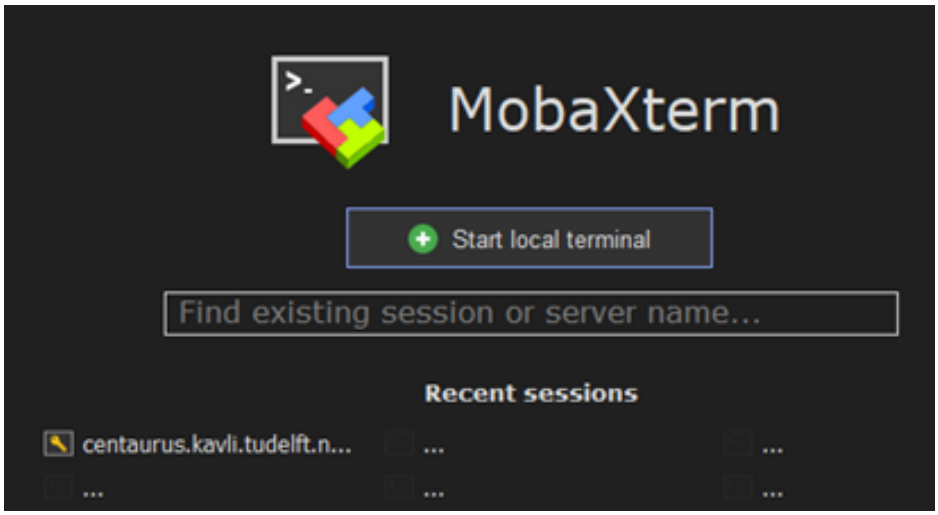
Buddy not required **v2.1 (12-09-2022)**

PATTERN DESIGN

1. Create your design in KLayout (or any CAD tool).
2. Save the design as a `.gds` file.

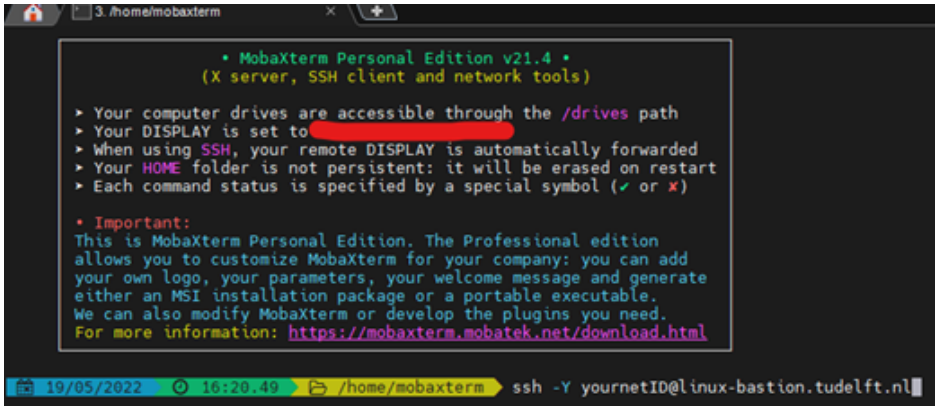
ONE-TIME SETUP OF THE TERMINAL

1. Install and launch MobaXterm (or equivalent).
2. Click `Start local terminal`.

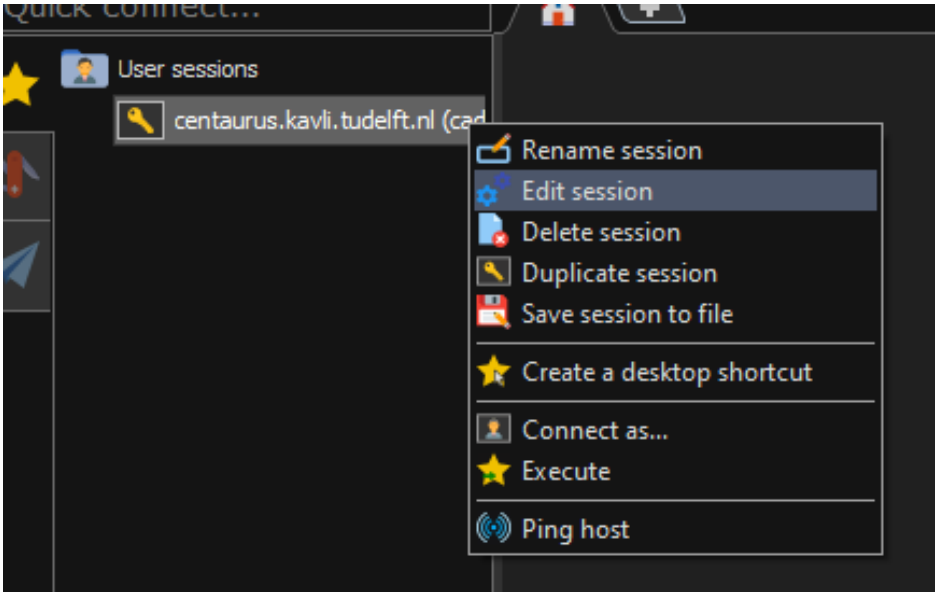


3. In the prompt, run:

```
ssh -Y yournetID@linux-bastion.tudelft.nl
```



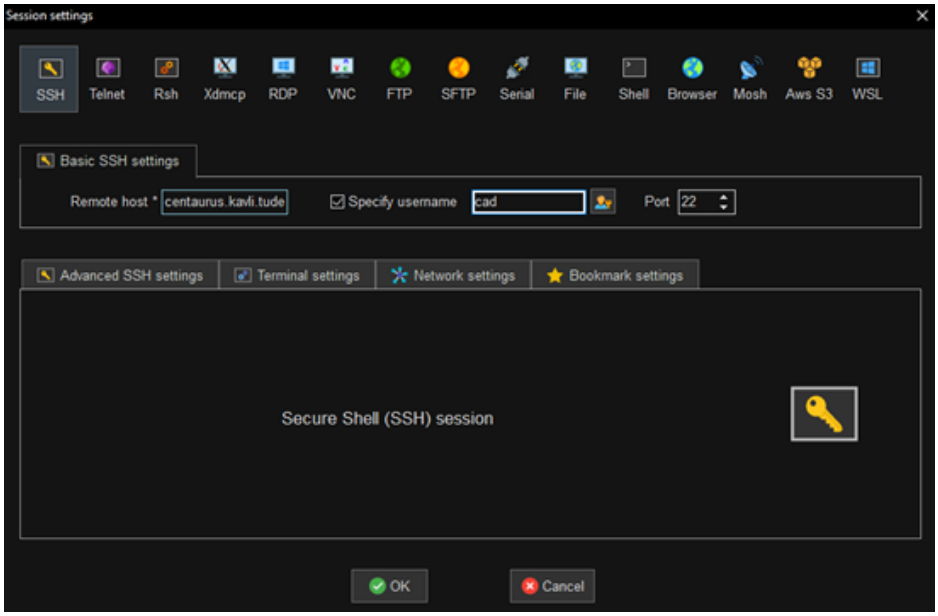
4. Enter your TU Delft password.
5. Then run:
   ```
   ssh -Y cad@centaurus.kavli.tudelft.nl
   ```
6. Enter the password when prompted (contact the responsible KN staff member).
7. Edit your session settings:



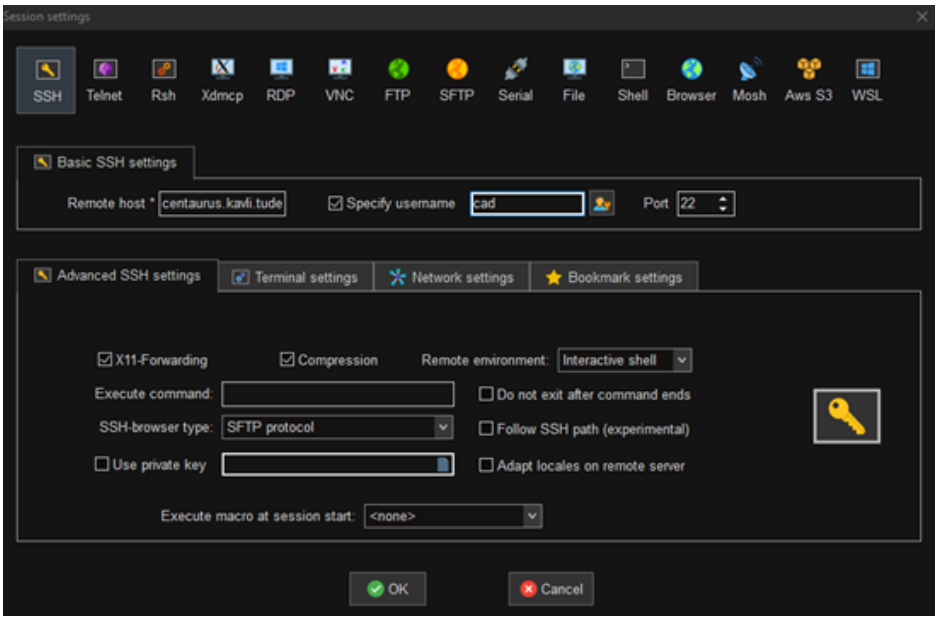
8. Go to **SSH** tab → **Basic SSH settings** and type in:

Remote host:	`centaurus.kavli.tudelft.nl`
Username:	`cad`
Port:	22

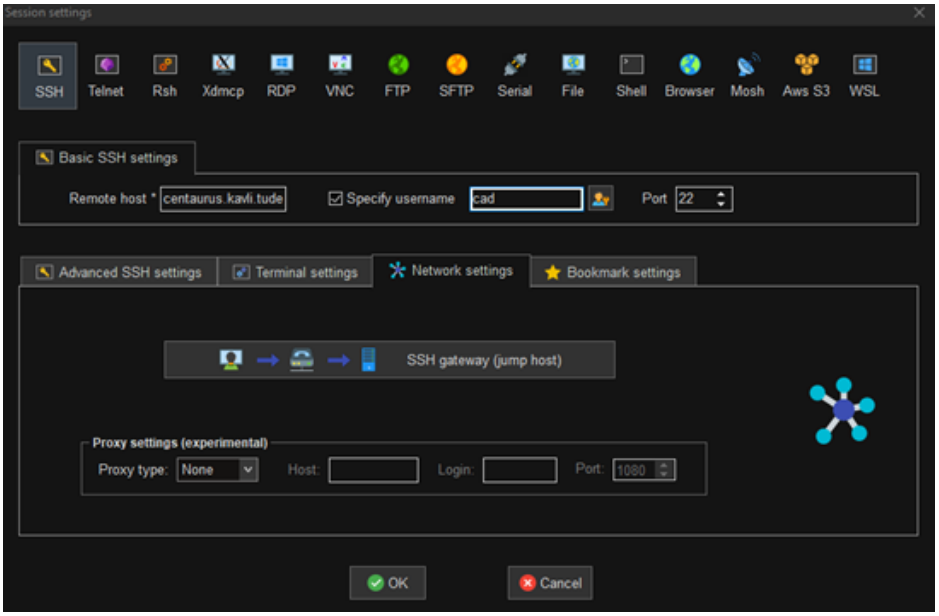
C


Session settings
SSH
Telnet
Rsh
Xdmcp
RDP
VNC
FTP
SFTP
Serial
File
Shell
Browser
Mosh
Aws S3
WSL
Basic SSH settings
Remote host *
centaurus.kavli.tude
Specify username
cad
Port
22
Advanced SSH settings
Terminal settings
Network settings
Bookmark settings
Secure Shell (SSH) session
OK
Cancel

9. Under **Advanced SSH settings** make sure that:
    - **X11-Forwarding** is enabled
    - **Compression** is enabled
    - **Remote environment** is set to **Interactive shell**
    - **SSH-browser type** is set to **SFTP**



10. Go to **Network settings**



11. Click on **SSH gateway (jump host)** and type in:

Gateway host:	`linux-bastion.tudelft.nl`
Username:	`yournetID`
Port:	22

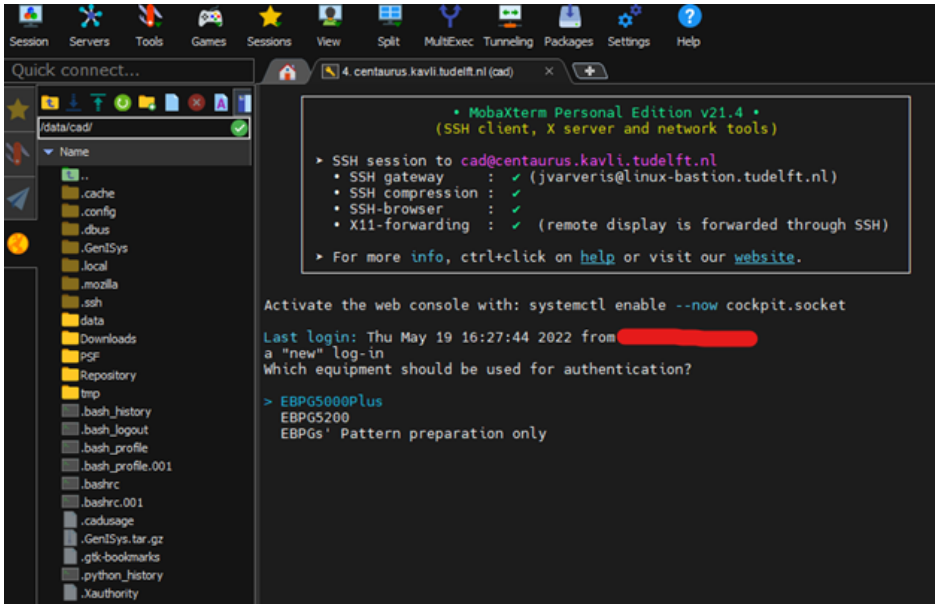


12. Click **OK** to save the session.

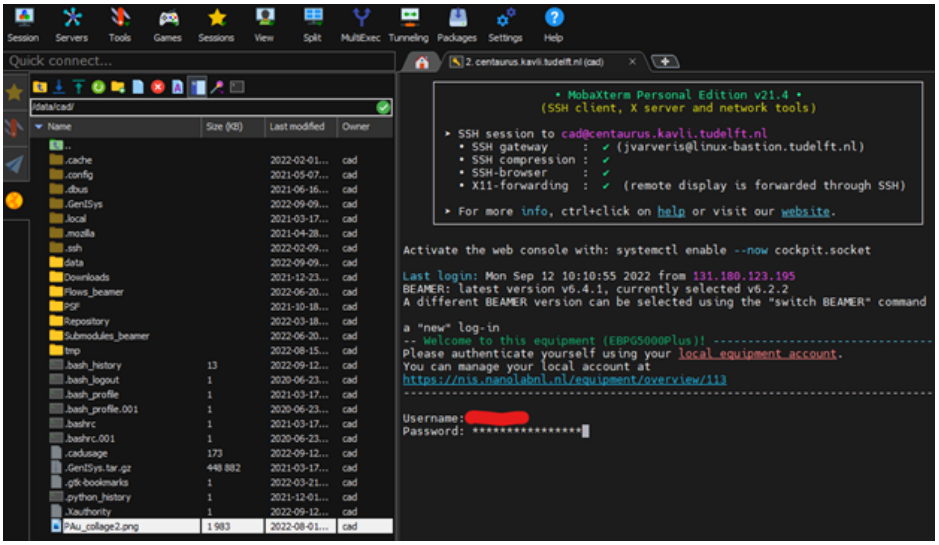
You can skip the above setup in the future by reusing the saved session.

WORKING IN THE TERMINAL & BEAMER

1. Launch the saved session and select `EBPG5000Plus`.

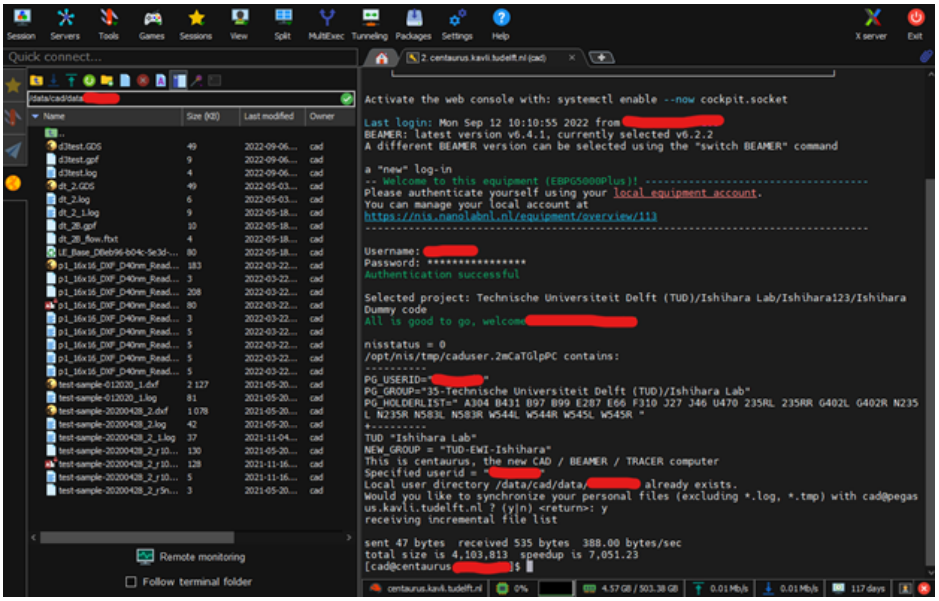


2. Authenticate with your NIS credentials.



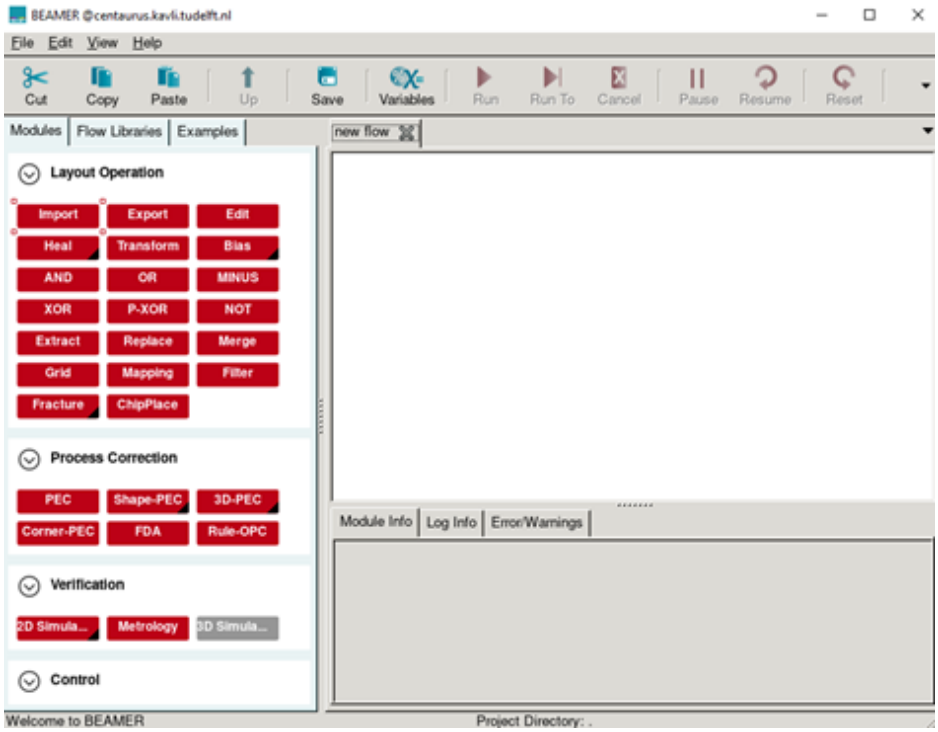
3. After having created a `.gds` file, navigate to your data folder:

   `/data/cad/data/username/`

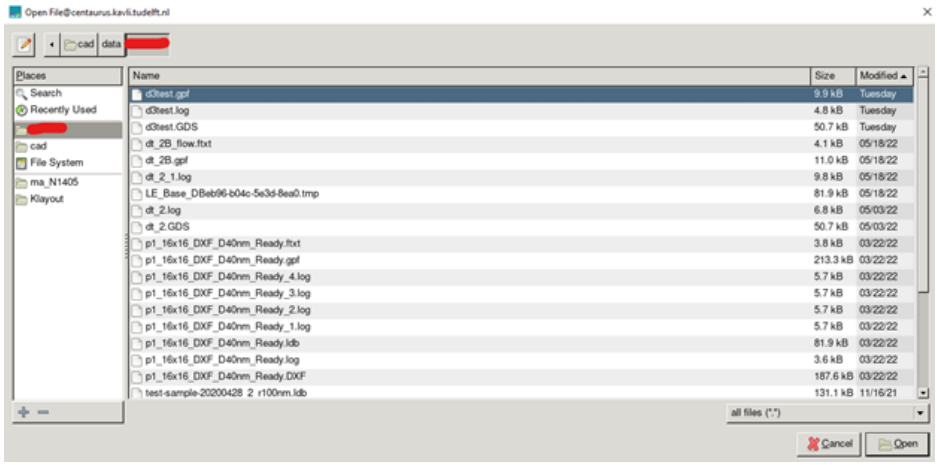


4. Drag your `.gds` file into this directory.

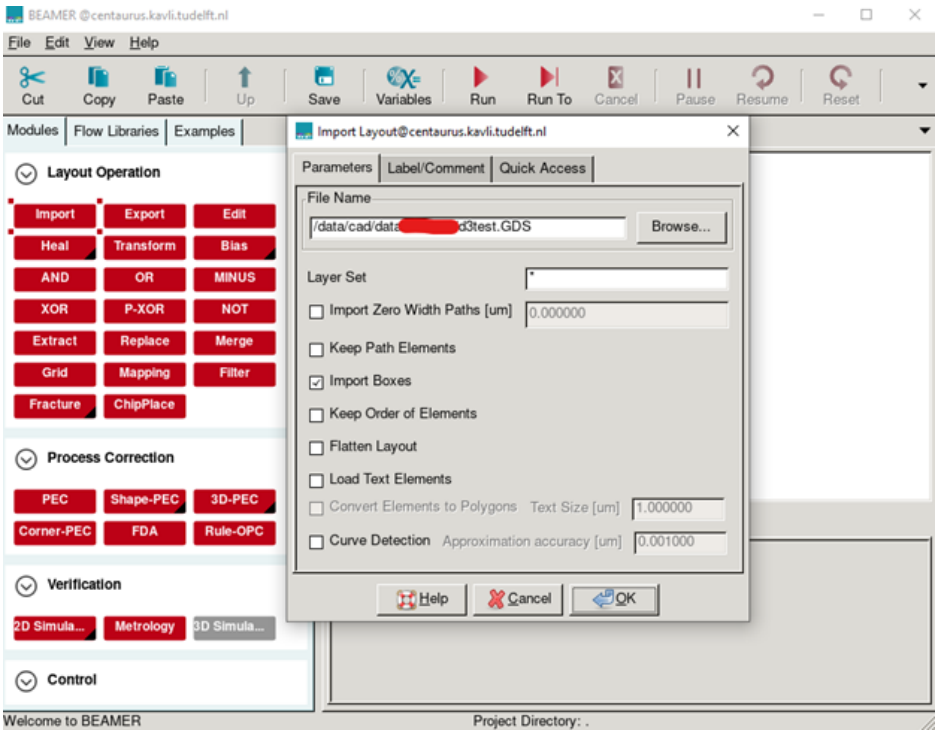
5. At the prompt, type `BEAMER` to start the GUI.



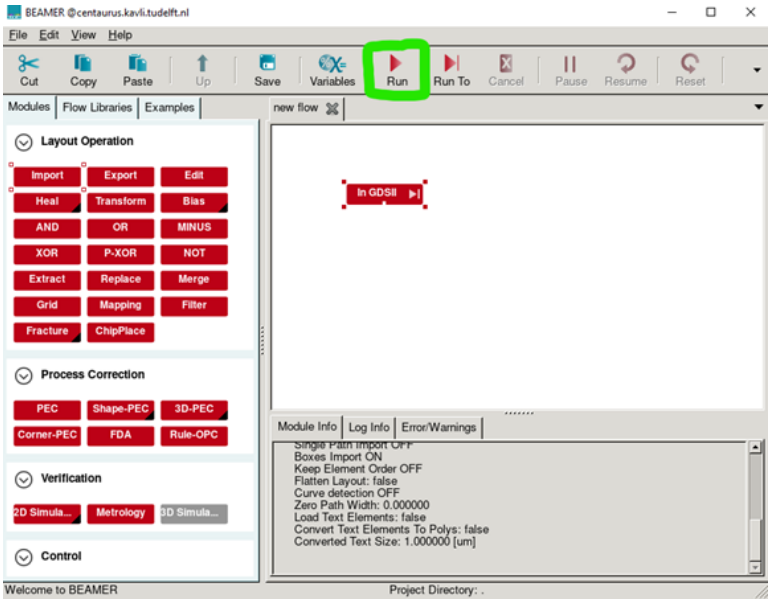
6. While In BEAMER, click **Import**, drag to **new flow**, and open your `.GDS` file.



7. Find and **Open** your `.gds` file. Click **OK** on the pop-up window.

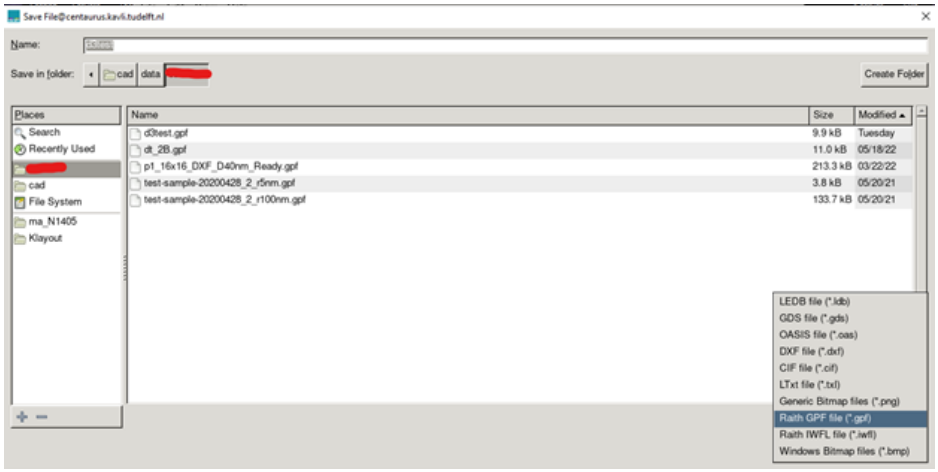


8. Click **Run**.

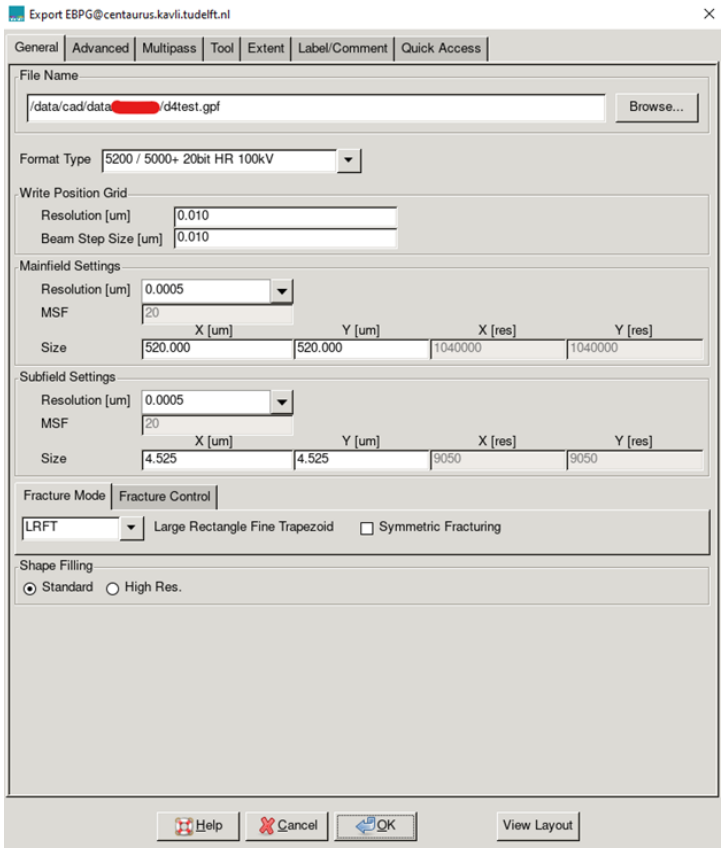


9. Drag and drop **Export** onto the **In GDSII** icon you created.

10. Name and save the output as a `.gpf` file.



11. The following window will pop-up:



12. In the parameter dialog, choose the appropriate parameters for your exposure:

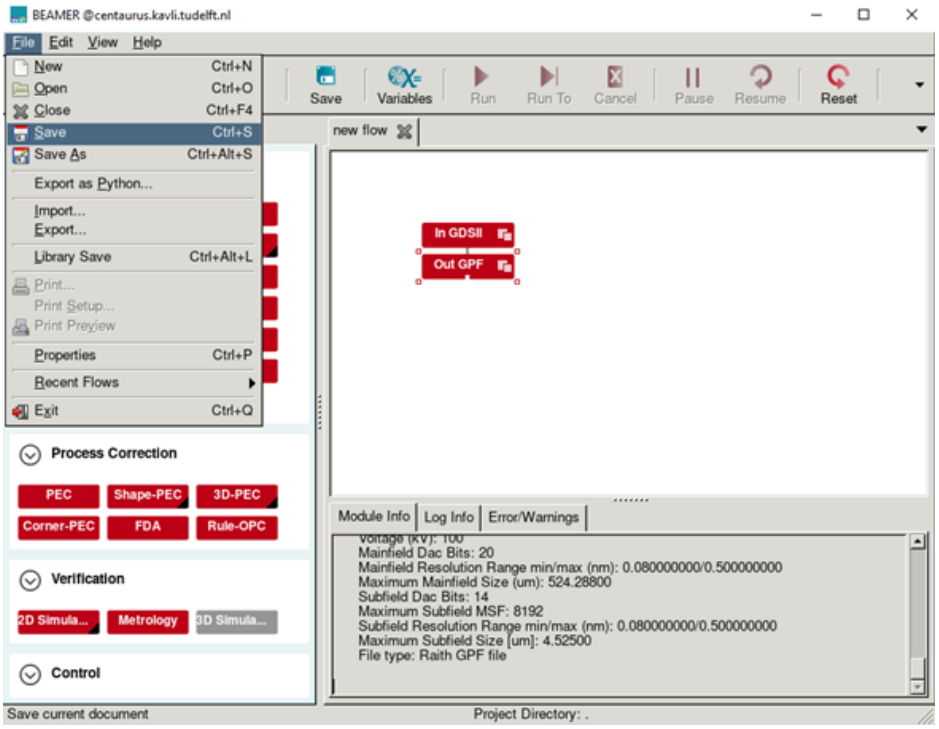
    - **Format type:**
        - `5200 / 5000+ 20bit HR UPG 100kV` or
        - `5200 / 5000+ 20bit HR 100kV`

- Calculate your **Beam step size (BSS)**: Assume d [nm] is the smallest feature in your pattern, then use:

$$\text{BSS} = \frac{d/4}{1.5}$$

- Choose similar **resolution**.

13. Click **OK** and then **Run**.
14. Save your process flow (**File** → **Save**)



15. Exit BEAMER and return to the terminal.
16. Useful shell commands:

`ls -1`	List files one per line
`ls`	List files horizontally
`ll`	Long listing (detailed file info)
`pwd`	Print current working directory
`cd /path/to/dir`	Change directory to the given path
`lo`	Logout from the remote session
`exit`	Exit the terminal

17. To transfer your `.gpf` file to the EBPG system, run:

```
putp5k filename.gpf
dirp5k filename.gpf
```

ACCESSING THE EBPG5000+ TERMINAL

You can access the EBPG5000+ terminal remotely or locally.

1. From your MobaXterm, launch your EBPG5000+ session, and then type:
   ```
   ssh -Y pg@epic-alfa.kavli.tudelft.nl
   ```
2. Enter the password (contact the responsible KN staff member).
3. Launch the job editor with:
   ```
   cjob
   ```
4. When finished, type `lo` or `exit` to log out.

MORE ADVANCED BEAMER AND JOB INSTRUCTIONS

- **Layout BEAMER:** In Phoenix terminal, run `LB`. Drag an "import" box, load your GDS, set layer/datatype 0–255, then "run" or "single step." Use "view layout" to inspect. To split for multiple resolutions, add a "split" box and follow with "extract."
- **Creating a writing job:** Run `cjob &`, choose substrate, add layout or exposure, configure heightcheck, dose update, pattern file, beam, and save as `.cjob`. Then export as `.job`. Check exposure time before submitting.

C.2.2. EBPG5000+ PROCESS

Buddy not required **v2.1 (18-02-2022)**

INITIAL SETUP

1. Verify the EBPG5000+ is powered on and no other user is logged in.
2. Log into the terminal with your username and password.
3. If necessary, enter `oper` to switch to OPER (operator) mode.
4. Mount your sample on an appropriate holder (see Figure C.1), and record the holder ID and sample position (e.g. W544L).

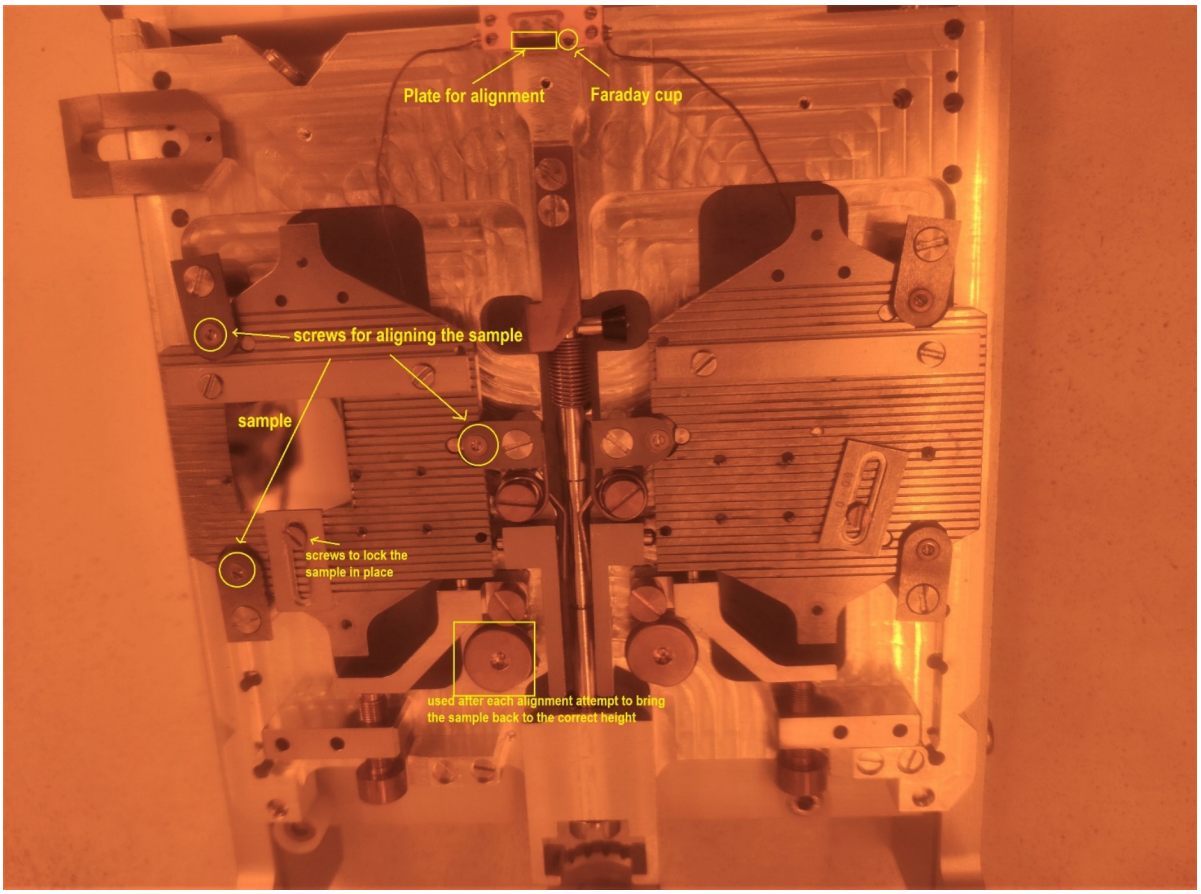


Figure C.1: Sample mounting holder.

ALIGNMENT

1. Secure the sample to the holder using the correct screwdriver.
2. Place the holder on the microscope stage and rotate the holder's lock screw to horizontal.
3. Turn on the microscope light and alignment laser (Figure C.2).

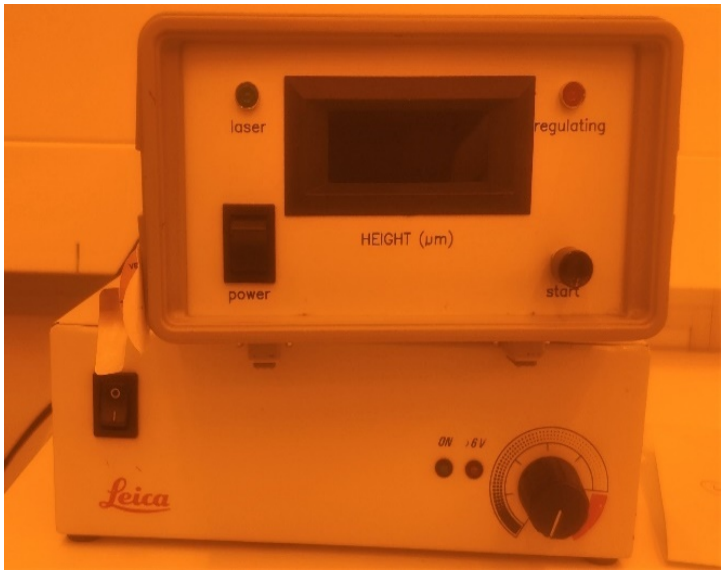


Figure C.2: Microscope light control system (bottom) and laser control system (top).

4. Direct the laser onto the metallic alignment plate (left of the Faraday cup) and note the height reading.
5. Point the laser at each corner of the sample, recording each height; all readings must agree within 10 µm.
6. Adjust sample tilt via the three holder screws and re-lock the holder after each adjustment.
7. Once aligned, switch off the laser and center the microscope light on the Faraday cup.

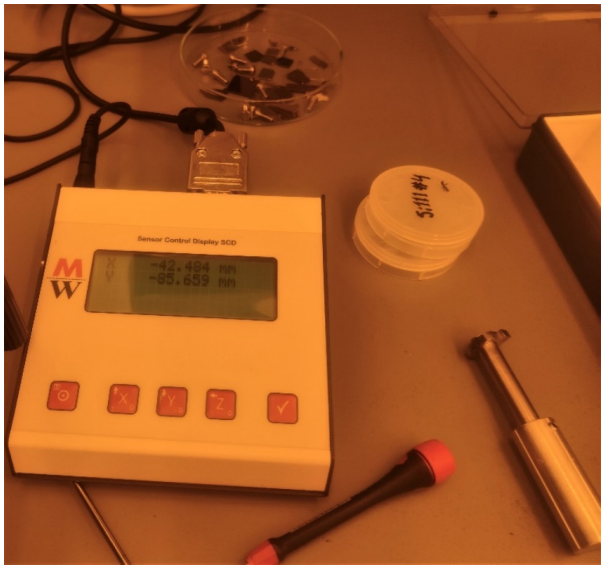


Figure C.3: Coordinate-measuring device.

8. Press the X & Y buttons on the coordinate-measuring device to zero at the cup center (Figure C.3).

9. Move the light to the sample's bottom-left and top-right corners, record (x, y) for each, and compute the average $\bar{x}, \bar{y}$.

10. Turn off the microscope light, return the holder lock to vertical, and remove it.

VENTING, PUMPING & LOADING

1. On the touch screen next to the EBPG5000+ tool, press `SET LOCK VACUUM` to vent

2. Wait for the V8 valve to cycle gray → green → gray.

3. Open the door by the handlebar, load the holder cassette (mind orientation), then close the door (Figure C.4).

4. Press the same button to re-pump the system.

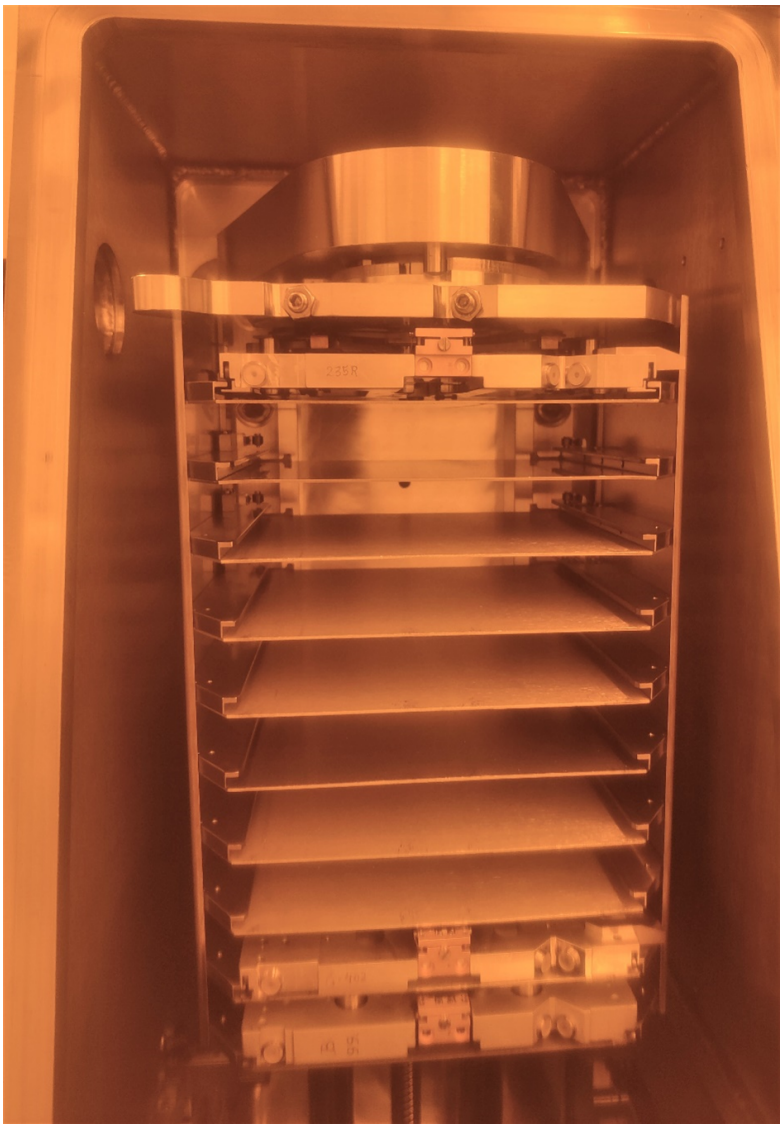


Figure C.4: Cassette-loading station within the EBPG5000+ tool.

EXPOSURE VIA TERMINAL

1. Place the magnetic pin corresponding to your holder on the whiteboard.
2. Open the terminal. If your pattern is not prepared in advance, run `cjob` to configure it (Figure C.5).

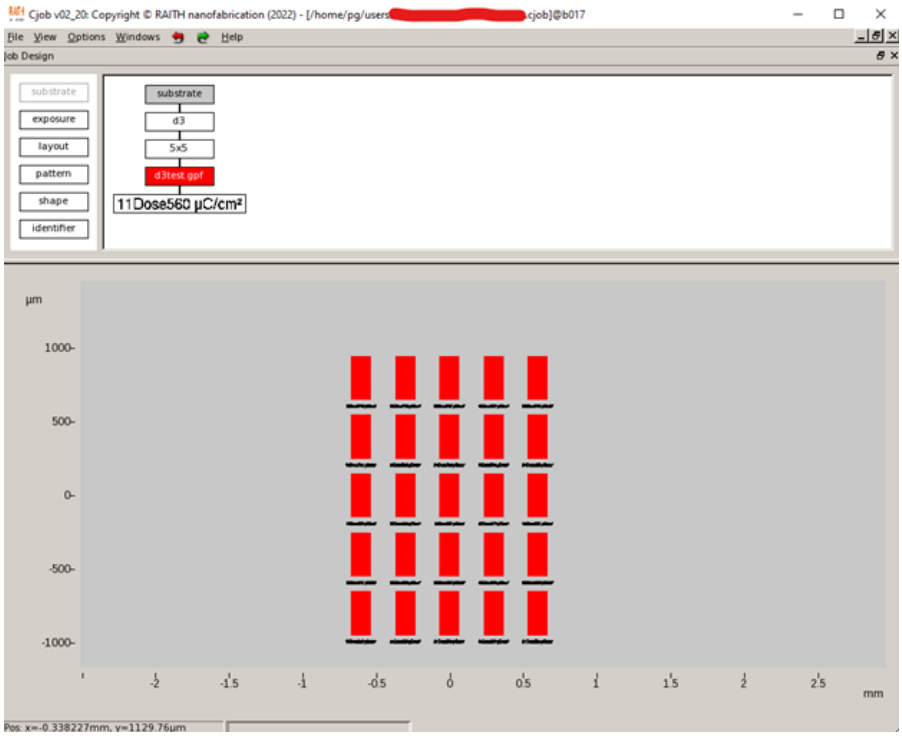


Figure C.5: Editing a "job" on the EBPG5000+ terminal.

3. When ready and pumping is complete, launch exposure with:

   ```
   batch FILENAME.job
   ```

   Optionally schedule it for a specific time (e.g. 15:30) via:

   ```
   batch FILENAME.job -a 15:30
   ```

4. Switch to SUPER mode by typing `super` and answer any [Y/N] prompts.
5. Provide the requested information as prompted, and press **Enter**:
   - Holder name (e.g.**W544L**)
   - Load/unload cassette position number (e.g. **4**)
   - Reference point: choose **F** for Faraday cup
   - Coordinates $\bar{x}, \bar{y}$ calculated earlier (in µm) (e.g. **55696, -40212**)
6. The exposure will then begin. When it finishes, repeat the venting and unloading steps, return the holder, re-pump the system, and logout with `lo`.

D

DIRECT BONDING PROCESSING PARAMETERS

D.1. ADDITIONAL PARAMETER TABLES

Parameter	Value
Diameter	100 ± 0.3 mm
Surface finish	Single-side polished
Grade	Prime
Flats	2, SEMI-Std
Growth Method	CZ (Czochralski)
Total Thickness Variation (TTV)	< 5 µm
Type/Dopant	N/Ph
Orientation	$\langle 100 \rangle \pm 0.5°$
Resistivity	1–5 $\Omega \cdot$ cm
Thickness	525 ± 15 µm
Bow	< 30 µm
Warp	< 30 µm
Particles	< 10 @ 0.3 µm
Producer	www.siegertwafer.com

Table D.1: Specifications of the silicon Wafer.

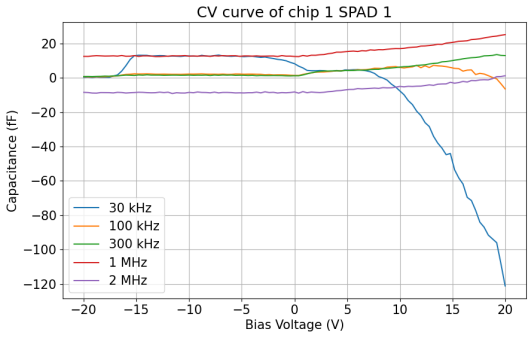
Parameter	Recipe Value
N_2 flow rate	3.15 sccm
SiH_4 flow rate	0.21 sccm
TN_2O flow rate	6.00 sccm
Deposition rate	3745 Å/min
High frequency power	1 kW
Pressure	2.2 Torr
Temperature	400 °C

Table D.2: PECVD process conditions for depositing 300 nm SiO_2 on a silicon wafer.

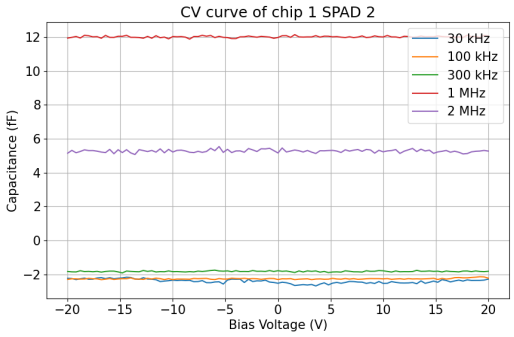
E

CV-IV Plots

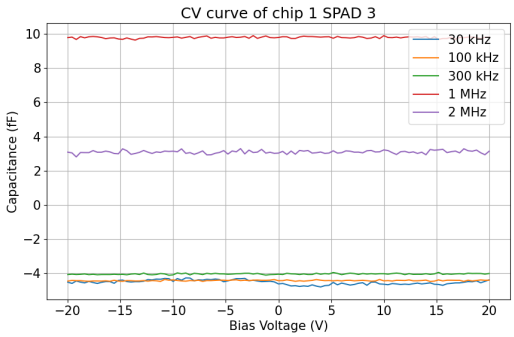
E.1. CV plots



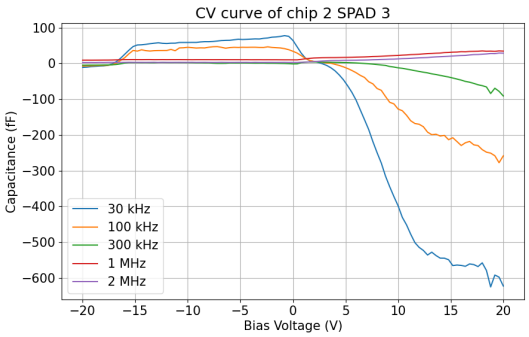
(a) Chip 1: SPAD 1



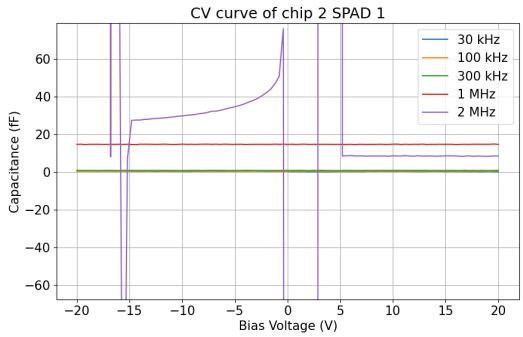
(b) Chip 1: SPAD 2



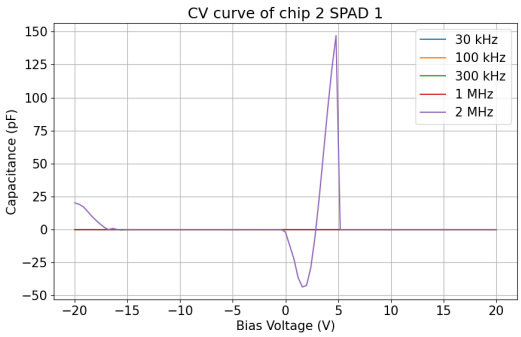
(c) Chip 1: SPAD 3



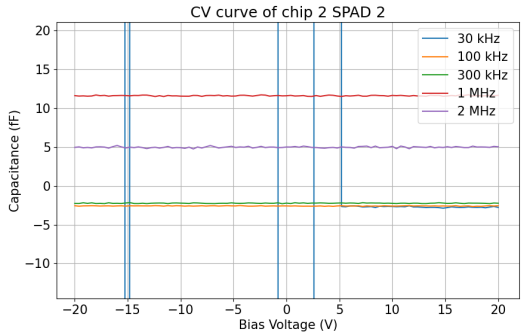
(d) Chip 2: SPAD 3



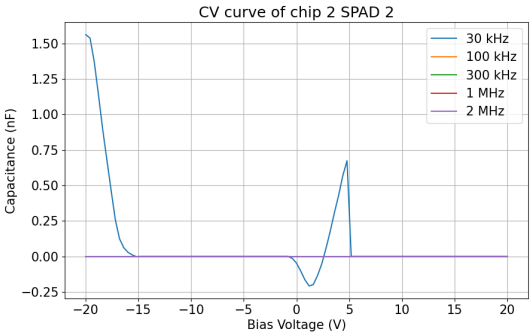
(e) Chip 2: SPAD 1 (zoomed-in view)



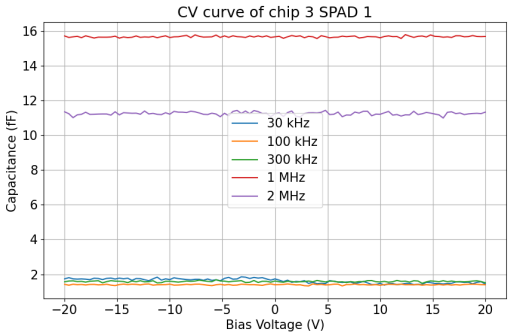
(f) Chip 2: SPAD 1



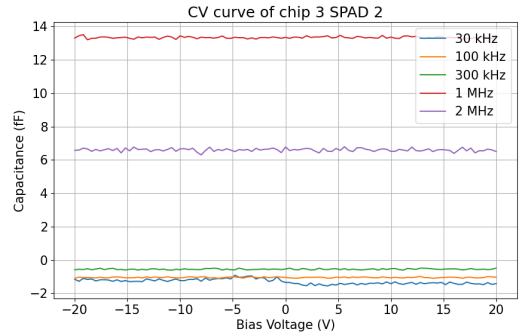
(g) Chip 2: SPAD 2 (zoomed-in view)



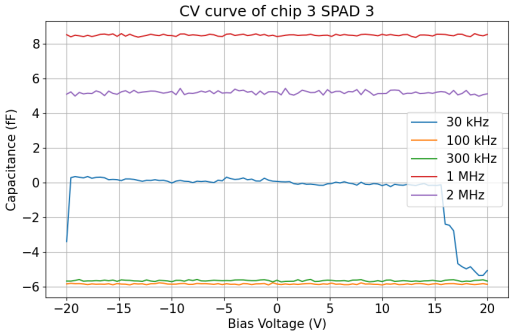
(h) Chip 2: SPAD 2



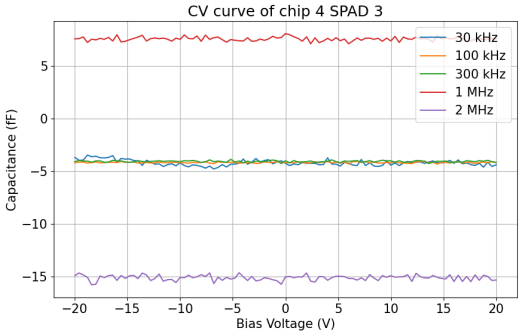
(i) Chip 3: SPAD 1



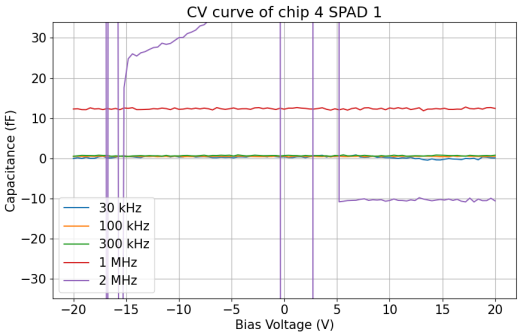
(j) Chip 3: SPAD 2



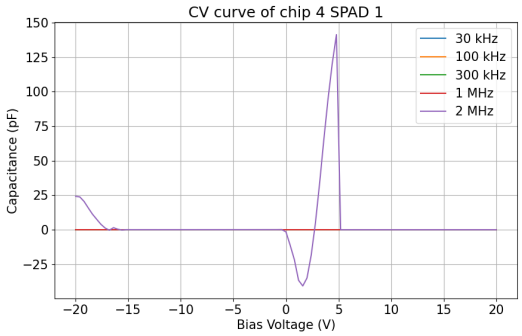
(k) Chip 3: SPAD 3



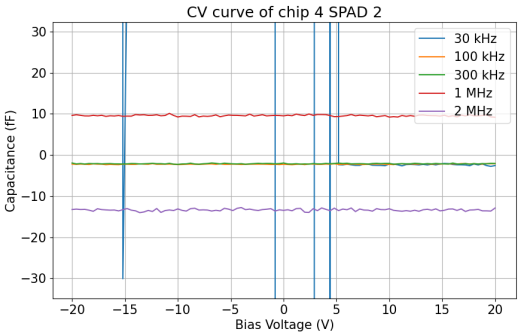
(l) Chip 4: SPAD 3



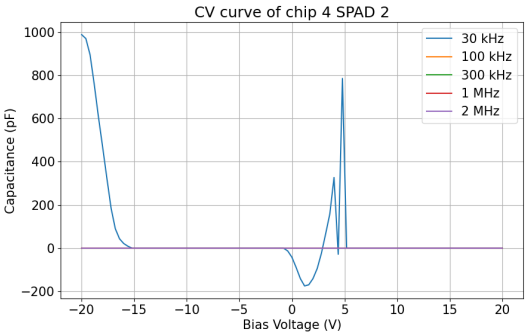
(m) Chip 4: SPAD 1 (zoomed-in view)



(n) Chip 4: SPAD 1

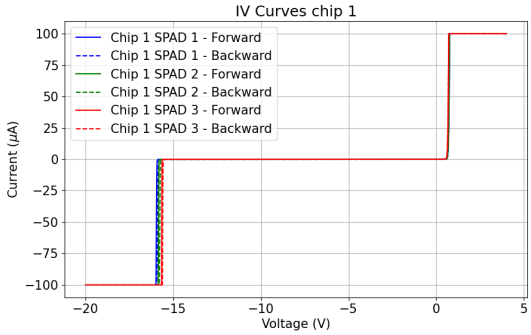


(o) Chip 4: SPAD 2 (zoomed-in view)

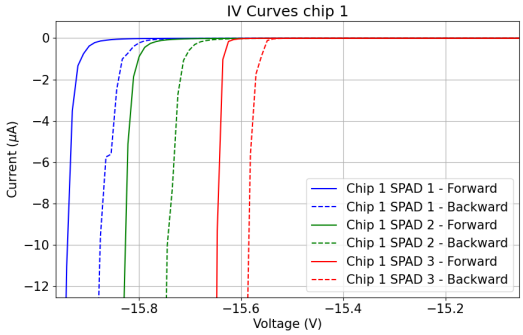


(p) Chip 4: SPAD 2

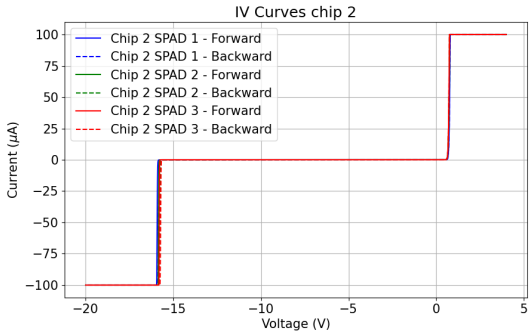
E.2. IV PLOTS



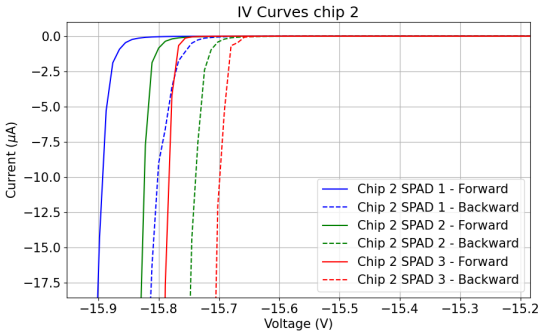
(a) Chip 1



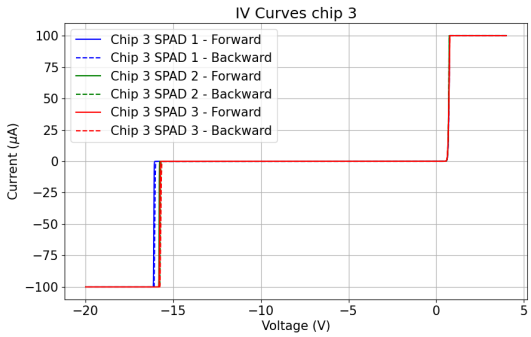
(b) Chip 1 (zoomed-in view)



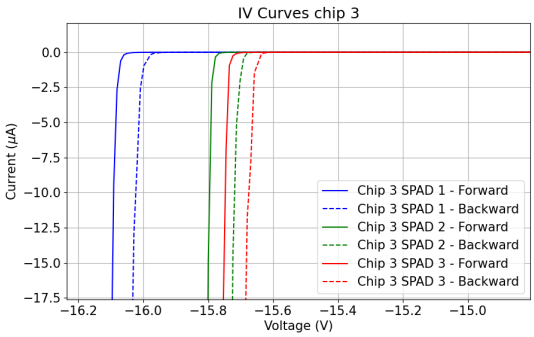
(c) Chip 2



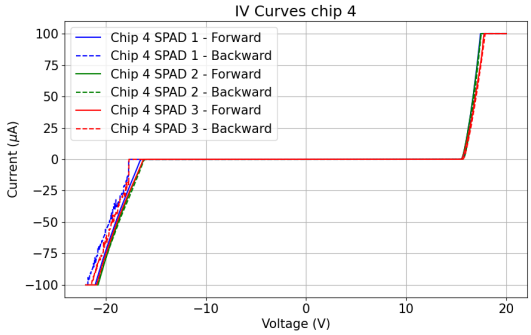
(d) Chip 2 (zoomed-in view)



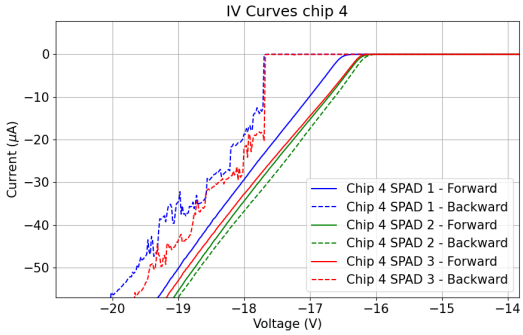
(e) Chip 3



(f) Chip 3 (zoomed-in view)



(g) Chip 4



(h) Chip 4 (zoomed-in view)

List of Publications

6. *Toward a CMOS-integrated quantum diamond biosensor based on NV centers*
   I. Varveris*, G. D. Aliberti*, S. Nur, R. Ishihara
   IEEE Transactions on Quantum Engineering (2026). Submitted.

5. *Strain Effects in a Directly Bonded Diamond-on-Insulator Substrate*
   I. Varveris, G. D. Aliberti, T. Chen, F. A. Sfetcu, D. J. W. Dekker, A. Schuurmans, N. K. Nitzsche, S. Nur, R. Ishihara
   Physica status solidi (a) (2025). Published.

4. *Femtosecond Laser-Induced Activation of Tin-Implanted Diamond: Insights from a Two-Temperature Model and Optical Characterization*
   E. L. Görk, J. Thieme, A. Miranda, **I. Varveris**, N. K. Nitzsche, T. Chen, L. D. A. Siebbeles, R. Ishihara, S. Nur
   European Optical Society Annual Meeting (EOSAM 2025). Abstract accepted.

3. *Near-deterministic placement of nitrogen-vacancy centers in diamond for quantum biosensing*
   I. Varveris, S. Nur, N. K. Nitzsche, S. Fakkel, R. Ishihara,
   RAISIN Workshop 2023, University of Surrey. Poster presentation abstract.

2. *Temperature dependent photoluminescence (PL) emission in $CsPbBr_3$ single crystals: micro-PL profiles and transient effects*
   A. G. Kontos, **I. Varveris**, M. Panagopoulou, M. Karnachoriti, V. Arsenis, D. Y. Chung, W. Lin, M. G. Kanatzidis, Y. S. Raptis
   Micro-Nano 10th International Conference (2023).

1. *Slow transient dependence of photoluminecence in $CsPbBr_3$ single crystals*
   I. Varveris, A. G. Kontos, M. Karnachoriti, D. Y. Chung, W. Lin, M. G. Kanatzidis, Y. S. Raptis
   XXXV Panhellenic Conference on Solid State Physics and Materials Science, Congress Center, NCSR "Demokritos" (2021).

* Equally contributing authors

CURRICULUM VITÆ

Ioannis Varveris

February 12th, 1994
Cholargos, Athens
Greece

2020–2025 **PhD in Experimental Physics & Engineering**

QuTech & Department of Quantum & Computer Engineering (QCE), Delft University of Technology, Delft, The Netherlands

Thesis: *Quantum sensing and fabrication of color centers in diamond: Toward a quantum biosensor based on CMOS-integrated NV centers*

Promotor: Dr. R. Ishihara

Copromotor: Dr. S. Nur

2012–2020 **Integrated Master's Degree**

School of Applied Mathematical and Physical Sciences, National Technical University of Athens (NTUA), Athens, Greece

Thesis: *Photoluminescence Spectroscopy Measurements of the $CsPbBr_3$ and $CsSnBr_3$ Perovskites*

Advisors: Prof. I. Raptis & Prof. A. Kontos

2009–2012 **High School**, 1st General Lyceum of Drapetsona, Greece

